Terahertz Diffractive Optics

Edward D. Walsby

A thesis presented for the degree of
Doctor of Philosophy
in
Electrical and Electronic Engineering
at the
University of Canterbury,
Christchurch, New Zealand.

July 2003

ABSTRACT

Terahertz radiation research is an emerging field with significant work only being possible in the last decade with the development of new high speed laser equipment. Sources of terahertz are a continuing problem however several methods now available are making this technology more reliable and less expensive. With these developments much research is being conducted into the potential applications of this window in the electromagnetic spectrum. An integral part of any such application is the ability to focus and manipulate beams. Traditional optics systems achieve this with reflective, refractive or diffractive elements the later of which has not been utilised in the terahertz frequencies and is the subject of this thesis.

The wavelength range of terahertz waves of the order of hundreds of micron make fabrication difficult with milling or machining. Planar fabrication techniques using microfabrication technology have been used to create micro-optics for much shorter wavelengths. This project has involved developing a microfabrication process that can be applied to the large structure sizes and depths required at terahertz frequencies. High diffraction efficiency demands the structuring of multiple level structures. This was achieved using a repeated binary fabrication process in silicon. A set of Fresnel lenses were produced and some anti-reflection structures to demonstrate the application of this technology to the formation of high quality terahertz diffractive optics.

Different applications may demand the use of either a continuous wave or pulsed emission and detection. An appreciation of the devices' performance in a single frequency and pulsed broadband system is given. These systems were set up for the measurements of anti-reflection gratings and both single and pairs of Fresnel lenses of varying complexity. These results demonstrate potential uses as frequency and or spatial filters and focusing elements for tomography applications.

Using Fresnel and Fraunhofer diffraction theory lenses have been simulated to further explain the results measured and to give an appreciation of how design modifications can be used to improve the efficiency. Because the fabrication process described is tailored for the construction of a broad range of optics in the terahertz frequency range there are a wide range of potential feature sizes and etch depths. A general guide to how processing defects inherent in the microfabrication process can effect lens performance is investigated to give a designer tolerances to remain within during production.

ACKNOWLEDGEMENTS

Completing this dissertation would not have been possible without the help and support of many people from around the world for which I am most grateful. I am extremely grateful to my supervisor Dr Richard Blaikie for his insightful discussions and unique ability to coordinate people and resources to have formed a most successful Nanotechnology research group of international repute. I also wish to thank my co-supervisor Dr Steve Durbin for his continued optimism and support throughout this project. I would like to acknowledge Dr David Cumming for proposing the original idea of introducing diffractive optics into the terahertz frequency range.

I am most appreciative of the enthusiasm and support of Dr Xi-Cheng Zhang who has devoted much time and the resources of his staff and research group at Rensselaer Polytechnic Institute. I am privileged to have been given access to the world class terahertz facilities of his department. In particular I must thank Shaohong Wang, Tao Yuan and Dr Jingzhou Xu for the amazing amount of time they have contributed to this project.

I wish to thank Karsten Siebert and Dr Hartmut Roskos for providing access to their continuous wave terahertz equipment and devoting their time to help get this system set up to facilitate CW measurements. I also am most grateful to Mark Thompson for assistance tuning this system and for his discussions on terahertz theory and simulation.

A lot of equipment has been used for the fabrication of the terahertz diffractive optics and I am indebted to Helen Devereux and Gary Turner for maintaining the microfabrication laboratory and for sharing their knowledge about this equipment and processing issues. I am also most appreciative of the help of Neil Andrews for his assistance with scanning electron microscopy used for imaging of the structures in this thesis.

I would like to acknowledge the continuing support of the Marsden Fund and the New Economy Research Fund for the grants that have enabled this work to be completed and presented at a number of international meetings.

I have been most fortunate to receive the good friendship and support of many fellow students during this project. I would particularly like to thank Jullada Homtientong, Ken Ma, Jared Peterson, Simeon Everitt, Lenny, Andrew Reid, Phillip Barclay,

Nikki O'Connor and Tim Llewellynn.

Lastly I would like to acknowledge the fantastic support continued interest of my family. I am most appreciative of the help I have received from Charles, Anthony and Fausta. The amazing assistance of my parents throughout my years of study is something I will be forever grateful for.

PREFACE

This dissertation describes work undertaken at the Department of Electrical and Electronic Engineering between March 2000 and July 2003. During this period research was also conducted at the Physikalisches Institut at the Johann Wolfgang Goethe-Universitat in Frankfurt, Germany and at Rensselaer Polytechnic Institute Center for Terahertz Research, in Troy, New York, USA.

Terahertz radiation has the potential to revolutionise a number of application areas however there is still significant research to be conducted to convert conceptual ideas into financially viable propositions. This work provides another tool to terahertz researchers in the form of diffractive terahertz optics. Development of this concept in the terahertz frequency range gives previously unachievable beam manipulation.

Aspects of this dissertation were presented at the following international conferences:

The 13^{th} International Conference on Ultrafast Phenomena, Vancouver, May 12-17, 2002.

The 46^{th} International Conference on Electron, Ion and Photon Beam Technology and Nanofabrication, Anaheim, May 28-31, 2002.

OSA Conference on Diffractive Optics and Micro-Optics, Tucson, June 3-6, 2002.

International Conference on Advanced Materials and Nanotechnology, Wellington, February 9-14, 2003.

and published in the following journals and proceedings:

E. D. Walsby, S. Wang, B. Ferguson, J. Xu, T. Yuan, R. J. Blaikie, S. Durbin, D. R. S. Cumming and X-C. Zhang, Investigation of a THz Fresnel Lens. In *Ultrafast Phenomena XIII*, 292-294, 2002.

S. Wang, E. D. Walsby, T. Yuan, J. Xu, R. J. Blaikie, D. R. S. Cumming, S. M. Durbin and X.-C. Zhang, Characterization of T-ray Binary Lenses. In *Optics Letters*, 27, 1183-1185, 2002.

E. D. Walsby, S. Wang, J. Xu, T. Yuan, R. J. Blaikie, S. Durbin, D. R. S. Cumming and X-C. Zhang, Multilevel Silicon Diffractive Optics for Terahertz Frequencies. In *J. Vac. Sci. Technol. B.*, 20, 2867-2871, 2002.

E. D. Walsby, R. J. Blaikie, S. M. Durbin and D. R. S. Cumming, Analysis of Silicon Terahertz Diffractive Optics. To be published in *Current Applied Physics*, 2003.

E. D. Walsby, T. Yuan, S. Wang, J. Xu, R. J. Blaikie, S. M. Durbin, X. -C. Zhang and D. R. S. Cumming, Silicon Diffractive Optics at THz Frequencies. In *Diffractive Optics and Micro-Optics Tech. Dig.*, 75-77, June, 2002.

Associated research using technology developed in this work has been published in the following journals:

S. Wang and X.-C. Zhang, Tomographic imaging with a terahertz binary lens. In *Applied Physics Letters*, 82, 1821-1823, 2003.

Y. Wang, W. Yun and C. Jacobsen, Achromatic Fresnel optics for wideband extreme-ultraviolet and x-ray imaging. In *Nature*, 24, 50-53, 2003.

CONTENTS

LIST OF FIGURES

LIST OF TABLES

Chapter 1

INTRODUCTION

1.1 A BRIEF HISTORY OF THE ELECTROMAGNETIC SPECTRUM

Humanity's fascination with and manipulation of the electromagnetic spectrum has evolved over several millennia with records from ancient Egypt of mirrors dating back to 1900 B.C. It took some time for theories to evolve that explained the behaviour of visible light and it is only in the last two centuries that knowledge of and research into the non visible parts of the electromagnetic spectrum have been explored.

The law of reflection was first described in 300 B.C. by Euclid. In Optica, Catoptrics he described the rectilinear propagation of light. He believed that vision involves rays going from the eyes to the object seen and he studied the relationship between the apparent sizes of objects and the angles that they subtend at the eye. Refraction was first studied by Cleomedes (50 A.D.) and later described by Claudius Ptolemy some 90 years later. In his work a study of refraction, including atmospheric refraction, was described. It was suggested that the angle of refraction is proportional to the angle of incidence. Research into optics then languished for over a millennia until the thirteenth century when Robert Grosseteste, Bishop of Lincoln, and Polish mathematician Witelo conducted investigations into reflection and refraction of light. Amongst other things, Witelo described a method of machining parabolic mirrors from iron and carried out careful observations on refraction. He recognised that the angle of refraction is not proportional to the angle of incidence but was unaware of total internal reflection. Roger Bacon extended Grosseteste's and Witelo's work on optics. He considered that the speed of light is finite and that it is propagated through a medium in a manner analogous to the propagation of sound. In Opus Maius, Bacon described his studies of the magnification of small objects using convex lenses and suggested that they could find application in the correction of defective eyesight. He attributed the phenomenon of the rainbow to the reflection of sunlight from individual raindrops.

In 1621 Willebrord Snell discovered the relationship between the angle of incidence and angle of refraction when light passes from one transparent medium to another.

This law of refraction was first published in terms of sines by Rene Decartes in what is today known as Snell's law $\sin i/\sin i' = c$ where i is the angle of incidence and i' is the angle of refraction.

The seventeenth century saw many great physicists such as Fermat, Descartes, Galileo, and Sir Isaac Newton conduct further investigation into the actual nature of light, supporting either a particle or wave theory. In this period Professor Francesco Grimaldi made the first observations of the diffraction of light. That being, the deviation of rectilinear light occurring when it passes beyond an obstruction. Also in this period Christiaan Huygens made the important conclusion that light effectively slows down when travelling in a more dense medium. Augustin Jean Fresnel continued the work of Huygens on the wave nature of light. In 1816 he presented a rigorous treatment of diffraction and interference phenomena showing that they can be explained in terms of a wave theory of light. As a result of investigations by Fresnel and Dominique Francois Arago on the interference of polarized light and their subsequent interpretation by Thomas Young, it was concluded that light waves are transverse and not, as had been previously thought, longitudinal. Several years later in 1819, Joseph Fraunhofer from Germany described his investigations of the diffraction of light by gratings which were initially made by winding fine wires around parallel screws. He later went on to publish his theory of diffraction in 1823. Around the same time Fresnel presented the laws which enable the intensity and polarization of reflected and refracted light to be calculated by his now famous formulae.

At the time Fresnel and Fraunhofer were determining the wave theory of reflection, refraction and diffraction of light, Danish physicist Hans Christian Oersted found that if he moved a wire carrying an electric current near a magnetic compass needle, the needle tended to turn at right angles to the wire. This was the first direct evidence that electricity and magnetism were physically related, leading to the onset of research into elctromagnetics and the discovery of the electromagnetic spectrum. In the following four decades, other physicists studied this relationship in more detail. Many of them tried to develop a theory to explain exactly how electricity and magnetism were related, but they encountered great mathematical and experimental problems.

In 1871 John William Strutt, third Baron Rayleigh presented a general law which related the intensity of light scattered from small particles to the wavelength of the light when the dimensions of the particles is much less than the wavelength. He also made a 'zone plate' which produced focusing of light by Fresnel diffraction.

Several years prior to this, James Clerk Maxwell from Scotland had been devoting time to the study of electromagnetics, culminating in the publication of his results in their complete form in a book in 1871 [1]. From his studies of the equations describing electric and magnetic fields, it was found that the speed of an electromagnetic wave should, within experimental error, be the same as the speed of light. Maxwell concluded

that light is a form of electromagnetic wave which can be expressed in four short equations called Maxwell's equations.

$$\begin{aligned} \nabla \times \widetilde{H} &= \delta\widetilde{D}/\delta t + j \\ \nabla.\widetilde{B} &= 0 \\ \nabla \times \widetilde{E} &= -\delta\widetilde{B}/\delta t \\ \nabla.\widetilde{D} &= \rho \end{aligned} \tag{1.1}$$

where $\widetilde{H}$ is the magnetic field strength, $\widetilde{D}$ is the electric displacement, t is time, j is the current density, $\widetilde{B}$ is the magnetic flux density, $\widetilde{E}$ is the electric field strength and ρ is the volume density of charge. Maxwell's equations allowed for the existence of electromagnetic waves with much longer wavelengths than light. No one had suspected the existence of such waves, but this gave the motivation to begin looking for them.

In a series of experiments beginning in 1886, the German physicist Heinrich Hertz proved that these long wavelength electromagnetic waves were real. He showed this when he generated what we now call radio waves with an electric spark, transmitted them the length of his laboratory, and made them produce a smaller spark at his receiver. By showing that these 'Hertzian waves' travelled in beams and could be focused like light rays, Hertz convinced the scientists of his time that he had discovered the long electromagnetic waves that Maxwell's equations predicted. At the time, applications of this discovery were not realised.

In the next decade, on November 8, 1895, a portion of the electromagnetic spectrum with wavelength shorter than visible light was accidentally discovered by William Roentgen. While testing cathode rays to see if they would pass through glass he noticed a glow emanating from a chemically coated screen lying a few feet away. Roentgen named the unknown rays that caused this fluorescence 'X rays'. Intensely researching his discovery for two months he found that X rays could penetrate some substances but not others. During one experiment, Roentgen tested the X-ray absorption of lead. While holding a lead disk up to the source of radiation, he inadvertently exposed his hand to the rays. The resulting shadows on the detecting screen revealed both the impenetrability of lead and the bones in his hand. Roentgen had discovered that X rays penetrate human flesh but not bone, a discovery which to this day is used in medicine.

It was not until the start of the twentieth century, following Hertz's discovery, when Guglielmo Marconi pioneered the world's first radio system. The vast usefulness of this concept led to millions of dollars being spent on research. The onset of World War I accelerated the development of the radio to a point where by the 1920s hundreds of radio stations were broadcasting news and music across the airwaves.

Since the development of these first applications of non-visible parts of the electromagnetic spectrum much research has been conducted to explore all frequencies.

Numerous applications have been devised in the last century utilising specific frequencies to facilitate communication, analysis, detection and manipulation of substances. The absorption spectra of different materials varies and also different frequencies can affect certain molecules uniquely. This means particular sections of the electromagnetic spectrum are ideally suited to specific applications. Conversely, some wavelengths can be damaging to tissue or samples subsequently limiting the extent which they can be used. The ease with which different wavelength radiation can be produced also varies widely.

Terahertz radiation was discovered by Heinrich Rubens and Ernest Fox Nichols at the University of Berlin in 1896 [2]. After Nichols left Berlin, Rubens continued the work, and in 1900 he isolated wavelengths of 6 THz (50 microns) and made careful measurements which he gave to Max Planck, who subsequently derived the Radiation Law. One such region of the electromagnetic spectrum which is quite difficult to produce is the terahertz frequency band ranging from the far infrared at 10×10^{12} Hz to the upper end of the microwave spectrum at 0.1×10^{12} Hz. First efforts to produce the radiation began in the 1970s using non linear photomixing of two laser sources. This was not overly successful and it has not been until the past two decades with recent advances in laser technology that reliable sources of terahertz have become available. What makes these waves so fascinating to scientists is their ability to penetrate materials that are usually opaque to both visible and infrared radiation, and the wealth of spectroscopic information that can be attained using it to analyse material.

1.2 THESIS ROADMAP

This thesis describes the design, fabrication, testing and simulation of terahertz Fresnel lenses. Taking the concept first proposed by John William Strutt in 1871 a high efficiency multiple level Fresnel lens, designed for terahertz operation, is described. Chapter 2 details the methods available to produce terahertz radiation. All these techniques are active areas of research as a cheap and reliable source of terahertz is still actively sought. This gives background into the methods of emission and detection that were used to test the devices made in the course of this work.

Chapter 3 outlines the microfabrication technology used to fabricate the lenses. This highlights the main issues that had to be resolved and developed to enable reliable production of the lenses. This multiple level technology can be specifically applied to the formation of a wide array of multiple level lenses or diffractive optics of any form. The multiple level fabrication technology enables a high diffraction efficiency for the formation of high quality terahertz holographic elements.

Chapter 4 reports the results from testing the lenses in a continuous wave terahertz system. This displays the ability of the lenses to focus and re-collimate terahertz radiation in a two lens system.

Chapter 5 presents a full analysis of a set of lenses of differing complexity. Measurements of the broadband intensity at positions beyond the lens give a relative performance comparison of the lenses. The focusing ability of the binary Fresnel lenses is compared to conventional refractive lenses that are currently used to focus radiation.

Chapter 6 presents simulations of the lenses using Fraunhofer wave propagation. The expected performance of the lenses fabricated and ideal lens structures is determined and compared. These results give further explanation of those results obtained from the physical measurements. Several design parameters are investigated highlighting how performance of the lenses can be optimised.

In Chapter 7 further simulations are conducted to provide an analysis of how processing defects that can arise from the microfabrication technique used can affect the efficiency. This provides general parameters that give a guideline for fabrication tolerances. As the structuring technique is applicable to a wide range of structure sizes these become of more importance in certain designs involving short focal lengths or higher terahertz frequencies. Chapter 8 presents the conclusions of the thesis along with an array of future directions that can be pursued.

Chapter 2

BACKGROUND

2.1 INTRODUCTION

The bounds of the terahertz frequency band lie in the region of electromagnetic spectrum below the infrared and above microwave frequencies. This defines a frequency band spanning from 0.1 to 10 THz equating to the wavelength range of 3 mm, on the boundary of electronics, to 30 μm overlapping the photonics or far infrared band (20 mm to 50 μm). The terahertz frequency band has remained less utilised and developed than the adjacent infra red and microwave fields. The main cause for the lack of development in this field is the lack of good radiative sources. Current sources are available that can provide both continuous wave and pulsed sources of THz. Most of this technology involves the use of laser systems that are prohibitively expensive. Currently this has limited the ability to incorporate the various terahertz applications into marketable products as cheaper competing technologies are favourable. However these sources have evolved over the last few years with advanced materials research that have seen new high power sources become available. There has been research into the production of THz laser sources which have seen the construction of a quantum cascade semiconductor laser. This section aims to provide a review of the current generation and detection technologies that are available and under development and also the immediate applications that appear to lend themselves to this frequency band.

Of the many applications proposed for THz the wavelength of the radiation can be a limiting factor which restricts the resolution attainable. At 1 THz the wavelength is only 0.3 mm and for conventional imaging systems the diffraction limited resolution or spot size is half this value. For some medical applications this may be insufficient to compete with existing technologies (such as x-ray imaging). Because of the benefits available from spectroscopy and the non-ionising nature of the radiation there is still much interest in utilising THz in the medical and biological fields. To a greater extend the resolution difficulties pose only a situational difficulty which in most cases can be overcome through operating in the near field or at higher frequencies. Researchers at

Delft University have recently improved the resolution by a factor of almost 1000. Small focal spots are achieved by using a sharp metal tip to locally bend and concentrate the electric field of the terahertz beam near the surface of a GaP crystal. This technique can be used in terahertz pump probe experiments by placing the samples on the crystal below the tip. The sample is illuminated by the pump beam from above and a tightly focused probe beam from below. Using raster scanning images with resolution as small as 8 μm have been demonstrated and it is envisaged that 1 μm may be possible [3].

2.2 TERAHERTZ EMISSION

Terahertz radiation can be produced with a variety of different techniques including lasers, nonlinear optics and electronics [4]. These bring different benefits, creating either pulsed or continuous wave radiation with a wide range of powers. Terahertz source development is a very active area of research as there is a push to make cheaper sources that can be incorporated into the ever growing list of applications.

The cheap reliable and high power sources that semiconductor lasers have afforded the communications industry have allowed broadband transfer of data across the world. This was enabled because of the microfabrication technologies that facilitated the mass production of cheap lasers. It is envisaged that if solid state laser operation can be extended to the terahertz wavelength range that this will form the most desirable source for most applications [5]. There has been limited success with this with pulsed terahertz lasers created that operate at cryogenic temperatures. Terahertz research is being pursued along multiple avenues, while some groups are working to produce new radiative sources others are working on the development of terahertz technologies and applications. Recent advances in ultrafast laser technology have lowered the cost of pulsed terahertz systems to a point were there is now a commercially available system for medical imaging made by Teraview [6].

2.2.1 Electronic Sources

Traditional electronic sources based on semiconductors such as oscillators and amplifiers are limited by reactive parasitics or transit times that cause high frequency roll off or have simple resistive losses that tend to dominate the devices at the long wavelengths. Electronic sources continue to be developed reaching higher frequencies of operation into the gigahertz regime [7]. Current research involves the development of electronic local oscillators for terahertz radio astronomy, remote sensing, atmospheric imaging and ultra broad-band intersatellite communication. These sources are currently still limited to operation in the lower end of the Terahertz spectrum in the hundreds of gigahertz with submilliwatt powers which limits their usefulness in the broader range of terahertz applications.

2.2.2 Broadband Terahertz Sources

A widely used method for the generation of terahertz radiation involves the production of broadband pulses. The main benefit of such a technique is that spectroscopic measurements can be taken without having to scan the source frequency. The conversion efficiency of these sources is currently low with terahertz powers in the nano to microwatt range being produced from optical sources of 1 W. Two common derivatives of this process are the use of photoconductive antennas or through optical rectification in a crystal with a non-linear response [8].

Terahertz radiation can be emitted by illuminating a gap between two closely spaced electrodes on a photoconductor with an ultrafast pulse to generate free carriers [9]. The electron hole pairs created are accelerated in an applied electric field from an applied voltage to form a transient photocurrent, which in turn results in the emission of a broadband terahertz pulse. Efficient terahertz emision requires short carrier life time meaning a fast photocurrent rise and decay time. The current surge, which is coupled to an RF antenna, has frequency components that reflect the pulse duration, hence a terahertz pulse is emitted. Other parameters that are important in the photoconducting material used are the drift velocity and the breakdown field. These determine the maximum bias that can be applied directly influencing the strength of the terahertz radiation emited. Typical photoconductors include silicon on sapphire, low temperature grown GaAs, InP and radiation damaged silicon wafers. The antennas are formed using microlithography techniques generally in gold in the form of slotlines [10], dipoles [11] or spirals [12]. Using this technique powers over 40 μW have been attained with bandwidths as high as 4 THz generally ranging from 0.2 to 4 THz [13].

Optical rectification is a commonly used alternative terahertz generation mechanism [14]. It has lower power than photoconductive generation but has the benefit of very high bandwidths. Spectra including measurable frequencies up to 50 THz have been reported with this technique. It involves applying short laser pulses to a crystal with a large second order susceptibility (field induced polarisation) [15]. With the nonlinear response of the crystal mixing occurs, producing a time varying polarisation with a frequency response representative of the pulse duration of the incident laser. By using femtosecond pulses terahertz emission is achieved. The most common crystals used are semiconductors such as GaAs and ZnTe although a number of other materials have been experimented with such as GaSe and InP.

2.2.3 Narrowband THz Sources

There are some specific applications where a narrowband high power source is desirable [4]. The telecomunications industry has significant interest in high frequency radiation as it provides the facility for high bandwidth links. First applications of this at terahertz

frequencies should be seen in intersatellite communication although it is envisaged once the field matures that terahertz radiation may be used for high bandwidth microcellular wireless networking. The narrowband terahertz field is largely driven by the space and communication fields although it also finds application in high resolution spectroscopy.

2.2.3.1 Up Conversion

The most common method of producing narrowband terahertz radiation is through up conversion [16]. This involves the nonlinear reactive multiplication of lower frequency microwave oscillators. These can be driven by commercially available microwave oscillators (voltage controlled oscillators), dielectric-resonator oscillators and millimetre-wave upconverters. Current technology typically achieves this using a chain of planar GaAs Schottky-diode multipliers [17]. Multiplier chains driven by amplified sources at 100GHz have reached 1.2 THz with 75 μW at room temperature [18]. Using the same techniques frequencies as high as 2.7 THz have been reported [19]. Research also continues to increase the frequency of Gunn and IMPATT diodes to the lower reaches of the terahertz region, which have been reported as high as 200GHz [20], using alternate semiconducting structures and improved fabrication techniques

2.2.3.2 Dual Laser Photomixing

One method that has shown considerable promise for the efficient production of high power terahertz radiation is heterodyne downconversion or dual laser photomixing [21]. Original investigation into this began in the 1970's using non-linear photomixing of two laser sources, but struggled with low conversion efficiencies [22]. In this technique, two continuous-wave lasers whose centre frequencies differ only slightly are combined in a material exhibiting a high second-order optical non-linearity such as 4-dimethylamino-N-methyl-4-stilbazolium tosylate (DAST) or Ti:sapphire. Mutual interference of the two laser frequencies in the non-linear material results in sum and difference frequencies which can be tuned such that the difference frequency component is in the terahertz band. For the generation of cw-terahertz radiation the beam is then focused on a photomixer such as a LT-GaAs resonant antenna [23, 24]. This arrangement is shown in Figure 2.1

This technique produces cw terahertz radiation with tunability from 0 to 50 THz. The availability of dual colour solid-state laser sources means systems like this could potentially be relatively compact [25]. The advantage over current broadband techniques is that the powers generated are much higher, with output powers in excess of 100 mW demonstrated [26], and the signal to noise ratio achievable is very high.

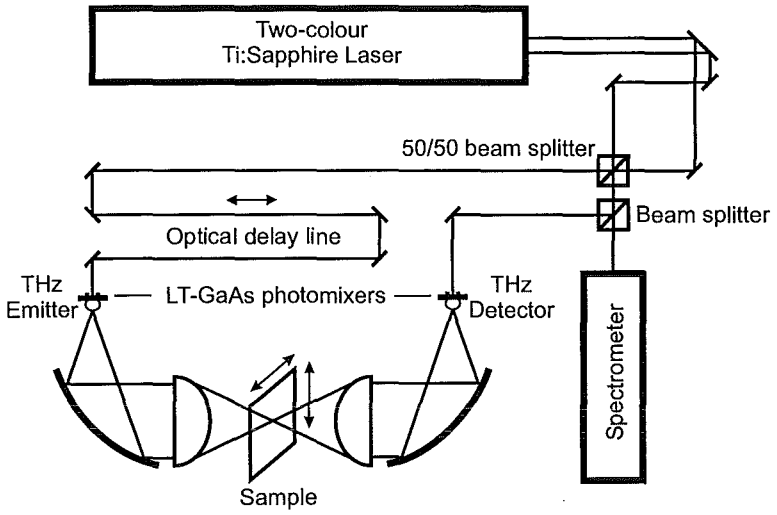

Figure 2.1 Component layout for continuous wave emission and detection.

2.2.3.3 Free Electron Laser

A Free Electron Laser (FEL) is a highly flexible source capable of producing radiation from millimeter waves up to the vacuum ultraviolet [27]. They are appealing as they have high tunability and the facility to produce high output powers with an electronic efficiency of up to 30%. Their main drawbacks are the large size, expense and complexity associated with the system putting them out of reach of most applications. They may generate continuous or pulsed waves, and provide an average brightness of more than six orders of magnitude higher than typical photoconductive antenna emitters. Free-electron lasers have significant potential in applications where improved signal-to-noise ratio is essential, or in the investigation of non-linear THz spectroscopy. Bench-top variations on the same theme, termed backward-wave tubes or carcinotrons, are also capable of providing milliwatt output powers at THz frequencies [28].

A FEL is essentially composed of three parts: an electron accelerator, a magnetic undulator and an optical resonator as shown in, Figure 2.2. They use a beam of high-velocity bunches of electrons propagating in a vacuum through a strong, spatially varying magnetic field. The magnetic field causes the electron bunches to oscillate and emit photons. Mirrors are used to confine the photons to the electron beam line, which forms the gain medium for the laser.

The electrons are forced by the magnetic field on an oscillating trajectory, thus emitting synchrotron radiation. In the electron frame reference the process can also be seen as a scattering between the electron beam and the virtual photons of the undulator. If an external field is present, the radiation is emitted in phase with this external field. The interaction between the laser field, the static magnetic field of the undulator and

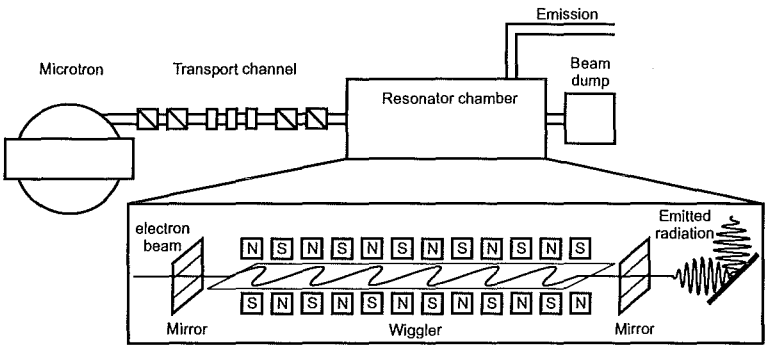

Figure 2.2 Free Electron Laser components.

the electron beam has as a final effect the spatial bunching of the electrons on the scale of the radiation wavelength, and the transfer of energy from the electron beam to the laser field. The undulator can be considered as the equivalent of the 'active medium' of a conventional laser system, while the electron beam is the equivalent of the 'pumping system'

2.2.3.4 Semiconductor Lasers

Lasers rely on the chemical properties of the materials they are made from to produce radiation at specific frequencies. Excitation of the material with either current or energy from light excites its electrons from one energy level to another. These electrons then lose the extra energy as they drop back down from this energy level by emitting a photon [29]. The bandgap required for a terahertz laser is much smaller than that required for conventional lasers as the energy difference is about 100 times smaller. It is possible to alter the size of the energy jumps an electron makes by trapping it in a thin layer of semiconductor material such as gallium arsenide [30]. The thickness of the layer determines the size of the jump allowing the creation of transition energies that are otherwise impossible. Such layers can be grown with atomic precision using molecular beam epitaxy. The first reports of terahertz laser emission were in lightly doped p-type germanium as a result of hole population inversion induced by crossed electric and magnetic fields [31]. These lasers are tunable by adjusting the magnetic field or external stress. Terahertz lasing in germanium has also been demonstrated by applying a strong uniaxial stress to the crystal to induce the hole population inversion [5].

A quantum cascade laser is made by making many of these layers on top of each other to create a superlattice. The structure consists of many coupled quantum wells (nanometre-thick layers of GaAs sandwiched between potential barriers of AlGaAs) [32]. In the repeating structure each repeat unit is made up of an injector and an active region. This synthetic crystal then acts as a material with an artificial energy

transition which can be used as a laser medium [33]. When a voltage is applied across it, electrons are forced to emit light at the frequency determined by the layer thickness in a 'quantum cascade'. In the active region a population inversion exists and electron transition to a lower energy level occurs, emitting photons at a specific wavelength. The electrons then tunnel between quantum wells and the injector region couples them to the higher energy level in the active region of the subsequent repeat unit. This technology has been used to create semiconductor lasers at frequencies that were previously unachievable and much research is being conducted to extend this concept to the terahertz band [34, 35].

Quantum cascade lasers have been demonstrated within the infrared spectrum, but until very recently several significant problems had prevented THz quantum cascade lasers from being realized. The principal problems are caused by the long wavelength of THz radiation. This results in a large optical mode, which results in poor coupling between the small gain medium and the optical field, and in high optical losses owing to free electrons in the material. One of the main problems with the semiconductor lasers is the terahertz radiation generated tends to get absorbed by the materials that create it. This has been overcome through the use of waveguides placed into the super lattice at regular intervals. This channels out the terahertz radiation before it is reabsorbed into the semiconductor lattice. Kohler et al. addressed these and other problems in their recent design of a THz quantum cascade laser operating at 4.4 THz. The laser consisted of 104 repetitions of the basic unit (shown in Fig. 3) and a total of over 700 quantum wells [36].

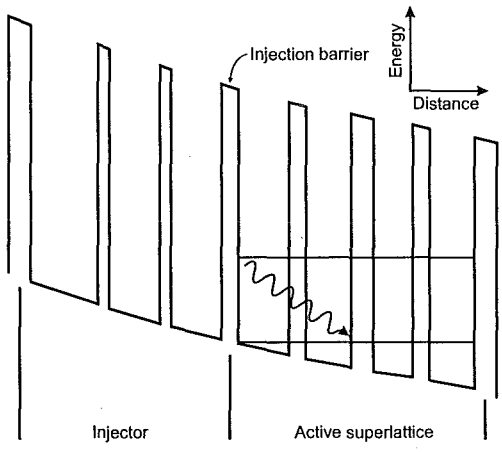

Figure 2.3 Simplified conduction band structure of the THz quantum cascade laser [36]. Electrons are injected through the AlGaAs injection barrier into the level 2 energy state of the active region. The active transition from level 2 to level 1 results in the emission of terahertz photons.

A quantum cascade laser operating at 3.4 THz with liquid nitrogen has been demon-

strated by researchers at the Massachusetts Institute of Technology [37]. The device can emit pulses at a maximum temperature of 87 K with a 1 mW power at liquid nitrogen temperature, 77 K. With helium cooling it can achieve a maximum power of 3.4 mW. This laser consists of 175 cascaded four-well modules created using GaAs/AlGaAs using molecular beam epitaxy. These lasers are a very promising future source of terahertz radiation, however there is still significant work required to make them viable for most applications.

2.3 DETECTION

There are a number of methods that can be implemented for the detection of terahertz radiation that can measure both broadband and narrow-band signals across the terahertz spectrum. The main difficulty in the detection of terahertz is that blackbody radiation at room temperatures is strong at terahertz frequencies requiring systems to be cryogenically cooled or for long integration time radiometric techniques to be used. Terahertz can be detected with simple bolometers but due to the blackbody radiation require helium cooling [38]. Although these detectors can be very sensitive they provide amplitude information only and as a significant amount of information can be obtained by the phase change of the terahertz signal for many applications these are not ideal. Also the need for cryogenic cooling is an extra expense and makes this technique unsuitable for certain applications such as sample measurement in the near field. Semiconductor heterodyne detectors are used in earth science, planetary applications and other passive systems. Again if higher sensitivity is required cryogenic cooling is required and several superconducting heterodyne detectors have been developed [39]. The Schottky diode downconverter equivalent in widespread use in the lower terahertz applications is the superconductor-insulator-superconductor (SIS) tunnel junction mixer. As bolometric techniques do not allow for the spectral information of the incoming terahertz beam to be identified, an alternative method is required for spectroscopy; one of the main intended terahertz applications. A pump probe configuration allows for far greater sensitivity and full coherent signal acquisition [40]. This technique is used in pulsed terahertz systems, which are those based on photoconductive antennae, optical rectification emitters and electro-optic detectors [41]. In a pump probe arrangement, as shown in Figure 2.4, the gated detector only operates when illuminated by the probe pulse. Shifting the timing of the probe beam pulse relative to the pump beam enables determination of terahertz content across the entire terahertz frequency band [42].

2.3.1 Photoconductive Dipole Antenna (PDA) Detection

In photoconductive detection an optical gating pulse, the probe beam, generates free carriers in the photoconducting medium. The terahertz electric field acts as a bias volt-

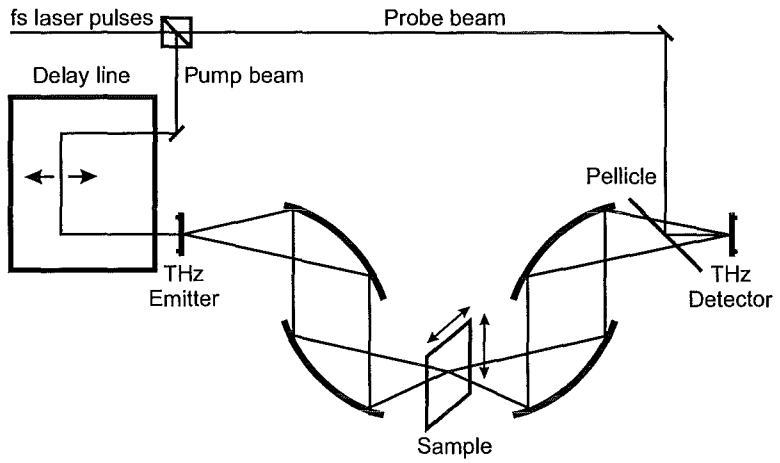

Figure 2.4 Pump-probe component layout for pulsed terahertz emission and detection using photoconductive dipole antennas.

age generating a current which can then be measured. Hence, the current only flows through the detector in the simultaneous presence of the laser pulse and the terahertz electric field. The total amount of the transported charge is proportional to the instantaneous terahertz electric field when the gating pulse arrived. By scanning the time delay between the terahertz pulse and the optical gating pulse enables the determination of the entire terahertz waveform. This mechanism was first demonstrated by Auston [11] using radiation-damaged silicon on sapphire. To operate well a low carrier life time material is required and other alternatives to silicon include low temperature grown GaAs, and InP [43]. Sensitivity up to 20 THz has been demonstrated using LT-GaAs with a carrier lifetime of 1.4 ps using 15 fs gating pulses [44]. PDA emitters are based on the inverse of the detector mechanism and are capable of generating high powers. The power of the emitted terahertz radiation is determined by the energy of the pump laser pulse and the bias that powers the current cascade. PDA detection has a high frequency limit determined by the speed of the photocurrent response. Hence such a system can be limited in that the spectral range is generally between 100 GHz to 1 THz with a peak power at around 500 GHz.

2.3.2 Electro-optic Sampling

Electro-optic sampling is based on the linear electro-optic effect [45]. A freespace electro-optic sampling (FSEOS) system utilises a non linear crystal for emission [46]. Ultrafast laser pulses with center wavelength of 800 nm incident on the emitter crystal cause the emission of pulses with terahertz center frequency. Although this technique has a lower power than a PDA its advantage lies in its much broader bandwidth limited not by carrier recombination rates but by the nonlinear characteristics of the crystal. Using this technique wavelengths as small as 7 μm have been generated. In electro-

optic detection the terahertz transient induces an instantaneous birefringence in the nonlinear detector crystal which influences the propagation of the optical probe beam. The phase shift between the ordinary and extraordinary part of the probe beam is

$$\Delta\varphi = \frac{2\pi\nu}{c}\Delta nL \tag{2.1}$$

where ν is the frequency of the probe beam and L is the thickness of the crystal. This can cause a linearly polarised probe pulse to be converted to a slightly elliptically polarised pulse which can then be detected using a set up as illustrated in Figure 2.5. An electro-optic crystal can be used to detect in excess of 40 THz [47] although at the higher frequencies the signal becomes increasingly harder to distinguish from the background laser noise. The power is lower than PDA emission as it is derived entirely from the incident laser pulse. A modification of this technique has been demonstrated with a chirped beam allowing single shot measurements to be taken doing away with the need to scan the timing of the probe beam [48].

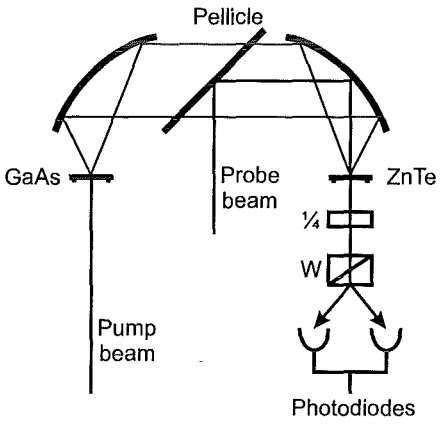

Figure 2.5 electro-optic sampling component setup, $\lambda/4$: quarter wave plate, W: Wollaston prism.

The most commonly used crystal for electro-optic sampling is ZnTe [49] for frequency ranges between 0.1 - 3 THz. GaP [50], DAST [51], $LiTaO_3$ and $LiNbO_3$ [52] have also been demonstrated to work as electro-optic crystals.

2.3.3 Scanned Detection for Imaging

In a pump probe terahertz emission/detection system in most cases a two dimensional image is formed by scanning a sample through space [53]. The probe beam is focused to a fine point and shifting the sample in a raster scan provides information about absorption and refractive index of the sample. Such a system can have a considerable image aquisition time as multiple scanning stages are necessary to form the two di-

mensional image. Two stages are required to shift the sample through x and y and a further stage is required for the delay stage of the probe beam. Each point of the image requires scanning of the delay stage to obtain the complete terahertz waveform. This enables spectral analysis from which a detailed chemical and physical analysis can be formed across the sample. If the signal to noise is high as is common in current systems averaging of each point may also be necessary. For terahertz imagers to become viable for most applications the image acquisition time needs to be much less than a scanning system and several techniques have been proposed such as the use of a chirped probe beam [54] which eliminates the requirement of the delay stage and the use of two dimensional imaging arrays [55]. Refinement of all these concepts should enable the construction of real time imaging systems.

2.3.4 Array Based Charged Coupled Device (CCD) Detection

Single shot terahertz images of samples can be taken by expanding the probe beam and using a large detector crystal and multiple detectors. Using electro-optic sampling, what is usually performed with a pair of balanced photodiodes in a scanning system, can be performed with a CCD array. Combining the CCD detection mechanism with a chirped expanded probe beam facilitates single shot two dimensional imaging [48]. Because the probe beam is expanded and lock in detection is not possible with a CCD array the signal to noise ratio is reduced compared to a scanned system. It is however possible to improve this through using a chopper to block the terahertz signal providing a two dimensional scan of the laser noise that can be subtracted [56]. This has been shown to give a two-order improvement in the signal to noise ratio.

2.3.5 Alternative Array Based Detection

Other potential array based detection techniques include bolometer arrays [57], which are already used in space applications and potentially in security, and photoconducting antenna arrays. Such arrays would have the advantages and disadvantages as previously described for their singular equivalents. An array of PDA's could potentially work better than an electro-optic based system being far less sensitive to laser noise. Large scale microlithographic techniques already available would be able to fabricate such arrays without difficulty. With the lithography resolutions now available the limitation in the resolution of such a detector would not be on the individual detector size but on the wavelength of the radiation which is 300 μm at 1 THz.

2.3.6 Terahertz System Summary

There are several methods available for terahertz imaging each with different benefits [58]. Because the current sources of terahertz radiation are still weak there is still a necessity to choose a detector type carefully to obtain the required signal to noise ratio across the required frequency band. The electro-optic system is characterised by low power and low efficiency generation and detection while giving very large bandwidth. The low terahertz power is due to the generation mechanism which is reliant on the power of the incident laser pulse. Photoconductive dipole antennas generate higher power, affected by the power of the pump laser pulse and the antenna voltage bias, but are limited in that they can detect up to an upper limit of about 4 THz.

Apart from the trade-off between terahertz power and bandwidth, two other issues contribute to selecting a terahertz system. The first has to do with supporting equipment, specifically lock-in amplifiers and regenerative laser amplification, and the second relates to the two dimensional imaging. Although electro-optic generation has a greater bandwidth than photoconductive switching, the power in the terahertz pulse derives entirely from the incident laser pulse power. In a PDA emitter, the output power scales both by incident pulse power and the bias voltage. The energy of an ultrafast laser pulse can be increased using a regenerative amplifier in addition to the ultrafast laser oscillator. Electro-optic detection is a weak effect and is very sensitive to optical noise. To eliminate the noise it is necessary to use a lock in amplification technique. Regenerative and lock-in amplifiers are large and expensive, limiting the development of portable and cheap terahertz systems

Two dimensional imaging has been demonstrated with electro-optic detection with a CCD camera. Performing this with an PDA array is yet to be implemented fully but would give an alternative parallel imaging system with increased tolerance to noise. Ultimately the performance of two dimensional imaging systems will be improved when higher power terahertz sources are available at which point the signal to noise ratio will be less of an issue.

2.4 SIGNAL PROCESSING FOR TERAHERTZ PULSES

Huge amounts of information are generated during terahertz imaging providing amplitude and phase information over a broad range of frequencies. Analysis for pulsed THz systems requires taking the time domain signal measured and processing it as quickly and efficiently as possible to extract the frequency information necessary for spectroscopic analysis. Algorithms need to be able to take incoming terahertz waveforms or

images, enhance salient features and present information for storage and interpretation [59]. This optimally needs to be performed in real time for imaging systems for security or medical applications. To a large degree the frequency information can be extracted simply by taking a Fourier transform of the pulse, however, wavelet analysis can better determine the wealth of information present [60]. Wavelet analysis extends the concept of Fourier decomposition to a more complicated time and scale decomposition. In wavelet analysis, a signal is decomposed into an array of pulsed-shaped wavelets, so that the time domain and spectral domain of a signal can be studied simultaneously. The basic premise of wavelet analysis is to construct the signal from the scaled wavelets instead of from infinite sinusoidal functions, as used in Fourier analysis. When applied to pulsed systems, like pulsed terahertz imaging, the wavelet function fits far more closely to the shape of the actual signal than any sinusoid would and thus the correlation coefficients are higher than for Fourier transforms [61]. Wavelet analysis gives faster signal detection and better noise reduction than simple Fourier analysis [62].

2.5 TERAHERTZ APPLICATIONS

Because terahertz lies between the infrared and microwave frequency bands many of the applications that have arisen are derivatives of existing technologies at these frequencies. However the terahertz band has unique absorption spectra and properties that make it particularly suited to some application areas [63, 64]. In many cases a level of analysis can be achieved that is impossible with other frequencies [65]. This section provides an overview of the current main application areas under development focusing on technologies currently in use and those being actively developed. Currently the only company solely devoted to the commercialisation of terahertz is Teraview [6]. Many of the applications described here detail the research surrounding the applications this company is developing.

2.5.1 Submillimetre Astronomy

Earth, planetary and space science have been the main drivers of terahertz technology to date. Submillimetre astronomy unveils several features of vital importance for astronomy [66]. There is a great deal of dust in the interstellar gas of our Galaxy and, like many other cool objects, it emits most of its radiation in the far infrared, as shown in Figure 2.6. Infrared observations of very young stars and their progenitors, forming in cool dusty regions of the galaxy, are currently the best way of developing stellar formation theories, a process not yet fully understood. At even shorter infrared wavelengths dust grains actually become transparent, making it possible to look deep inside regions that are obscured at optical wavelengths. Many abundant molecules of interest - water, oxygen, carbon monoxide and nitrogen - can be probed in the terahertz regime

enabling the identification of star system, galaxy and planetary composition [67]. Far-infrared observations also offer us our best opportunity yet to probe the Universe as it was not long after its creation in the Big Bang, about 15 billion years ago. The Universe was much hotter and denser in the past but the relic radiation, the Cosmic Microwave Background Radiation, has since cooled to just below 3K and now peaks at millimetre wavelengths. A number of satellites are in place and in planning for launch for the detection of radiation in the terahertz band [68].

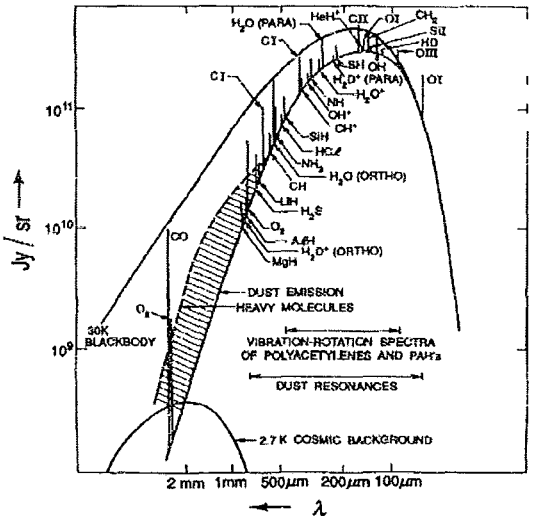

Figure 2.6 Radiated energy versus wavelength showing key molecular emissions in the submillimeter wavelengths [66].

2.5.2 Ranging and Tomography

Two obvious modalities for pulsed radiation are ranging and tomography, both of which rely on reflective geometry. Ranging involves measuring the time of flight of the terahertz pulses and thus calculating the distance and shapes of objects. This can be used in certain radar applications such as weather radar. Terahertz wavelengths are also of a convenient size for creating radar profiles of large objects, such as tanks and planes, using scale models. Tomography is a similar application, looking at the flight time of pulse reflections from subsequent boundaries inside an object. Thus the internal structure of, for example, a floppy disc can be observed non-invasively. Terahertz tomography can be combined with spectroscopy to provide three dimensional information about the composition and structure of an object

2.5.3 Spectroscopy

Spectroscopy describes the technique of producing spectra, through either transmission or reflection from a material, analysing their constituent wavelengths and using them

for chemical analysis or for the determination of energy levels and molecular structure. The most common terahertz spectroscopy system is terahertz time domain spectroscopy (THz-TDS) [69]. THz-TDS relies on PDA detection and emission technology. In its most simplistic form, the Fourier spectrum of a free space terahertz pulse is first characterised, then compared to the spectrum of a pulse that has passed through the sample. The difference between the two spectra reveals the sample's molecular absorbtion lines. THz-TDS has been used to measure the refractive index of dielectrics, thin films, semiconductors, liquids and superconductors. It has also featured in the study of dielectric properties of polar liquids [70, 71], in recognising gases and gas mixtures [72], in observing the rotational absorbtion spectra of hot water vapour in flames [73] and in classifying terahertz material parameters [74]. Certain groups of molecules tend to absorb at characteristic frequencies in the terahertz frequency band which enables molecular identification and the study of the dynamics of chemical reactions. Pulsed imaging techniques such as THz-TDS and FSEOS can provide full spectroscopic analysis in the terahertz band with a single pulse [74]. Which particular technique is used is determined by the bandwidth of interest where FSEOS can give better determination of the higher frequencies.

When using reflection spectroscopy the phase needs to be considered [75]. This is because unlike transimission geometry, the path length will change depending on the placement of the sample. For accurate measurement the phase information has to be referenced to a measured distance or referenced to a known surface.

2.5.4 Microscopy

One of the main limiting factors of terahertz microscopy is the poor spatial resolution due to the long wavelengths of the radiation. Because of this considerable effort is being made to establish near field microscopy techniques for terahertz systems. Such a system is sought after because of the ability of terahertz imaging to distinguish chemicals and biochemicals from their spectroscopic signatures or optical properties. Near field methods enable imaging at resolutions below the diffraction limit which is achieved by detecting the evanescent components of the field scattered by the object being imaged [76]. This is achieved by introducing an aperture type probe into the near field region of the object and then scanning the object to build up a raster scanned image. Using this technique resolution down to 7 μm has been demonstrated [77].

2.5.5 Biomedical Applications

The medical and biological professions are very interested in imaging and diagnosis techniques that can provide diagnosis without tissue damage [78]. The vast benefits

of imaging techniques that could obtain information unobtainable through observation with the naked eye were first realised with Roentgen's discovery of x-ray imaging. Since then a wide array of other imaging techniques have been developed for different applications and diagnosis [79]. This includes ultrasound, positron emission tomography (PET), computer aided tomography (CAT), magnetic resonance imaging (MRI), flourescence microscopy, multiphoton-induced flourescence microscopy, infrared imaging and Raman imaging [80, 81, 82]. Like these techniques terahertz imaging is favourable as it can be performed *in vivo*, meaning images can be taken without killing the sample or patient.

Terahertz radiation can give much improved information for diagnosis as it is easy to determine the water content, and molecular makeup by analysing phase delays from materials of different refractive index. The terahertz energies correspond to levels of molecular vibrations and rotations of proteins [83] and DNA [84]. This enables the differentiation of biological tissues with greater precision for disease identification. The fact that terahertz is strongly absorbed by water [71] can be exploited for detection of hydration states to assess tissue condition [85]. Terahertz radiation has absorption peaks due to stretching modes at 6 THz and librational modes at 19.5 THz [86]. This means deep tissue analysis requires either sectioning or endoscopic inspection [87].

Terahertz Pulse Imaging (TPI^{TM}) has the potential to make a major impact on medical imaging and other aspects of health care [88]. Medical imaging is largely dedicated to oncological (cancer) imaging. Although terahertz will not penetrate deep into the body 85% of all cancers lie in the epithelium, the area near the surface of various tissues located either inside or on the outside of the body. Epithelial tumors are not adequately addressed by conventional imaging modalities due largely to their lack of sensitivity to small density changes in soft tissue. Terahertz has great potential in the early detection of epithelial tumors of skin, breast, prostate, or lung cancer [89].

Terahertz imaging has huge potential for medical applications [90]. Due in part to its ability to recognize spectral fingerprints [74], TPI provides good contrast between different types of soft tissue, and is a sensitive means of detecting the degree of water content as well as other markers of cancer and other diseases [91]. Because of the ubiquitous presence of such markers in tumors, TPI can be applied to a number of different cancers, as well as other diseases in medicine, oral health care, and related areas.

2.5.5.1 Cancer Detection

The ability of terahertz imaging to differentiate very acurately betweeen materials of different molecular composition and density [92] makes it a very attractive technology for cancer detection [93]. This technology will potentially be able to detect cancerous tissue at a much earlier stage than methods currently in use. This avoids the spread

of tumors which can lead to the required removal of large amounts of tissue and helps with early detection to avoid morbitity from malignant cancer. Epithelial tissues give rise to more than 80% of all adult cancers and include common cancers of the skin, lung, breast, colon, bladder, liver and prostate. This technique has been demonstrated to accurately detect such cancers distinguishing between healthy tissue and basal cell carcinoma [94].

Skin cancer is the most common form of cancer worldwide in white populations with millions of reported cases each year. Detection of Basal cell carcinoma is currently performed via visual inspection of the skin. Some tumors are well defined and can be removed directly with surgery however others take the form of ill defined, micronodular, infiltrating and sclerosing tumors which can extend beyond that visable with the naked eye. Such tumors require sectioning and examination during surgery to enable complete removal. Terahertz imaging of such tumors would avoid this time consuming and costly procedure ensuring all of the cancerous tissue is removed while minimising the amount of tissue damage. With this method it is also possible to detect tumors lying under the skin, as demonstrated in Figure 2.7 allowing for earlier cancer detection [6]. This is especially important for areas such as the face and neck to minimise the amount of reconstructive surgery required.

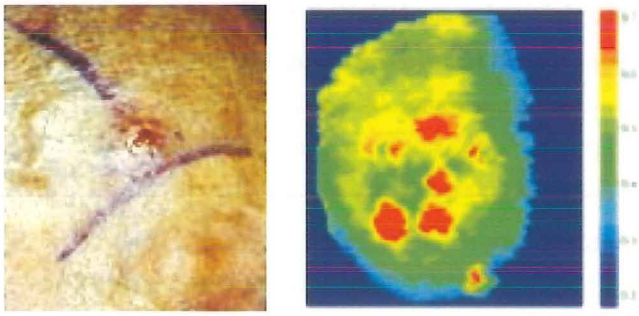

Figure 2.7 Terahertz image of a section of skin identifies areas of skin cancer clearly [6].

2.5.5.2 Cosmetics

The stratum corneum is the outer most dead layer of skin. The hydration level and hydration profile of which influences its permeability and elasticity to give its cosmetic appearance. The permeability is important as it determines the level of water loss from the underlying skin tissue and the penetration of external substances. Most skin-care products such as moisturisers act to increase the retained water content of this layer of the skin to enhance its appearance. Hydration levels of the outer skin layers after application of different products enable determination of the relative effectiveness of a desired cosmetic effect. Current imaging techniques such as MRI or ultrasound lack the water sensitivity and resolution to give accurate information about this skin layer

[95]. Terahertz radiation enables in vivo analysis of skin tissue being highly sensitive to water content [96]. The analysis of skin also finds application in the transport of medication in the form of creams or gels where the permeability of the skin plays a direct role and in the determination of wound repair rates.

2.5.5.3 Dentistry

Current detection of tooth decay is by the way of X-rays however this method reveals the decay at a very late stage where only drilling and filling can be used to halt the decay. Tooth decay starts with the formation of caries in the enamel layer of the tooth. Caries are initiated at the tooth surface with localized destruction of the enamel. This happens because of demineralisation of the enamel causing erosion from acids in the plaque deposits adhering to teeth. Caries proceed by the creation of a subsurface lesion in the enamel. The lesion may extend to the next tissue layer in teeth, the dentine, without macroscopically visible breakdown or even microcavity formation at the tooth surface [97], as seen in Figure 2.8.

The absence of visual features on the tooth surface makes early detection of tooth decay difficult. If decay can be detected early enough it is possible to reverse the process without the need for drilling by the use of either fissure sealing or remineralization. The difference in the refractive index and absorption of the enamel and dentine in a tooth facilitate caries detection using terahertz imaging [98].

Another dental application where terahertz imaging can be used is in the characterisation of enamel erosion. This form of erosion is different to that caused by bacteria effecting the whole tooth, typically being from acidic food and beverages. TPI enables non-destructive measurements to be taken to determine the thickness of enamel. This allows monitoring of tooth erosion which is important as if erosion is significant the

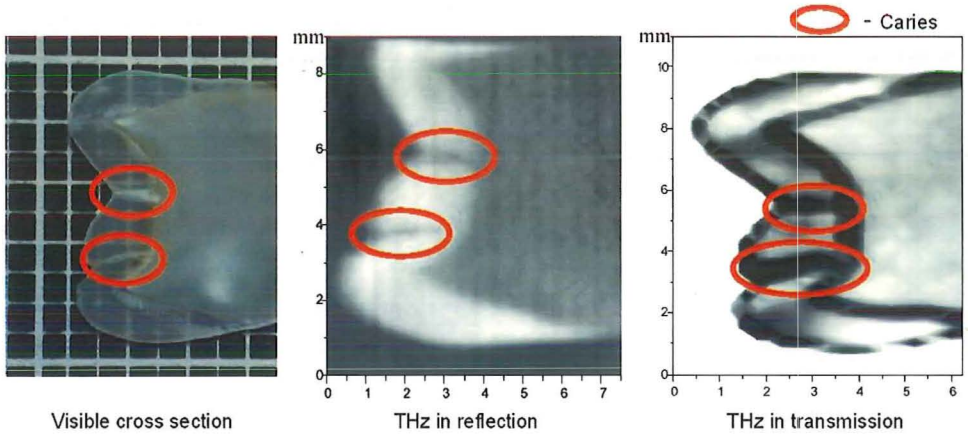

Figure 2.8 Reflection and transmission mode imaging of a tooth clearly show caries in a tooth cross section. The enamel and dentine are clearly discernable from their differing refractive index [97].

dentine will be exposed leading to pain and eventual death of the tooth [99].

2.5.6 Pharmaceutical Applications

The unique spectral imaging characteristics that can be obtained with a combination of Terahertz Pulsed Imaging (TPI^{TM}) and Terahertz Pulsed Spectroscopy (TPS) has been used to investigate applications of solid dosage forms in the pharmaceutical industry and in new and emerging areas of drug discovery [100]. The technique has advantages that excitation is not via a powerful laser source, as used in Raman spectroscopy [101], so phase changes or photochemical reactions in polymorphs do not occur. The method has a wide range of applications in pharmaceutical science including formulation, high throughput screening, and inspection in storage for the rapid characterisation of stability.

Many drug molecules after purification can crystallise in many different forms, these are known as polymorphs. Analysing the terahertz absorption spectrum provides a rapid technique for the identification of different biological molecules [102]. Polymorphs can have different solubilities, stabilities or bioavailabilities. Such analysis enables the determination of whether a certain drug can exist as different polymorphs and if there is any interconversion with time.

The main benefits of terahertz analysis in this field are that the unique spectral information is obtained, photochemical reactions are not induced in the polymorphs as they are in existing techniques and the transparency of packaging materials allows for sample inspection in packaged goods.

This molecular analysis technique has also been used in protein analysis. Proteins can trigger or deactivate genetically linked diseases such as Alzheimers, cancer and diabetes and analysis of their structures is key to understanding these diseases. Proteins, not genes, are the endpoints of life sciences investigations, since proteins ultimately regulate metabolism and disease in the body. Proteins regulate the structure of cells and tissues in the body and a clear method of identifying them is important in the understanding of the human body's biochemistry [103].

2.5.7 Security

Because most packaging and clothing materials are transparent to terahertz radiation it is a good candidate for security applications [104]. One of the main benefits that this has over x-ray screening currently in use is that it can detect both metallic and non metallic objects and also provide spectroscopic information to aid in the determination of the chemical composition of material. A number of applications have been proposed for human or object screening for the detection of drugs, hazardous chemical agents,

explosives or weapons [105].

2.5.7.1 Postal Inspection

The use of terahertz radiation for the detection of illegal or dangerous substances shows great potential. The majority of packaging materials such as paper, cardboard, plastics and fabric are virtually transparent to terahertz frequencies enabling easy non-invasive investigation of package contents, as seen in Figure 2.9. Terahertz spectroscopy is excellent at identifying the nature of a wide range of such materials as explosives, illicit drugs and biological agents such as anthrax. Not only can these substances be detected inside packages but also upon people which could potentially provide increased security in airports and other high risk areas. The fact that terahertz radiation is not harmful to tissue also makes this radiation promising in these application areas.

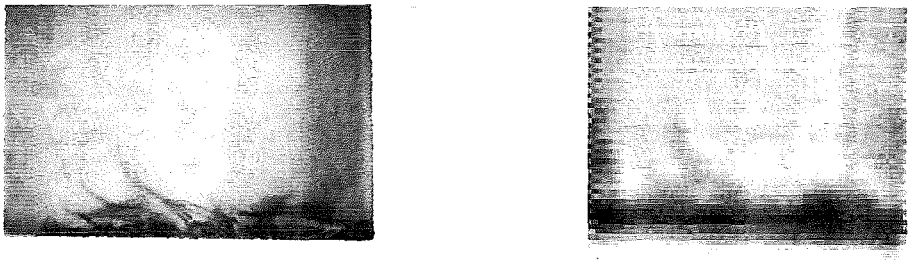

(a) (b)

Figure 2.9 (a) Back lit visible image of an envelope containing spore flakes (b) Terahertz image of an envelope clearly identifies the spore flakes inside [106].

The speed of measurement can be dramatically increased with the use of a chirped probe beam imaging system [54]. Instead of using a single pulse to read a portion of the terahertz spectrum at a time with a scanned delay stage the entire spectrum can be read out using the chirped probe beam. With current source technology it has been reported that envelopes can be scanned for such substances at a rate of 12/minute [106]. This system should be able to detect and determine powders with a concentration of 80 milligrams/cm^2. By obtaining signatures of the powder or substances of interest a classification algorithm can be used to differentiate and identify hazardous materials.

2.5.7.2 Concealed Weapon Detection

Concealed weapons or explosives can be a cause for concern in many situations. Current inspection is performed using x-rays and metal detectors which are very poor at detecting nonmetallic substances. Detection of weapons is even more difficult on individuals as routine scanning with x-rays is not suitable because overexposure to ionising

radiation can be dangerous to health. This currently leaves simple metal detectors and frisking as the only security available and makes a terahertz imager a very promising alternative [107]. It is likely that a terahertz system will be able to be used in airport security or other similar environments for the detection of handweapons [105].

2.5.7.3 Chemical and Bioagent Detection

The threat of terrorist attack with explosives is a challenge faced by law enforcement authorities worldwide. Suicide bombing is a particular threat in some parts of the world which can be difficult to detect or avoid. In addition to the ability of terahertz pulsed imaging to detect the structure of concealed objects spectroscopic information can be used to determine the object's chemical composition [108]. This aspect of TPI is critical as a means of screening for explosives or other prohibited or dangerous chemicals [109].

2.5.7.4 Landmine Detection

Unexploded landmines from past wars continue to cause extensive loss of life and mutilation in many countries around the world. Current methods of detection are very inefficient as the anti-personel mines tend to be non-metallic. The ability of terahertz pulse imaging to detect both metalic and nonmetalic objects means it may potentially be used for land mine detection. Mines tend to be buried about 1 cm below the surface and a terahertz imaging system has been shown to be able to locate concealed metal and non-metallic objects at this depth [110]. A terahertz beam is shone at the ground and a 3D image of objects below the surface can be built up using reflection mode imaging.

2.5.8 Non-destructive Testing

Terahertz radiation will pass, with very little attenuation, through many non-metallic materials such as plastic, cardboard and paper. This enables the non-destructive testing or analysis of objects for defect analysis [111]. Signal analysis can identify either concealed materials of different types or cracks and holes within a solid. This involves observing the reflections from different depths and evaluating the spectral content and signal delay [112].

Three dimensional images of an object can be taken either by rotating the sample (or detector) [113] scanning the sample in reflection mode or using a focusing element with chromatic dispersion [114]. This has been demonstrated as a technique for integrated circuit package inspection, as seen in Figure 2.10, where the internal layers of a chip can be viewed showing the size, integrity and location of the silicon and the internal interconnects [64].

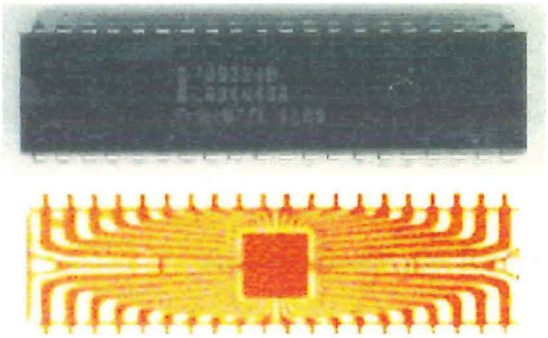

Figure 2.10 Terahertz image of an integrated circuit identifies the chip and interconnects inside the packaging [64].

2.5.9 Passive Devices for Terahertz Applications

For many of the aforementioned applications integration of passive devices for terahertz beam manipulation is necessary. Currently the only technique available is the use of refractive lenses made from plastics or silicon. These lenses enable only very simple focusing of radiation and many applications would benefit from the ability to manipulate the terahertz beam uniquely. Many of the imaging systems currently in use suffer because of their long acquisition times. Lens arrays can speed the analysis of samples by enabling parallel processing and lenses with a chromatic focal change with frequency may be used in tomography applications to produce quick three dimensional images of people or objects. This thesis discusses the formation of terahertz diffractive optic passive structures giving the ability to manipulate broadband beams into arbitrary patterns.

2.6 DIFFRACTIVE OPTIC ELEMENTS

Most optics such as those found in corrective eye-wear, telescopes and microscopes use their shape to bend light, their design being based around the law of refraction. A diffractive optical element (DOE) relies on a different mechanism diffraction to manipulate an incident beam. Diffractive optics work by breaking up incoming waves of light into a large number of wavelets, which recombine to form completely new waves [115]. Complex designs are possible that can create three dimensional focal patterns beyond the optic for a wide range of applications, many of which are not possible with conventional refractive optics. DOE's can function as gratings, lenses, aspherics, holographic elements or any other type of optical element. Large optical apertures, lightweight and low cost fabrication are their main features of interest. They can be fabricated in a wide range of materials including aluminum, silicon, silica, plastics, depending on

the specific wavelength of operation intended, providing the user greater flexibility in selecting the material for a particular application.

2.6.1 Features of Diffractive Optic Elements

The broad application of diffractive optics is better understood by analysing the features and restrictions of the devices. The focal length and aberration characteristics of a diffractive element vary with wavelength. A diffractive lens has a linear change in the focal length identified as a chromatic aberration. As such they are inherently narrowband devices for most applications but the chromatic aberration finds uses in some applications where the wavelength dependent focal distance can be exploited.

There is great flexibility in the design and fabrication of a DOE. Several different optical elements can share the same substrate without interfering with one another. For example, a single DOE could be used as a lens, beam splitter and spectral filter simultaneously. Diffractive elements are very light, as they are formed in thin films or substrates of a few wavelengths thickness only. Because of this there is much greater flexibility in the shape of the surface on which they are constructed. Several applications see hybrid refractive-diffractive optics to generate unique optical functions [116]. The use or integration of diffractive optics in a system can provide functions that are not possible by conventional reflective or refractive optical elements. The size and materials involved find a majority of DOE's being constructed with the use of planar microfabrication technologies. This is relatively cheap and lends itself to easy mass production.

A DOE can be formed in any substrate by creating areas where the radiation is either blocked, or where the phase is delayed. Simple lenses can be created using this mechanism called zone plates. When designing a DOE it is desirable to maximise the diffraction efficiency, so as much of the incident radiation is transmitted to the desired pattern. Phase retarding structures give the best efficiency as all of the radiation passes through. The diffraction efficiency of these structures can be improved if the discontinuities have a blazed or sloped profile. As this can often be difficult to fabricate an alternative is to approximate this profile using steps. The method in which these steps are created, results in the complexity increasing by a factor of 2 with each processing step. This fabrication process is referred to as a binary process which is used for the production of lenses in this work.

2.6.2 Aberrations of Diffractive Optic Elements

DOE's exhibit chromatic and or non-chromatic aberrations resulting in a change in the reconstruction beam parameters and or a change in wavelength from the refer-

ence beam. Large aperture DOE's can incur aberration from the fabrication process, where alignment of masks in the multiple level processing becomes increasingly difficult. Analysing the signal passing through a lens, and identifying the deviations caused in the intensity pattern, from the free space beam can the help with abberation correction during an image reconstruction process. To a certain extent this means that aberrations can be corrected for with post measurement signal processing.

2.6.3 Applications of Diffractive Optic Elements

Most of the applications achievable with conventional refractive optics can be achieved with DOE's if the system operates over narrow spectral bandwidth or requires chromatic dispersion. Some of the unique functions that DOE's provide are multiple function optics, unusual configuration, and narrow spectral response features otherwise hard to attain [117]. These typical characteristics of DOE's provide advantages in beam shaping optics, spectral filters, compact rugged spectrometers, diode laser couplers, beam combiners, head-mounted displays, laser resonators, laser material processing, laser collimators, computer interconnects, solar concentrators, and wavelength division multiplexers/demultiplexers. Large aperture DOE's are useful for null optics, laser scan systems, laser beam delivery systems, and projection displays. To date very little has been reported with respect to the use of diffractive optics for terahertz radiation. This thesis addresses this enabling the incorporation of diffractive optic technology into terahertz applications.

2.7 SUMMARY

Terahertz technology promises to revolutionise a number of fields including areas of biology, medicine, security and analysis. Further research into high power, large bandwidth sources and detectors will see the cost of terahertz systems become viable to an increasing number of applications. At present systems can be found in the space and medical fields however soon terahertz may be found in dental surgerys, airports and postal systems. At any wavelength diffractive optic technology can facilitate otherwise unachievable beam manipulation. The terahertz wavelengths demand diffractive optic feature sizes too small for accurate milling. This work describes a microfabrication technology that enables high efficiency diffractive optics to be constructed bringing the benefits of diffractive optic technology to this unique frequency band.

Chapter 3

FABRICATION OF TERAHERTZ DIFFRACTIVE OPTICAL ELEMENTS

3.1 INTRODUCTION

The aim of this project has been to fabricate high efficiency silicon diffractive optics for use in the terahertz frequency band using a specially developed binary planar microfabrication technique. The sub-mm feature sizes required from these devices make it hard to create these structures mechanically and a planar fabrication technique also gives scope to create arbitrary multilevel diffractive optics for terahertz applications. Prior to this work no such technology had been available and it is desirable to bring the benefits of diffractive optics into this region of the electromagnetic field. This section describes all the fabrication issues that have arisen during the course of the technique development. Creating deep multi level structures of the order required for terahertz applications introduces some unique microfabrication challenges.

Prior to the description of the microfabrication research conducted the experimental equipment is described. This section is followed by an outline of previous work on multilevel diffractive optics. A complete process has now been developed capable of creating a broad range of terahertz diffractive optics. The completed process is outlined with its current limitations at the conclusion of this chapter.

3.2 LENS MATERIAL CHOICE

There are a number of different criteria that need to be considered in choosing a good material for the fabrication of a diffractive lens. Because diffractive optics have proved to have broadband applications these properties must be considered for the complete frequency range of interest. One needs to consider the cost of the material, the absorption spectra, the refractive index and the ease with which the material can be processed.

The refractive index of the material influences the degree to which the speed of radiation passing through it is changed. Hence to get the required change in phase at

a point in a diffractive optic one is interested in the refractive index of the material and the depth of the etched structure. The depth required to give a wavelength phase shift is determined from $\lambda/(n-1)$, where λ is the wavelength of the radiation, n is the refractive index of the lens material. Hence the higher the refractive of the material the less deep the structuring needs to be which reduces the cost and complexity of the fabrication process.

Of all the materials silicon proves to have a number of traits that make it stand out. Firstly it is relatively cheap and easier too obtain than the other alternatives. It also is practically transparent to terahertz frequencies and has a fairly uniform refractive index making it more suited to broadband applications. The refractive index and absorption spectra of silicon at terahertz frequencies are shown in Figure 3.1 [118]. The refractive index varies by less than 0.1% from 0.1 to 2.0 THz and losses can be less than 0.05 cm^{-1}.

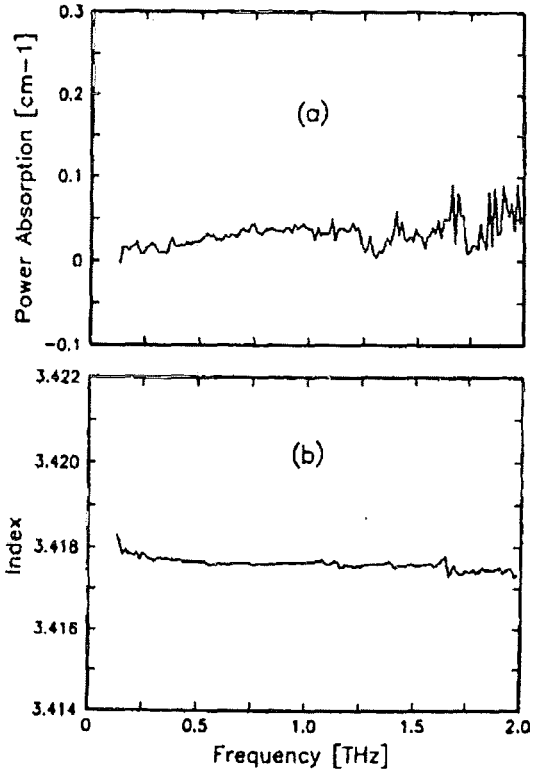

Figure 3.1 Time Domain Spectroscopy (TDS) measurements of crystalline high-resistivity silicon. (a) Power absorption coefficient (b) Index of refraction [118].

The importance of using high resistivity silicon is highlighted in the THz TDS measurements of several different experiments where semiconductors of lower purity were used in the analysis. Here it can be seen that the absorption of terahertz is much different to the results of [119] in silicon of 1 Ωcm as shown in Figure 3.2. The importance of using high resistivity silicon was recognized in this work where the standard bulk

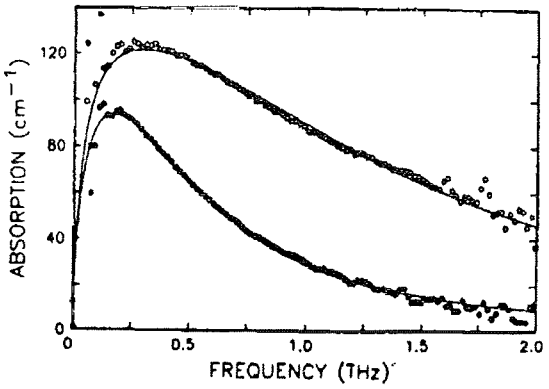

Figure 3.2 TDS measurements showing power absorption of low resistivity crystalline silicon, n-type 1.15 Ωcm (dots) and p-type 0.92 Ωcm (circles) [119].

silicon that is used in microfabrication with a resistivity of around 10 Ωcm displayed a transmission of about half that of the 4000 Ωcm material used to create most of the lenses described herein.

When using a crystal wafer it is possible to chose the crystallographic orientation of the lattice. This means the particular wafer plane that faces the surface can be elected, which can be important as far as semiconductor fabrication is concerned. In the etching of silicon in a dry environment the etch rate in various directions is determined by the conditions of the process. However a crystal etched in a wet solution will etch at different rates depending on the placement of crystal planes. The very directional nature of wet etching makes it a nonviable process for the fabrication of lenses as they are round. However in selecting a wafer that has a crystal flat on a plane that etches at a very slow relative rate wet etching can be used as a post production procedure to aid in the removal of surface roughness. To make this possible wafers with orientation $< 111 >$ were used.

3.3 EXPERIMENTAL TECHNIQUES

Microstructure engineering involves the definition and then transfer of patterns on substrates using either adsorption, chemical reaction, deposition or an etching technique. Although the technique of lithography has been around for many years its application to pattern definition on crystalline wafers has only become widely used since the invention of the integrated circuit in 1958. Development of this technology was largely driven by the need for faster integrated circuits and later by the communications industry with the production of lasers and gratings for high speed data transfer. More recently it has also been applied to micromachining applications for the production of micro-optics, micromachines and microfluidic applications. Although it is now possible to structure with features down to tens of nanometers many of these applications de-

mand features of hundreds of microns in dimension or combinations of features in the nanometer and micrometer range. The diverse range of new devices being constructed using microstructuring require the development of unique fabrication processes. This section describes a binary fabrication process designed to create stepped structures over 100 μm deep with feature sizes ranging from several millimeters to tens of microns in diameter. To achieve this several processing technologies including oxidation, photolithography and reactive ion etching were required.

3.3.1 Oxidation

Oxidation of silicon to silicon dioxide occurs at temperatures around 1000°C. This will occur in atmospheric conditions at these temperatures however the speed of oxidation can be increased with a modified atmosphere. This is achieved by venting oxygen into the chamber either with or without the addition of steam. The fastest oxidation rates are achieved in a wet oxygen atmosphere. A diagram of the furnace used in this work is shown in Figure 3.3 consisting of a 3 zone quartz tube heated with resistive coils. The chamber has an inlet at one end where oxygen and steam can be let in via a flow rate controller.

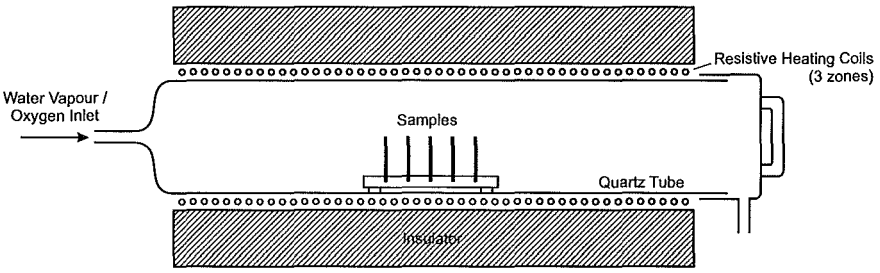

Figure 3.3 Oxidation tube with a 3 zone resistively heated chamber.

3.3.2 Photolithography

Photolithography describes the transfer of patterns from a mask into a photosensitive polymer with the radiation exposure and subsequent development. The complexity and expense of this process is dependent on the topology of the substrate, and the feature size and aspect ratios required. A number of different techniques have been developed including contact printing [120], proximity printing [120] and projection printing [120, 121] each having different resolution capabilities and cost [122]. In this work a contact lithography procedure was used using a g-line (436 nm) Hg UV radiation source.

A typical photolithographic process first requires the spinning of photoresist onto the surface to obtain a smooth even layer. The solvent in the resist that enables it to be spun needs to be baked out using either an oven or element. The hardened

resist is then exposed for a time dependent on the thickness, radiation intensity and photosensitivity of the resist such that the polymer is exposed completely to the wafer surface. Processing needs to be conducted in an environment isolated from sources of the radiation that will react with the photoresist. Immersing or spraying the wafer with developer will then reveal the pattern.

There are two types of photoresist; positive and negative, that form different patterns from the same mask as shown in Figure 3.4. Exposure of positive resists affects chemical structure so that it becomes more soluble in developer. Sufficiently exposed resist is washed away in the developer solution exposing the wafer surface. The opposite occurs for a negative resist where exposure leads to polymerisation or cross-linking leading to unexposed areas being removed on development. Negative resists require an additional post exposure bake to aid this cross-linking process. Hence, a positive resist will create a replica of the mask pattern, and a negative resist the photographic negative.

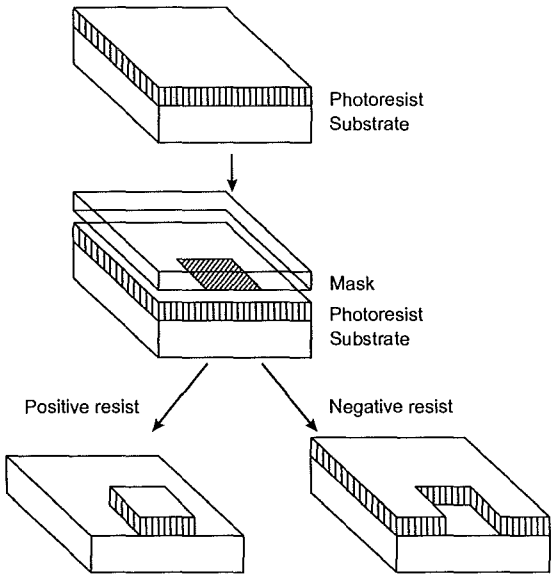

Figure 3.4 Pattern formation from positive and negative photoresists from the same mask.

3.3.3 Reactive Ion Etching

Reactive ion etching (RIE) is a dry process used to remove material from a substrate. It is a chemical / physical process where ions react with the surface to etch away the material. The placement of the different masking materials on the surface enables the transfer of patterns into the substrate. Using lithography such patterns can be formed on the surface to a thickness where the substrate can be etched to the required depth before the etch mask is etched away itself. Here selectivity is important, which refers to the rate at which the etch mask is etched relative to the substrate material.

Reactive ion etching gives several benefits over other etching techniques such as wet chemical etching [123]. Because it is a dry process there are fewer waste products than in a wet etch process. Also unlike wet etching the direction of the etching is not dependent on the crystallographic orientation of the wafer [124]. This gives much more flexibility in the patterns that can be constructed. Because of the circular nature of the patterns in this project a dry etch process was necessary.

There are several parameters which can be tightly controlled with RIE such as the chamber pressure, temperature, gas flow rates and the RF power which determines the DC bias. Because all these parameters can be controlled precisely this gives the ability to have a high degree of control over the lateral etch control, selectivity, surface texture and etch rate [125]. Obtaining a desirable operating point requires optimising this multidimensional parameter space [126].

3.3.3.1 Principles of Reactive Ion Etching

Two independent mechanisms occur to etch material from a substrate. These are ion bombardment to ballistically remove material and chemical reaction and desorption of the reactive ions with the surface. The balance of these two etching processes is set by the choice of power, pressure and temperature such that the desired etch rates, selectivity and profile are achieved. Application of a radio frequency voltage, typically at 13.56 MHz, causes electrons to oscillate and to collide with gas molecules leading to a sustainable gas plasma. This consists of negative anions, positive cations, radicals, vibrationally excited polyatomic species and photons formed from the introduced etchant gases.

In the areas of the plasma adjacent to the electrodes an area of low charge density forms from the recombination. This appears as dull areas in the plasma known as the sheath. The increased mobility of electrons relative to the positive ions leads to a higher concentration of positive charge within the plasma. The electrons charge up the capacitively coupled electrode and since no charge can cross the capacitor this electrode retains a negative DC bias. The low charge density of the sheath leads to the creation of large fields that then accelerate the reactive species to the sample surface. The magnitude of this self-bias voltage determines the velocity that the ions impact the surface and hence the etch mechanism and result.

3.3.3.2 Machine description

The RIE machine used was an Oxford Plasmalab 80 plus system [127]. This has two parallel plate electrodes the lower of which can be heated with an element, or cryogenically cooled with liquid nitrogen, to give an operating range of $-150°C$ to $200°C$. The main components of this system are shown in Figure 3.5.

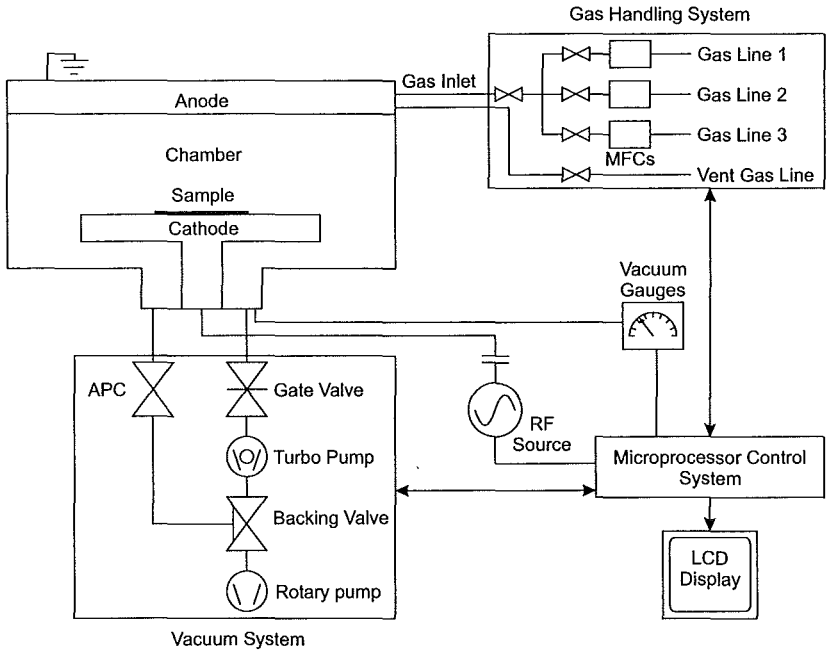

Figure 3.5 Schematic of the Oxford Plasmalab 80 Reactive Ion Etcher.

Etching is performed in a controlled pressure environment. Two pumps, a rotary and turbomolecular pump, are used to first evacuate the chamber and then maintain a set pressure controlled with an automatic pressure controller (APC). Prior to the introduction of any gases the chamber is evacuated to a base pressure lower than 7×10^{-5} Torr to remove contaminants. This is performed in a two stage process with the rotary pump first reducing the pressure from atmospheric followed by pumping with the turbomolecular pump. At this point the rotary pump acts as the backing pump for the turbomolecular pump. Typically this will achieve pressures of 10^{-6} to 10^{-7} Torr. During the etch process the gate valve is shut and all the process gases and waste material are removed with the rotary pump. Two vacuum gauges are used to monitor the system, a capacitance manometer gauge for high pressures and a Penning gauge for low pressures.

This system has the facility to introduce three different gases to the chamber simultaneously. The proportions of each gas are set in the microprocessor control system and the respective flow rates are then controlled by mass flow controllers (MFCs) on each line. The process gases available are SF_6, CHF_3, CH_4, 0_2, N_2 and Ar. Two additional lines provide N_2 to vent the chamber and He to increase thermal coupling to the electrode.

Samples sit on a 4" wafer which is clamped to the lower electrode or cathode. This wafer is coated with metal or oxide depending on the process requirements. The cathode is the drive electrode supplied with RF energy at 13.56 MHz.

A central processing unit controls all pressure, temperature, power and gas flow rates. Single recipes can be manually entered or saved as single or multiple automatic processes.

3.4 BACKGROUND RESEARCH

Work from the author's previous Masters thesis [128] explored the concept of large scale multi-level microfabrication with the aim to create a process that could be applied to the formation of silicon diffractive optics. Using this process it was possible to create structures with up to four levels with reasonable reliability [129]. There were several problems with this process that required significant research and development to overcome. The aim of this work has been to extend this from a proof of concept to a high efficiency device which can be tested and a process that can be extended to an industrial production line. In detailing the adaptation in processing that has resulted in a reliable process and functional lens set, some background into the previous work completed on this work needs to be highlighted.

3.4.1 Fabrication steps of existing process

The existing process used a binary fabrication scheme in which a set of masks are used with decreasing size. Each step in the process requires a mask where the dimensions are half that of the previous step and an etch of half the depth. Using this technique a stepped structure can be performed. The processing steps required for a four level structure include two main stages. In the first stage a nichrome mask, chosen for its high selectivity, was used as an etch mask to etch to two thirds of a target depth (to form the third level of the final four level structure). In the second stage a thick organic photoresist (XP SU-8 25 developed by IBM and produced by the Microlithography corporation [130]) is used for planarisation, lithography and as the etch mask for reactive ion etching [131].

The substrate is first cleaned using a combination of three solvents; acetone, methanol and isopropyl alcohol. By using progressively weaker solvents the amount of residual solvents that are left on the surface is decreased. It is important that these are removed as much as possible as they can lead to poor resist adhesion. Shipley 1813 photoresist is spun onto the wafer to a thickness of approximately 1 μm and the first stage pattern is created using a standard photolithographic procedure.

The first etch mask was created by evaporating 100 nm of NiCr onto the substrate. A negative of the pattern defined by photolithography is obtained with lift off of the metal on the areas covering photoresist by dissolving the resist in an acetone solution.

A dry etch process using a reactive ion etcher was used to transfer the nichrome pattern to the required depth of 77 μm. This process was optimised for a high etch

rate and conducted in cryogenic conditions to promote side wall passivation for lateral etch reduction and increased anisotropy. A two gas mixture was used consisting of SF_6 and O_2, which with the chamber conditions as outlined in table 3.1 gave an etch rate of about 1 μm/min. This etching process was used with both steps where NiCr and SU-8 were used as etch masks.

SF_6 flow rate	100 sccm
O_2 flow rate	35 sccm
Chamber pressure during etching	0.1 Torr
RF power	100 W
Etch temperature	173 K
Etch rate	1 μm/min

Table 3.1 Anisotropic Reactive Ion Etch conditions of existing process.

After the silicon etch is complete the metal mask was removed using either a chrome etchant or concentrated HCl. The NiCr etch is a wet etch procedure that works at room temperature. A 200 ml solution comprises of 33 g of ammonium ceric nitrate, 8.6 ml of $HClO_4$ in distilled water. Fresh solutions of this mixture proved to be faster and more effective than HCl.

The second stage of the binary process which creates a four level structure utilises XP SU-8. SU-8 is an ultra-thick negative tone resist that is designed specifically for use in micromachining. This resist was chosen as its high viscosity enables it to be planarised across an etched surface, to produce high aspect ratio features using UV photolithography, and also to be used as strong organic etch mask.

The SU-8 is coated on to the wafer using the procedure outlined in table 3.2 so as to planarise the first etch and leave an excess over-layer of 40 μm. A second photolithographic process is performed to leave patterned SU8 on the silicon as illustrated in Figure 3.6. The thickness of the photoresist is determined by the spin speed. The deposition volume only has an influence on the thickness if a sufficiently slow spin speed is used where the excess is not flung from the wafer. However if a thicker layer is required it is advisable to use a higher solid volume version of the resist as better planarisation will be achieved.

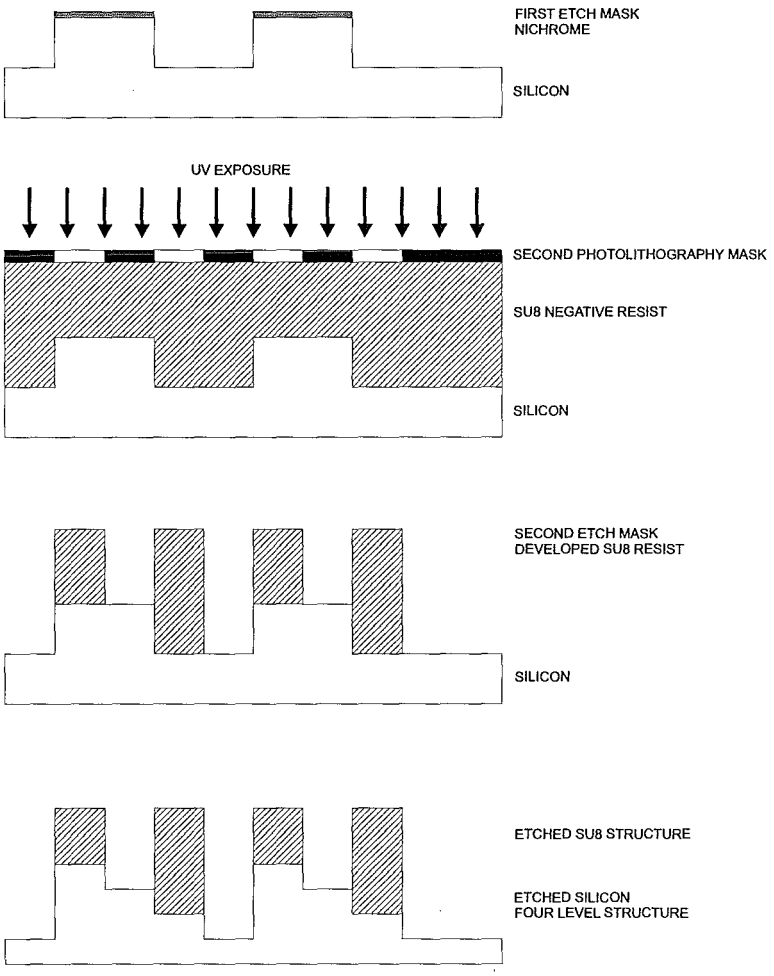

Figure 3.6 Flow diagram showing major processing steps of the previous process. Two stage process uses nichrome as the first etch mask and XP-SU8 photo resist for planarisation and as the second stage etch mask.

1. Dispense volume	200 μl/cm2
2. Spinning	15 seconds at 500 rpm Ramped spin from 500 rpm to 1500 rpm over 10 seconds 15 seconds at 1500 rpm
3. Settling time	100 min on a hot plate at 95°C - 100°C
4. Soft bake	200 seconds
5. Exposure	173 K
6. Post exposure bake	20 min on a hot plate at 95°C - 100°C
7. Cooling	Gradual cooling over 10 min to minimise cracking
8. Development	20 min with agitation

Table 3.2 SU-8 processing conditions.

To increase the resistance to etching of the organic mask the sample was hard baked in an oven at 95°C. This increases the selectivity of the SU-8 to silicon during RIE with a one hour hard bake resulting in a silicon:SU-8 etch selectivity of 4:1. This is a sufficiently high selectivity to etch to the required silicon depth without etching through the etch mask. The second reactive ion etch of 38.5 μm creates the second step and takes the fourth step to the target depth of 115.4 μm as seen in Figure 3.6. This uses the same cryogenic etch process as the first stage used for its high speed and anisotropic profile.

The resulting multi-level structure achieved with this process is shown in Figure 3.7. This result is attained following stripping of the SU-8 resist. This removal is assisted

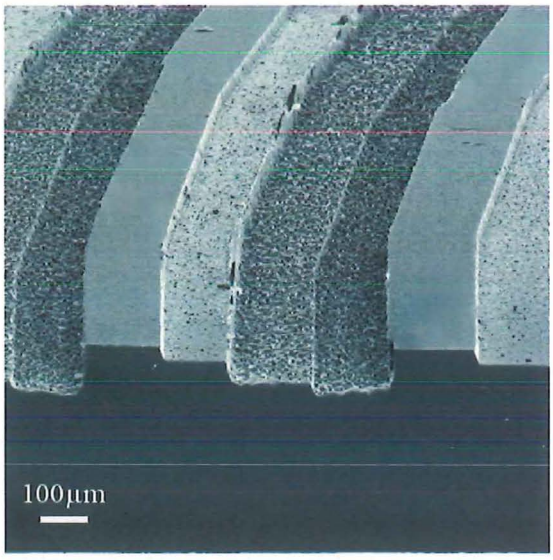

Figure 3.7 The relief profile of a completed 4 level lens fabricated using the previously developed process.

though placing the sample in an HF solution which etches the underlying native oxide layer causing the SU8 to float off. This resist removal technique proved to be unreliable and, as the SU8 is notoriously difficult to etch, a modified resist removal process had to be developed. This is described in the next section. Part of the reason for this removal process being unreliable was due to the roughness of the etched surface that was also the cause of other problems during processing such as alignment.

3.4.2 Mask design

A mask set was constructed to make 25 mm focal length 30 mm diameter converging lenses. The masks are made using a D.W.Mann Model 3000 Pattern Generator and mask writer where single rectangles can be formed serially. Each rectangle can have a defined angle, width height and location on the mask area. Through creating a set of keystones a circle or ring can be defined, and the accuracy to which this approximates a curve is determined by the number of keystones used. As the write process is serial, increasing the complexity can lead to very long write times so there is a limit to which the complexity can be extended. The greater complexity of the mask features removed the sharp corner features that can be observed in the micrograph of figure 3.7. This helps with the alignment of the second and subsequent masks as being a circular pattern eliminates the voids or peaks that can arise from an axial misalignment.

The mask for an eight level lens and grating has been constructed in raw pg format being the code input accepted to the pattern generator in a .pg file. This is a specific unit format used by this machine where 1 pg = 0.254 μm or 0.00001 in. The smallest definable unit size is 5 pg and the largest rectangle dimension is 11375 pg. The angle can be specified in units of 0.1 degree, ranging from 0 to 89.0 degrees in steps of 0.1 degree. An example of a rectangle definition in pg format is as follows:

X123450Y001000H12000W03200A450;

where X and Y are the center location of a rectangular box of H $\times$ W dimension, all in pg units, and A is the angle of the box in units $\frac{1}{10}$ of a degree.

A 14 zone lens was made according to the formula for the Fresnel zone radii r_i:

$$r_i = \sqrt{(f + i\lambda) - (f)^2} \tag{3.1}$$

where r_i is the i^{th} Fresnel zone radius, f is the focal length and λ is the wavelength. This point defined by equation 3.1 gives the center of the each blaze, the steps either side of this point are simply found by halving the distance to the next point. Steps for subsequent stages are created by halving the distance of each individual band or gap. This is done to ensure that the rounding restriction of 5pg units does not lead to an accumulated error that will eventuate in band misalignment. Where the bands did not

divide evenly such that either the band or gap of the next stage had to be 5pg units larger the larger figure was given to the gaps as during fabrication these are the areas that will become masks. It is likely that the inevitable lateral etching that will occur will even any discrepancy that arrives from this. Due to the undeveloped nature of the process and the uncertainty in the amount of lateral etching that would be present a linear blaze was deemed sufficient for this prototype lens design. These radii were used in a C++ program written by the author to create the Fresnel zone plate patterns in pg code. The script for this can be seen in Appendix A. The mask produced from this can be seen in Figure 3.8 and the details of the mask are highlighted in table 3.3

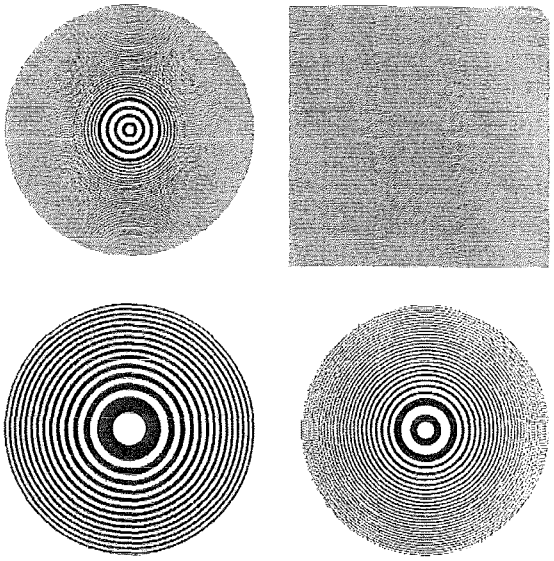

Figure 3.8 Lens and grating mask used for photolithography.

Lens diameter	30 mm
Focal length	25 mm
Number of zones	14
Smallest feature width	88.6 μm
Largest feature width	3.46 mm
Rectangles per ring	64
Total no. rectangles	10169
Grating period	60 μm
Grating mark to space ratio	1:1

Table 3.3 Photolithographic mask statistics.

3.5 PROCESS MODIFICATIONS

As described above, there are a number of design and material choice problems that are apparent in this process. These are separate to the fabrication problems that cause structural inaccuracies making it difficult to make multilevel structures accurately or to complete them at all. This section highlights all of the changes made to the design and the fabrication process that have resulted in a testable set of 2-, 4- and 8-level lenses. Radical changes to the fabrication process design were required to transfer this prototype concept to a viable technique applicable to the formation of a broad range of lenses.

3.6 SURFACE ROUGHNESS

Surface roughness resulting from the reactive ion etching caused several problems. The surface obtained over a large proportion of the lens took the form of black silicon, that being the formation of high pyramidal structures, as shown in the micrograph of Figure 3.9. Because of the light trapping nature of these structures it is very difficult to determine the etch depth that has been obtained from a specific etch.

The surface roughness also effects the optical alignment in a multiple level process. Because the alignment already needs to be made through deep opaque resist it is necessary to have as smooth a surface as possible or the structure edges that lie below the resist can be difficult to make out accurately. It was found that this made a marked effect on the alignment accuracy that was achievable with this process and was what prevented the structuring of lenses with greater than four levels.

A further problem that this roughness caused was the inability to remove the SU8 following etching. Using HF to strip the resist and relying on the native silicon oxidation layer formed proved to be insufficient when the surface was too rough. The vastly increased surface area and the hook like nature of the roughness increased the adhesion of the resist significantly often to a point where the resist could not be removed at all. Generally for resist removal physical abrasion was required to assist in removing the resist from the surface.

Aside from the problems that surface roughness can cause to various stages in the fabrication process it will also degrade the terahertz properties if sufficiently large. The converse may be true if the roughness is smaller as the rough surface may then act as an antireflection structure enabling a higher transmission of terahertz radiation through the lens.

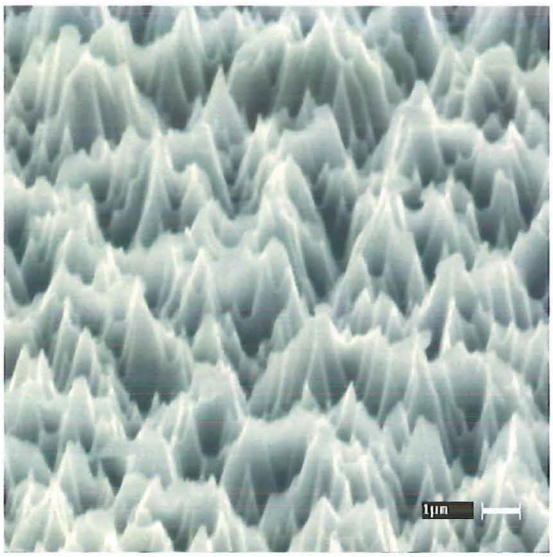

Figure 3.9 Pyramid type structures of similar size to the wavelength of light which act as light traps giving the silicon a black appearance.

3.7 ETCH DEPTH DETERMINATION

There are a number of methods for determining etch depths which all become unreliable when the silicon takes on a very rough nature. Optically one can measure the difference in the step depths through moving an optical microscope through focus from the different step depths. If the surface is rough it is difficult to determine where the true bottom lies where the uncertainty is the height of the surface distortion. If the surface structures are black silicon in nature then it is difficult to gain a focus at all on this surface.

Another optical method is the use of a split section microscope where a beam of light shone at an angle to the surface reflects off the features of different height and appears to the observer as discernible bars of light that can then be read out. With this method when the surface becomes rough the light of the reflected bars is diffused and even a small surface roughness can make the margin of error of this method large. A final method is to use scanning electron microscopy (SEM), however this requires cleaving which destroys the sample. Also it can be difficult to determine in an SEM where the true normal is and subsequently readings can be inaccurate.

It is also possible to determine etch depths physically by dragging a needle across the surface and measuring the deflection as with a Dektak surface analyser. However when roughness is present the accuracy of these measurements is dependent on the sharpness of the needle and the speed with which the needle is dragged across the surface. Because of this such a method will often give a shallower reading than is correct.

3.8 REDUCING SURFACE ROUGHNESS

There are several different ways in which surface roughness can evolve in an etching process. Firstly the randomness of the physical etching process will cause roughness simply from the fact that the impacting ions will not be perfectly uniform. This is just a factor of the inability to control the ionization of the molecules in the plasma perfectly which is a random process. The roughness from this effect is only minor relative to other causes. The other way surface roughness can occur in reactive ion etching is from micromasking. This refers to the formation or deposition of a material on to the surface that has a higher selectivity than the substrate being etched. These can take the form of a reactive bi-product or product from a parallel reaction of the reactant species from the etching process or from small fragments of material from the chamber or sample. The size and selectivity to the etch chemistry of the micromask will determine the nature of the subsequent roughness.

It was discovered that there where three main components causing the roughness of the surface. These being: sputtering of material from the mask, the formation of oxide micromasks, and sputtering of material from the electrode.

Sputtering from mask

During a multiple level etch process there are areas of unetched silicon exposed at each successive stage of the fabrication process. There are also areas that are exposed to several etches or all etches in the course of the lens production. Because of this it is easy to monitor if a specific etching stage or surface effect arises from a specific stage of the processing. It could be expected that surfaces that are exposed to all etches will evolve as the roughest especially as these will lie in the deepest areas of the lens and where there are associated problems of etch by-product removal and ion availability. It was evident that the first etch stage of the original process resulted in a considerably rougher surface than the later stages. In the original process this was the longest etch and it was possible that the build up of contaminants in the chamber where the cause of the unwanted structures.

During the long vertical etch noticeable lateral etching occurs causing a lip of nichrome from the etch mask. This was protruding from the edge where it could be seen that the smoothness of the edge was much reduced from that when the mask was first created. It can be assumed from this that ions bombarding this edge were chipping off small fragments of nichrome, that were then falling to the silicon surface along with fragments dislodged from the planar surface which were then acting as micromasks. An example of this is shown in the micrograph of Figure 3.10 where clear damage can be seen on the NiCr surface and a resultant rough surface is observed.

Initially a nichrome mask was used as the first etch mask as no planarisation is

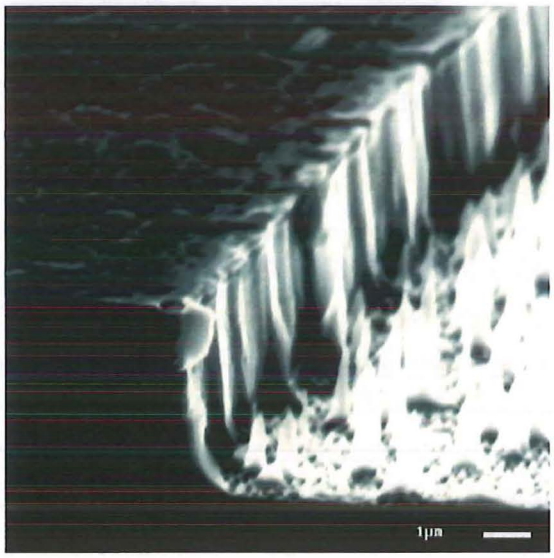

Figure 3.10 Damage to a nicrome mask can lead to sputtering onto the surface which leads to micromasking and subsequent roughness.

required in the first etch stage and nichrome has a very high selectivity to silicon, making it good for the long etch stage required. With the revised etch procedure the selectivity of the silicon to SU8 was 3. Using a single spin of SU8-25 to the silicon surface structures with a height of 45 μm were attained. This is more than sufficient to etch the required silicon depth.

Oxide micromasking

The initial reactive ion etching process utilized a combination of SF_6 and O_2 where the SF_6 ions formed in the plasma are mainly responsible for etching the silicon and the O_2 species are introduced so that $Si_xO_yF_z$ compounds form on the sidewalls for lateral etch passivation. Although this is a very effective method of minimizing lateral etching and preserving an anisotropic side wall the oxygen in the chamber can react with the surface to also form Si_xO_y compounds which have a higher selectivity to silicon. Although the majority of these compounds on the exposed floor of a trench can be removed through the physical bombardment of ions on the surface accelerated by the DC bias between the electrodes some will remain and form pyramidal structures on the surface. The main problem with this is that once formed the peaks are self sustaining in that a high surface area peaked structure is a preferential site for oxidation.

Work from [132] suggested that the introduction of CHF_3 to the gas mixture would create a chemistry that would assist in the removal of surface oxides. Combinations of this gas were introduced while trying to maintain the maximum number of reactants in the chamber possible while keeping the same chamber pressure at 0.1 Torr during

etching. By maintaining as many reactant species as possible in the chamber the etch rate of the process is maximized. A final gas flow rate of 60sccm SF_6, 15 sccm O_2 and 20 sccm of CHF_3 was used which succeeded in giving an improvement in the surface over the entire sample.

This process gave an etch rate of around 0.3 μm / min. The particular reactive ion etcher is specified to give a maximum etch rate of about 0.5 μm / min for silicon which is comparable to the rate achieved in this process. Etch rates have been achieved even in excess of the machine specifications with etch chemistries containing purely SF_6 and O_2 where the non presence of the CHF_3 allows for more reactive species to etch the silicon. Once this etch result was obtained some of the parameters were varied slightly but gave little improvement it was assumed that with this set of etching conditions an approximate etch rate maximum was achieved. When SU8 was used instead of nichrome as the first etch mask using this three gas process trenches of over 120 μm could be etched with a surface roughness under 50 nm peak to peak, with sporadic micromask formed structures under 500 nm high. This means the maximum surface roughness height for this etching procedure is under 0.4% of the depth etched. The surface of a trench etched to 124 μm was imaged using an atomic force microscope as seen in Figure 3.11.

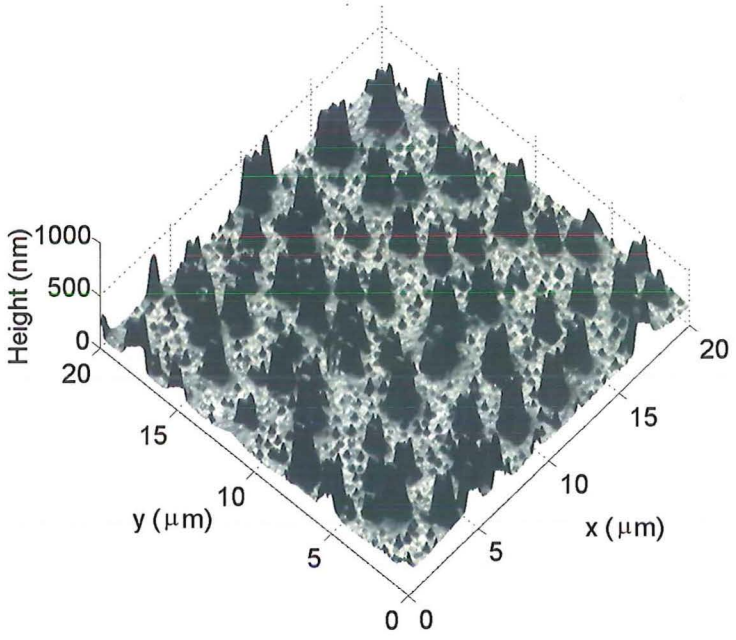

Figure 3.11 Surface roughness of a sample etched to 124 μm deep is under 500 nm high.

Sputtering from electrode

A final cause of surface roughness became evident after several successive etch processes. Random pyramids typical of micromasking were appearing at the outer zones of the lens. These were most dense at the outer four zones and where virtually nonexistent at the inner most exposed areas. It was deduced that this resulted from electrode sputtering. Material deposited on the electrode from many hours of etching and probably material sputtered from the damaged nichrome electrode were being deposited on the silicon surface at the edges. Repeat experiments with old and new electrodes proved this to be the case and not a localised sample problem. Regularly replacing the electrode was determined to be the only solution to this problem effectively eliminating edge localised roughness.

Table 3.4 details the conditions used for the revised etching process. The introduction of additional CHF_3 to the chamber required reducing the quantity of SF_6 so that the pumps could maintain the pressure of 0.1 Torr. As SF_6 provides the primary radicals for silicon etching the etch rate dropped, however remained at a satisfactory rate with an increased RF power of 0.3 μm/min.

SF_6 flow rate	60 sccm
CHF_3 flow rate	20 sccm
O_2 flow rate	15 sccm
Chamber pressure during etching	0.1 Torr
RF power	150 W
Etch temperature	173 K
Etch rate	0.3 μm/min

Table 3.4 Anisotropic Reactive Ion Etch conditions for deep smooth surface etching.

3.9 RESIST ADHESION

There were some problems during etching with resist structures shifting and sometimes lifting off completely from the surface. Being within the reaction chamber it is difficult to determine at which point in the etching process this was occurring. However looking at the etch result it is clearly happening near the beginning of the etch. This can be determined through analyzing the quantity of etching that has occurred around the shifted resist structure. The micrograph of Figure 3.12 shows that the second ring has shifted and subsequently had its pattern transferred to the wrong location. As there is no transfer of this ring in its correct central position the ring must have shifted at the beginning of the etch process.

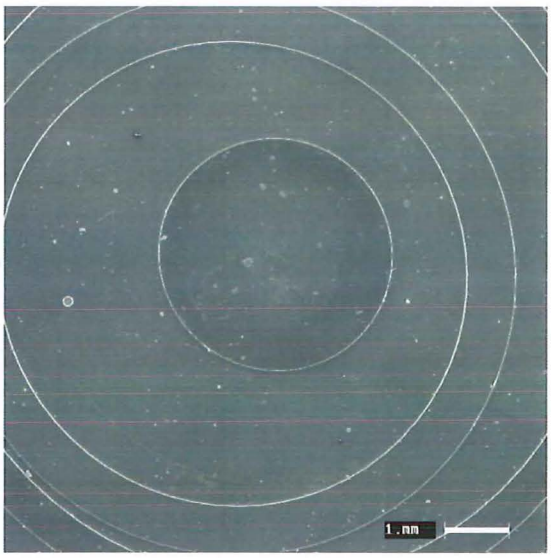

Figure 3.12 A shifted SU-8 ring from poor adhesion causes undesired feature development.

For a feature to shift the bond between the silicon and the SU8 needs to be weak and then a force applied. It was assumed that the thermal expansion difference in the two materials described in the previous chapter is in part due to a weakening of this bond. Another potential cause of poor adhesion may be due to the diluted form of resist used. As the SU-8 25 used was made by mixing SU-8 50 in Gamma Butyrolacetone (GBL) thinner it is possible that this was influencing the adhesion. Localised areas of undissolved solvent in the photoresist will result in a weak bond formed during photolithography. Two possible mechanisms that could shift the photoresist structures are a charging effect from the plasma or from the influx of gas to the chamber at the onset of etching. These being integral parts of the etching process are subsequently hard to fix, hence a better solution to this problem is to investigate ways to improve the adhesion with resist processing. Care was taken to ensure that during any baking process long ramped heating and cooling was used to minimise thermal stress in the resist prior to etching. Also a hard bake prior to etching in an oven at 95 degrees was performed for 4 hours to remove any solvent or developer remaining and help strengthen the silicon-SU8 bond. The problem was not apparent after long hard bake times were implemented and a new mix of photoresist was made.

3.10 RESIST CRACKING

The initial design of the Fresnel lenses placed a circular lens in the middle of a square wafer. As a result there were large areas of resist at the edges which are considerably larger than the features of the lens itself. A problem with these areas arose during etching where these features would crack and subsequently shift to cover the areas of

the outer zones. Although this generally only affected the outer most zones it would still lead to a lowering of the efficiency of the lens. The cracks would also result in etching through to the surface where there should be none. Depending on how the lens would be illuminated would determine whether these areas where exposed. If the lens structure was isolated with an aperture then these should have no effect however if not the etched trenches caused by these cracks would cause sites of diffraction which would further lower the lens efficiency.

More importantly because this effect is feature-size dependent it places a bound on the types of lenses that can be created. Increasing the focal length or optimising the lens design for a lower frequency than 1 THz will result in larger feature sizes than that of the current design. Figure 3.13 shows a section of a larger 45 mm^2 lens design, with a focal length of 250 mm, where the final stage of etching with large SU8 features has lead to significant cracking and lift off. Although there is a fair amount of scope to change the design parameters with the current process the bounds with which this process can be used could be expanded if this problem was overcome.

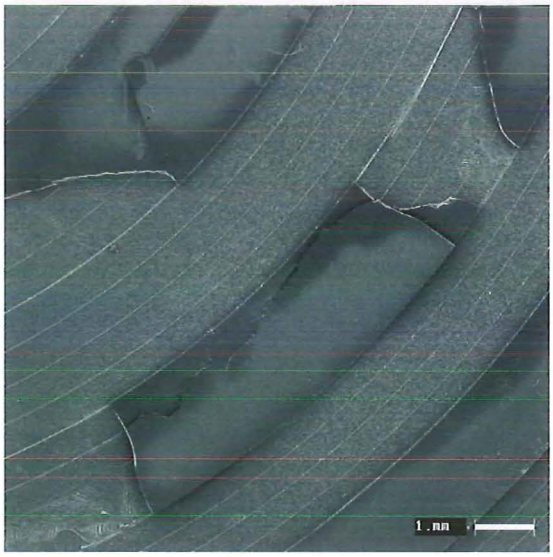

Figure 3.13 Cracked resist causing lift off.

The problem arises because the etching is performed cryogenically and the thermal coefficient of expansion of silicon and SU-8 are considerably different. SU-8 has quite a high value at 50 ppm/K compared to silicon of 20 ppm/K. As the substrate is cooled by 122 K there is a significant variation in the expansion of the two materials which results in high internal stresses in the photoresist. When the resist is particularly thick as in the second and subsequent stages of the fabrication, or the features are particularly large these stresses result in cracking and or lift off of areas of resist.

For this project the problem was overcome through a mask design change. Through designing the mask such that the zones extend to the corner of the lens large features are eliminated and the problem of outer regions cracking and shifting is eliminated. This has the additional benefit that if the entire wafer is illuminated with radiation it will focus more efficiently even though the zones at the corners are not complete. Because of the wide band nature of current terahertz sources available at the moment such a design will have a performance advantage over a circular design. As wafers are always square this design feature will give an additional 20% of focusing area.

There are three possible methods of avoiding the problem of cracking resist. Firstly it is possible to use polymerised epoxy silicon wafers that have the same thermal coefficient of expansion as SU-8. It is also possible to get low stress SU-8 which has a CTE as low as 21 ppm/K [133]. Both of these methods will alleviate the stresses caused by the difference in thermal expansion of silicon and SU-8. However the best solution is to use an alternative etching procedure. This would be ideally performed using a Bosch process etcher which can etch deep structures in silicon with an SU-8 etch mask at room temperature [134]. Adapting the current process used with a standard reactive ion etcher requires reformulating an etch process that will work at room temperature. This is a trade off between gaining an improvement in the integrity of the resist at the detriment of the quality of the etch. Because this type of etcher relies on a cryogenic process for lateral etch suppression and the creation of an anisotropic profile these characteristics are much harder to achieve. However this could be overcome to some degree with lateral etch compensation in the mask design. A room temperature process for this etcher, derived from the process described in this section, has been formulated and is described in section 8.2.3.

3.11 LITHOGRAPHY FEATURE RESOLUTION

A problem with the lithography was evident in that the transfer of patterns into trenches where additional tendril like resist structures were appearing in a particular sector of the lens as seen in Figure 3.14. The degree to which this unwanted resist development appeared seemed to vary in identical processes both in the area which it covered and the severity of the distortion. Initially these were thought to be only very thin but closer analysis proved the resist in unwanted areas could be as deep as 10 μm. With a resist to silicon selectivity in etching of 3 this means the areas of covered silicon would remain covered for a large proportion of the etch resulting in the stepped structure not being transferred in places as it should.

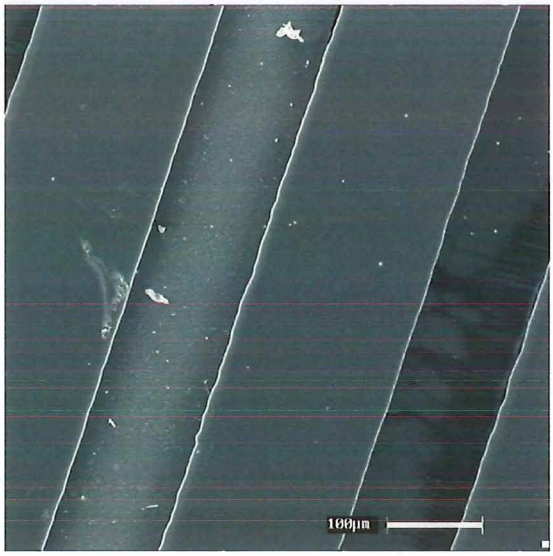

Figure 3.14 Poor planarisation leads to the formation of unwanted SU8 features in the deepest trenches when performing lithography over an etched wafer in a multi level process.

Coupled with the unwanted masking the surface was also ruined in these areas causing a rough dark surface that made alignment difficult. This defect would be the cause of significant astigmatism in the focus and also reduce the overall efficiency through both its own detrimental effects and follow on effects in other processes. In most trenches these features appeared on one side only forming a sloped resist feature against one wall.

Mask Aligner Beam Collimation

Initially it was thought that this problem was due to a non parallel beam from the mask aligner causing exposure into areas that would otherwise be unaffected. This would have explained the shadowing effect that was resolving resist on one side only and in one sector. The mask aligner has a set of mirrors that collimate the UV beam onto the substrate and it was thought that the clear misalignment of some of these mirrors was causing this problem. Poor collimation of light onto the substrate may allow light to enter into areas that should be masked. The effects of this can be amplified somewhat with the fact that the silicon surface is reflective and the SU8 - air boundary is also reflective to a certain extent. Thus any light that enters on an angle will reflect back and forth as the SU8 acts like a waveguide. Although this will die off quite rapidly with the low reflectance of the SU8 - air interface it will still be a contributing factor. Replacement of the mask aligner reflector made some but not a significant correction to the resist problem.

Planarisation

It is possible since this effect was observed over a certain sector of the wafer only that the entire SU8 layer has a slope of some degree which has come about from a non uniform reflow of resist following the pre-exposure bake. During this bake the resist moves considerably and if the hotplate is not perfectly level the resist will not flow uniformly across the substrate. During processing attempts were made to try and ensure the hotplate was as level as possible using a spirit level. However when there are so many possible contributing factors and a wide variation in the degree with which this problem manifests itself it is hard to ascertain whether an improvement has been made. The only way this could be determined is through a very large sample space which is impractical or if the effect was removed or greatly reduced which did not happen.

SU-8 planarises very well, however over large trench widths there was a slight dip in the surface. When light impacts, these curved surfaces will act like a lens causing refraction into areas that should not be exposed. There are many effects which probably were all contributing in part to these unwanted features being resolved. Combined with an edge bead that would prevent intimate contact between the mask and substrate there seemed no clear way to change the lithographic steps to avoid these features. Because of this an alternate solution to the problem was sought.

SU8 etching with reactive ion etching

An investigation was performed into the removal of this unwanted resist. As the unwanted features were thinner than the surface etch mask resist it was assumed that performing a specific dry etch to remove only organic material would etch away the resist material and clear the trenches prior to a silicon etch process. This etch took the form of an oxygen mixture. The process was conducted at high pressure to enable a highly physical process. Oxygen in a reactive ion etch process should aid in the removal of organic material and since SU-8 is a carbon based compound, should work. Initial tests on this process proved very successful enabling the removal of material in a 20 minute etch with conditions as shown in Table 3.5. However the variability of this detrimental resist processing effect meant that structures as deep as 10 μm could be experienced. Sometimes this was to such a degree that the resist filled the entire base of the trench.

O_2 flow rate	50 sccm
Chamber pressure during etching	0.1 Torr
RF power	200 W
Etch temperature	295 K

Table 3.5 Reactive Ion Etch conditions for SU-8 etching.

Although it seemed that the descumming process was applicable when the unwanted feature development was minor when the silicon etch was performed the nature of the SU-8 resist proved to have changed. The silicon gas mixture turned the SU8 resist remaining to a brownish yellow colour and caused significant resist cracking to a point where the cracks penetrated to the surface and resist features shifted from and lifted off their original positions. This was an interesting result as after the descumming the resist showed no signs of any change of form or decolouration. Modifying the etch conditions to have a lower power would reduce the energy of the impacting ions as it was suspected that the ballistic nature of this process may have been to the detriment of the resists structural integrity. This did not help. A second modification tried was the introduction of argon to the mixture. This is an alternate organic etch mixture which unfortunately also resulted in a damaged resist structure following the silicon etch. The manner in which the resist was being effected by this pre-silicon-etch descumming process was very hard to discern as after reactive ion etching the unwanted material was cleared and the remaining SU-8 appeared to be undamaged. Despite several modifications to the gas chemistry and etch conditions it was determined that relying on such a method was not going to work.

Lithography solution

The final solution to this problem proved to be in reversing the structuring process such that the small features are etched first. This avoids the problem of developing fine features in deep trenches. Changing the process in this way has one drawback in that the deepest etch is then performed last. When spinning SU8-25 onto a plain silicon wafer a resist depth of about 45 μm can be attained. However when spinning this resist onto a substrate which already has trenches etched to 46 μm the surface thickness of the resist can be as low as 15 μm. With a silicon to resist selectivity of 3 in this process this is insufficient to etch the remaining 63 μm to make an eight level structure. To overcome this problem a multiple spin lithography process was used for the final step of lens fabrication. This involved performing a first spin followed by a bake to remove the solvent in the resist for 100 minutes. After cooling a second etch was performed to increase the total thickness of resist to over 50 μm at the surface. Performing the later lithography stages on this dual resist layer proved to work using the previously defined

processing times. The large feature sizes and relatively non challenging lithography gave good results with no unwanted feature development. Performing the stages of fabrication in this manor also makes the structure more resistant to the detrimental effects of lateral etching as explained in chapter 7.

3.12 RESIST REMOVAL

It had been shown that soaking the sample in hydrofluoric acid after etching can assist in the removal of the SU8 resist from the surface. Although it is possible to remove the photoresist using a long organic etch this has proved to be both costly from its duration and damaging to the silicon surface in that subsequent processing has resulted in a rougher than expected surface. As a result an improvement on this process for the removal of the resist was sought.

Currently the process relied on the removal of the thin native silicon oxide from the silicon surface to lift the resist form the surface. This process works with a fairly high degree of success on the first stage of the process where the resist is built on the polished silicon surface only. However as soon as some topography is present where the resist is adhered to the trench sidewalls and the surface has a degree of roughness resulting from etching, the SU8 proves to be a lot harder to remove.

Two processes were investigated to increase the thickness of the silicon oxide layer. Firstly silicon oxide can be evaporated on to the surface of the silicon. Using an off axis rotating mount a sample can be suspended upside down in a vacuum evaporation chamber. By having the sample rotating off axis the etched sidewalls and trenches can be covered over the entire lens. Silicon oxide is deposited by heating SiO powder in an evaporation boat. Following this process through as a sacrificial layer for post etch SU8 removal proved successful however it has a few downfalls. Firstly the topography of the silicon oxide would not be as smooth as would be preferable due to the randomness of the evaporation process. Also the uniformity of this across the wafer was shown to be non-ideal from the colouration change from the centre to the edge. Because this layer of silicon oxide needs to be removed in the etcher before the silicon is etched any non-uniformity either on a micro or macro scale across the lens is reproduced. On the macro scale where the thickness of deposition varies across the lens a bullseye effect will arise where the areas of silicon at the edges will begin etching before the centre. As this is an effect already present in the etching from other effects further amplification is undesirable. On the micro scale non-uniform deposition will lead to surface roughness.

In the course of this work a dry process was used with an oxygen enriched atmosphere to produce a silicon dioxide layer. This furnace was operated at 1050°C and samples were placed in the chamber for a period of 2 hours. Relating this to the graph of Figure 3.15 [135] it can be seen that an oxide thickness of 0.15 μm could be expected. The approximate thickness of a thermally grown oxide layer on silicon is most easily

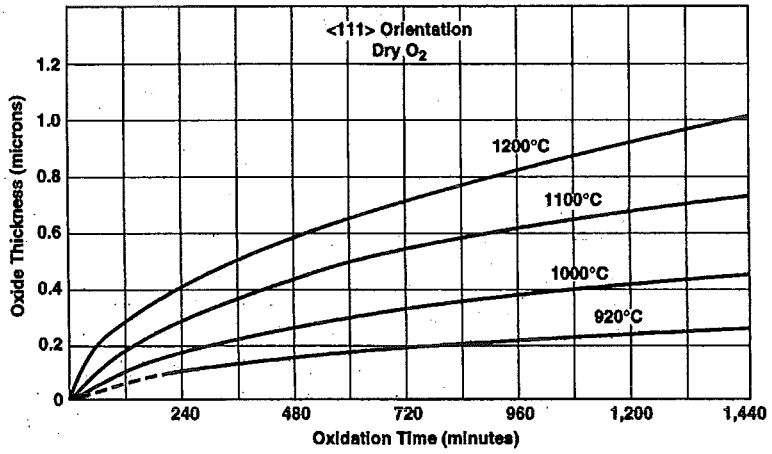

Figure 3.15 Silicon oxidation rates in a dry oxygen atmosphere [134].

determined by looking at a colour chart as in table 3.6 [136]. Because the oxide thickness is of the order of the wavelength of visible light when the layer is at a one quarter wavelength thickness it will cause that colour of light reflecting off the silicon surface to interfere constructively. Hence as the thickness of the oxide layer increases, the colour of the substrate shifts from blue to red. As the layer gains additional wavelengths in thickness this colour cycle will repeat from blue to red.

Film Thickness (μm)	Color
0.05	Tan
0.07	Brown
0.10	Dark violet to red violet
0.12	Royal blue
0.15	Light blue to metallic blue
0.17	Metallic to very light yellow green
0.20	Light gold or yellow - slightly metallic
0.22	Gold with slight yellow orange
0.25	Orange to melon
0.27	Red violet
0.30	Blue to violet blue
0.31	Blue
0.32	Blue to blue green
0.34	Light green
0.35	Green to yellow green

Table 3.6 Surface color of different thickness layers of silicon oxide [135].

Initially the oxidation was performed in a furnace at 900°C with standard atmospheric air and humidity for a period of 2 hours. This gave a tan colour indicating a 0.05 μm silicon oxide layer. This was improved upon by placing samples in a dry oxygen environment where the oxidation rate was tripled taking on a light blue colour indicating a thickness of approximately 150 nm. This measurement is in line with the predicted thickness of Figure 3.15. With a sacrificial oxide layer of this thickness there seemed to be no problems with the removal of photoresist from etched surfaces.

Oxidation improving surface roughness

Creating an oxide layer on the etched silicon surface will also assist with the smoothing of the surface to some extent. Any roughness present on the surface of the silicon appearing as a spike will form a site for preferential oxidation due to the increased surface area. Because these areas have a much greater rate of oxidation the entire feature can be oxidised during the time taken to create the sacrificial oxide layer. As this entire layer is removed during the HF lift off procedure the surface roughness features are also removed. Even if the oxide layer is only thin there will be some improvement in the surface.

3.13 PROCESS SUMMARY

A complete multiple level fabrication process has been developed which has been used for the fabrication of a set of terahertz Fresnel lenses optimised to perform at 1 THz. The aim of this project was not just to develop a process that was solely limited to a single design. Although these optics have been shown to focus over a broadband they are optimised to perform at a certain frequency and to focus to a set distance for that frequency. The fabrication process is applicable to the production of terahertz diffractive optics in a broad range of frequencies over a wide range of focal distances. The binary process requires repetition of a lithography and etching procedure as highlighted in Table 3.7 and shown in the flow diagram of Figure 3.16. For each repetition a larger mask is used with twice the etch depth of the previous stage. Where a single spin coat will be insufficient to last the required etch depth a multiple spin technique has been shown to work.

Process Limitations

There are limits to this range defined by the change in feature sizes required. Increasing the focal distance for a set frequency leads to an enlargement of the features on the mask. Also creating a lens optimised to work at a lower frequency will demand larger feature sizes. Larger features require slight modifications to this process to avoid resist cracking. These modifications are described in section 3.10 and a modified high temperature version of this process is described in chapter 8. More importantly such

Oxidation	
Atmosphere	Dry oxygen
Temperature	1050°C
Duration	2 hrs
Photolithography (SU-8)	
Dispense volume	200 μl/cm2
Spinning	15 seconds at 500 rpm 10 seconds ramp from 500 rpm to 1500 rpm 15 seconds at 2000 rpm
Soft bake	100 min on a hot plate at 100°C (Repeat spin and soft bake for last stage)
Exposure	200 seconds
Post exposure bake	20 min on a hot plate at 100°C
Cooling	Gradual cooling over 10 min
Development	5 min with agitation
Hard bake	2 hours
Reactive Ion Etching	
SF_6 flow rate	60 sccm
CHF_3 flow rate	20 sccm
O_2 flow rate	15 sccm
Chamber pressure during etching	0.1 Torr
RF power	150 W
Etch temperature	173 K
Etch rate	0.3 μm/min
SU-8 Removal	
HF emersion	45 min

Table 3.7 Processing steps required for each increase in step complexity where progression of masks is from smallest to largest feature mask.

lenses have reduced numbers of zones due to wafer size limitation leading to diminished focusing efficiency. At higher design frequencies an issue could arise with feature resolution. However using contact UV lithography it has been possible to develop SU-8 features down to 5 micron. Because small resolutions are possible it is possible to make practically all lens designs in the upper terahertz frequency band. At 10 THz the focal length would have to be reduced to 1 mm before feature resolution became a significant processing issue. As such designs require a smaller etch depth a thinner resist layer can be used which will enable higher resolution lithography. When the features are reduced to this size, as there are a range of different feature sizes across the wafer, the smaller features may etch slower due to the difficulty of removing waste material from the trenches.

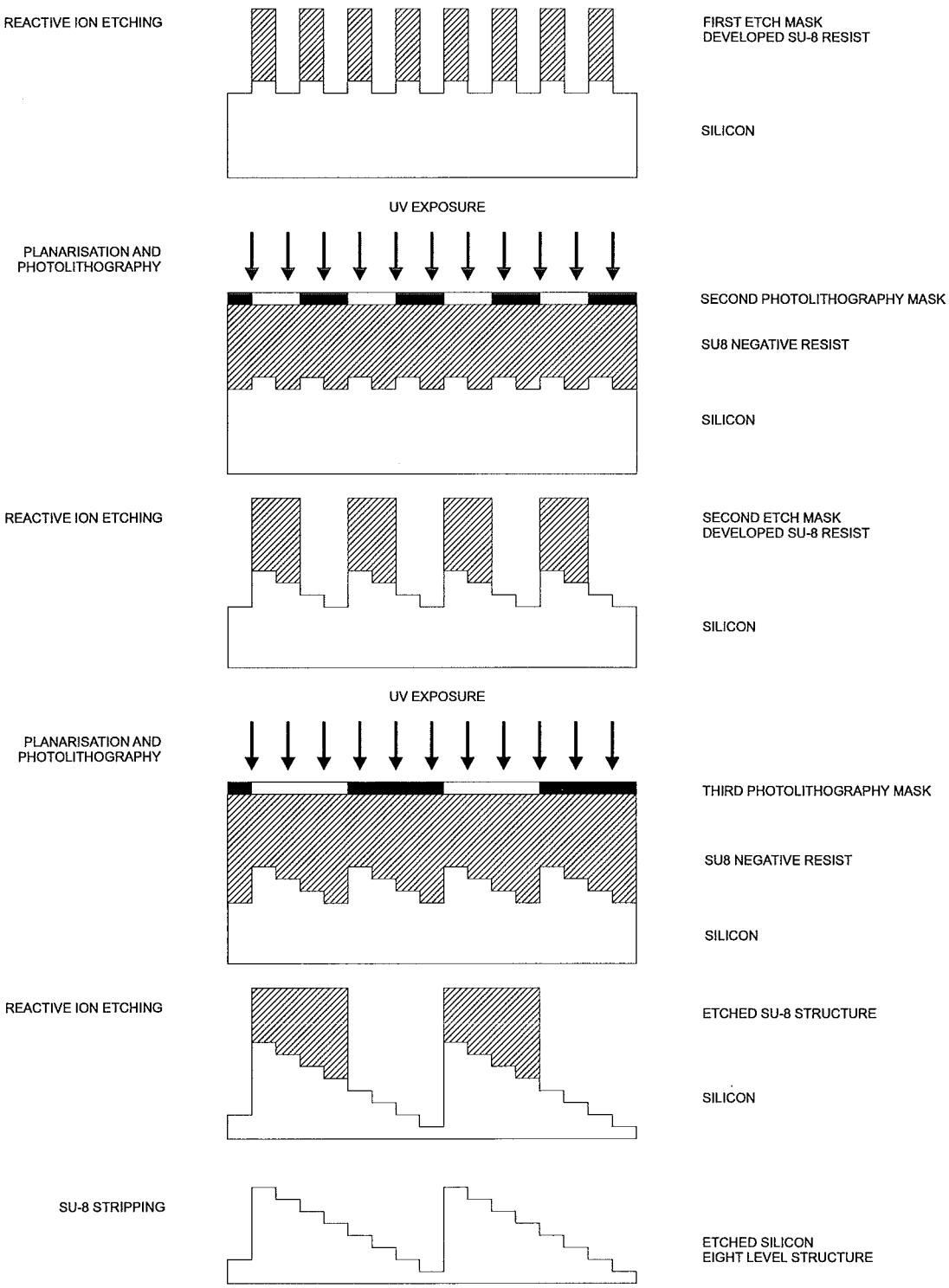

Figure 3.16 Flow diagram showing the three stage process required for the formation of eight level diffractive optic structures. This involves a set of three repeated photolithography and etching stages.

The size of optic is limited to an extent in that the microprocessing equipment is limited in the size of wafer that can be handled. For the laboratory equipment used in this work the maximum wafer size possible is 4" although wafer technology exists enabling 12" wafer fabrication. Aside from the physical size limitation the uniformity that can be achieved in the respective pieces of equipment needs to be considered. This is especially pertinent for etching where uniform etching across the entire electrode is difficult to achieve. This does not necessarily restrict the size but reduces the benefit of creating a larger lens as there will be a loss in efficiency due to the non-uniformity.

3.14 SUMMARY

Significant modifications have been made to a previously developed process to change this initial concept into the reality of a completed structuring technique. Although this previous work accurately described fabrication of a structure of the desired dimensions of four levels in complexity the inaccuracies and hence reliability of the process would have made it difficult to extend to a commercially viable process. Also, the deficiencies in the design and materials used resulted in a lens with a much reduced efficiency. Identifying all of the contributing factors to a specific problem can be a complex matter as it was found that more than one effect was the cause of some of the defects making solving these problems experimentally very difficult. Also the process takes a long time to run to completion so discerning a downstream problem requires significant pre-processing before the experiments can be conducted. Using this process a set of 2- 4- and 8-level lenses were constructed. A cross-section of an 8-level lens is shown in Figure 3.17 and images of the three different complexity lenses are shown in Figure 3.18, which were used for continuous wave and pulsed terahertz characterisation.

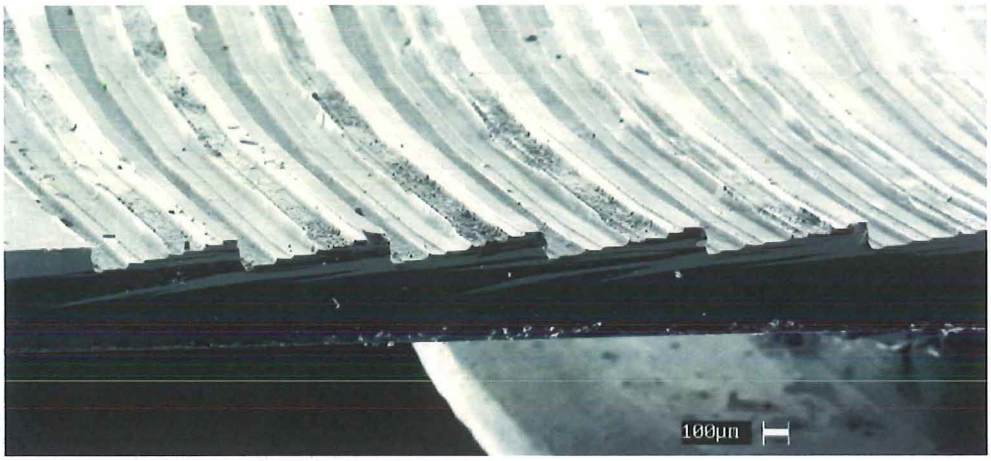

Figure 3.17 Cross-section of an 8-level lens.

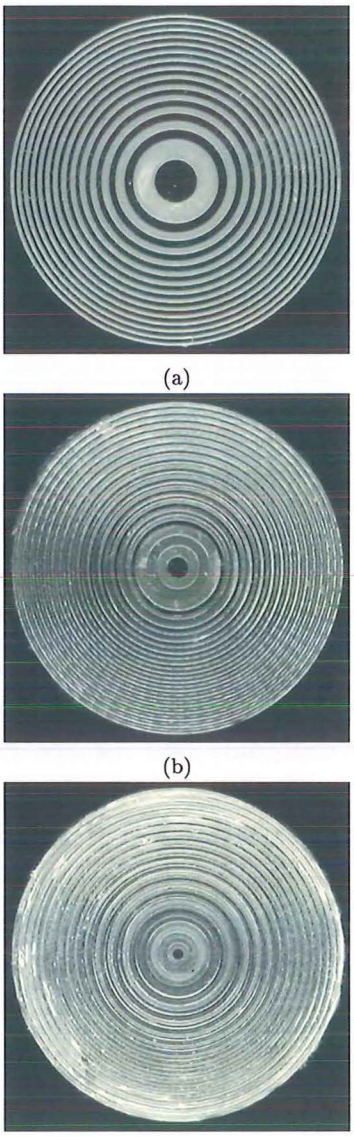

Figure 3.18 30 mm^2 Lenses tested created for testing; (a) 2-level, (b) 4-level and (c) 8-level.

Chapter 4

CONTINUOUS WAVE TESTING

4.1 INTRODUCTION

A set of diffractive optic lenses and gratings of different complexity were used in testing. As this is a new device technology in this field there was no predetermined method for testing their functionality. A method for assessing their performance had to be established. Because the lenses were designed to operate optimally as a narrow band device at 1 THz it was envisaged that a continuous wave single frequency source would provide an excellent assessment of their performance. The majority of terahertz systems currently in use are pulsed but in recent years several laboratories have had success in producing continuous wave (CW) radiation at terahertz frequencies [137]. A collaboration with the Physikalisches Institut at the Johann Wolfgang Goethe-Universitat in Frankfurt, Germany provided access to a high quality tunable CW terahertz system [138] where testing was performed on a set of 4-level binary Fresnel lenses. The author performed these tests during a two week visit to this laboratory.

The existing scanned imaging system was modified to image the focal plane of the lenses to be tested. Due to the fact that the development of this continuous wave system is in its infancy there was considerable tuning required to obtain the stable terahertz beam required to make reliable assessments of the optics. This chapter details the method with which the continuous wave terahertz beam is generated and detected and then details the testing method and the results obtained for silicon etalons, an anti-reflection structured silicon sample, and a pair of four level lenses.

4.2 EXPERIMENTAL TECHNIQUE

A recently designed CW terahertz generation and detection setup was used, as shown schematically in Figure 4.1. In this system a two colour CW Ti:Sapphire laser is used. This generates two optical waves with independently tunable wavelengths centered around 800 nm. The Ti:Sapphire lasers share a single gain medium, pumped by a 5 W Coherent VERDI all-solid-state laser [139]. The two beams are spatially combined with a 50/50 beam splitter cube yielding two beams which are intensity modulated at

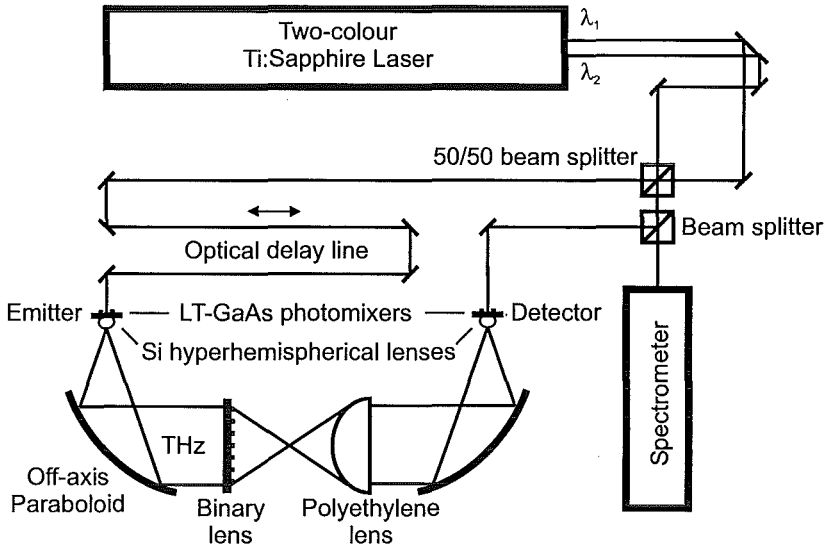

Figure 4.1 Optical table component layout for continuous wave terahertz emission and detection.

the difference frequency, tunable between 0 and 10 THz. One of these optical beams is guided via an optical delay line to the emitter antenna and the other is used to gate the receiving antenna. A fraction of the detector beam is split to a spectrometer for the tuning of the difference frequency. The antennas used were H-shaped photomixers each having a 50 μm long dipole and a 5 x 10 μm^2 photoconductive gap printed on LT-GaAs. The emitter, grown at 270°C, had a measured carrier trapping time of 1.2 ps and the detector, grown at 200°C, a trapping time of 0.35 ps. The reason for having these differences is to achieve higher output power at the emitter and a broader detection bandwidth at the detector. Both photomixers are illuminated with 100 mW of optical power. The detector antenna acts like a switch where the terahertz radiation generates free carriers in the GaAs allowing current to flow.

To improve the signal to noise ratio the emitter is biased with a 25 kHz square wave signal between ±12.5 V enabling lock in detection. This is preferential to using a chopper, which can cause feedback into the two-colour laser source. Terahertz radiation emitted from the antenna is coupled out using a hyperhemispherical silicon substrate lens of 2 mm in diameter. This radiation is then collimated into a beam using an off-axis paraboloid mirror and then focused onto the detector antenna using another off-axis paraboloid. The beam was 5 cm in diameter traveling approximately 30 cm through free space between the mirrors. Considerable effort is required to align the system such that a collimated beam is obtained. Because there are many degrees of freedom in all the optical components and the terahertz beam is invisible to the human eye it is necessary to align the system using the optical beam that impacts on the terahertz emitter antenna. Removal of the antenna enables the visible laser beam to pass through the off-axis paraboloid setup. Once this has been collimated and aligned

to the detector antenna the emitter can be replaced and the only alignment required then is tuning of the antenna position and the position of the hyperhemisperical lens that sits on the emitter. Additional tuning of both the emitter and detector position is required to maximize the signal strength of the received terahertz beam. Part of this alignment involved trying to obtain a Gaussian shaped terahertz beam, which proved to be difficult. The non ideal beam shape that was ultimately used in the testing may have clouded the results somewhat. This is because it was harder to determine whether specific anomalies in the results were due to effects of the antenna or optical alignment of the terahertz system or due to alignment or performance of the two lenses within the beam. This is discussed further when the lens characteristics are given.

Analysis of the lenses was conducted in the collimated beam by placing the T-ray binary lens on the emitter side to focus the beam, then recollimate the beam using a second lens as in Figure 4.2. By placing an aperture between the two lenses the signal strength at different locations in the x, y, z planes was determined to build up an image of planes in front of the lens. To achieve this, a 500 μm aperture was placed on a computer controlled stage that can be programmed to raster scan a plane in the terahertz beam path. Each lens was placed on a set of micrometers that allowed them to be moved in all directions such that they lie on the same axis down z. Initial measurements of the binary lenses were taken using a plano-hyperboloidal lens to recollimate the beam, which was manufactured on a lathe from high-density polyethylene. For later results this re-collimation was performed using a second binary lens. From these scans it was possible to ascertain the three-dimensional (3D) spatial composition of the two lens system.

One of the main problems with testing the lenses in the cw source was the irregularity of the beam, which made it difficult to gain good comparisons between different setups. Instability in the laser system also meant the laser needed to be retuned regularly and the operating point could not be accurately duplicated. There seemed to be poor correlation between what would appear to be a good beam alignment and the results when two lenses where introduced to the system. One of the main contributing factors of this is that the optical system alone has some 14 axes of freedom and the alignment of the lens system to lie parallel in the optical beam was hard to achieve. An angular misalignment in this could lead to a strange result in the inter lens aperture scans. Combining the poor beam shape, difficult optical alignment, and laser instability it was difficult to make clear measurements of the performance of different lens combinations. It seemed that the CW THz system performed better at higher frequencies as can be seen in the following beam scans with the same optical alignment.

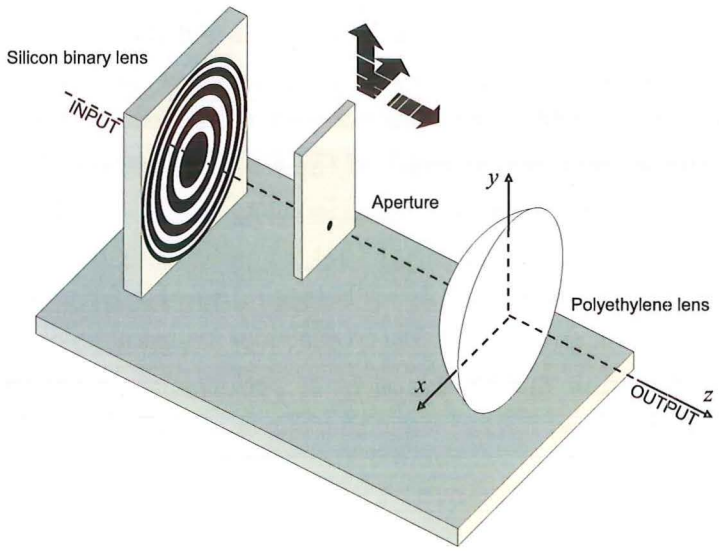

Figure 4.2 Focal plane imaging set up between a silicon and polyethylene lens.

4.3 ANALYSING THE INPUT BEAM

A significant period of the two weeks available to conduct measurements was taken trying to generate a Gaussian beam shape at 1 THz. Some of the best beam shapes that were achieved at different frequencies are shown in Figure 4.3. In this figure, the intensity is shown in the left hand figures and the phase profile in the right hand figures, for frequencies 1, 1.25 and 1.5 THz. This data was obtained by scanning a 1 cm diameter aperture in the beam between the paraboloid mirrors prior to inserting the lens pair. It can be seen that the beam shape is not consistent at different frequencies. It was often the case that there was a more uniform beam profile with more stable phase at higher frequencies.

Because the lenses were designed to operate optimally at 1 THz, much effort was put into trying to get a good beam at this frequency. It is possible that there was a problem with the antenna that causes it to operate poorly at 1 THz. This seems to be the only logical assumption as the optical system was untouched in the above three scans; only the difference frequency which determines the frequency of operation was altered. Hence, as a redesign of the antennae was beyond the scope of this project, the non-ideal beam profile at 1 THz of Figure 4.3 (a) was used for CW lens characterisation.

4.4 SILICON TRANSMISSION ASSESSMENT

Before the lens characterizations were performed the transmission properties of the silicon used for their fabrication was measured. The high refractive index of silicon [118] makes fabrication of diffractive optics considerably easier than a lower refractive

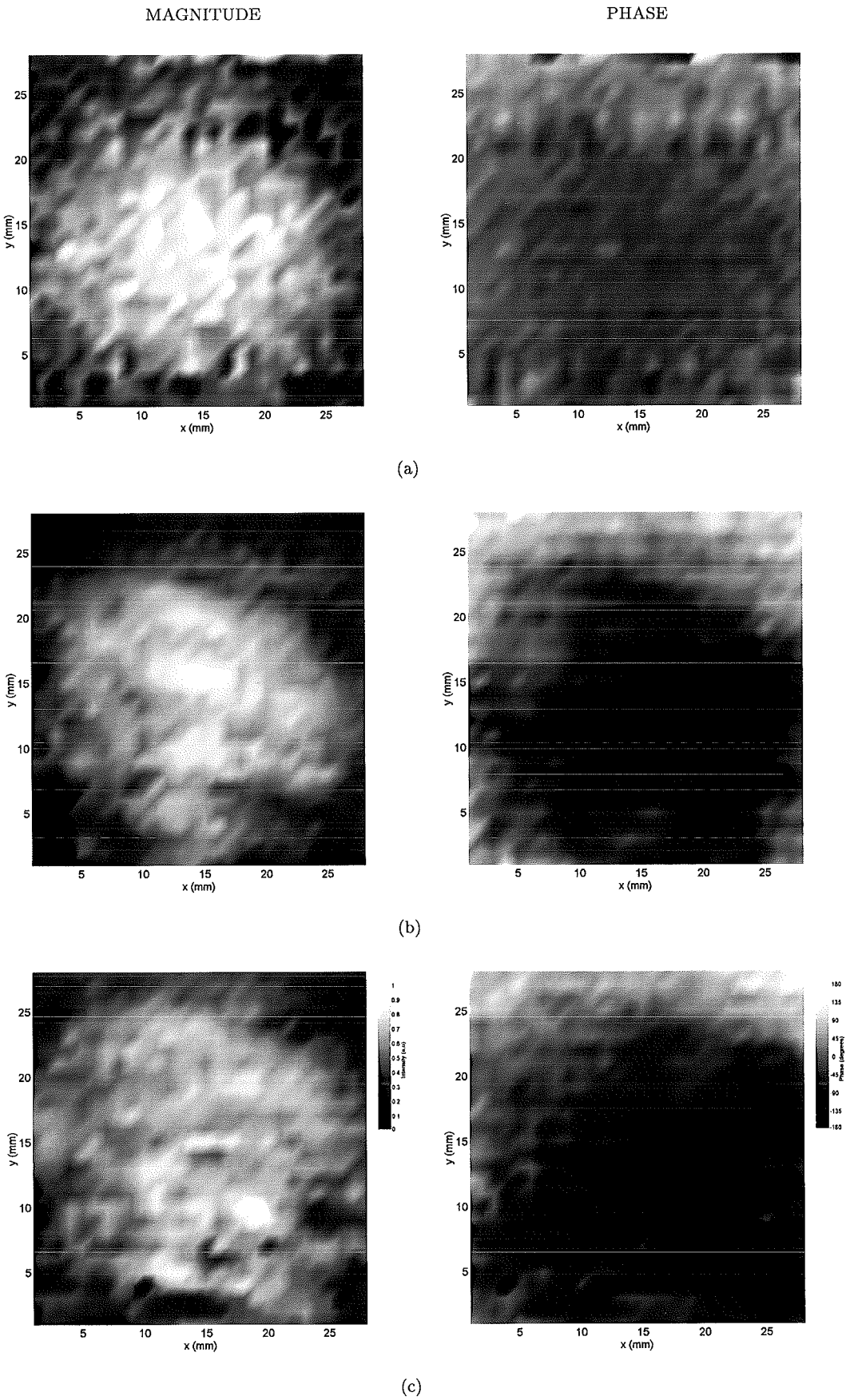

Figure 4.3 Magnitude and phase of a continuous wave terahertz beam at (a) 1 THz (b) 1.25 THz and (c) 1.5 THz.

index material by reducing the required etch depths. However it was expected that because the difference in refractive index at the silicon air interface is large that there would be considerable reflection from all the lens' surfaces. In addition the effects of absorption losses could be assessed in this experiment.

Because all terahertz sources, be they continuous wave or pulsed, have low power it is desirable to maximize the transmitted power. The lenses were fabricated on high resistivity silicon (1000 Ωcm), compared to conventional bulk silicon which has a resistivity of around 10 Ωcm. The two wafer types were compared to determine the benefits of using the higher resistivity material. Figure 4.4 shows the time domain terahertz waveform comparing the current generated at the detector antenna for the free space beam, and for the beam with the different resistivity plain silicon wafers placed in the path. This illustrates that only 20% of the radiation passing through the high resistivity silicon is lost compared to 50% with the lower resistivity material as compared to the free space beam.

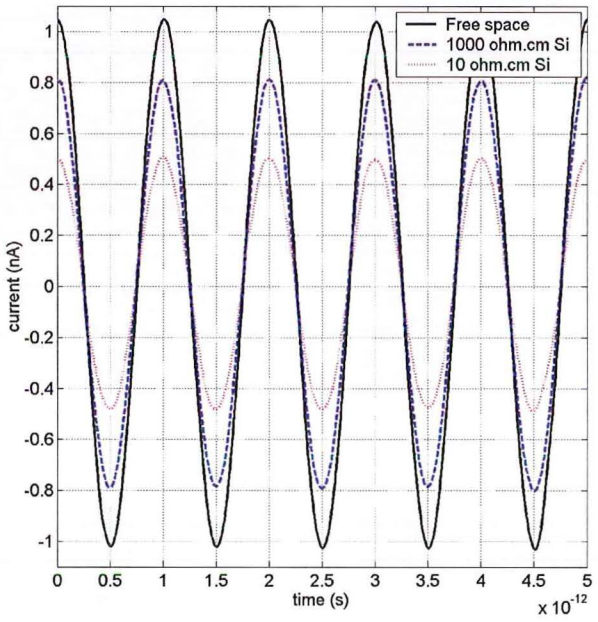

Figure 4.4 Time domain CW signal for a free space beam and beams with different resistivity silicon wafers placed across.

4.4.1 Anti-reflection coating characterisation

Transmission of radiation between materials with a large difference in refractive index can be increased by using an anti reflection coating or by creating anti-reflection structures on the surface to create an artificial dielectric. This is well documented [140, 141] and involves creating a smoother transition of refractive index between the two mate-

rials. A simple grating, Figure 4.5, was fabricated to see if this could successfully be used as a backside structuring technique for silicon terahertz diffractive optics.

The plot of Figure 4.6 illustrates how this grating is effective in increasing the amount of terahertz radiation at 1 THz passing through the silicon. Relative to a plain silicon wafer the signal is increased by 10%. As the terahertz radiation is linearly polarized the grating allowed more radiation to pass in one orientation while reducing the power in the other orientation. When the grating was placed in vertical orientation the signal went down 4%. Gratings such as this can be optimized to work at a single frequency or to be more broadband by etching saw tooth gratings [142].

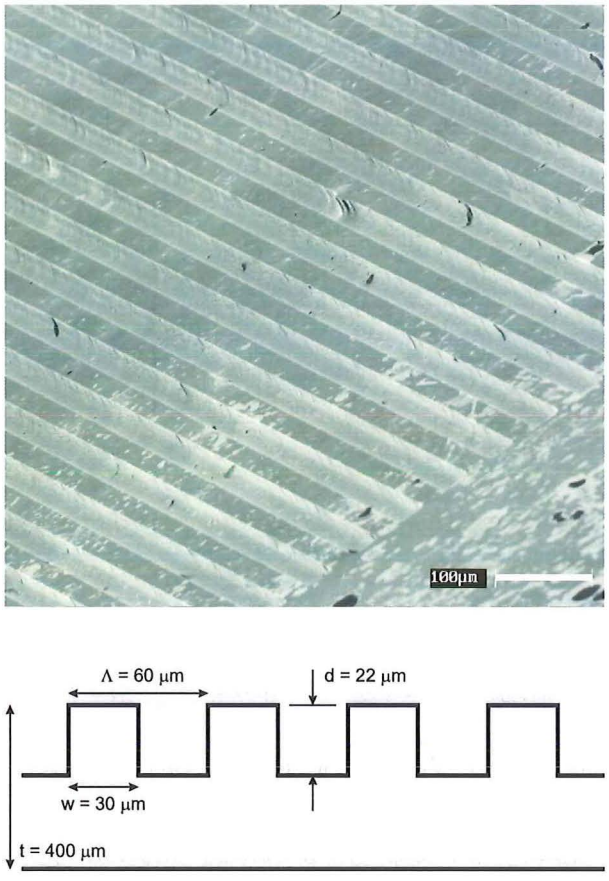

Figure 4.5 60 μm pitch grating etched into silicon.

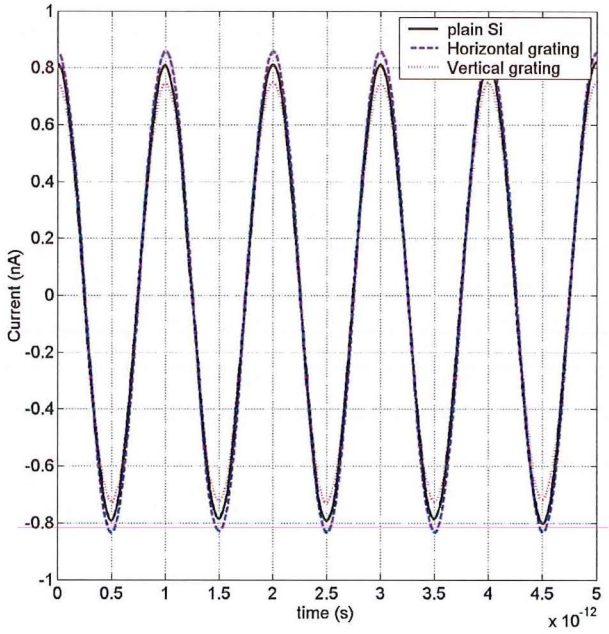

Figure 4.6 Time domain CW terahertz waveform of a silicon wafer structured with a linear grating placed in different orientations.

4.4.2 Fabry Perot Etalon

The ability to create terahertz lenses on silicon wafers yields many benefits for fabrication techniques and enables formation of very compact optics. However the high refractive index of silicon at terahertz frequencies and the sub-millimeter width of the wafer introduces potential problems for terahertz optics. Reflection at an interface can be treated as a special form of refraction. For normal incidence, the fraction of light reflected is equal to

$$(n-1)^2 / (n+1)^2 \tag{4.1}$$

where n is the relative refractive index. In the case of terahertz at an air-silicon boundary, $n = 3.42$ meaning there will be 30% reflection. Because the wafer is of the order of several wavelengths thick with 2 reflecting surfaces it can act as a Fabry-Perot etalon. A Fabry-Perot etalon (or simply, an etalon) is the simplest form of a Fabry-Perot interferometer. Its primary optical property is that if a monochromatic light ray travels back and forth between two mirrors and the round trip optical distance between the mirrors equals an integral number of wavelengths (λ, 2λ, 3λ, etc.), then the light passes through the etalon. The silicon wafers used in the course of this work were 400 μm thick. The expected transmission through an unstructured silicon wafer disregarding absorption was calculated using Gsolver [143] as shown for wavelengths between 200 μm to 400 μm in Figure 4.7.

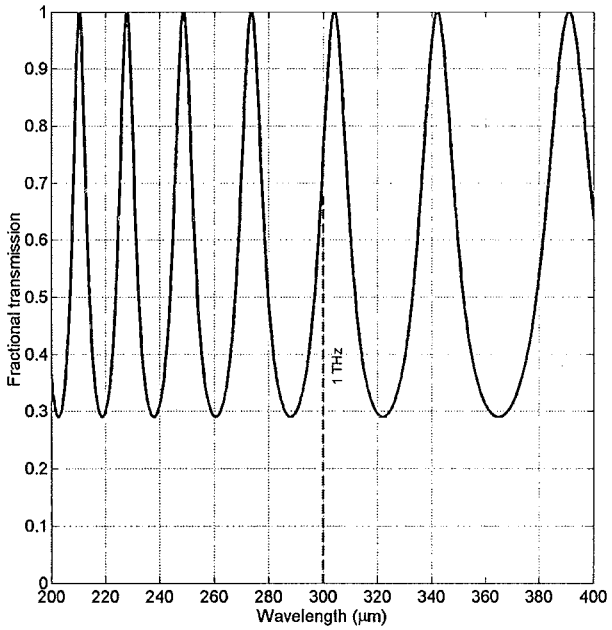

Figure 4.7 Simulation of a 400 μm thick silicon wafer showing expected transmission of terahertz.

At the design wavelength of the lenses, the wavelength in the silicon is 87.7 μm. This means the wafer thickness is 4.56 wavelengths at 1 THz resulting in high transmission of the radiation.

There are several factors that will determine the total amount of transmission through the lens. As the surface is structured the depth will vary between 0 to 108 μm. This means different wavelengths will have different amounts of transmission at different steps of the lens blaze. Neither of the surfaces will be perfectly smooth which will reduce the reflection at each interface. Also the amount of radiation absorption will influence the amount of transmission which is dependent on the thickness in different locations. For the lenses to work well in broadband applications it is desirable to avoid these reflections which can be achieved through the use of an anti-reflection grating or coating. Figure 4.8 shows broadband transmission through a simulated 22 μm grating. At 1 THz the transmission is increased by 14% with this single side grating. This is a similar gain achieved with the silicon grating constructed (Figures 4.5 and 4.6).

This section highlights how anti-reflection structures show great prospect for increasing the signal strength of a silicon diffractive optic. It is possible to create these structures on the opposite side of the lens to boost efficiency. These structures were not constructed on the lenses used for any measurements so that any effects or non-

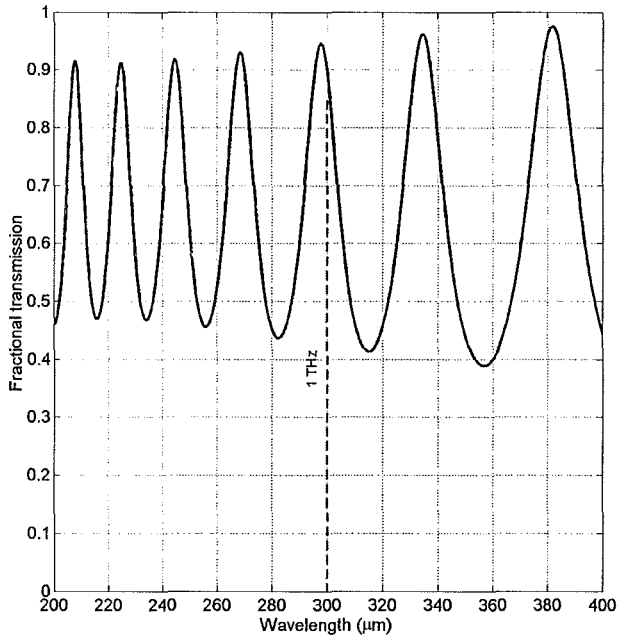

Figure 4.8 Simulation of a linear grating showing expected transmission of terahertz.

uniformities in the radiation patterns of the lenses would not be clouded by any irregularities of a grating. Such a structure should however be incorporated into any lens intended for a specific application.

4.5 SINGLE SILICON LENS ASSESSMENT

Following the transmission experiments, a silicon and polyethylene lens were placed in the beam as in Figure 4.2. The seperation between the two lenses was 54 mm with each lens approximately 15 cm from the center of the respective parabolic mirrors. An assessment of the ability to focus can be attained by placing the binary silicon lens to be tested at the emitter side and reading out the focal pattern with a scanned 500 μm diameter aperture and the polyethylene lens. From this several plots were obtained showing x, y focal plane images and an x, z axial scan. All values of z are measured from the face of the source side silicon lens. This gives an appreciation of the focal spot size and the depth of field.

A cross section of the beam profile at $z = 25.6 \pm 0.2$ mm is shown in Figure 4.9. From this it is possible to determine the focal spot size at the beam waist. This measured 745$\pm$10 μm. The full width half maximum (FWHM) has also been measured as 570$\pm$10 μm. For a Gaussian input signal the FWHM can be calculated for a zone

plate according to the formula [144] $FWHM = 1.22\Delta r$, where Δr is the outer zone width. With an outer zone width of 708.8 μm this predicts a FWHM of 865 μm. Thus the measured value is 86% of that expected of a zone plate, a reflection of the performance gain achieved from a four level lens. Regardless of the non-uniform input beam the beam shape at the focal point, as seen in figure 4.9(b), appears to be quite symmetric.

Measurements were also taken at other z positions. Figures 4.10(a-f) show the intensity and phase at x, y planes moving through focus. The plane with the most intense focal spot, Figure 4.10(c) is at $z = 25.6$ mm, which is close to the design focal length of 25 mm. Here the beam intensity has a Gaussian shape and a flat phase profile as would be expected.

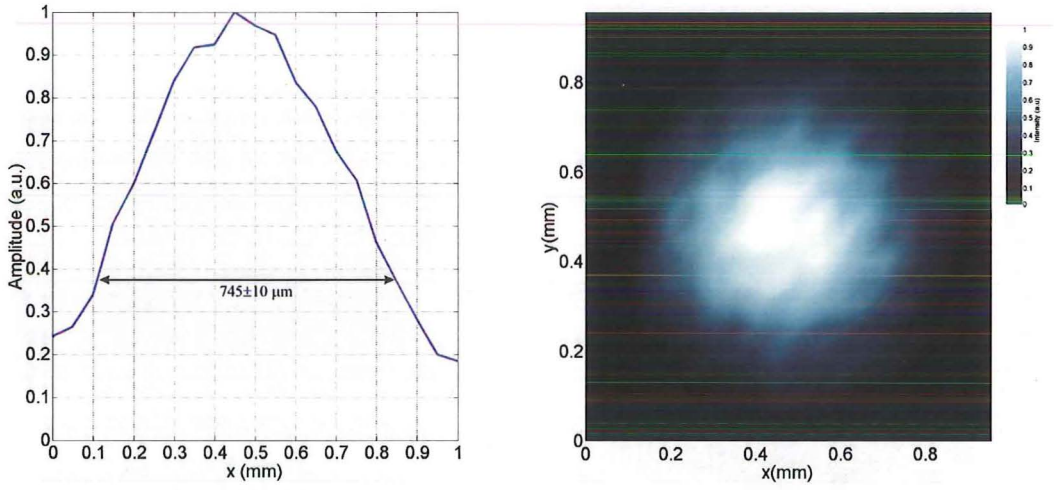

Figure 4.9 (a) beam cross section at the focal point illustrating a 745±10 μm FWHM (b) intensity distribution at the focal plane $z = 25.6$ mm.

Taking a scan in the x, z directions as in Figure 4.11 shows how the focusing changes down the axis moving away from the lens. This gives a determination of the depth of focus. For a Gaussian beam passing through a lens the depth of focus (DOF) can be calculated as [144]

$$DOF = 2\Delta r^2/\lambda \tag{4.2}$$

For this lens with an outer zone width of 708.8 μm at 1 THz ($\lambda = 300$ μm) the theoretical DOF is 33.5 mm.

The Rayleigh range is defined as the point where the beam waist is $\sqrt{2}$ of the minimum beam waist and the DOF is generally accepted to be twice the Rayleigh range. Determining the point in z where the 1/e radius of the beam amplitude is expanded to $\sqrt{2}$ of the minimum, yields a measurement for the DOF of 34±2 mm. This is slightly larger than the theoretical value for a zone plate.

MAGNITUDE PHASE

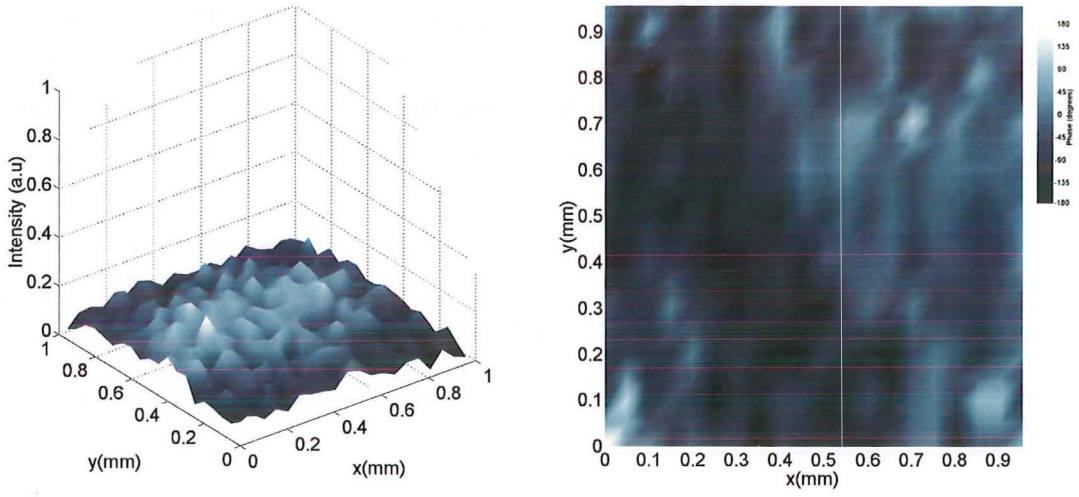

(a)

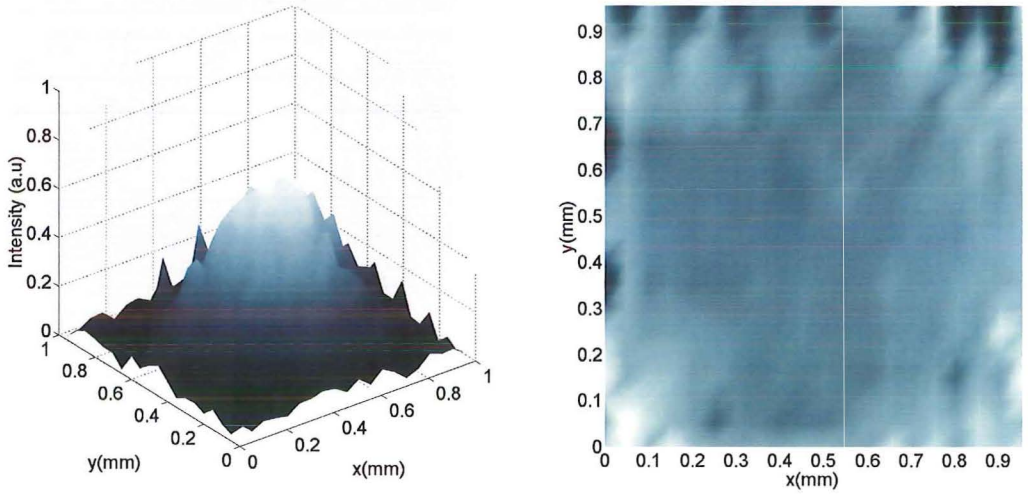

(b)

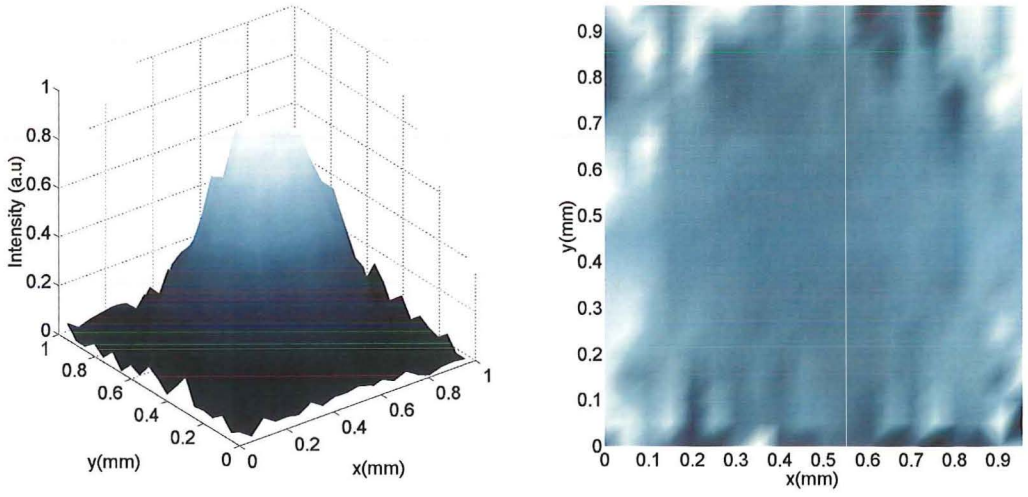

(c)

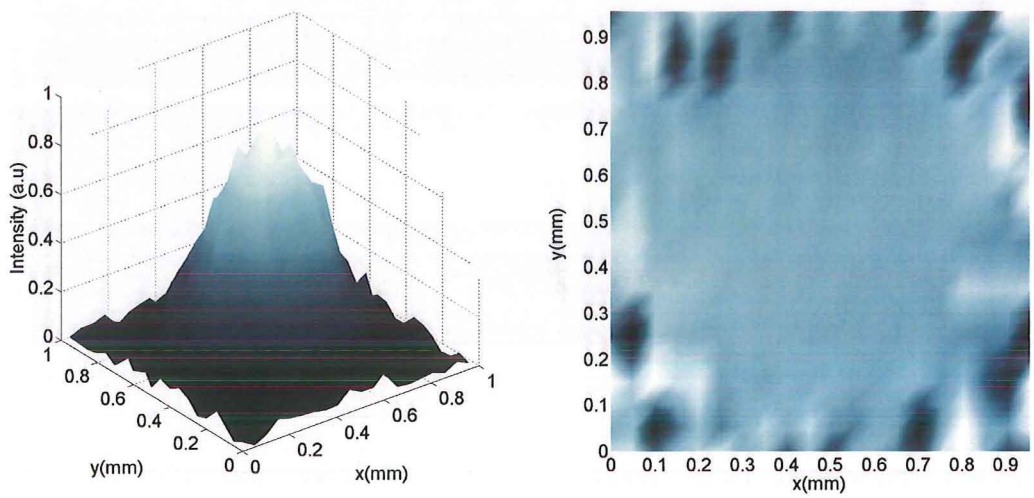

(d)

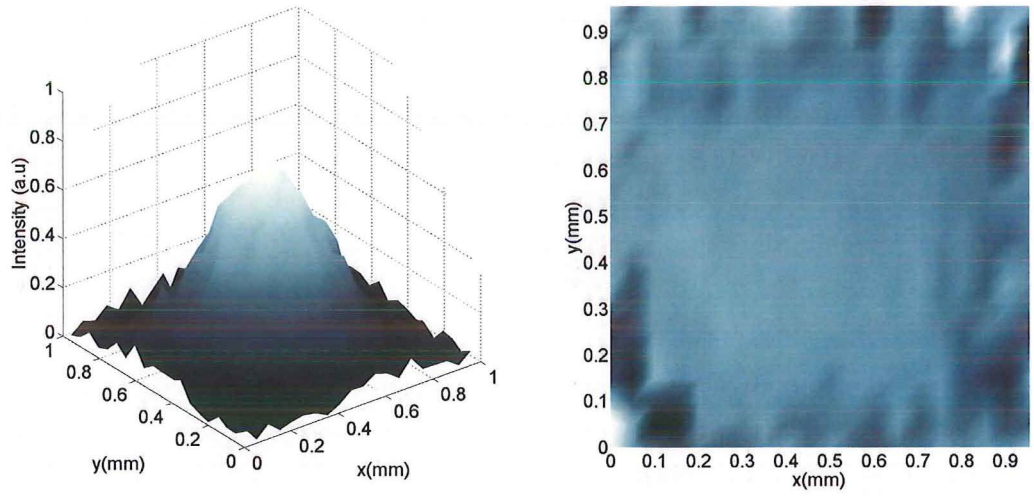

(e)

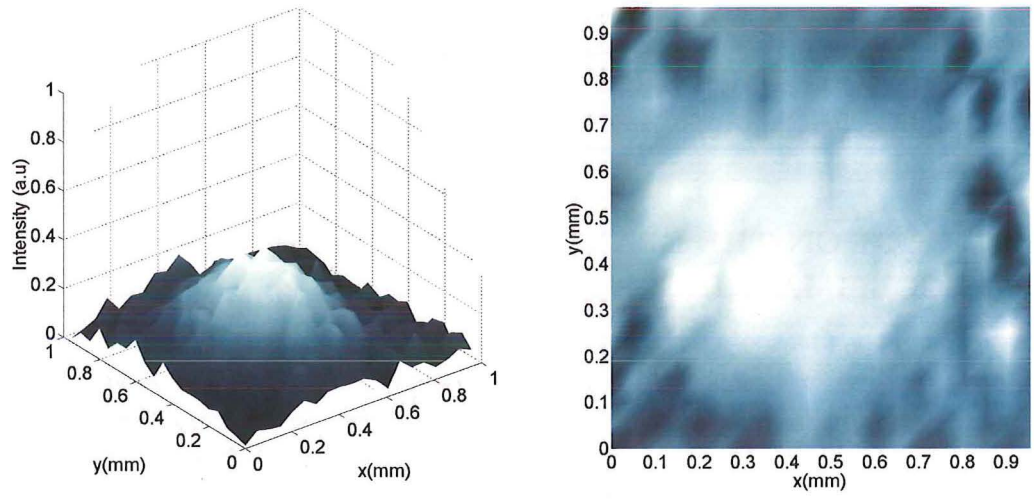

(f)

Figure 4.10 Magnitude and phase of planes around the focus at $z = 24.1$ mm (a) 25.1 mm (b) 25.6 mm (c) 26.1 mm (d) 26.6 mm (e) 27.1 mm (f).

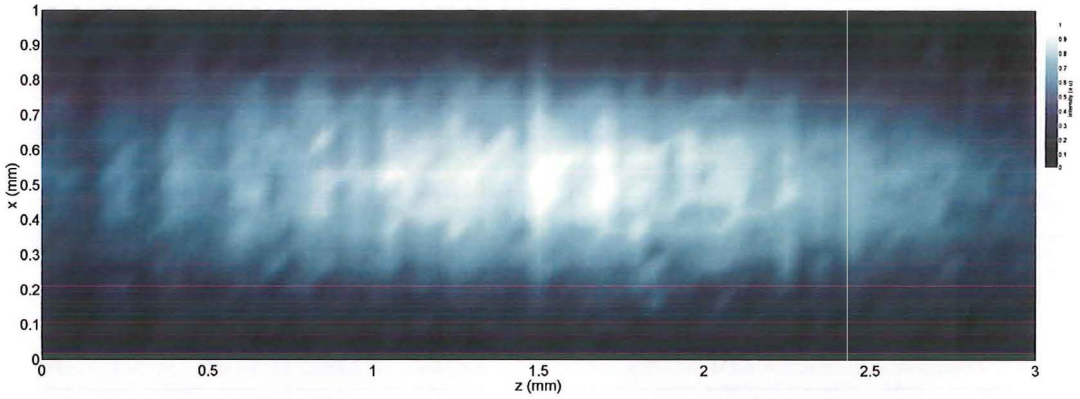

Figure 4.11 The intensity of an x, z scan around the focal point between a silicon and polyethylene lens.

The four level lens should give tighter focusing than a zone plate, due to the improved diffraction efficiency. In this case the theoretical and measured DOF values are in fairly close agreement. The measured value may be biased to a degree, with the influence of the refractive polyethelene lens. In having a two lens system it is likely that the alignment in z may be imperfect. This will have the effect of blurring the DOF of both lenses leading to a larger than normal reading. It is also likely that the imperfections in both the etch depth and the step widths of the silicon binary lens will have an influence on both the FWHM and the DOF.

For a lens the DOF gives an indication of the range over which an acceptable beam focus. A small aperture, short focal length lens can be expected to have a large DOF. When using these lenses for depth imaging as in tomographic applications the limits can be much tighter for increased resolution. In this case the z resolution is limited by the system noise where focal distance rather than image clarity is of interest.

Further experiments to improve the incident beam were not possible but, as will be shown in the next chapter, lens characterisation using a pulsed measurement system show that diffraction limited focusing is possible with these lenses.

4.6 EFFECT ON THE BEAM FROM FOCUSING AND RECOLLIMATION

The beam profile was also characterized after being focused and recollimated by the lens pair. This provides information of how an imperfect input beam is affected by this two lens system. A 1 cm aperture was shifted from between the lenses to either side of each lens to see how the input intensity pattern had changed. Figure 4.12 illustrates the points at which the aperture was placed either side of the two lens set up.

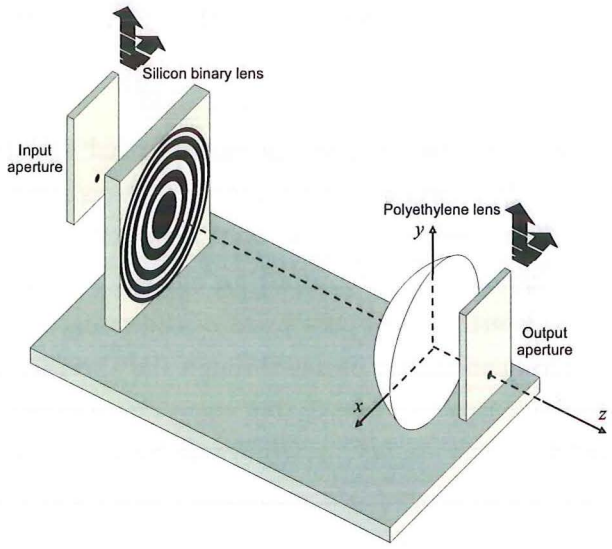

Figure 4.12 Aperture positions for assessment of the effect of collimation on the beam.

It is clear from the input beam, Figure 4.13(a), and the output beam Figure 4.13(b), that the focusing and recollimation of the beam changes the beam pattern. The emitter side intensity pattern appears to be donut shaped while the detector side intensity pattern is more Gaussian in shape. This indicates a degree of spatial filtering is occurring with the two lens arrangement. This is as would be expected with the focusing nature of a Fresnel lens where only the primary diffracted order is transmitted. There will be some bias introduced in the first intensity pattern, as the aperture inhibits the interference process to a differing degree across the scan. The SNR is too low to perform any detailed quantitative analysis which is a problem with this set up.

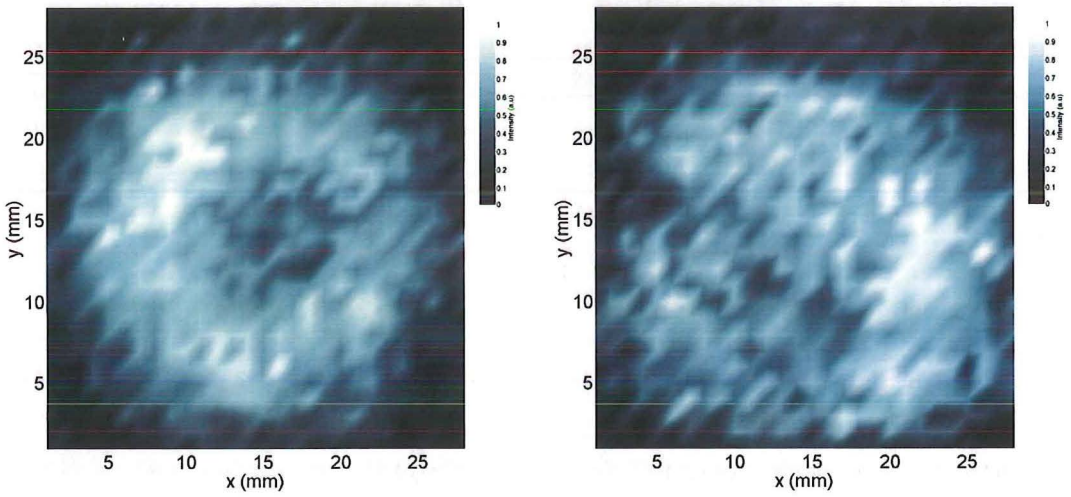

Figure 4.13 (a) Intensity pattern of beam before lens pair (b) and after lens pair.

4.7 TERAHERTZ BANDPASS FILTER - TWO FRESNEL LENSES

The above arrangement with a two lens set up was repeated with two binary optics as illustrated in Figure 4.14. It is envisaged that such a two lens system, with an aperture at the focal point, could be used as a narrow band terahertz filter. Because there is a linear shift in the focal distance with frequency for a diffractive optic lens, the distance between the lenses will determine the pass band of the radiation. Increasing the distance will increase the frequency that passes through the aperture and into the output beam. Placing one of the lenses on a translation stage would facilitate the formation of a variable pass band filter. The aim of this experiment was to assess if such a two lens arrangement would focus and recollimate a terahertz beam which in this case was set at 1 THz. The use of two binary Fresnel lenses should give greater frequency selectivity than a Fresnel-Polyethylene combination. The lenses were placed 50 mm apart in line with double the expected focal length of 25 mm. It was difficult to determine an initial clear point of intensity in z due to the poor signal to noise, hence, picking this lens separation was the best.

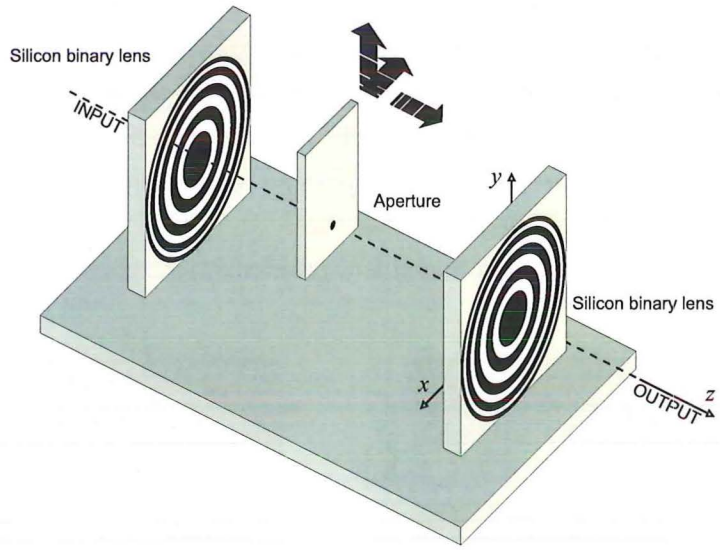

Figure 4.14 Focal plane imaging setup between two silicon lenses.

As with the previous experiment a series of x, y scans were taken around the focal point, and an x, z scan was taken to illustrate the depth of focus. At the conclusion of these measurements the input beam was analysed. It is of benefit to view the beam magnitude and phase, Figure 4.15, prior to the focused results as a clearly non ideal beam distribution was present. This poor beam shape which can be seen imaged through to the focal plane intensity patterns clouded the results somewhat however

focusing and recollimation is clearly demonstrated. Figure 4.16 shows the x, y scans taken at $z = 23.5$ mm, 24 mm, 24.5 mm, 25 mm and 25.5 mm. The dual lobe nature of the input beam made alignment of this lens pair very difficult exacerbating the effect on the signal strength at the focus. This explains why the intensity and phase plots are of a lesser quality than the measurements taken with a silicon and polyethylene lens pair. Time constraints prevented a recalibration of the system to try and improve the beam quality and it is not perceived with the current terahertz system stability that a reliable comparison could be made between different lens types. The objective of this section to observe the functionality of a 2 Fresnel lens system was not impaired.

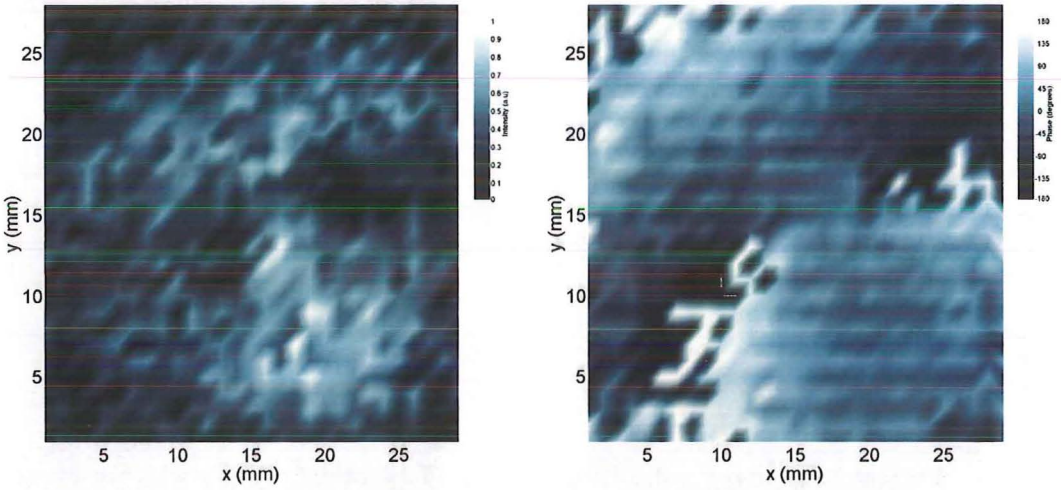

Figure 4.15 Input terahertz beam intensity (a) and phase profile (b) to lens pair.

Analysing the relative intensity of the radiation from the magnitude plots demonstrates a point of maximum transmitted intensity at the $z = 25$ mm point. It would appear that in some of the measurements taken that there was a blurring of the focal point. This is probably a combined effect arising from the difficulty in aligning the 2 lens system and what turned out to be a non Gaussian input beam which was measured again between the lenses after the measurements were taken. As with the measurements of the silicon and polyethylene lens the phase profile is flat at the focus. At the focus the shape of the beam was extracted and is shown in Figure 4.17. A roughly Gaussian shape can be observed with a beam waist of 1200±100 μm. This is larger than that measured with the silicon and polyethylene arrangement of 745±10 μm. Although the poor beam shape is evident in this focal spot image (Figure 4.17(a)) the focal spot shape is relatively uniform. This indicates a degree of spatial filtering occurred as with the Fresnel-polyethylene arrangement in the previous section.

MAGNITUDE PHASE

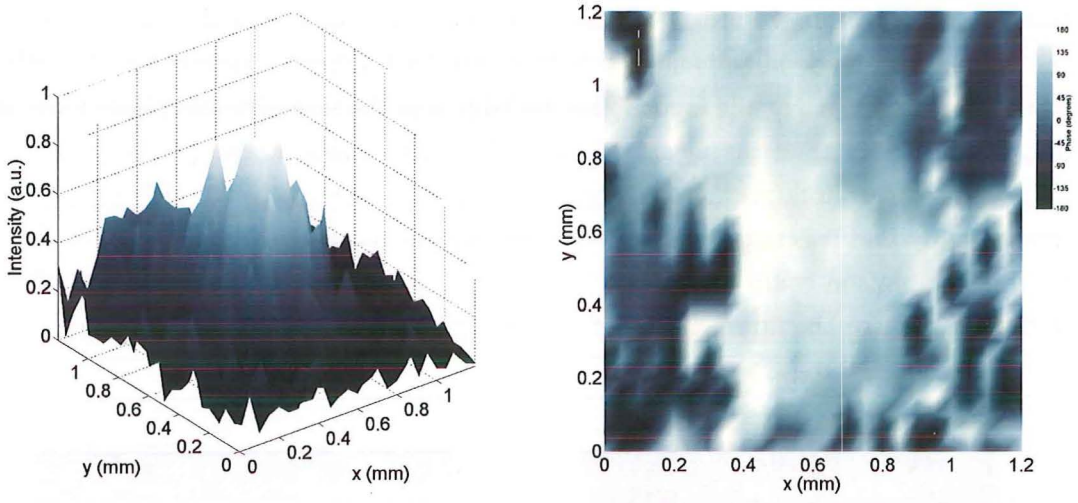

(a)

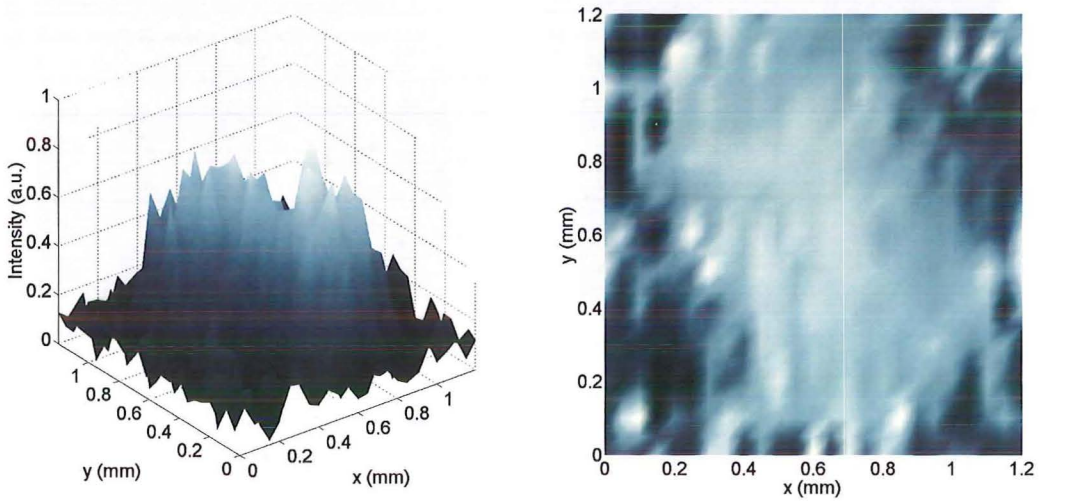

(b)

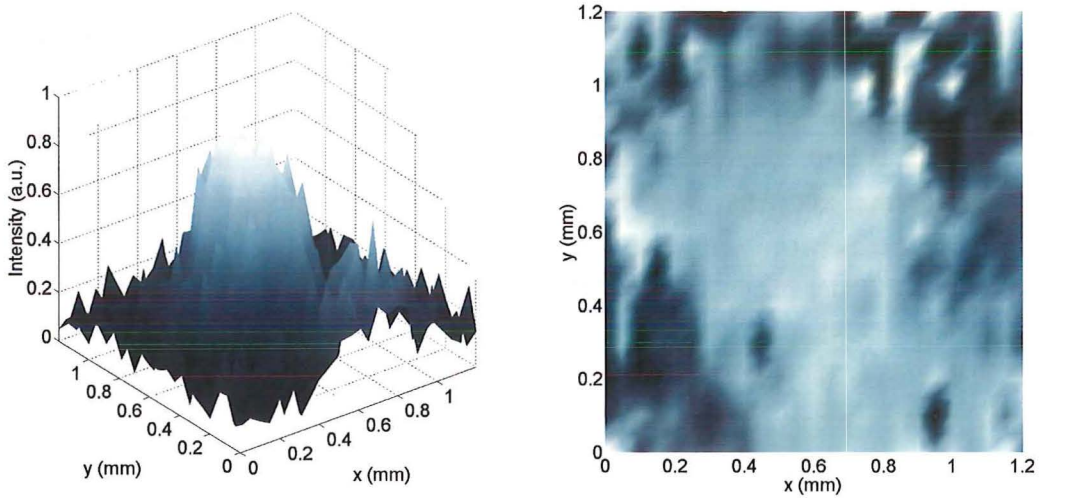

(c)

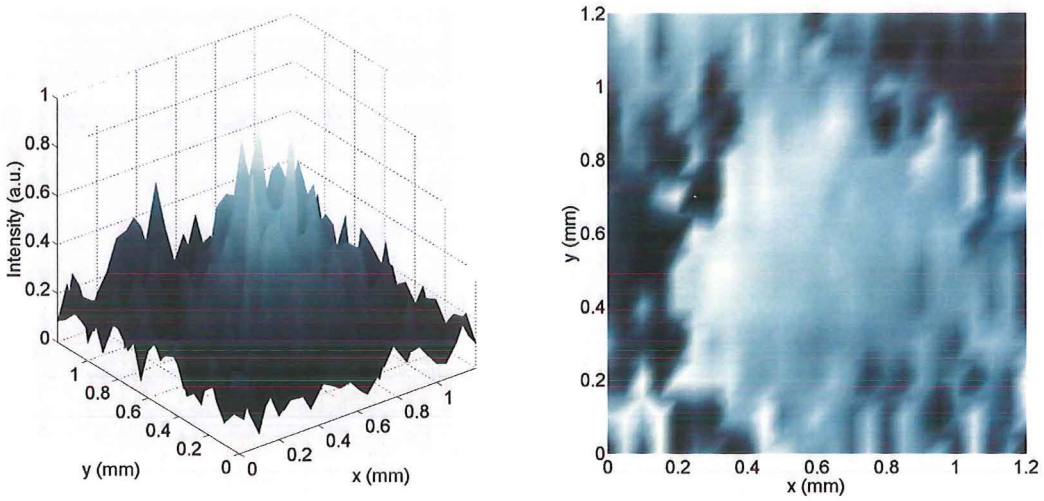

(d)

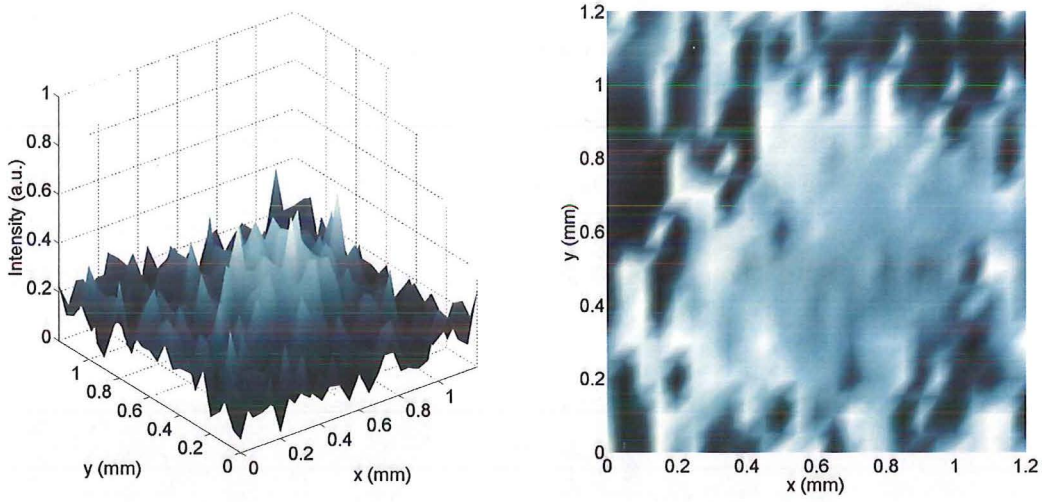

(e)

Figure 4.16 Magnitude and phase of planes around the focus at (a) 23.5 mm (b) 24 mm (c) 24.5 mm (d) 25 mm (e) 25.5 mm.

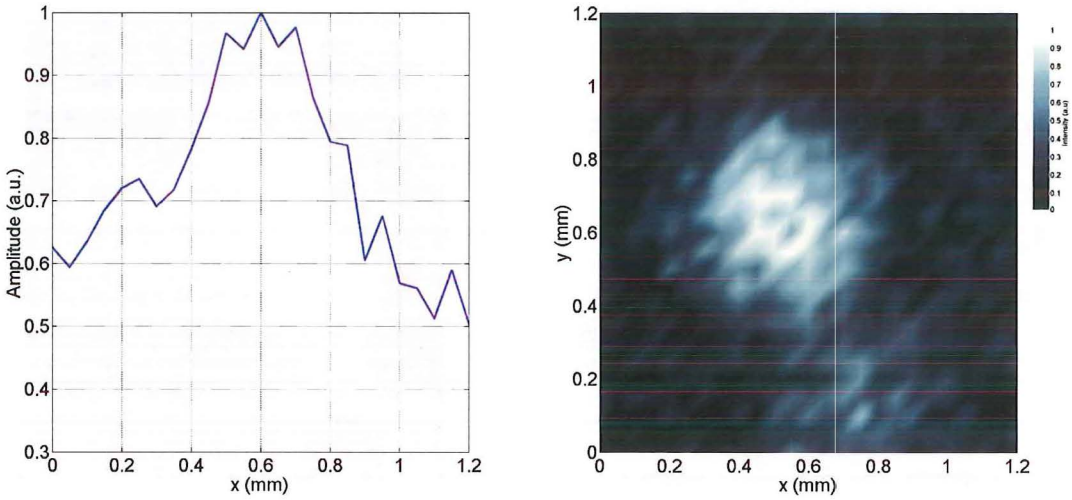

(a) (b)

Figure 4.17 Cross section of the focal point intensity (a) and focal plane intensity map (b).

A scan down the x, z plane was conducted for the two binary lens arrangement which as can be seen in Figure 4.18 is similar in dimension to the result obtained in the single silicon and polyethylene lens setup. The intensity and phase patterns are considerably more noisy than the other result. Figure 4.18 shows the considerable noise present during this measurement relative to the silicon-polyethylene arrangement.

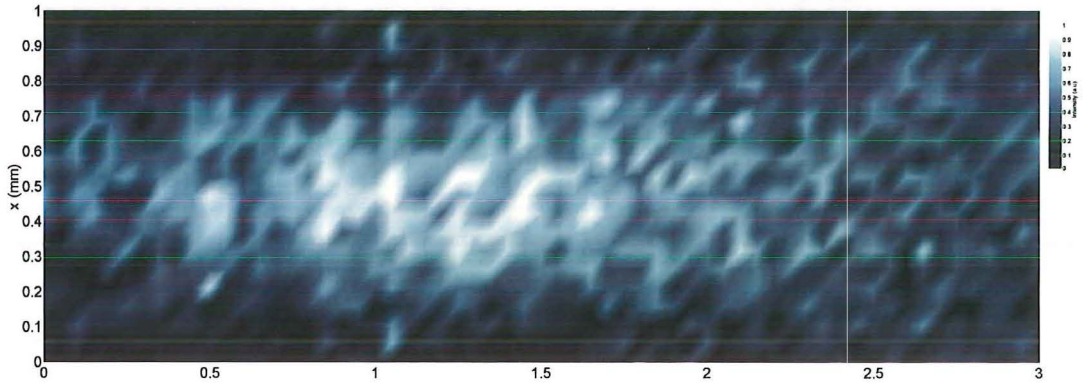

Figure 4.18 The intensity of an x, z scan around the focal point between two four level binary silicon lenses.

The signal quality in the x, z scan makes the measurement of a value for the depth of focus difficult and of little value due to the margin of error. Comparing this result with the x, z scan of the silicon and polyethylene set up indicates a range of intensity and beam width over what would appear a smaller range. However quantifying this

would require further measurements. This would indicate a depth of focus less than 34 mm.

4.8 SUMMARY

Binary Fresnel lenses have been shown to work well in a dual lens system where continuous wave radiation at 1 THz was focused and recollimated successfully using a combination of a silicon and polyethylene lens and two four level binary lenses. It was shown that an anti-reflection grating could be increase the terahertz transmission through a silicon wafer. Structuring these gratings on the back side of a lens would help increase the focal point intensity. The developmental nature of the CW terahertz system introduces a degree of uncertainty in the results as it is extremely difficult to align all the components and to identify what specific misalignment may be causing specific results.

The measured FWHM and DOF of the lenses are of the same order as the theoretical values indicating the lenses operate as would be expected. The high signal to noise ratio in some of the measurements made it difficult to obtain accurate values for the lens characteristics. Further experimental characterisation was required to fully assess the performance of the silicon lenses.

Chapter 5

LENS TESTING USING PULSED TERAHERTZ EMISSION

5.1 INTRODUCTION

The majority of Terahertz measurement systems currently in use emit broadband pulses with frequency content as high as 50 THz [15] as described in section 2.2.2. The large number of potential spectroscopic applications [75] makes a pulsed system desirable as it eliminates the requirement for tuning of the source. It was therefore important to test the Fresnel lens in such a pulsed terahertz system to determine the broadband performance difficult to obtain with the CW system described in the previous chapter.

A collaboration was arranged enabling these measurements to be taken at the laboratory of X.C- Zhang at the Rensselaer Polytechnic Institute (RPI), in Troy, New York, during a single three week research visit. Some additional scans with improved SNR were taken following these measurements. An emission method was chosen that would give high power around the 1 THz design frequency and large bandwidth [46]. A pulsed measurement system has the benefit over a continuous wave system in that it can demonstrate the performance of the lenses over a large section of the terahertz bandwidth in a single measurement. This section details two independent systems that were set up by the author with the assistance of the researchers at RPI, for the testing of 2-, 4-, and 8-level lenses and an aluminium zone plate in a pulsed terahertz system. Specific details of each of these systems are explained along with the broadband measurements obtained.

5.2 SCANNING TERAHERTZ SYSTEM

Initial pulsed measurements of the lenses were performed on a three dimensional scanning system, shown schematically in Figures 5.1 and 5.2. Because the efficiency of the lens in such a system was undetermined it was desirable to use a system where maximum power would be obtained at the detector. This method measures a single point in the focal plane which can be detected with a lock-in amplifier [145] using electro-optic

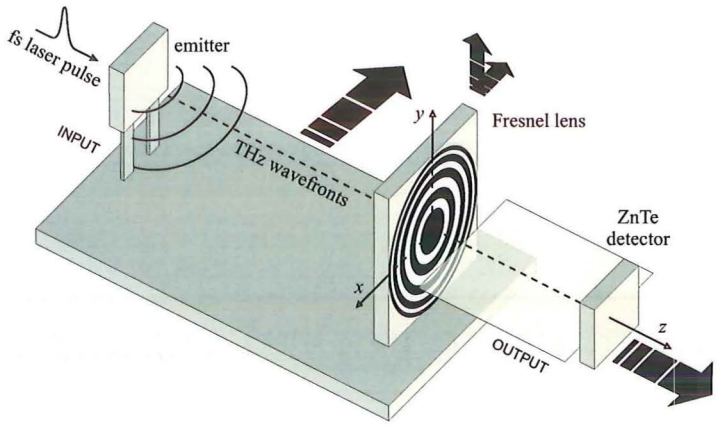

Figure 5.1 Translation stage arrangement for scanning beam testing. Bold arrows indicate the major stage movements that are possible.

detection [47]. For the measurement of the Fresnel lenses the terahertz emitter and the lens were fixed on an translation stage that could be shifted through x, Figure 5.1. On this stage the lens was such that it could be moved through x and y. These two micrometers enabled the lens to be aligned to the center of the input beam. The ZnTe detector crystal was placed on another set of micrometers such that it could also be aligned to the center of the beam. These were placed on a translation stage so that it could be shifted 45 mm through z. In this manner the x, z plane could be imaged. By assuming that the beam shape of the emitted terahertz radiation and the lens should both be rotationally symmetric, imaging a single x, z cross-section of the image plane should provide a good determination of the three dimensional focal patterns. By placing the emitter and lens on the same stage and shifting the detector and not the lens through z any ambiguity in the results from a change in the terahertz beam is avoided.

The details of the emission and detection mechanisms and a photograph of the layout of the optical table are shown in Figures 5.2 (a) and (b). The Ti:sapphire laser used to drive the terahertz system produced pulses with a 250 fs duration, a repetition rate of 250 kHz, and an average power of 600 mW. The pump beam is directed to the GaAs emitter crystal for the production of a terahertz pulse through nonlinear rectification of the incident laser pulse, and the probe beam is directed to the ZnTe detector crystal. A half wave plate was placed before the beam splitter to adjust the amount of power channeled into each of these beams. This enables most of the power to be used for terahertz emission. The path length of the pump beam is adjusted by a motorised delay stage which enables the timing of the terahertz pulse arriving at the detector crystal to be shifted relative to the probe pulse. This enables the temporal shape of the terahertz pulse to be determined at each point assessed. Subsequent Fourier analysis can be performed to find the frequency response of the Fresnel lens.

Several lenses were placed in the pump beam optical path to first expand and then

collimate it onto the emitter. By doing this and arranging the path between the emitter and Fresnel lens to be as far as possible the terahertz radiation impacting the Fresnel lens should have a close approximation to planar wavefronts.

The emitter used was a low temperature grown GaAs (LT-GaAs) crystal which was biased to 1200 V to give additional output power. Optical rectification of the femtosecond laser pulses impacting the emitter leads to the emission of a terahertz pulse. As described in section 2.2 there are a number of different emission methods

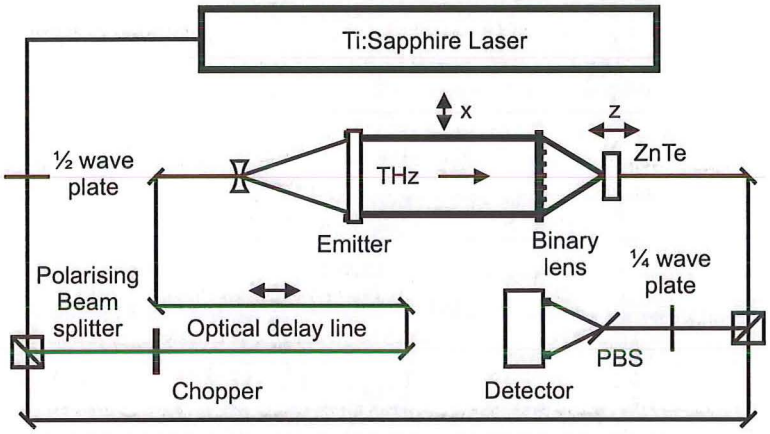

(a)

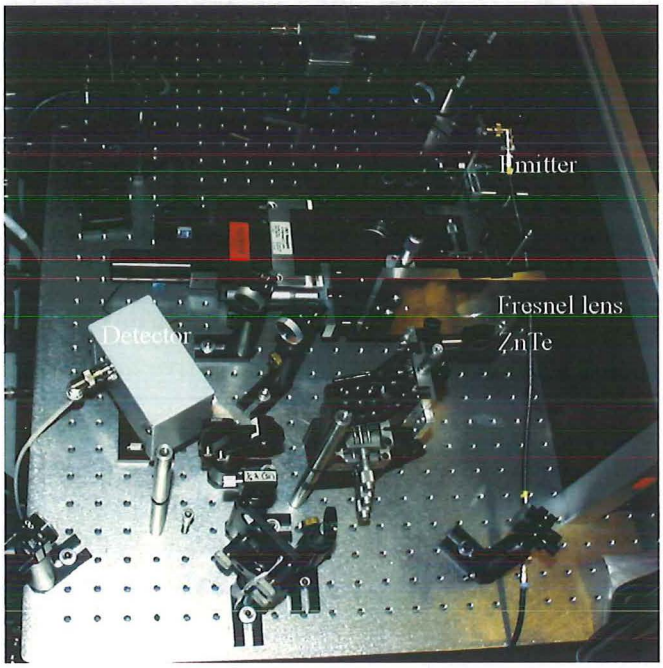

(b)

Figure 5.2 Optical table component layout schematic (a) and photo of layout (b).

available. This particular emitter was chosen for its high power in the around the design frequency of the Fresnel lens (1 THz). Because of the inherently narrow band nature of the lenses the performance in the higher region of the terahertz band was not expected to be great. The spectral response of the terahertz emitter can be seen in the plot of Figure 5.3, which shows the spectrum of the terahertz pulse measured in the setup of Figure 5.3 with no Fresnel lens in place. The inset shows the temporal pulse waveform from which this spectrum is derived. Although half the pulse energy is below 0.5 THz, there is still good SNR at and above the 1 THz design frequency.

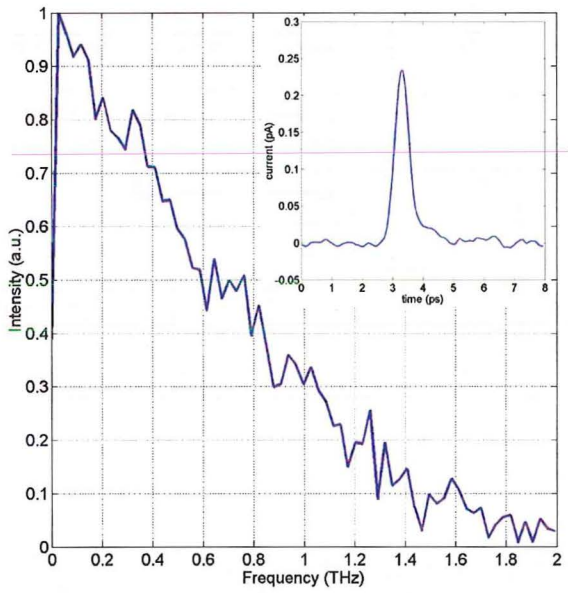

Figure 5.3 Terahertz spectrum from GaAs emitter and measured pulse (inset).

An electro-optic measurement is used to characterize the terahertz pulse (Figure 5.4). The probe beam is reflected from the front and backside of the ZnTe detector crystal. The impacting terahertz beam modifies the refractive index of the detector crystal and the probe beam reads this information out as a change in its polarisation. Because of this the back side reflection needs to be separated and blocked using an aperture. A slight difference in the reflected angles enables the two beams to be discriminated from each other. To achieve this the detector crystal needs to be on a slight angle as illustrated in Figure 5.4 The change in the probe beam's polarization is measured using a $\frac{1}{4}$ wave plate, polarizing beam splitter and a balanced photodetector pair (see Figure 5.2(a)). For each x, z data point the delay stage needs to be swept to measure the temporal pulse shape, which makes the entire measurement process quite slow. Ideally, to accurately raster scan the lens it would be necessary to place the emitter and lens on a y translation stage and change the angle of the optical pump beam such that

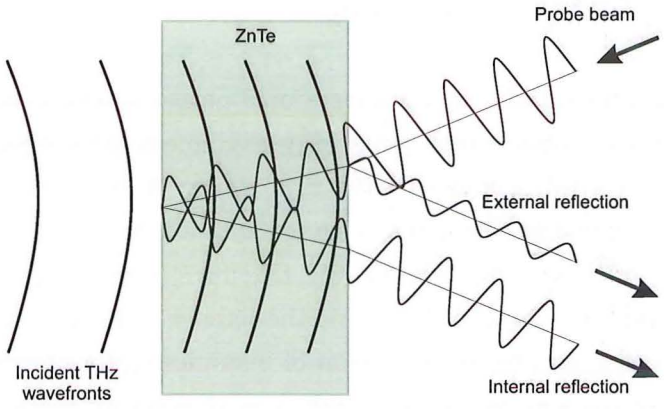

Figure 5.4 Backside, internally reflected beam used for detection.

it still impacts on the emitter at the same point when the stage is shifted vertically. This would be non trivial to arrange, so there are some alignment issues that will have introduced a bias in the results.

In this setup the probe beam was aligned so that when the detector crystal was removed the laser beam could be seen with an infrared camera impacting on the centre of the lens. An accurate measurement of the focus would require that the emitter crystal and the lens were aligned parallel to each other and perpendicular to the path of the probe beam. A slight misalignment in either of these can cause the focal spot to shift from the probe beam axis meaning that an x, z sweep may not pass directly through the centre of the focal point. This is illustrated in Figure 5.5 where it can be seen that a vertical shift in the position of the focus may give a misleading result. Because the focal spot is very small (of the order of a few hundred microns) and the peak of this covers an even smaller area the one dimensional results will contain some inaccuracy.

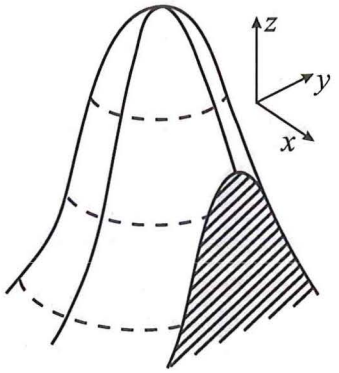

Figure 5.5 Effect on perceived intensity of a mis-aligned x, z scan.

5.3 SCANNED BEAM RESULTS

The scanning experiments gave a two dimensional measurement of terahertz intensity for each of the lenses. Because each point of measurement is time consuming it is not practical to perform a full analysis on the x, z plane. A sweep was taken down the central z axis of the lens and a broadband assessment at 1 mm steps along this axis was taken. When each of these measurements was taken a spectral analysis was performed on the data in MATLAB [146] to determine the intensity of the radiation at different frequencies in the terahertz band. The point of maximum intensity was determined to be the focal spot of the lens and at this point a set of measurements in the x axis was taken. This procedure was followed for each of the 2-, 4-, and 8-level lenses and the Al zone plate. In this manner the image plane on the central x, z axis could be determined for each lens. The plane definitions and area imaged is shown in Figure 5.6.

Figure 5.7 shows the variation of intensity for a range of frequencies at positions on the lens axis moving away from a 4-level lens. The spectrum of the incident illuminator as shown in Figure 5.3, which is weighted toward frequencies in the lower part of the spectrum, explains the difficulty obtaining reliable signal strength and subsequently measurements above 1 THz. There is a definite shift in the focal length with changing frequency where higher frequencies have a longer focal length as would be expected with a Fresnel lens.

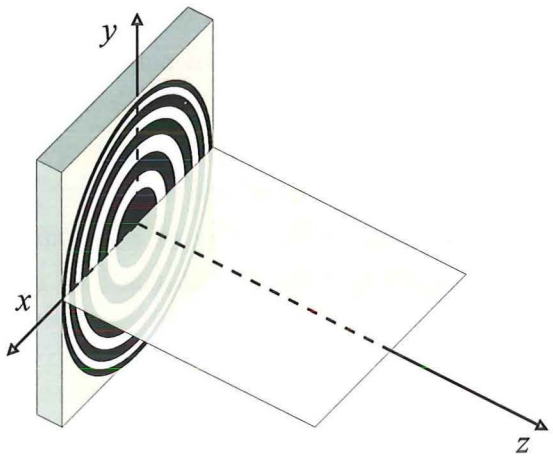

Figure 5.6 Three dimensional definitions of x, y and z for planes imaged beyond the lens.

Observing the positions of frequency maxima in the plot of Figure 5.7(b) it can be seen that the linear relationship passes through the origin as would be expected. The lenses were designed to have a focal length of 25 mm at 1 THz however in this data the focal point appears to be several mm beyond this value (29±2 mm at 1 THz). The focal point dispersion from these results can be compared with theoretical analysis. The diffracted wave amplitude $u(z)$ along the z axis with the binary lens can be written

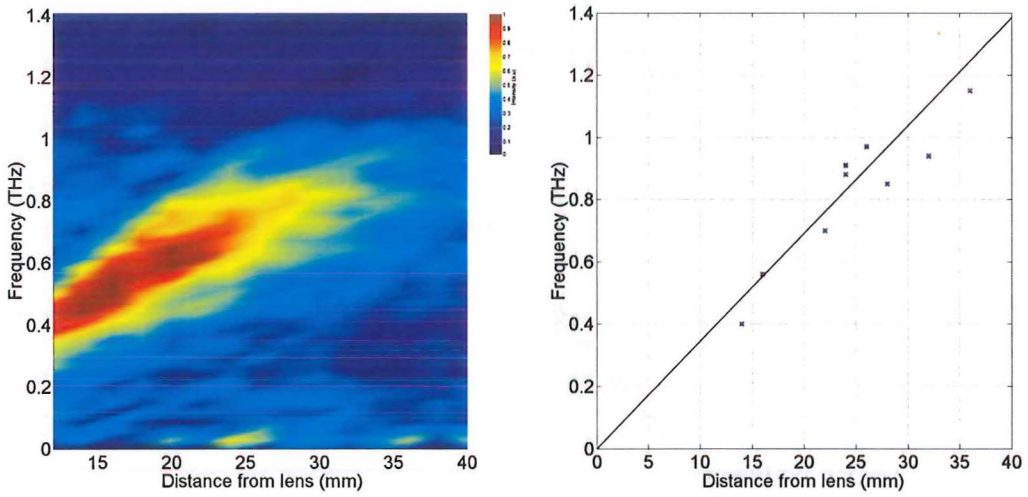

(a) (b)

Figure 5.7 (a) Spectral intensity pattern at different positions beyond the lens and (b) plot of frequency at maximum intensity versus distance.

as [147]

$$u(z) = \sum A_n \int\int exp\left[i2\pi\left(\frac{n}{r_p^2} + \frac{1}{2\lambda z}\right)(x^2 + y^2)\right] dxdy \tag{5.1}$$

where $A_n = sinc(n/L)$, L is the number of levels of the binary lens, n is an integer, r_p is the Fresnel zone radius, and λ is the wavelength. If $r_p^2 + 2\lambda n z_n = 0$, a maximum diffraction intensity can be obtained at the focal point z_n:

$$z_n = -\frac{r_p^2}{2\lambda n}, n = \pm 1, \pm 2, ... \tag{5.2}$$

For these lenses $r_p = 3.9$ mm hence for the primary focus, where $n = 1$, a plot of the theoretical focal length at different frequencies in the terahertz band can be generated and compared to the experimental values. This is illustrated in the plot of Figure 5.8 where a focal distance for T-ray binary lens is predicted to be 25 mm at 1 THz as designed. This equation assumes an infinite source where the beam impacting the lens is perfectly collimated. In practice the source was placed at a distance of 30 cm from the lens which will cause a lengthening of the focal distance, according to the lens law concerning a non infinite object and its image through a lens,

$$\frac{1}{z} + \frac{1}{z'} = \frac{1}{f_v} \tag{5.3}$$

The focal points are recalculated at different frequencies with a 30 cm source using this formula yielding longer predicted focal lengths. There is a very close comparison between this theoretical result and the experimental values shown in Figure 5.7.

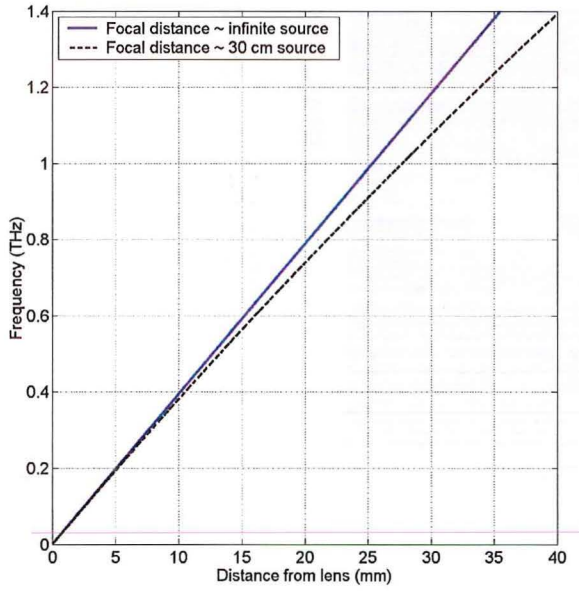

Figure 5.8 Theoretical focal distances for a 25 mm Fresnel lens for both an incident source (solid lines) and a point source 30 cm in front of the lens (dashed lines).

5.4 FOCAL POINT ASSESSMENT

At the point in z along the axis where a maximum was observed for the four level lens a scan along x was performed for each of the four lenses to analyse the performance improvement that is achieved using multilevel structures. Line plots of the beam profile at 1 THz are shown in Figure 5.9 for 2-, 4-, and 8-level lenses together with an Al zone plate. Using multilevel lenses significantly improves the profile and the intensity of the beam focus. The 4-level lens is more than two times as efficient as the 2-level lens or zone plate, as expected [148]. The eight level lens performance should be slightly better than the four level lens however this is not the case in these experimental results. This difference in performance can be accounted for by the effects shown in Figure 5.5. It is likely that the eight level scan was not taken directly through the point of maximum focusing intensity. This assumption is confirmed with the two dimensional scans that were performed later, which have a better spatial resolution (section 5.9).

For applications such as tomography the frequency content at any given plane needs to be as narrow band as possible. This enables more accurate determination of the distance of an object. An x scan of the frequency content of a 2-, 4-, and 8 level lens and an Al zone plate at the focal plane along the maximum in y as illustrated in Figure 5.10 was performed as shown Figure 5.11. Each of these intensity values were normalised by the free space beam intensity of Figure 5.3 to give a more accurate appreciation of the focused intensity at each frequency.

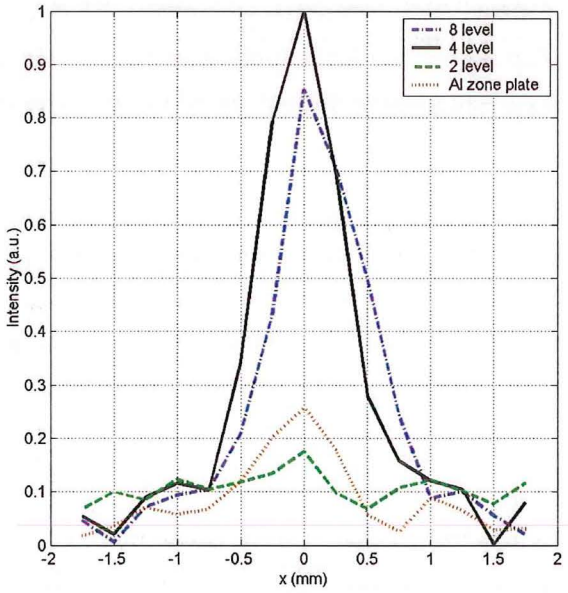

Figure 5.9 Efficiency comparison of four different lens structures. Measurements were taken at the focal plane.

These plots show the improved focusing performance of the more complex optics. Not only do these appear to focus radiation more tightly at 1 THz but also have minimal intensity in the neighboring frequencies. The zone plate and the 2 level lens have significant frequency content as low as 0.5 THz while the 4- and 8- level lens have little signal strength below 0.8 THz. The 2 level lens in particular seems to perform

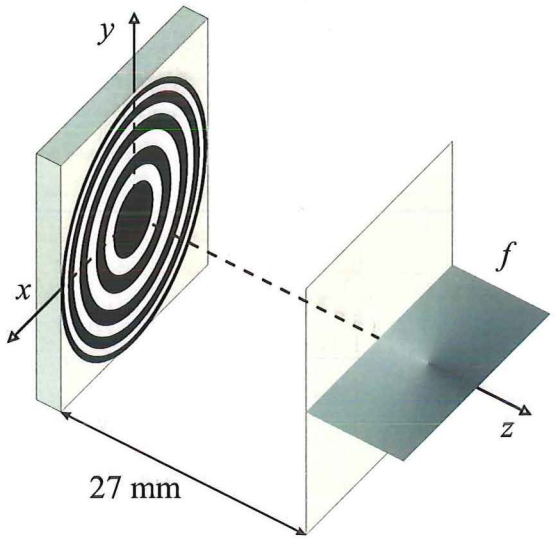

Figure 5.10 Plane being imaged - frequency content in an x plane.

very poorly compared to the other optics containing a broad range of poorly focused radiation. These plots show very symmetric patterns with the smallest spot size at the design frequency. The size of the focal spots is smaller in the more complex lenses as would be expected with the greater diffraction efficiency attained from the multiple level construction.

Analysing the intensities of the focused radiation peaks which have been plotted relative to the free space spectrum showed that an intensity of approximately 10 times of the input is achieved at the focus. The higher complexity four and eight level lens have a clear improvement in focusing with a smaller spot size.

For the four level lens which in the scanned results appeared to have the best performance, several x scans were taken at different points in z to analyse the focusing ability at different frequencies and the degree to which the beam waist at the focus changes with frequency for these lenses.

The shift in the focal points and the change in the intensity pattern of different frequencies at distances around the 1 THz focus (Figure 5.11 (c)) are shown in Figure 5.12. Low SNR at the higher frequencies make analysis of focal points difficult. According to the lens design certain frequencies are expected to peak at specific distances as shown in Figure 5.8. The measured peaks from these plots are compared to those predicted theoretically in Table 5.1. At the further distances from the lens lower frequencies are measured as peaking than predicted, as the higher frequencies have a much lower input power. Intensity patterns before a given frequencies focal point illustrate a series of ringed structures and a more blurred pattern at points beyond the focus as is characteristic of a Fresnel lens. This trend of radiation patterns before and after the focal point mirror those observed in the simulations of Chapter 6.

Distance from lens	Expected frequency peak (THz)	Measured frequency peak (THz)
12.5	0.45	0.45
20	0.75	0.7
32	1.15	1.05
42	1.45	1.25

Table 5.1 Comparison of theoretical and measured frequencies of maximum intensity and positions around the focus of a 4-level lens.

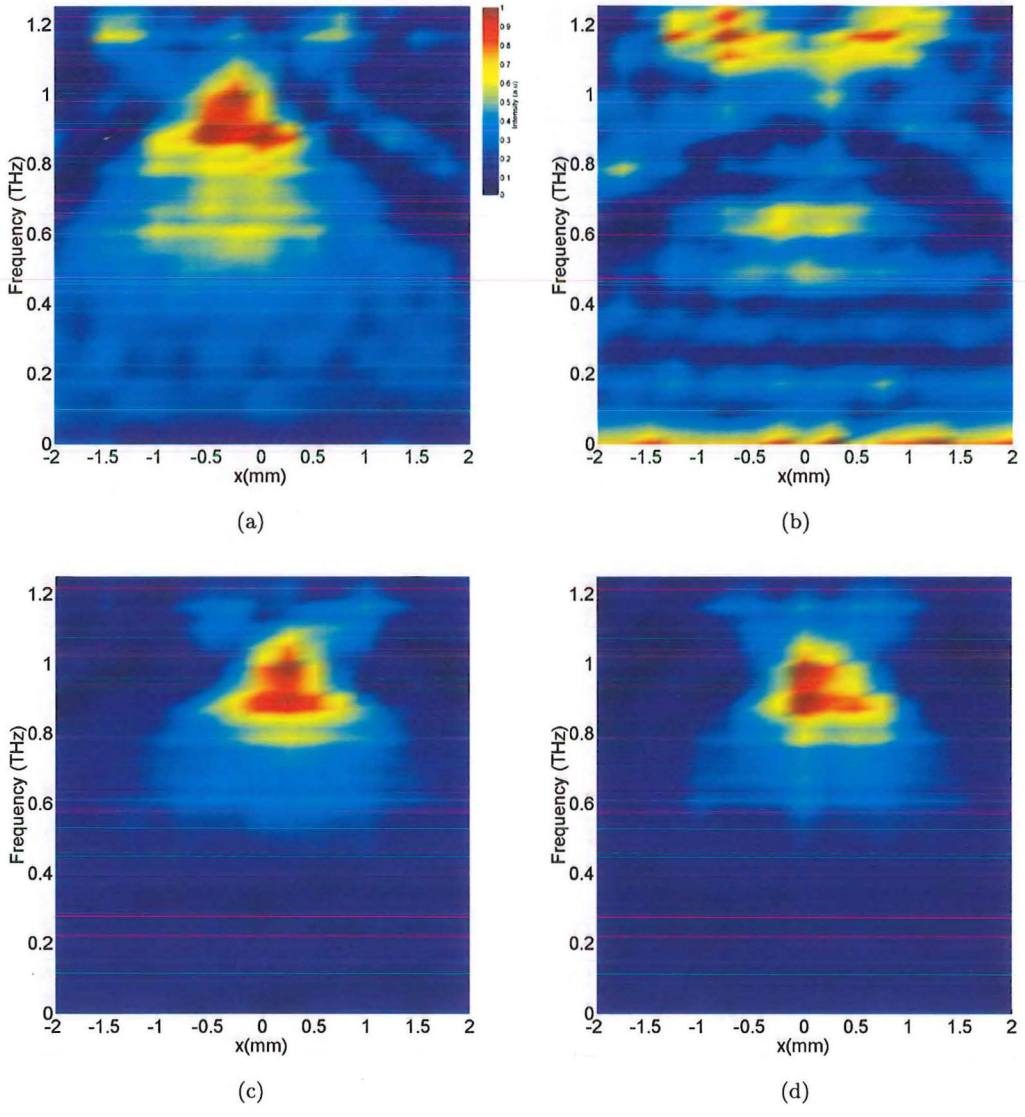

Figure 5.11 Frequency distribution at the y maximum across x on the focal plane of (a) an Al zone (b) a 2 level lens and (c) a 4 level and (d) an 8 level lens.

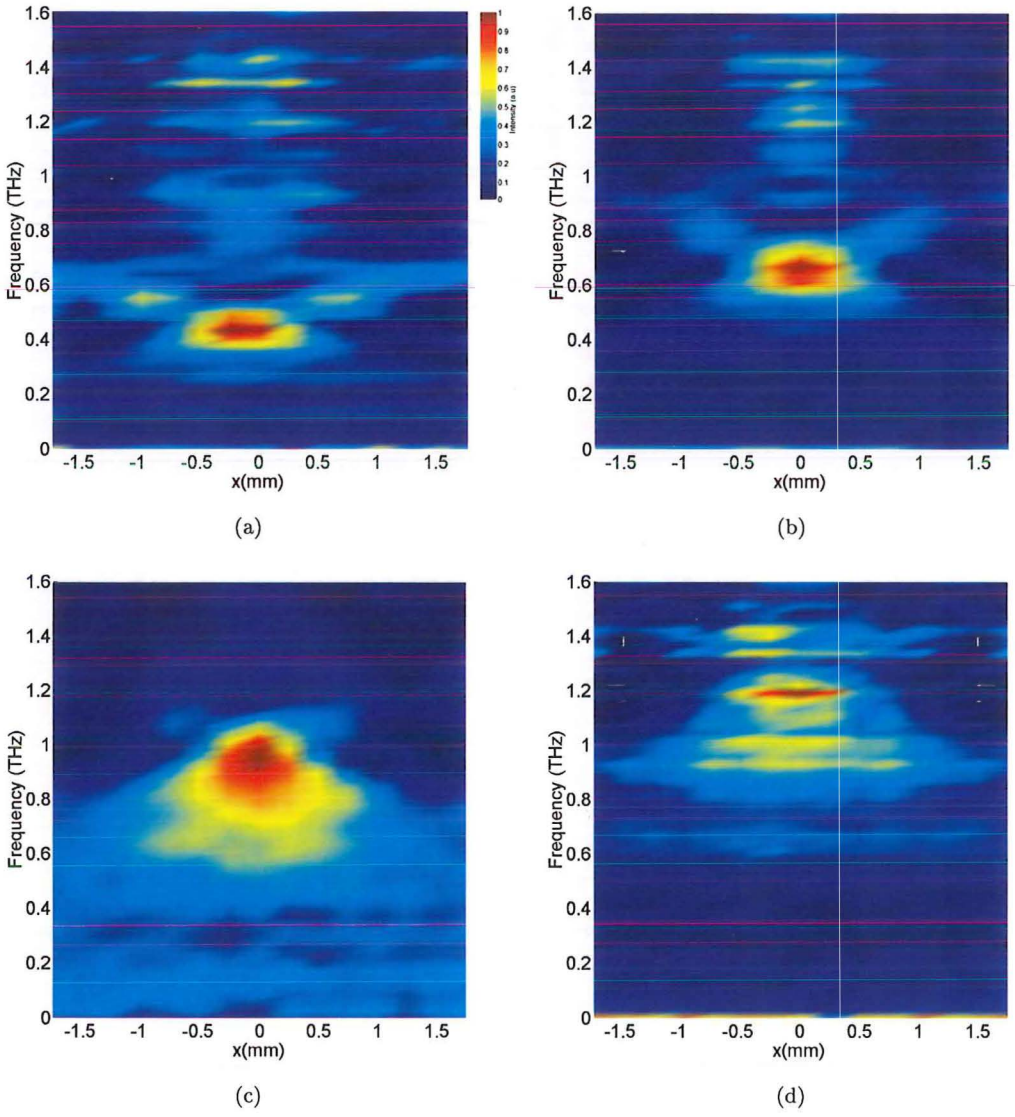

Figure 5.12 Frequency distribution at the x maximum on several planes of a 4 level lens at (a) 12.5 mm (c) 20 mm (d) 32 mm and (e) and 42 mm.

5.5 TWO DIMENSIONAL IMAGING USING A CCD ARRAY

The problems with spatial resolution of the point-by-point scanning method were overcome by changing the detector from a scanned single point system to a CCD array. This apparatus has been modified from a similar tomography set up [113]. The generation and detection follows the same principle as the scanning point-by-point experiment. The optical set up is illustrated in the diagram of Figure 5.13 and in the photograph of figure 5.14(b). The number of translation stages is reduced in this system with only two required. One is used to shift the ZnTe detector crystal in front of the lens and the other is to shift the timing delay of the pump beam.

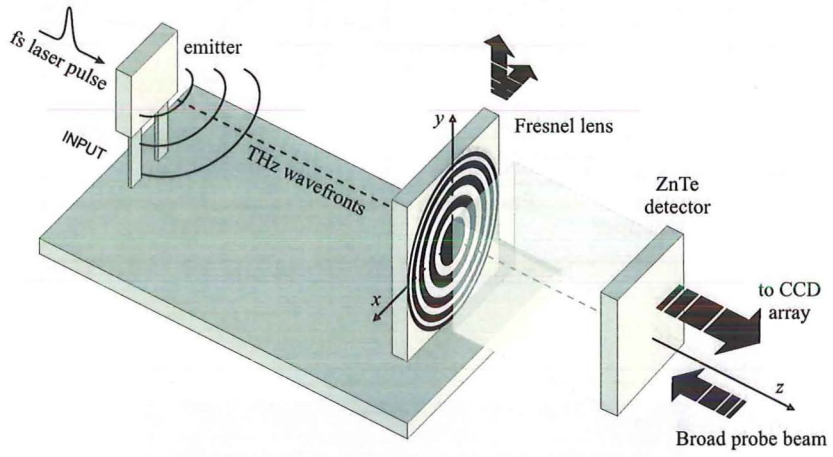

Figure 5.13 Emitter, lens and detector stage set up for CCD terahertz imaging system.

Figure 5.14(a) schematically illustrates the electro-optic imaging set up with a CCD camera. The laser is a 1-kHz repetition rate amplified Ti: sapphire laser, capable of generating 100 fs pulses with energy of 700 μJ. The laser beam is split into a pump beam and a probe beam; both beams are expanded to 2.5 cm diameter and collimated. Through a 3 mm thick <100> ZnTe emitter, the pump beam generates terahertz pulses via optical rectification. The 2D THz image formed on the ZnTe electro-optic (EO) crystal is encoded onto the probe beam; a 4 mm thick <100> ZnTe with a effective aperture of 2 cm was used as an EO sensor. The image carried by the probe beam was focused onto a CCD camera. In this experiment, we define a laboratory coordinate system as follows: the axis of binary lenses was selected as the z axis, the x axis is parallel to the optical table and the y axis is perpendicular to the optical table. By scanning the time delay between the pump and probe beams and moving the binary lenses along the z axis, we are able to obtain the spatial and temporal terahertz distribution for each lens.

Because a lock in amplifier can not be used to improve the signal to noise ratio with the CCD arrangement an alternative noise reduction technique was employed. By

gating the terahertz pulse with a chopper it is possible to determine the background signal which can then be removed from the signal received. This is achieved by placing a chopper in the path of the section of the laser beam before the terahertz emitter. Every time the laser beam is blanked by the chopper the signal received at the CCD is just that from the probe beam. This signal can then be subtracted from the signal when terahertz is present, reducing the influence of the laser noise in the measurements.

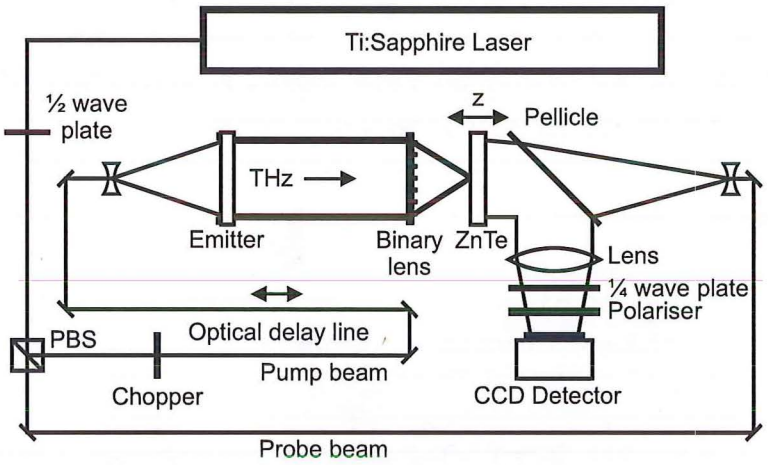

(a)

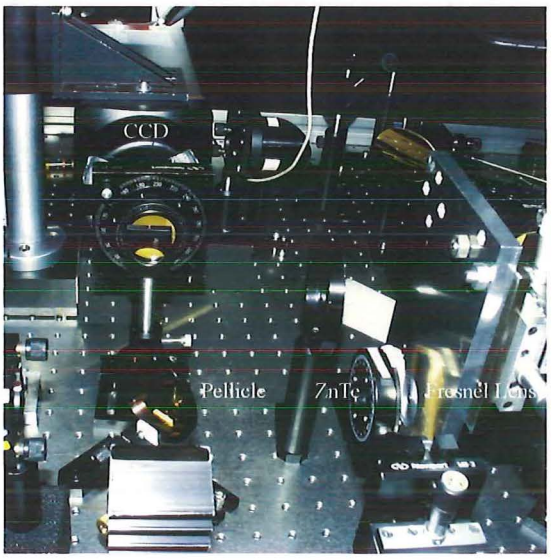

(b)

Figure 5.14 Optical table component layout schematic (a) and photo of layout (b).

This system has a much better spatial resolution than the scanning system, with a 175 μm pixel size over a 20 mm^2 area, making it easier to identify a correct focus. At each of the planes in x, y a two dimensional reading of the terahertz pulse can be

obtained by shifting the delay of the pulse in the pump beam. From this the spectral content at each pixel can be determined by taking the FFT of this pulse. Scanning the detector crystal through z then allows for collection of a complete four dimensional data set. With this any plane in three dimensional space beyond the lens can be assessed for its terahertz intensity at a broad range of frequencies.

Complete data sets were taken for each lens between 10 and 50 mm in front of the lens. From this any plane can be imaged, typically x-y and x-z slices are presented here, as illustrated in Figure 5.15.

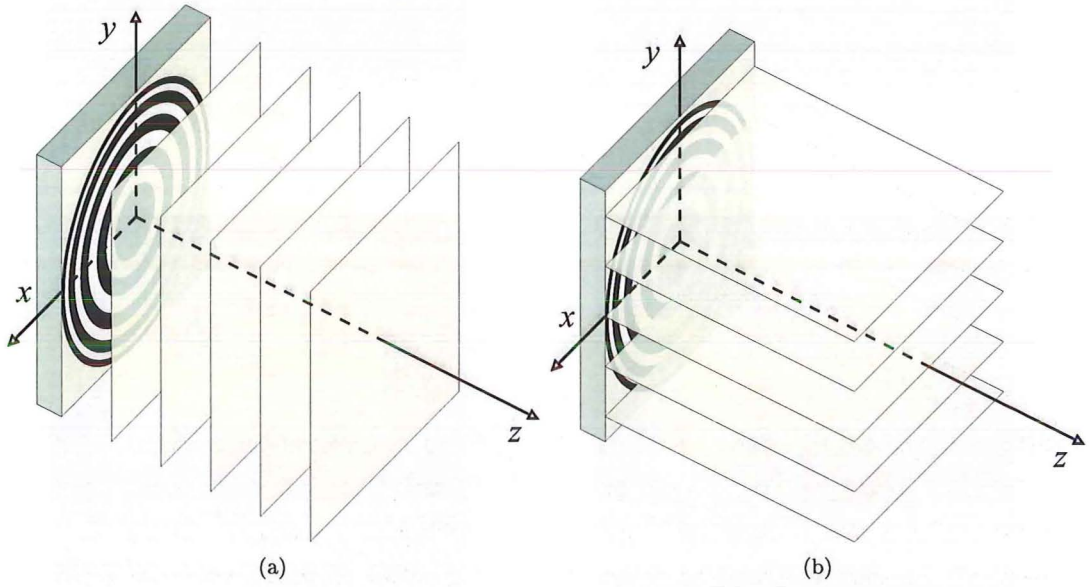

Figure 5.15 Planes that can be imaged with CCD system (a) x-y planes and (b) x-z planes.

5.6 INPUT BEAM

The input beam was first characterized by removing the Fresnel lens. Figures 5.6 shows the free space beam intensity at frequencies in the range from 0 to 4 THz. As mentioned in the introductory chapters, it is still difficult to generate good, uniform sources of terahertz radiation. The two dimensional intensity plots show that the terahertz beam is far from uniform and that the point of maximum intensity at different frequencies shifts spatially. It is important to note the non-uniform distribution apparent in all of these plots which is then transferred to the intensity patterns when a lens is placed in the beam. The input beam spectrum is shown in Figure 5.6 (f), where it can be seen that the signal strength above 1.5 THz is quite weak. The inability to use lock in detection in the signal acquisition with a CCD reduces the signal to noise ratio compared to the point-by-point measurements which prevents the accurate determination of higher frequency terahertz information.

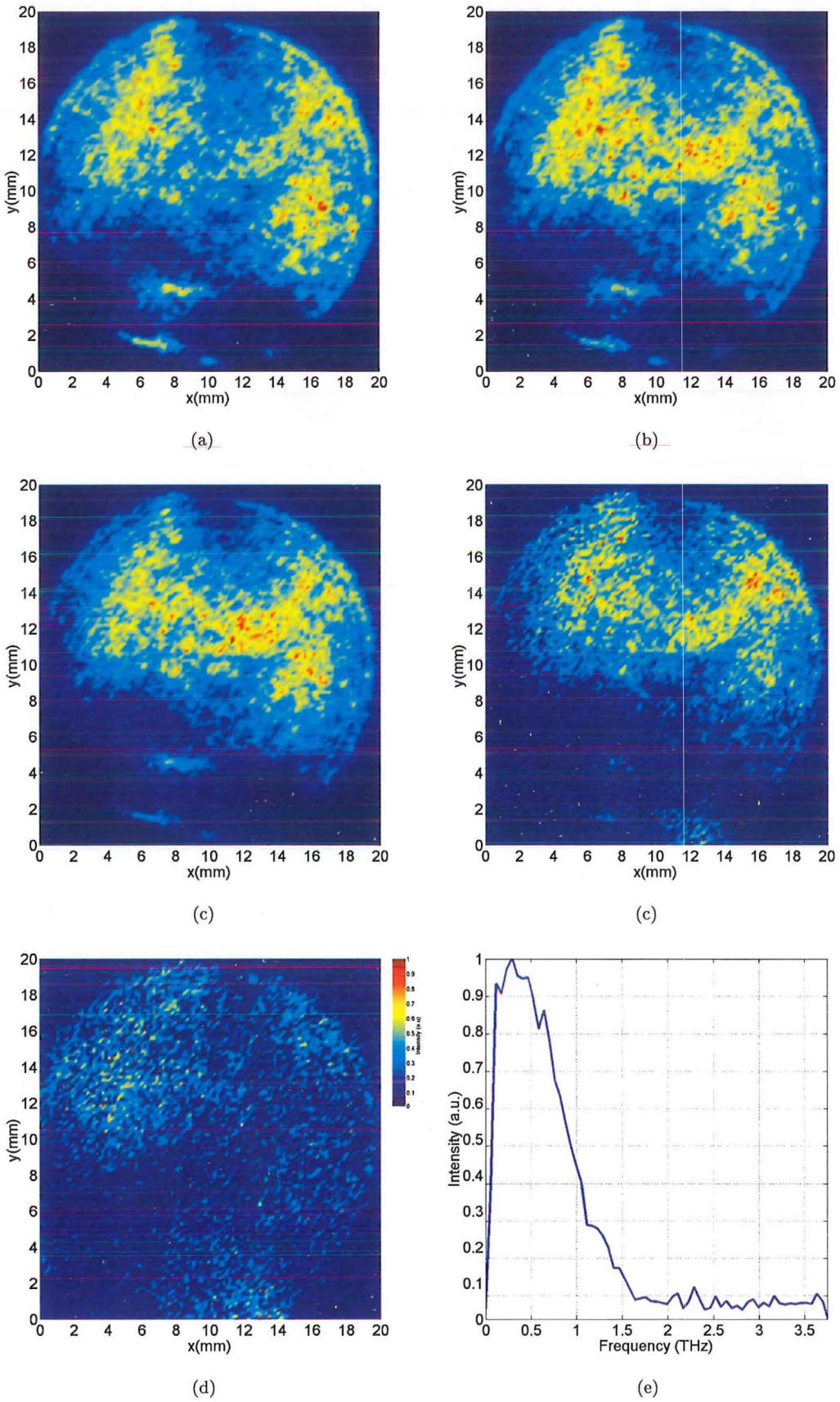

Figure 5.16 Free space terahertz intensity of the input beam at (a) 0.3 THz (b) 0.5 THz (c) 1 THz (d) 1.5 THz (e) 2 THz and (f) the source spectrum.

5.7 FOCAL LENGTH MEASUREMENTS

The various lenses and zone plates were placed in the beam. The focal point as a function of frequency was determined first. At each z point the maximum intensity on the x, y plane at each frequency around 1 THz was extracted to give a plot showing how broadband terahertz radiation is focused at different distances from the lens, Figure 5.17. Analysing the focal plane images of different frequencies this point of intensity lies within a constrained space in the centre of the x, y plane. Because of the drop off in power of the terahertz source at higher frequencies it was necessary to divide the focused intensity by the intensity profile of the free space beam to give a relative focusing representation. From these intensity maps the frequency of maximum intensity at each z point was extracted and plotted in the right hand figure of Figure 5.17.

Each of the lenses show a linear trend in the shift in focal point with frequency which, as expected, is the same for each lens. The linearity and clarity of each of these plots is improved in the more complex lenses which have better focusing ability. As with the scanned results it is possible to compare this shift in focus with the calculated shift which compare very closely. The line on the right hand plots is the calculated focal distance for each frequency with a 30 cm distance between source and lens as derived in section 5.3.

Looking in more detail, several observations can be made. It can be seen that the Al zone plate performs very poorly where, although there is a clear line of focal intensity that follows the same pattern as the other lenses, the intensity is not high and the differentiation between the intensity at the focus and at other regions beyond the lens is not great. The two level lens illustrates much clearer focusing ability than the zone plate, although it performs quite poorly around the design frequency of 1 THz with a significant drop in the intensity. The reason for this unexpected drop off in intensity is explained in the simulation chapter in section 6.4.2. Unlike the zone plate there is a clear distinction between the intensity at the focus and other regions. The four level lens shows what appears to be an area of high intensity over a large z range which in some regions appears to form a focus at two separate positions in z. This lens illustrates much improved focusing into the higher frequencies, something which is observed to be improved upon even more in the eight level lens.

5.8 X-Z SCANS

Analysing the x-z plane intensity pattern on a plane intersecting the focus (Figure 5.18) gives an indication of a lens's depth of focus. The depth of focus (DOF) is defined as the distance through which satisfactory focus can be maintained either side of a lens's focal point. It is generally accepted that this is between the region where the focal spot size remains less than $\sqrt{2}$ times its smallest value. This distance is also related to the

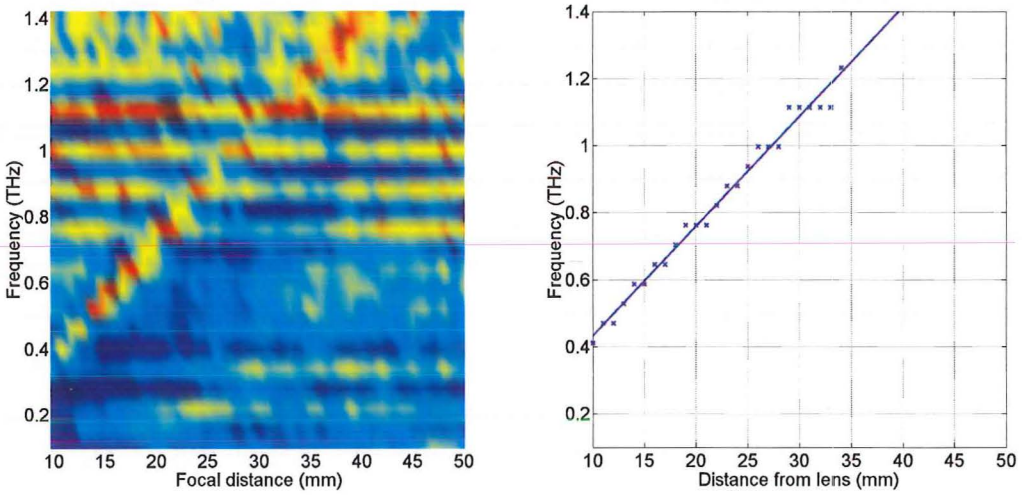
Frequency (THz)
Focal distance (mm)
Frequency (THz)
Distance from lens (mm)

(a)

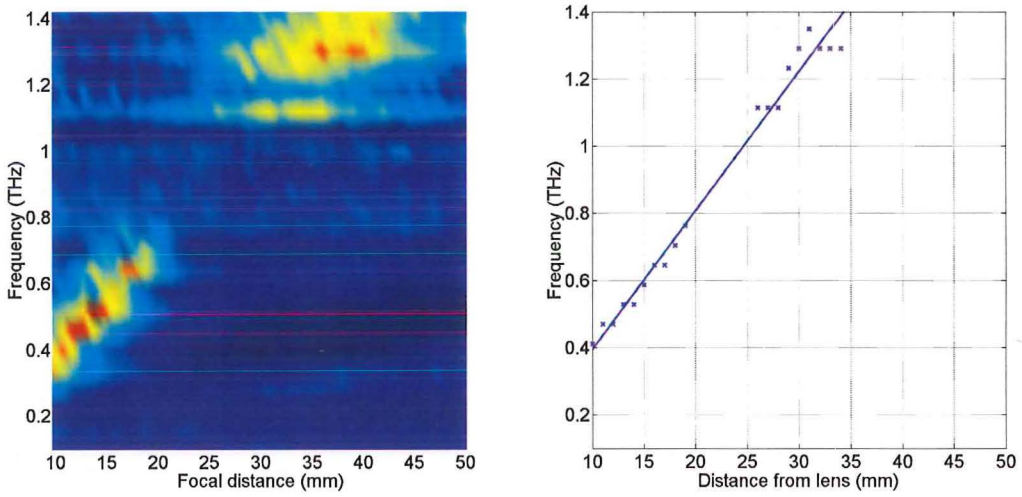
Frequency (THz)
Focal distance (mm)
Frequency (THz)
Distance from lens (mm)

(b)

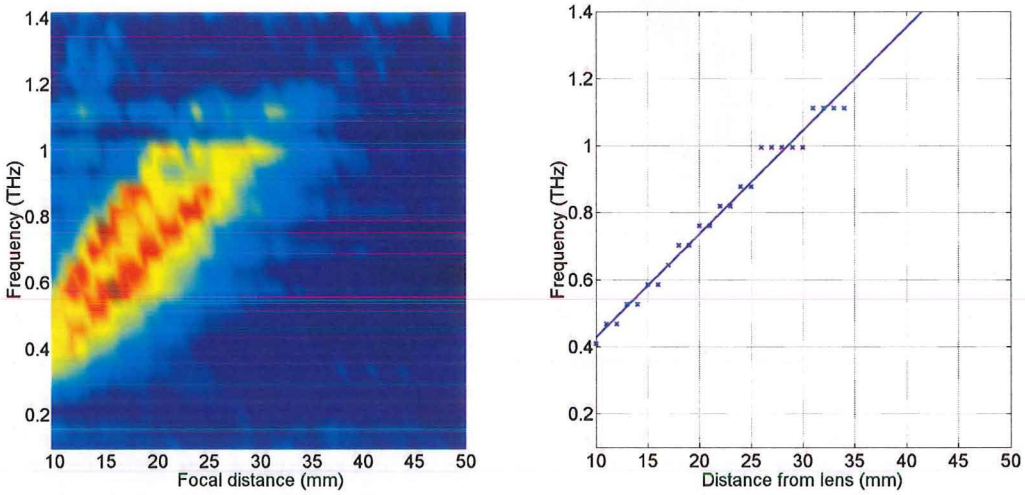

(a)

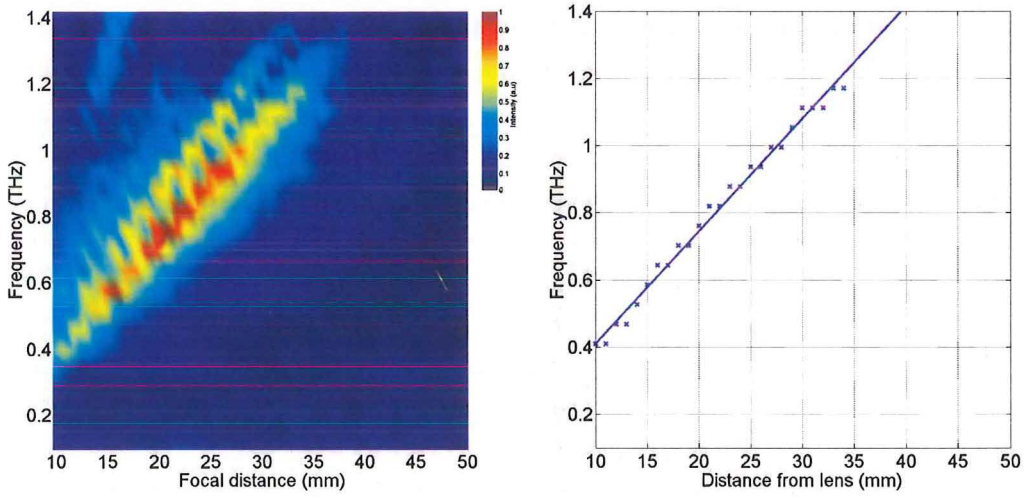

(b)

Figure 5.17 Spectral intensity distribution (left) and maximum intensity (right) of broadband THz normalized to the free space intensity down the z axis of (a) an Al zone plate, (b) a 2 level, (c) a 4 level (d) and an 8 level lens.

Rayleigh range, specifically meaning the DOF is twice the Rayleigh range [115].

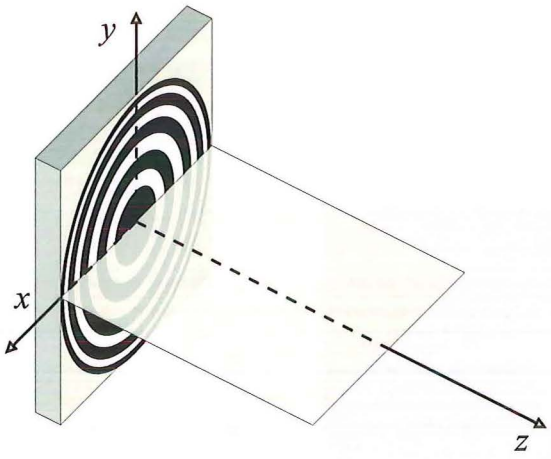

Figure 5.18 Plane being imaged x, z intensity map at 1 THz

Analysing each of the lenses at 1 THz gives an indication of the tightness of the focus along the x, z plane which is shown in Figure 5.19. The non-uniformity of the free space beam can be seen propagated into all of the patterns in Figure 5.19 which are not symmetric. At locations around the focal point the FWHM was extracted to determine the Rayleigh range where the beam waist is increased by 1.4. The apparent poor focusing of the 2-level lens at this frequency meant there was little point extracting a DOF. However a value could be determined for the other three lenses. These values and the expected uncertainty in the measurement are shown in table 5.2

Lens type	DOF	Error
Zone plate	12.6 mm	±1 mm
4 level lens	5.2 mm	±0.5 mm
8 level lens	2.64 mm	±0.25 mm

Table 5.2 Depth of focus for different lenses (Increased noise in lesser complexity lenses results in a larger measurement error).

As is characteristic of a Fresnel lens, each of the optics form a ringed radiation pattern, which converges to a focal point. These results illustrate how these patterns are less prominent with a multiple level diffractive optic where a tighter focus is obtained. In section 4.5 a DOF of 3.35 cm is determined for a zone plate. The 8-level DOF was measured to be 79% of this and the other lenses had a larger measured value. This will in part will be due to the diverging input beam, the non-Gaussian input and also the difficulty determining the measured value accurately due to noise.

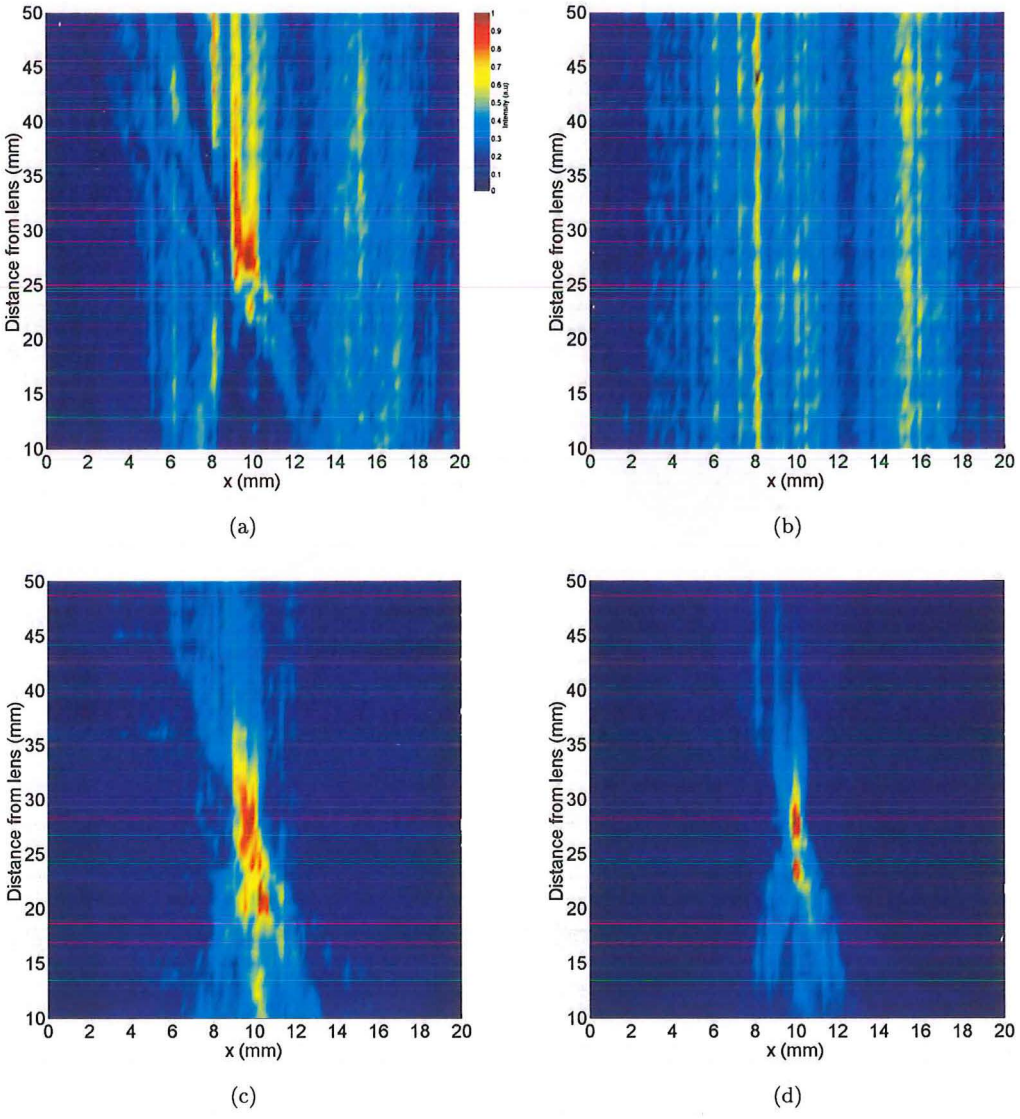

Figure 5.19 Intensity plot at 1 THz along the x, z plane of (a) an Al zone plate (b) 2 level lens (c) 4 level lens (d) and 8 level lens.

5.9 X-Y SCANS

An x, y scan at the measured focus ($z = 27$ mm) at the design frequency of 1 THz gives information about the relative focusing ability and focal plane intensity distribution of the different lenses. Intensity plots were analysed on the plane as in Figure 5.20. A range of different lenses were used in the testing so that a relative comparison could be attained to enable an assessment of the multi-level lenses. At each point in the focal plane at 25 mm from the lens the FFT was taken of the terahertz pulse from which the 1 THz intensity could be extracted.

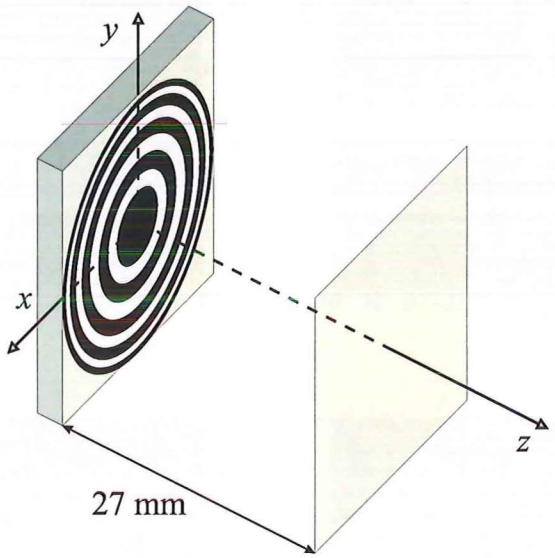

Figure 5.20 Plane being imaged - x, y plane intensity at 1 THz focal length

For an L-level binary lens the theoretical diffraction efficiency is

$$\eta = sinc^2\,(1/L) \tag{5.4}$$

The point at n = - 1 is defined as the main focal point with the focal length $f = z_{-1} = r_p^2/2\lambda$. The diffraction efficiency increases rapidly with the number of phase levels L [148], and the calculated diffraction efficiency theory versus L is shown in Table 5.3. For a binary lens with L=8, the diffraction efficiency reaches 95% in contrast with a 2-level lens with 41% efficiency. The Al zone plate would not be expected to have a very high efficiency. Half of the radiation is blocked from passing through the lens by the Al pattern. Coupling this and the limited amount of radiation in the first diffracted order, a theoretical maximum of under 10% of the radiation impacting on the lens would be expected to be measured at the focus.

Lens	Expected efficiency
Zone plate	<10%
2 level lens	41%
4 level lens	81%
8 level lens	95%

Table 5.3 Theoretical lens diffraction efficiencies.

The 1 THz focal plane image is shown for each lens in Figure 5.21. For each lens the plan view of the intensity map is shown illustrating the size and position of the focus, as well as an isometric view normalized to the maximum intensity of the 8-level lens to give an appreciation of the relative focusing ability of the different lenses. Both the zone plate and the 2 level lens illustrate low efficiency and a focal spot intensity only just larger than the noise. The 4-level and 8-level have a much increased focal spot intensity and a much reduced quantity of terahertz radiation in the plane around the focal peak than is evident in the basic structures.

There are several issues that need to be taken into consideration when trying to measure the efficiency of the lenses. These issues will lead to a reduction in the intensity at the focus. Firstly, the terahertz beam incident on the lens will not pass through completely. The high refractive index of the silicon will result in a large reflectivity at each air silicon interface (30% for a bare air-Si interface). There will also be some losses due to the absorption in the silicon; measurements using a high resistivity wafer of about 1000 Ωcm showed more than twice the transmission of an equivalent wafer of resistivity 10 Ωcm. These reflection and absorption losses are on top of the losses incurred from the fabrication errors or complexity of the respective lenses. Because of this, a relative comparison of the different lenses is of most interest. What is of particular interest is the degree to which the more complex optics outperform their simpler counterparts. Because there is a significant difference in the structuring complexity of an eight level lens and a zone plate it needs to be ascertained if such a structure will yield significant benefits.

From purely assessing the intensity maximum of each lens it is clear that the more complex multilevel lenses perform better. As the level number of the binary lens increases, a smaller focal area and sharper focused THz peak are observed. The two level lens performed very poorly as seen from the performance in the x, z plot (Figure 5.21(a)) where there is a little to no focusing in the 1 THz region. The reason for this is that the depth to which this was etched was not ideal as explained in the simulation section (section 6.4.2). The performance improvement of the eight level lens is significant displaying an improved intensity and a much tighter focus than the other optics. The relative peak intensities for each lens are shown in Table 5.4

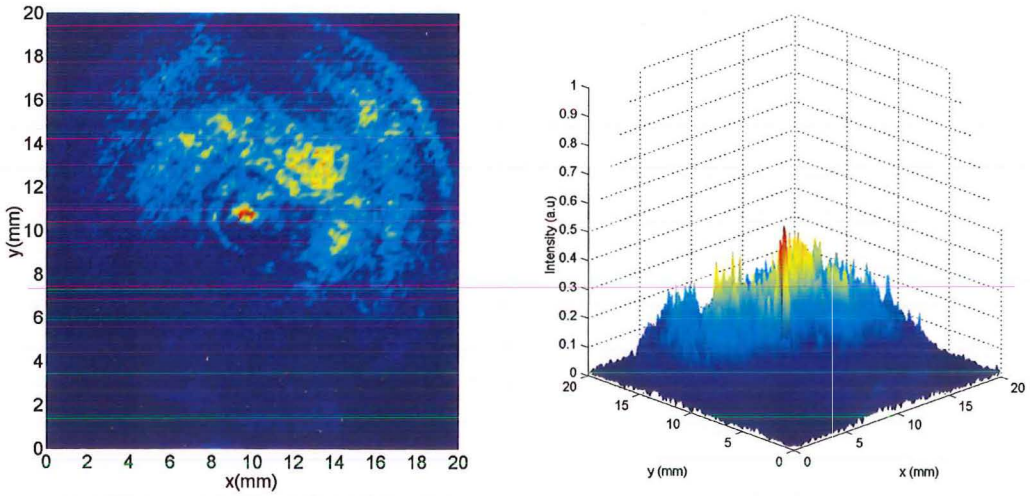

(a)

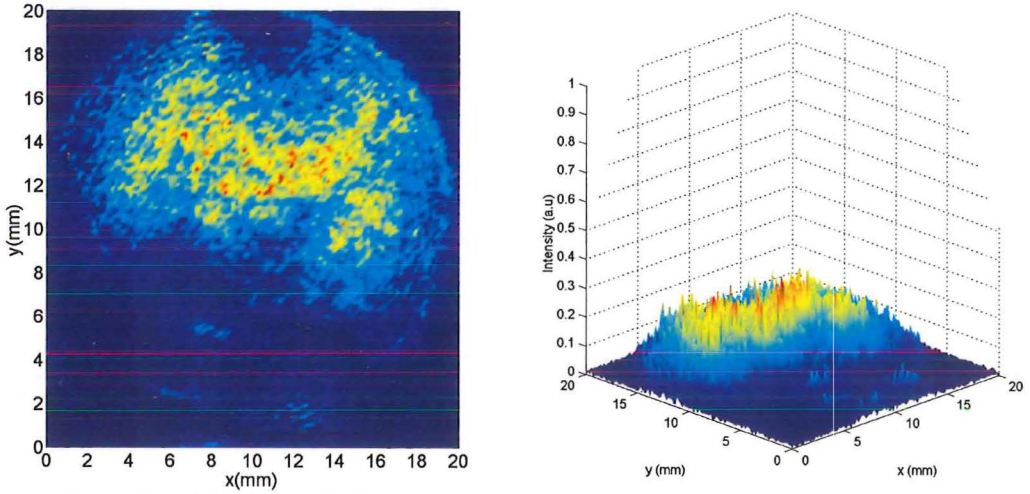

(b)

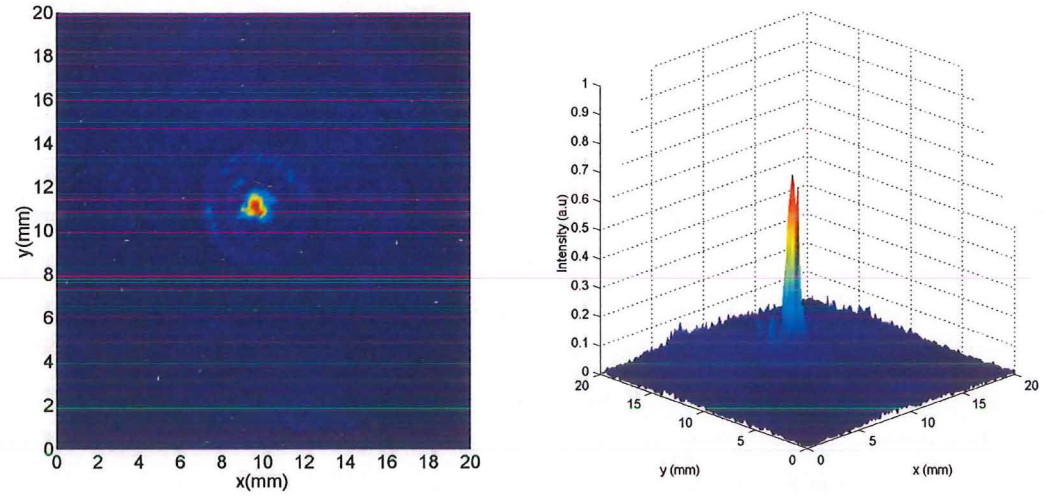

(c)

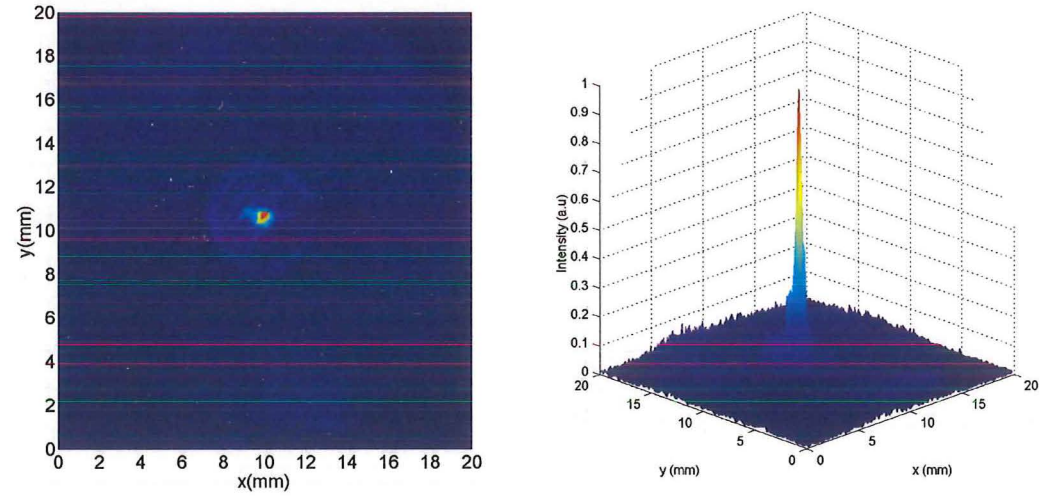

(d)

Figure 5.21 Focal plane intensity plots at 1 THz for (a) an Al zone plate (b) a 2 level lens (c) a four level lens and (d) an 8 level lens.

Lens	Measured Relative peak intensity	Theoretical Relative peak intensity
Zone plate	0.38	0.11
2 level lens	0.2	0.42
4 level lens	0.75	0.85
8 level lens	1	1

Table 5.4 Theoretical lens diffraction efficiencies.

The theoretical relative peak intensity values, derived from the expected diffraction efficiency of the different lenses, give an indication of how the different structures should perform. Although there is a general upward trend in the peak intensity of the optics this trend does not follow the theoretical values. This can be explained through the design and fabrication incongruities, see section 6.4.2. The focal pattern of the zone plate shows that although the peak intensity is higher than expected, relative to the other lenses, the radiation is poorly focused. This indicates that this terahertz distribution is probably mostly noise.

These results show the clear performance benefits obtained from creating multiple level lenses. It is possible to expend this fabrication technique to create a 16 level structure. However the expected performance enhancement is small as a theoretical 4% gain in diffraction efficiency may be reduced through problems incurred with alignment of the multiple masks. However the significant improvement in the DOF of the more complex lenses from the result in section 5.8 may make a more complex structure desirable for certain applications.

5.10 FREQUENCY CONTENT AT THE FOCAL PLANE

The frequency content at the focal distance of 25 mm was also measured to show how well these devices could perform for spectroscopic and tomographic applications. At the focal point it would be expected that there was only significant frequency content in the region of 1 THz (ie; the Fresnel lens is expected to have a significant chromatic aberration). This can be exploited in applications such as tomography [113] however for a lens to be useful in this respect it needs to uniquely focus radiation of different frequencies at different distances. This was assessed at the focal plane by taking a cross section at the point of maximum intensity in y and looking at the frequency content across x as shown in the diagram of 5.22.

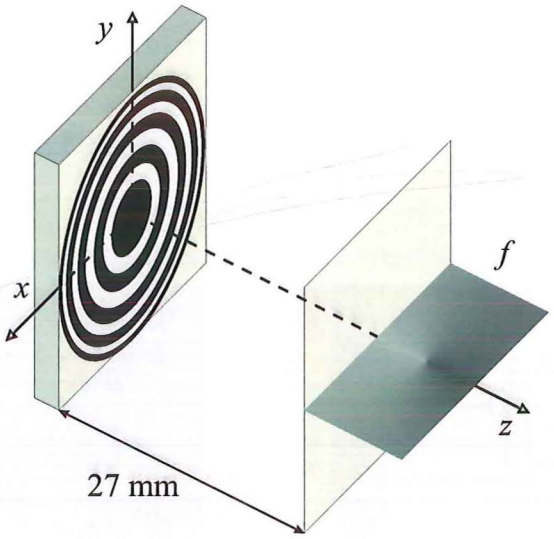

Figure 5.22 broadband focusing assessment at the 1 THz focal plane.

Focal plane frequency spectra are shown in Figure 5.23. Again the performance trend follows the same pattern, with the 8 level lens containing a radiation intensity in a very narrow band compared to the other lenses. The 2 level lens and Al zone plate show a much higher intensity in the frequency band below 1 THz than do the 4-level and 8-level lenses. The 8-level lens clearly shows the best performance, with the spectrum at the focal point (x=10 mm) having a FWHM of only 427 GHz. This is suitable for spectroscopic or tomographic terahertz applications, as has already been demonstrated with this lens [114].

5.11 COMPARISON OF FRESNEL LENSES WITH REFRACTIVE LENSES

Currently any focusing of terahertz is performed using either reflective lenses or refractive lenses made of polyethylene or silicon. It is of interest to compare the diffractive optic lenses that were fabricated with these existing refractive lenses. For this comparison a four level lens with focal distance of 2.5 cm was compared to a biconvex polyethylene lens of focal distance 5 cm and biconvex silicon lens of focal distance 10 cm. The Fresnel lens, polyethylene lens and silicon lens have the $F_{\#}$ (focal distance / lens diameter) of 0.83, 1 and 2.5 respectively. Figure 5.24 provides the THz amplitude distribution along a line across the focal center on the focal plane for each lens measured with the CCD terahertz system.

On the focal plane of the Fresnel lens, a sharp THz focal point and a THz ring were formed (Figure 5.24). The focused THz distribution of the Fresnel lens is more symmetric compared to that of the silicon or polyethylene lenses. This means the spherical

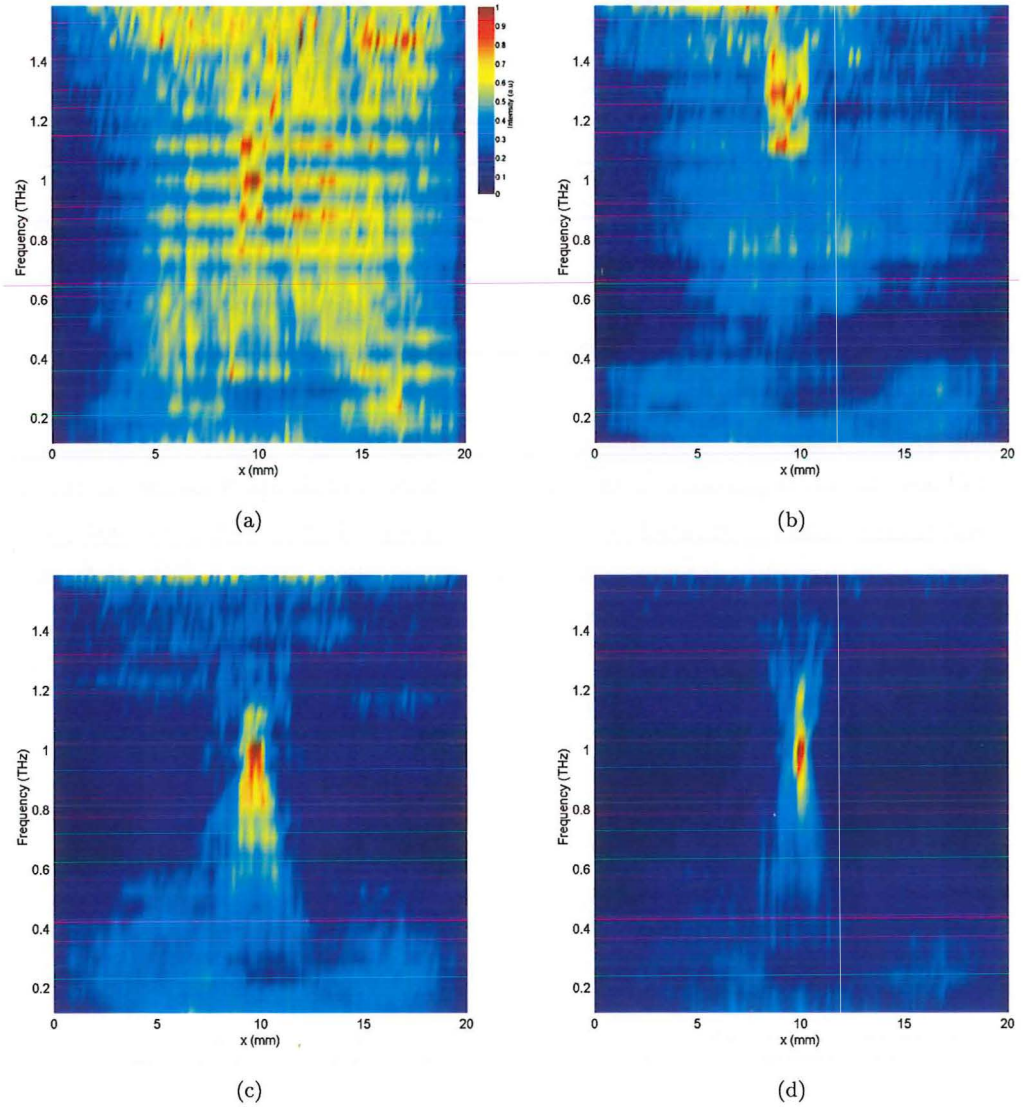

Figure 5.23 Frequency distribution at the x maximum on the focal plane of (a) an Al zone plate (b) a 2 level lens (c) a 4 level lens and (d) an 8 level lens.

aberration of the Fresnel lens is less than that of the silicon lens or polyethylene lens.

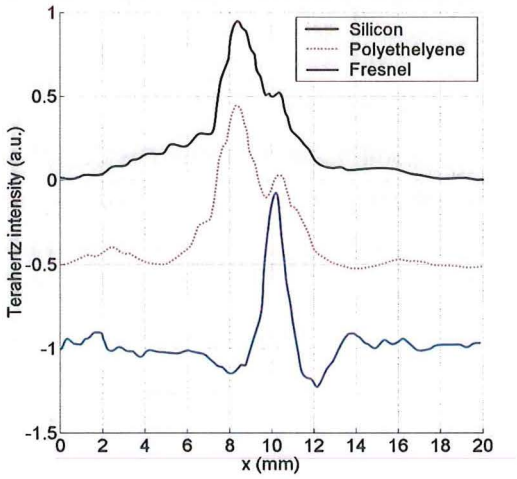

Figure 5.24 THz intensity distribution along a line across the focus center on the focal plane for all three lenses. (For clarity, the curves were vertically shifted).

The THz pulse waveform and Fourier spectrum of the three lenses at the focal point were also obtained and are shown in Figure 5.25. As can be seen, the Fresnel lens focused THz waves more efficiently in the frequency range of 0.5 to 1.1 THz whereas the spectrum for the other lenses is almost identical to the source spectrum (Figure 5.6(f)).

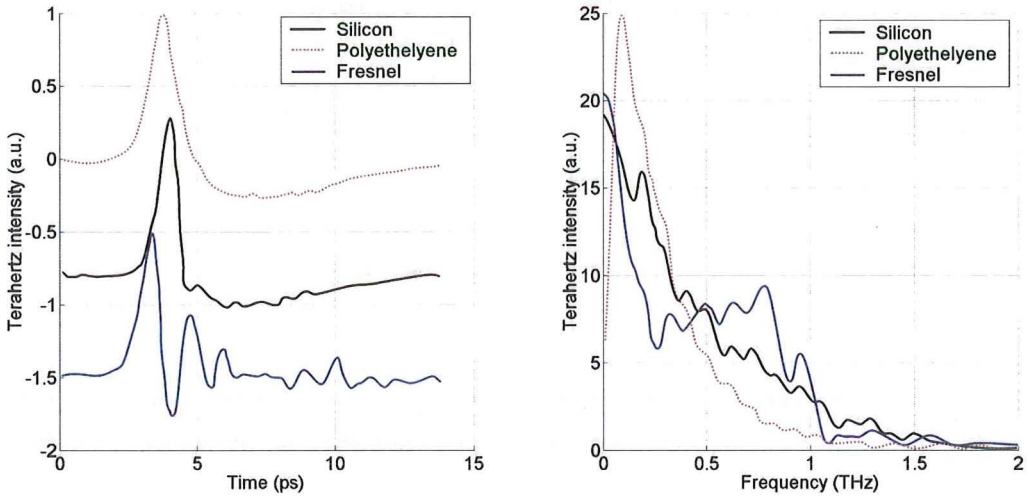

(a) (b)

Figure 5.25 (a) THz waveforms and (b) Fourier spectra of 3 lenses at their focal point. (For clarity, the curves in (a) were vertically shifted).

This result suggests that the Fresnel lens could be used as a focused terahertz band pass filter. The focusing performance of the three lenses is compared at different terahertz frequencies and is shown in Figure 5.26. The theoretical minimum focus spot is [149]

$$w_0 = \frac{4\lambda}{\pi} F_{\#} \tag{5.5}$$

where w_0 is the minimum focus radius, is the focus wavelength and $F_{\#}$ is the F-number of the lens. For convenience of comparison, the focal size is normalized by dividing by the F# number in Figure 5.26. The Fresnel lens shows good focusing performance at frequencies from 0.7 to 1.4 THz, and is comparable to the silicon lens at 1.4 THz.

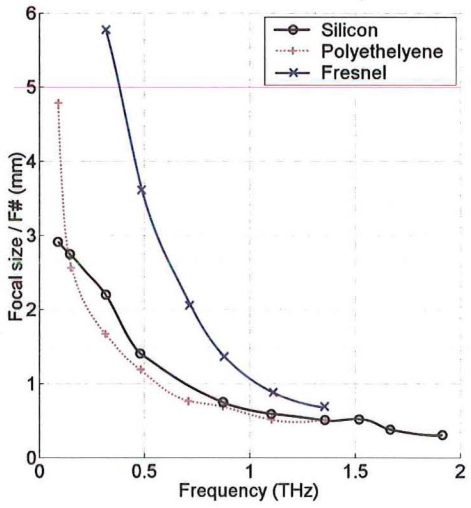

Figure 5.26 Normalised spot size variation with terahertz frequency for diffractive and refractive lenses.

5.12 SUMMARY

The temporal and spatial THz distribution for an amplitude and a set of increasingly complex phase zone plate T-ray binary lenses were fully assessed. The eight level silicon binary lens performed best in all aspects of focusing. As the level number of the T-ray binary lens is increased, not only does the diffraction efficiency increase, but also the THz spatial distribution shows a tighter focus and a reduced loss of power into side lobes, giving a more comparable performance to conventional refractive THz lenses. The 8-level lens showed an order of magnitude increase in the intensity at the focus compared with a simple 2-level device. There is a linear relationship between frequency and focal distance for each lens which again is more clearly defined in the more complex structures. The multiple level lenses also show a more narrow band nature at the focal point making them more desirable for spectroscopy and tomography applications.

Chapter 6

LENS SIMULATIONS

6.1 INTRODUCTION

The complexity and time involved in creating different multilevel lens structures makes experimental optimisation a daunting task. Modeling enables the formulation of numerous different lenses and gives insight into the effects on different designs or fabrication issues that will affect the efficiency of these structures. Many of these structural changes may be hard to measure experimentally. Simulation can give a less ambiguous determination of how the physical process can be improved to give minimum turn around to a better device. Analysing how deviating from different aspects of the microfabrication process can effect the efficiency of the structure is important. This highlights which processes need strict control and helps minimise the cost of fabrication by avoiding unnecessary accuracy in techniques that have little bearing on the efficiency. A detailed sensitivity analysis is provided in the following chapter.

This Chapter first describes some of the techniques that are available to simulate diffraction problems. The accuracy and practical computing requirement of the Fraunhofer approximation lends itself well to the simulation of these large complex structures. The formulation of this simulation technique is described in detail. Using this model the lens characteristics are investigated to show how structures of different complexity are expected to perform. These simulations are used to explain some of the results of the previous measurement chapters. The final section highlights some design issues and their effects on the efficiency and versatility of different designs including zone step positions, focal distances and effect of wafer sizes. This gives some information on the potential limits of application for diffractive optic terahertz lenses.

6.2 OPTICAL DIFFRACTION ANALYSIS TECHNIQUES

Diffraction occurs when a wave encounters an obstruction. Whether the obstacle be transparent or semi-transparent, certain regions of the wavefront will have their amplitude or phase altered. Beyond the obstacle altered segments of the wavefront will interfere to form a diffraction pattern. The wave nature of electromagnetic radiation

means that these resultant wavelets will combine at every point in the region beyond the obstruction. The adjusted optical path lengths of certain wavelets may interfere with others either constructively or destructively depending on their phase at the given point.

The Huygens-Fresnel Principle states that every unobstructed point of a wavefront, at a given instant, serves as a source of spherical secondary wavelets (with the same frequency as that of the primary wave) [150]. The amplitude of the optical field at any point beyond is the superposition of all these wavelets (considering their amplitudes and relative phases)

The relative size of an obstruction or aperture to the wavelength will determine the wavefront shape at points beyond the structure. If the wavelength is large compared to a given diffracting feature, the waves will spread out at large angles from the region beyond it. As the waves propagate away from the feature they will tend to approximate a parabolic and then a more linear form. It is at these different points in space that different forms of scalar diffraction apply.

6.2.1 Scalar vs Vector analysis

There are a number of different techniques for analyzing optical diffraction. These can be divided into two classes, vector and scalar. A scalar technique does not take into account the field direction (where all fields are in the same direction). Comparatively vector analysis takes into account the direction of all fields.

Scalar treatments include Huygens' Principle, Rayleigh-Sommerfeld theory, and the Kirchhoff formulation [151, 152]. Fraunhofer and Fresnel approximations are derived from the Kirchhoff model. Each of these theoretical models has strengths and weaknesses which lead them to be particularly suited to a range of different problems. The choice of which model is appropriate for a given problem is dependent on accuracy requirements and computational capability.

It can be difficult to discern which scalar diffraction model is appropriate for a certain problem. In applying a diffraction model there are usually two main points to consider. First the fields exiting a diffracting object need to be obtained. The second step involves propagating those fields to the desired observation point. These are distinct and separate parts of the scalar diffraction models listed above. If the resulting diffraction pattern is at all inaccurate, it is difficult to determine how much of the error in the resulting fields is due to incorrect boundary fields and how much is the result of the propagation calculation.

In any case, scalar theory calculations based on simple assumptions about boundary fields generally depart somewhat from experimental data. This is particularly true for cases when the diffracting aperture or features therein are not large compared to a

wavelength. Approximation of the boundary field distribution is at least partly to blame.

Vector models are capable of obtaining more accurate solutions, particularly for near fields. Such treatments apply electromagnetic boundary conditions, derived from Maxwell's equations [1], to the diffracting aperture. The accuracy of boundary fields obtained in such a manner depends on the ability to solve the boundary condition equations. Again, for complicated diffracting objects, the calculation is often extremely difficult if not impossible.

Vector solutions are more accurate while becoming computationally more complex. The spatial position of interest of a problem will determine which calculation method is the best to employ. This is determined by the size of the aperture or feature involved and the corresponding distance to the point of interest. Moving beyond a given structure to increasing distances in space we can assume the form of the wavefronts to move from circular to parabolic to planar in shape. It is important to delineate where sufficient accuracy can be obtained while minimising the computational power required. This is especially pertinent when considering large complex three dimensional structures that require large matrix complexity to accurately represent their form. The next sections provide a review of different vector and scalar models.

6.2.2 Vector techniques

Maxwell's equations describe the behavior of electromagnetic waves in all practical situations. They connect vector quantities applying to any point in a varying electric or magnetic field. Diffraction problems can be simulated in terms of these equations and boundary conditions, however simplifying approximations are required to allow the simulation of complex geometries. A number of vector numerical techniques are available for the solution of electromagnetic problems. Each numerical technique is well suited for the analysis of a particular type of problem. These techniques can be defined as integral or differential methods depending on whether they solve the integral or differential form of Maxwell's equations.

6.2.2.1 Finite Difference Time Domain

The FDTD (Finite Difference Time Domain) algorithm was first established by Yee as a three dimensional solution of Maxwell's curl equations [153].

$$\frac{\delta \widetilde{H}}{\delta t} = -\frac{1}{\mu}\nabla \times \widetilde{E} \tag{6.1}$$

$$\frac{\delta \widetilde{E}}{\delta t} = \frac{1}{\varepsilon}\nabla \times \widetilde{H} \tag{6.2}$$

In principle, a volume of space containing any object or collection of objects is subjected to an electromagnetic disturbance, FDTD then solves for the fields throughout the volume as a function of time. Application of FDTD requires that the diffracting structure and surrounding space are divided into two interleaving grids. One contains nodes where the electric field is solved and the other contains nodes where the magnetic field is solved.

Figure 6.1 shows a 'Yee unit cell' in which the E and H field components are considered to be interlaced. The four E components surrounding the point (i, j, k) trace out a clockwise path and therefore have some curl. The equations state that the H_y increases in response to a curl in this direction, with a constant of proportionality given by $1/\mu$. This constant specifies the magnetic permeability at location (i, j, k). Similarly the rate of change of the E_s to the curl of the H components can be determined with a constant of proportionality of $1/\varepsilon$

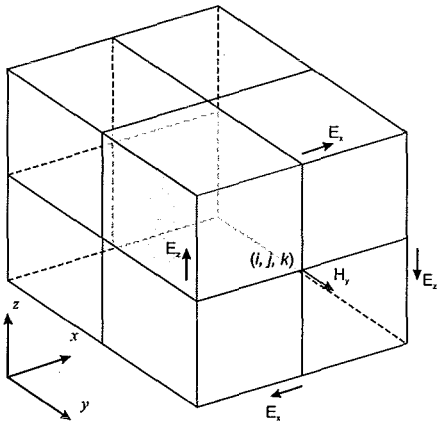

Figure 6.1 Yee cube illustrates the interaction of the electric and magnetic fields.

FDTD calculations can provide significantly more accurate near fields than the approximations often encountered in scalar diffraction theory [154]. Given that the near fields produced by the FDTD computational method can be close approximations of Maxwell fields, all that should be required of a propagation model is that it retain the Maxwellian nature of those fields as they propagate away from the near zone. Any such propagation model should produce an accurate diffraction pattern from accurate fields on the surface of a diffracting aperture [155].

Accurate solutions require a grid spacing much smaller than the structure geometry. For the 3D simulation of the terahertz lens structures the grid size required is prohibitively large. Although this model can potentially provide very accurate solutions the problem is too large for current computing capabilities.

6.2.2.2 Finite Element analysis

Similar to FDTD, the Finite Element Method (FEM) involves dividing the configuration into a number of small homogeneous pieces or elements [156]. The elements can be smaller in areas where geometric details exist or in highly conductive regions where there can be rapid changes in the fields. In each finite element, a simple variation of the field quantity is assumed. The corners of the elements are called nodes and it is at the nodes that the field quantities are determined. The major advantage that finite element methods have over other electromagnetic modeling techniques is that the electrical and geometric properties of each element can be defined independently. This enables more efficient calculation by creating larger elements in relatively open regions and large numbers of small elements in regions of complex geometry. Calculation times are typically long and although more suited to lens simulation than FDTD this method is still too computationally intensive.

6.2.2.3 Rigorous Coupled Wave Analysis

Rigorous Coupled Wave Analysis (RCWA) is a differential method of solving Maxwell's equations for infinitely periodic structures. First developed for the solution of planar gratings [157] it has since been developed for the solution of surface relief gratings [158]. In RCWA the permittivity of the grating region is represented by a Fourier expansion. This allows the treatment of a wide class of gratings (planar or surface relief, lossy or lossless, single grove or multigroove) in a unified way. Non-rectangular gratings are constructed by making grating stacks in a staircase structure to approximate the profile. Obtaining good accuracy of such structures requires large numbers of layers which can become computationally intensive. This simulation method was used for grating simulation in this work with the use of the package GSolver [143].

6.2.3 Scalar techniques

The analysis of structure defects in the simulation of these lenses demands the ability to create structures in three dimensions such that effects can be introduced to a three dimensional structure at different stages of fabrication. Because the matrix complexity required to create such a three dimensional structure is significant and the structure size is large, forms of vector analysis become computationally prohibitive. Hence a scalar method is required. Different scalar techniques are reviewed here before the Fresnel/Fraunhofer propagation method that was used is described.

6.2.3.1 Geometric ray propagation

Some simple optics problems can be solved with basic ray propagation. This simply involves analysing the refractive indicies and path distances to determine the direction

of beams through a set of media. At a very basic level this can predict the reflection and refraction of radiation as it passes through a structure using Snell's law, Fresnel reflection coefficients and trigonometric functions.

According to Snell's law of reflection and refraction

$$v_i = v_r \tag{6.3}$$

$$sinv_t = \sqrt{\frac{n_1}{n_2}} sinv_i \tag{6.4}$$

where v_i is the incident angle, v_r is the reflected angle and n_1 and n_2 are the refractive index of the two media as shown in Figure 6.2

When a plane wave is incident on an interface between two media some of the beam can be reflected and some refracted. If the incident field is electrically polarised, $V_z = E_z$ the reflected and refracted components are given by

$$E_z^r = R^e exp\left(-jk_1 s^r\right) \tag{6.5}$$

$$E_z^r = T^e exp\left(-jk_2 s^t\right) \tag{6.6}$$

Similarly, if the incident field is magnetically polarised, $V_z = H_z$ the reflected and refracted components are given by

$$H_z^r = R^m exp\left(-jk_1 s^r\right) \tag{6.7}$$

$$H_z^r = T^m exp\left(-jk_2 s^t\right) \tag{6.8}$$

where k is the absorption coefficient and R and T are the reflection and transmission coefficients [159].

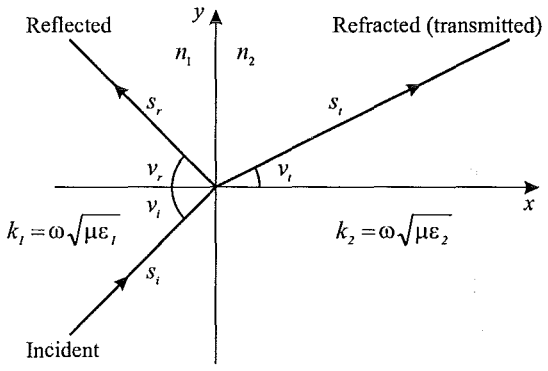

Figure 6.2 Rays impacting an interface are reflected and/or transmitted according to Snell's law.

Ray tracing is a widely applicable technique for modeling the propagation of light through an optical system, however ray tracing is not appropriate for all modeling tasks. Rays are incoherent in the sense that the path a ray takes during propagation

is not affected by the presence or absence of other rays and subsequently is not ideally suited for simulation of diffractive optics. However, this technique can be used in the lens design.

6.2.3.2 Ray Matrices

For many optical components a 2 × 2 ray matrix or ABCD matrix can be defined. The effect of the component on a ray can then be determined by multiplying this ABCD matrix with the ray vector[160]. The effect on rays of complex systems of multiple lenses can be evaluated by multiplying the ray matrix for each component together with the ray vector.

A light ray can be defined by two co-ordinates, its position, x, and its slope θ from the optical axis. For most optical components where the displacements and angles are small the system can be defined in terms of partial derivatives.

$$x_{out} = \frac{\delta x_{out}}{\delta x_{in}} x_{in} + \frac{\delta x_{out}}{\delta \theta_{in}} \theta_{in} \tag{6.9}$$

$$\theta_{out} = \frac{\delta \theta_{out}}{\delta x_{in}} x_{in} + \frac{\delta \theta_{out}}{\delta \theta_{in}} \theta_{in} \tag{6.10}$$

These can then be written in matrix form

$$\begin{bmatrix} x_{out} \\ \theta_{out} \end{bmatrix} = \begin{bmatrix} \frac{\delta x_{out}}{\delta x_{in}} & \frac{\delta x_{out}}{\delta \theta_{in}} \\ \frac{\delta \theta_{out}}{\delta x_{in}} & \frac{\delta \theta_{out}}{\delta \theta_{in}} \end{bmatrix} \begin{bmatrix} x_{in} \\ \theta_{in} \end{bmatrix}$$

where $\frac{\delta x_{out}}{\delta x_{in}}$ is the spatial magnification and $\frac{\delta \theta_{out}}{\delta \theta_{in}}$ is the angular magnification. As with other ray propagation methods ABCD matrices do not deal with the interaction of waves well and hence are ill suited for diffraction analysis.

6.2.4 Fresnel and Fraunhofer propagation

As previously mentioned the point at which a scalar diffraction propagation method becomes valid is where the wavefronts approximate a certain shape. Beyond the point where $z > \lambda$ where vector solutions should be used the Rayleigh Sommerfield solution becomes valid. At this point the wavefronts should be spherical in nature. Beyond this where the waves become parabolic in nature the Fresnel approximation should be used. Here

$$z > \sqrt[3]{\frac{k}{8\pi} \left[(x_2 - x_1)^2 + (y_2 - y_1)^2 \right]^2_{max}} \tag{6.11}$$

where $k = \omega n/c$ and the spatial limits are as shown in Figure 6.3.

In the far field the wavefronts are approximately linear where the Fraunhofer ap-

proximation becomes valid. At this point

$$z > \frac{k}{2\pi}\left[(x_2 - x_1)^2 + (y_2 - y_1)^2\right]_{max} \tag{6.12}$$

A general guide to when Fraunhofer diffraction is applicable at an obstacle or aperture of greatest width a is when

$$R > a^2/\lambda \tag{6.13}$$

Where R corresponds to the smallest distance to either the source illuminating the aperture or the point of interest beyond.

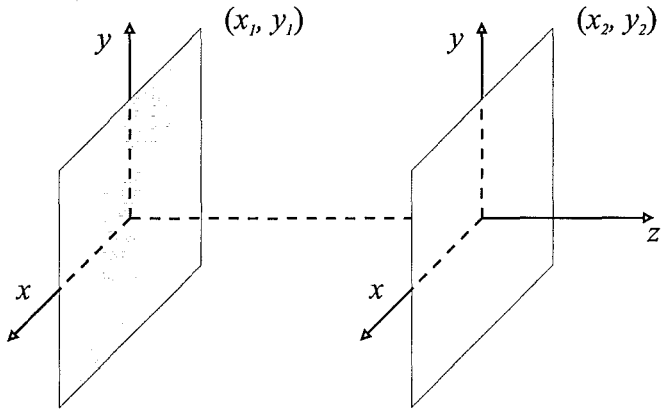

Figure 6.3 Coordinates of scalar model limit.

The feature sizes relative to the wavelength and the large distances beyond the lens that are the points of interest mean the Fraunhofer approximation is valid. The following derivation illustrates how the Fraunhofer approximation of far field intensity planes can be determined by calculating the phase profile after the lens and then propagating this to the plane of interest using a Fourier transform.

6.2.5 Derivation of the Fraunhofer far field approximation

In free space from Maxwell's Equations we have

$$\frac{\delta^2\psi}{\delta^2 x^2} + \frac{\delta^2\psi}{\delta^2 y^2} + \frac{\delta^2\psi}{\delta^2 z^2} = \frac{1}{c^2}\frac{\delta^2\psi}{\delta^2 t^2} \tag{6.14}$$

In this equation ψ can be a component of electric or magnetic field. If the radiation is monochromatic and coherent, then

$$\psi(x, y, z, t) = \psi(x, y, z, t)e^{-j\omega t} \tag{6.15}$$

Substituting this into the differential wave equation yields Helmholtz's equation

$$\frac{\delta^2\psi}{\delta^2 x^2} + \frac{\delta^2\psi}{\delta^2 y^2} + \frac{\delta^2\psi}{\delta^2 z^2} = -k^2\psi \tag{6.16}$$

where $\omega/k = c$ and k is the propagation number equal to $2\pi/\lambda$. Consider propagation which is nearly parallel to the z axis giving

$$\psi(x, y, z, t) = f_z(x, y)e^{-j\omega t} \tag{6.17}$$

where $f_z(x, y)$ varies slowly with z. Substituting this into the Helmholtz equation yields

$$e^{jkz}\left[\frac{\delta^2 f_z}{\delta^2 x^2} + \frac{\delta^2 f_z}{\delta^2 y^2} + \frac{\delta^2 f_z}{\delta^2 z^2} + 2jk\frac{\delta f_z}{\delta z} - k^2 f_z\right] = -k^2 f_z e^{jkz} \tag{6.18}$$

This paraxial approximation neglects $\frac{\delta^2 f_z}{\delta z^2}$ since f_z is assumed to vary very slowly with z. With this assumption we get the paraxial wave equation

$$\frac{\delta^2 f_z}{\delta^2 x^2} + \frac{\delta^2 f_z}{\delta^2 y^2} + 2jk\frac{\delta f_z}{\delta z} = 0 \tag{6.19}$$

The paraxial wave equation can be solved to yield the paraxial diffraction integral using the two-dimensional Fourier transform.

Let $F_z(u, v)$ denote the two-dimensional Fourier transform of $f_z(x, y)$ so that the Fourier transformed paraxial wave equation is

$$(j2\pi u)^2 F_z + (j2\pi v)^2 F_z + 2jk\frac{\delta F_z}{\delta z} = 0 \tag{6.20}$$

Rearranging this yields

$$\frac{\delta F_z}{\delta z} = \left(\frac{2\pi^2}{jk}\right)(u^2 + v^2)F_z(u, v) \tag{6.21}$$

which can be directly integrated to give

$$F_z(u, v) = F_0(u, v)exp\left[-\frac{j2\pi^2}{k}(u^2 + v^2)z\right] \tag{6.22}$$

Since the two-dimensional inverse Fourier transform of $exp[-j2\pi^2(u^2 + v^2)z/k]$ is

$$h(x, y) = \frac{1}{j\lambda z}exp\left[\frac{jk}{2z}(x^2 + y^2)\right] \tag{6.23}$$

where $\lambda = 2\pi/k$.

Taking the inverse Fourier transform of 6.22 gives the convolutional relationship that is the paraxial diffraction integral

$$f_z(x,y) = \frac{1}{j\lambda z}\int_{-\infty}^{\infty}\int_{-\infty}^{\infty} f_0(x_0,y_0) exp\left[\frac{jk}{2z}\left((x-x_0)^2+(y-y_0)^2\right]dx_0dy_0\right. \tag{6.24}$$

This equation states that the field amplitudes at the plane at z are related to those at the plane $z = 0$ by a linear, shift-invariant filtering operation with an impulse response $h(x,y)$. Whenever this equation is valid the point of observation is in the Fresnel region of diffraction. This is the point where $z > \frac{k}{(\varepsilon^2+\eta^2)}$, where k is the wavenumber and ε & η are spatial coordinates. The quadratic terms in the exponential of the diffraction integral can be expressed as

$$\begin{aligned} exp\left[\frac{jk}{2x}\left((x-x_0)^2+(y-y_0)^2\right)\right] = exp\left[\frac{jk}{2x}(x^2+y^2)\right] \times \\ exp\left[-\frac{jk}{z}(xx_0+yy_0)\right] exp\left[\frac{jk}{2z}(x_0^2+y_0^2)\right] \end{aligned} \tag{6.25}$$

Which simplifies to

$$\begin{aligned} f_z(x,y) = \frac{1}{j\lambda z P_z(x,y)}\int_{-\infty}^{\infty}\int_{-\infty}^{\infty} f_0\left(x_0,y_0\right) P_z\left(x_0,y_0\right) \times \\ \exp\left[-j2\pi\left(-j2\pi\left(\frac{xx_0+yy_0}{z\lambda}\right]\right)\right) dx_0dy_0 \end{aligned} \tag{6.26}$$

where $P_z(x,y) = exp\left[\frac{jk}{2z}(x^2+y^2)\right]$, which is a phase factor with unit modulus. Breaking the paraxial diffraction integral down for propagating a field through a distance z in free space may be interpreted as a sequence of three operations

1. Multiplication of $f_0(x_0,y_0)$ by the phase factor $F_0(x_0,y_0)$

2. Calculation of the two dimensional Fourier transform with spatial-frequency variables $x/(z\lambda)$ and $y/(z\lambda)$

3. Multiplication of the result by a further phase factor $p_z(x,y)$

The field at the plane $z = 0$ can be assumed to be nonzero over a relatively small region determined by the diffracting structure in that plane. Considering a point at z which is sufficiently far the phase factor $p_z(x_0,y_0) \approx 1$ over the entire region of the

(x_0, y_0) plane in which $f_0(x_0, y_0)$ is non-zero. Hence

$$f_z(x,y) = \frac{1}{j\lambda z P_z(x,y)} \int_{-\infty}^{\infty}\int_{-\infty}^{\infty} f_0(x_0,y_0) \times exp\left[-j2\pi\left(-j2\pi\left(\frac{xx_0+yy_0}{z\lambda}\right)\right)\right] dx_0 dy_0 \tag{6.27}$$

From this one can observe that $f_z(x,y)$ is just the two-dimensional Fourier transform of $f_0(x_0,y_0)$ except for a multiplicative phase factor which will not affect the intensity of the diffracted light. This is the Fraunhofer approximation and is valid for the region where $z > \frac{k}{2\pi}\left[(x_2-x_1)^2+(y_2-y_1)^2\right]_{max}$ [161].

6.2.6 Technique comparison

With the exception of the original Huygens' Principle, all of the diffraction theories contain propagation models derived from Maxwell's equations. Propagation models in the scalar Rayleigh and Kirchhoff theories are based on the Helmholtz wave equation, which is obtained directly from Maxwell's curl equations. After application of Green's Theorem, the propagation models are derived. The scalar propagation models are then applied to each vector component of the boundary field. If the vector near fields adhere to Maxwell's equations, the component-by-component propagation of those fields employing a method derived from the wave equation should, in theory, produce Maxwell far fields.

The differences between scalar theories result from different aspects of the boundary fields employed in their respective propagation models. As a result, incorrectly specified boundary fields can lead to different diffraction patterns from these scalar theories. Conversely, given the same accurate boundary values, these propagation models should produce the same diffraction pattern. So for many electromagnetic problems there are several simulation methods available the choice of which is determined by computational ability. In this work Fresnel and Fraunhofer propagation methods were used because they provide relatively fast accurate solutions.

6.3 IMPLEMENTATION OF FRESNEL/FRAUNHOFER PROPAGATION

The code was developed in MATLAB, a matrix manipulation script language from Mathworks [146]. The multiple level lenses were built up in an array as they would be in the fabrication process. Through doing this, features such as surface distortion, depth control, mask alignment and step dimension could be investigated at different stages of the process. As each stage is exposed to different amounts of etching a more

accurate representation of the effect on focusing efficiency from a particular defect is obtained.

The phase profile is determined by determining at each pixel the phase of the radiation of interest after passing through a distance of silicon and a distance of air,

$$p_{(x,y)} = \frac{2\pi}{\lambda}(n_{Si}(D - d_{(x,y)}) + n_{air}(d_{(x,y)}) \tag{6.28}$$

where n is the refractive index, D is the thickness of the wafer and d is the etch depth at point (x, y).

This is dependent on the thickness of the wafer, which in these simulations was set to 400 μm replicating the wafers used, and the depth etched at each location. An input beam is created in the form of a three dimensional Gaussian wave which is multiplied with the phase profile. From this the two dimensional Fourier transform can be used to determine the intensity profile at any position beyond the lens. From this the important details of the lens focusing ability can be extracted such as the focal distance, depth of focus and the full width half maximum.

As highlighted in section 6.2.4 the Fresnel and Fraunhofer diffraction models can be applied at z values defined by equations 6.11 and 6.12 respectively. At a particular z value the appropriate propagation method is chosen depending on this formula which for a square lens simplifies to $z < 2D_2/\lambda$, where D is the lens diameter. The Fresnel approximation is obtained by convolving the Fourier Transform of the phase profile with the Fourier transform of the kernel and taking the inverse Fourier Transform of the result. The Fraunhofer approximation is obtained by multiplying the phase profile by a phase factor, taking the Fourier Transform and then multiplying by a further phase factor. A flow diagram of the code algorithm is shown in Figure 6.4

The resolution of the structures simulated was varied depending on the nature of the effect being simulated. Where a variation in feature height was under investigation the matrix size need not be as large. Where any lateral feature dimension was under investigation as large a matrix as possible was used where a 4000 x 4000 matrix would require approximately 8 Gb of memory to run. Because there is a memory and processing time restriction some of the simulations have a degree of uncertainty introduced from pixelisation of the matrix. This is due to the inherent problem of simulating a round structure on a square grid. This becomes especially relevant when considering a change in the structure size that is smaller than the grid size. In trying to simulate a small change in the structure dimensions of a large object which is created on a grid it is desirable to use as large a matrix as possible. However decreasing the pixel size by half leads to an expansion of the matrix size by a factor of four. Because it is not feasible to create matrix sizes that would eliminate this problem the results of some simulations do not have perfectly smooth trends.

To illustrate this problem a small grid is shown in figure 6.5. On this grid is drawn

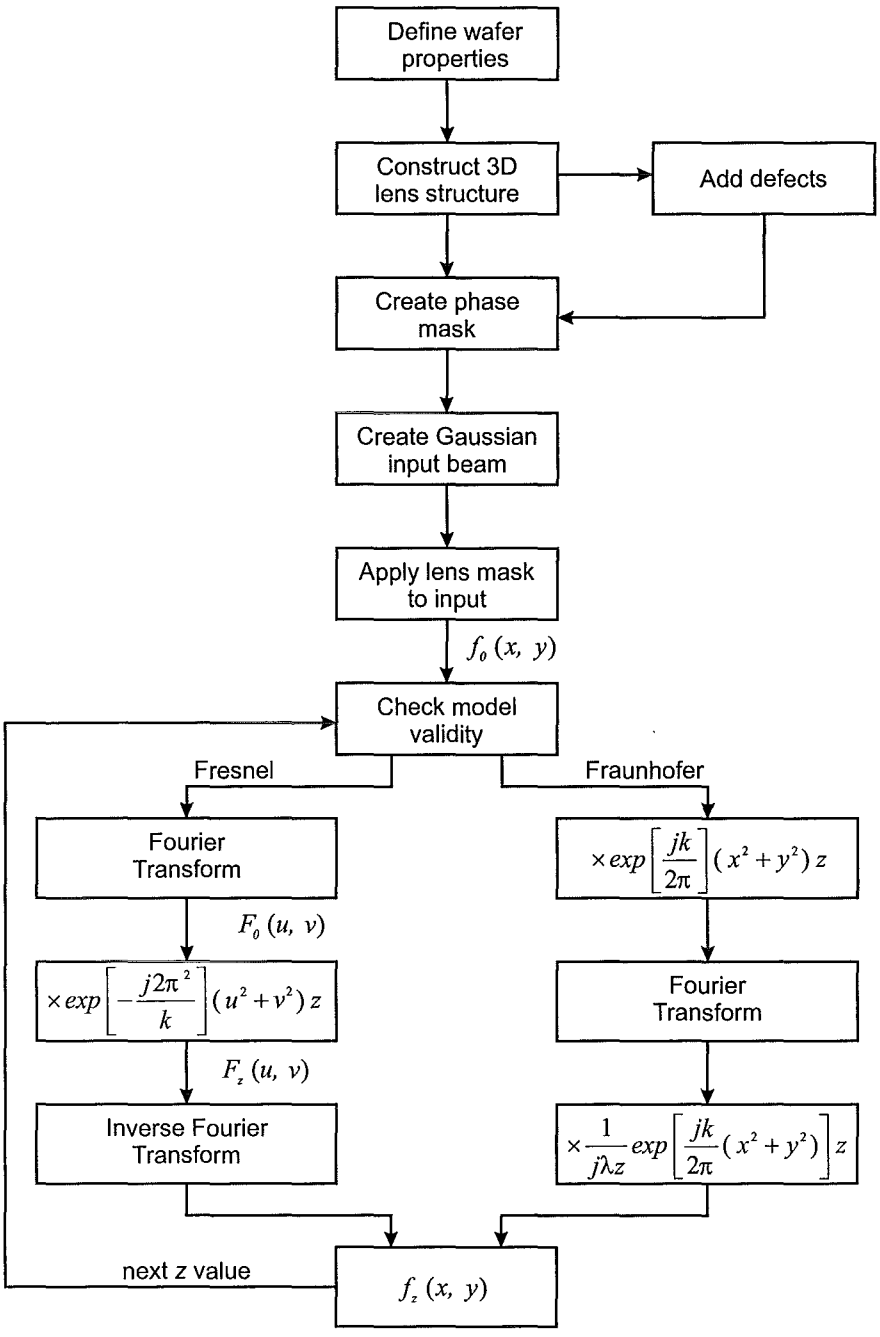

Figure 6.4 Algorithm used for the simulation of lenses with Fresnel and Fraunhofer propagation methods.

a set of rings that are increased in size progressively in quarter pixel increments. The different coloured grid crosses illustrate how the structure is then built up as a matrix in MATLAB.

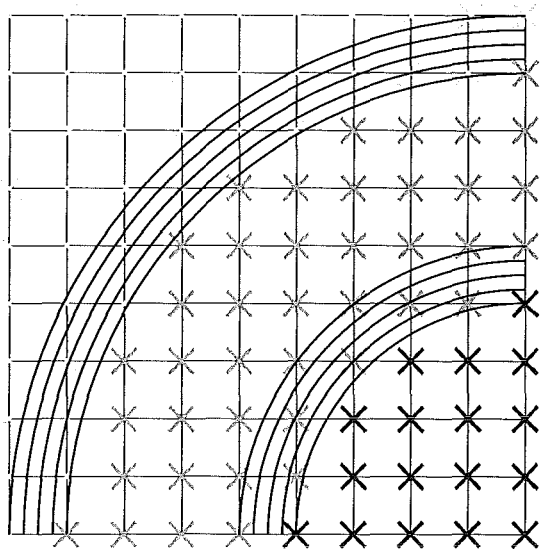

Figure 6.5 Formation of a circular structure on a square grid.

How the inability to create a grid that properly accounts for pixelisation errors can effect the trend of simulated results is illustrated with the following example. Figure 6.6 illustrates a lateral change in dimension as in a lateral etching problem. This shows a sub-pixel size shift in the dimension of two step boundaries. The two boundaries are increased in size progressively by one quarter of a pixel and the area of each step

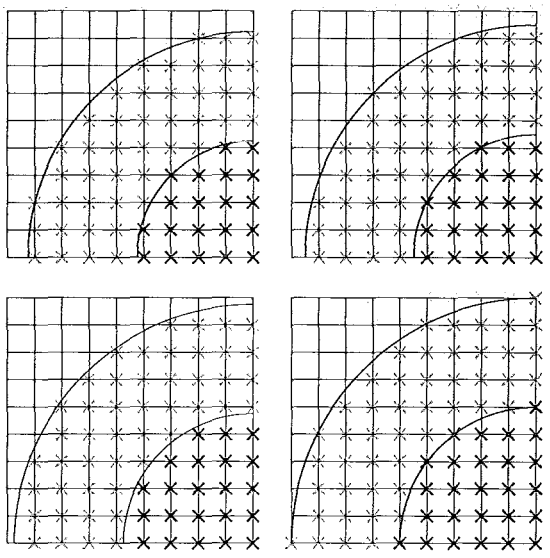

Figure 6.6 Distribution of pixels in a step as the boundaries are shifted in partial pixel increments.

measured. This area is determined by the number of pixels in each step.

Analysing the number of elements in each zone it can be seen that even though there is a linear change in the dimensions of the structure there can be a nonlinear change in the elements in each zone as shown in Figure 6.7. In fact it can be seen that at one point in this example the number of elements in the outer zone decreases slightly. There is a clear upwards trend in the pixel numbers, however this is not a smooth trend. The result of this could be improved or worsened depending on the choice of matrix size and on whether a particular pixel size and structure dimension works out favorably or not. This example shows how the choice of the array size is important and how sub grid size effects can still be simulated with a degree of error. In the simulations where lateral effects of surface details were of interest as small a pixel size as possible was used. This gave a grid spacing of 5% of the smallest feature size.

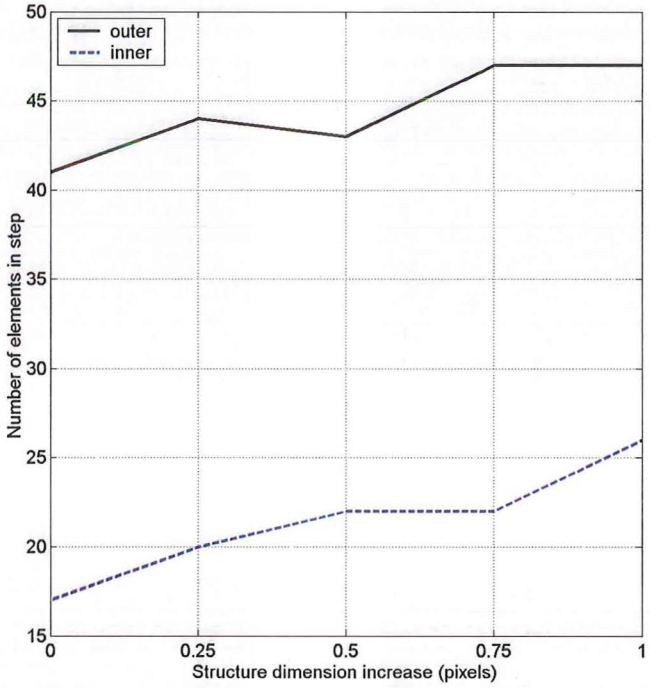

Figure 6.7 The effect of simulating a circular pattern on a square grid where a change in dimension is required can lead to error from the limited resolution available.

6.4 SIMULATION OF IDEAL MULTIPLE LEVEL DIFFRACTIVE OPTICS

This simulation technique was applied to the simulation of lenses for the determination of various structural effects. The lenses fabricated are simulated and compared to ideal structures which are then compared with the experimental data. A number of design

parameters are investigated to give an appreciation of the importance of lens sizes and other design parameters such as step dimensions. The following chapter provides a defect analysis showing the effects of processing variations on lens efficiency.

6.4.1 2, 4, 8, 16 level Lens Comparison

To illustrate the relative benefits of creating lenses with 2, 4, 8, and 16 levels a set of lenses were simulated as shown in Figure 6.8 which have total etch depths as shown in Table 6.1. These were like the lenses created and tested with a 30 mm diameter and a 25 mm focal length. To gauge the benefits of the different lenses as accurately as possible these structures were formed with the ideal etch depths and without the

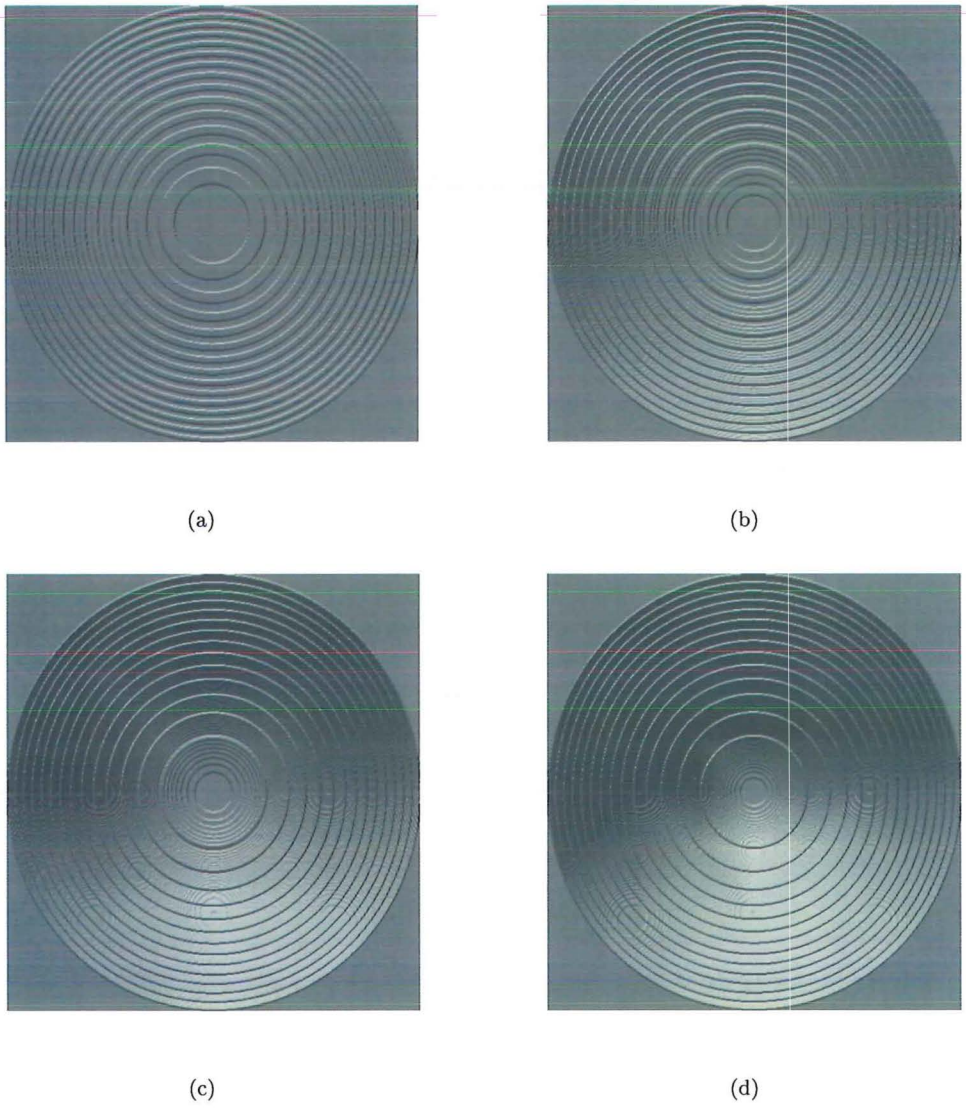

Figure 6.8 Ideal lens structures of increasing complexity (a) 2 level (b) 4 level (c) 8 level and (d) 16 level.

addition of any simulated processing defects. The performance of these lenses was assessed over a range of frequencies from 0 - 2 THz. From this it is possible to see how the focal point varies at different frequencies, the intensity and position of second order maxima, the variation in the FWHM and DOF.

Lens type	$\frac{L-1}{L}\frac{\lambda}{(n-1)}$ (μm)
2 level lens	62
4 level lens	93
8 level lens	108.5
16 level lens	116.2

Table 6.1 Etch depths for ideal binary lenses.

Figure 6.9 shows the relative intensity of the primary focus between 0 to 2 THz. The simulated results mirror the relative diffraction efficiency between lenses where it can be seen that there is only a very marginal gain (a maximum of 4%) from creating a 16 level lens. The additional cost of taking fabrication to this level may not be worth while.

The broadband intensity variation at positions between the lens and twice the

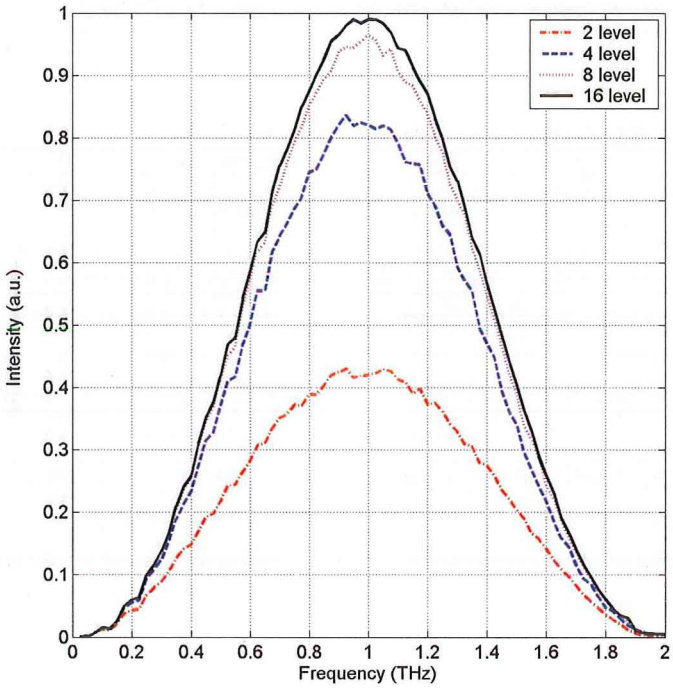

Figure 6.9 Intensity comparison in the primary focus (25 mm) between 1 - 2 THz for ideal 2, 4, 8 and 16 level lenses.

focal length for each lens is shown in figure 6.10. The position of the primary focus which shifts with frequency according to the formula $z_n = -\frac{r_p^2}{2(\lambda)n}, n = \pm 1, \pm 2, ...$ has identical position for each lens as would be expected. The intensity of this varies both with frequency and lens complexity. The position of the radiation from the higher diffracted orders shifts away from the lens with increased lens complexity. Radiation is focused most efficiently at the design frequency of 1 THz. These results indicate that there is a 2 THz bandwidth over which the diffractive optic should enhance the signal strength at the focus above the background intensity. The relative focusing ability of each lens is dependent on the diffraction efficiency of each lens, which is increased with step complexity according to $sinc^2(1/L)$ where L is the number of steps of the lens.

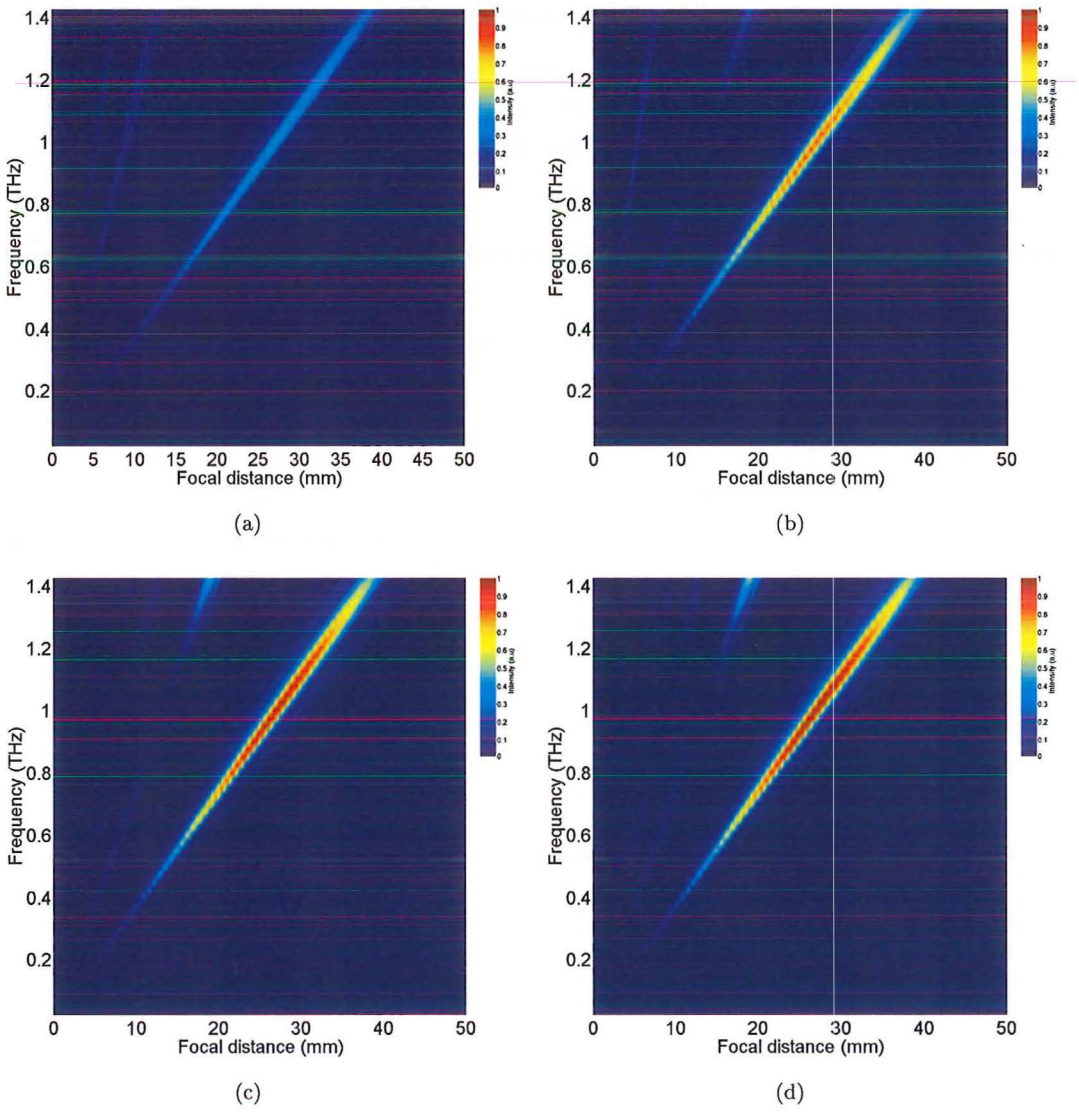

Figure 6.10 Spectral intensity distribution along the focal axis for 30 mm diameter lenses designed to have 25 mm focal length at f = 1 THz. Ideal lens structures of increasing complexity are compared (a) 2 level (b) 4 level (c) 8 level and (d) 16 level.

6.4.2 Discussion Against Experimental Results

The structures that were fabricated and tested as described in chapters 3 - 5 were also simulated, their form being constructed as accurately as possible in MATLAB. These differ from the lenses simulated in the previous section in that they each had a total depth of 124 μm and a difference in depth between the inner and outer zone of 5%. They also incorporate a linear blaze profile as per the mask design for these lenses. The simulated intensity between 0 - 1.4 THz is shown in Figure 6.11 for each lens with the measured result from the CCD measurements plotted to the right. Most noticible from these results is the fact that the primary focus remains in approximately the same position albeit with different intensity to the ideal structures simulated. However it is apparent that the intensity lost in the primary focus is instead focused into the higer diffractive orders. The simulated intensity map in this frequency region compares well with the measured results.

The simulated intensity of the primary focus for each lens is extracted and plotted in Figure 6.12. The difference in this plot and that of the ideal lens is primarily due to the etch depths used. The broadband intensity variation seen here is similar to that of the result shown in the following sensitivity analysis chapter investigating etch depth (section 7.2). Because the Fresnel lens is an inherently narrow band device it is expected to perform best at a particular wavelength determined by the depth of the structure. This is illustrated well in this result where the deeper than optimal etch depths shift the frequency where each lens is expected to perform optimally to a lower frequency. Interestingly the 8 level lens has a similar predicted intensity at 1 THz to the ideal structure. As was observed in the measured results, the 2 level lens, which suffers most at 1 THz from having a 124 μm etch depth acts as a notch filter. The simulations actually indicate that this lens performed better than expected which may be due to non-uniform etching of the substrate. Such behavior forms another potential application for diffractive optic lenses.

The measured and simulated 1 THz intensities are compared in table 6.2. These compare quite well although the simulated results indicate a higher relative efficiency of the 8 level lens than measured. It is expected that this is due to the resist removal and lithography problems that were present in the 8 level lens. From these results it would be expected that with lenses of these structural dimensions the 8 level lens should have had an additional 10% more power in the focus. This further highlights the problems in creating higher complexity optics indicating how a 16 level lens may yield little benefit.

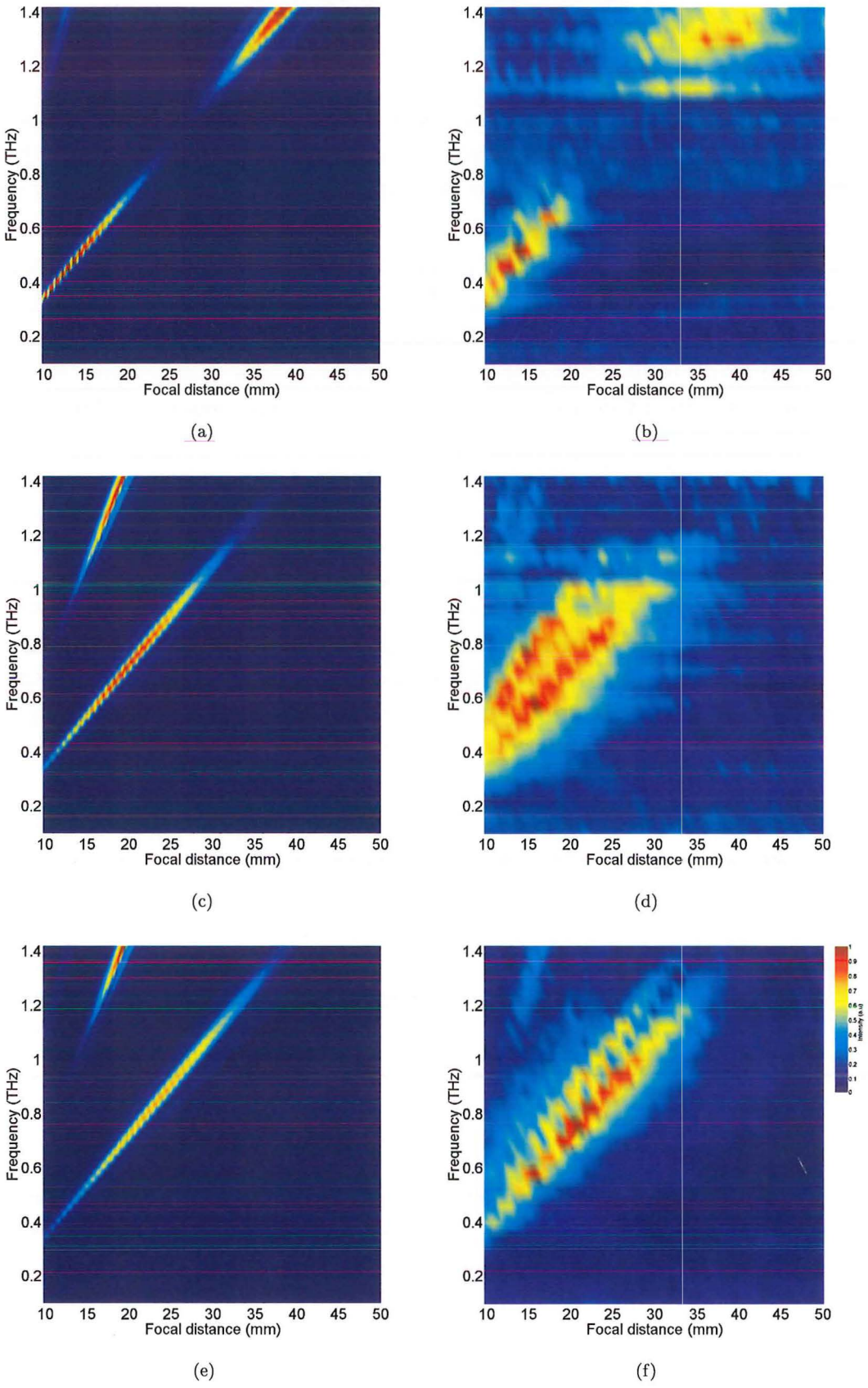

Figure 6.11 Comparison of simulated and measured broadband results, (a) simulated 2 level (b) measured 2 level (c) simulated 4 level (d) measured 4 level (e) simulated 8 level and (f) measured 8 level.

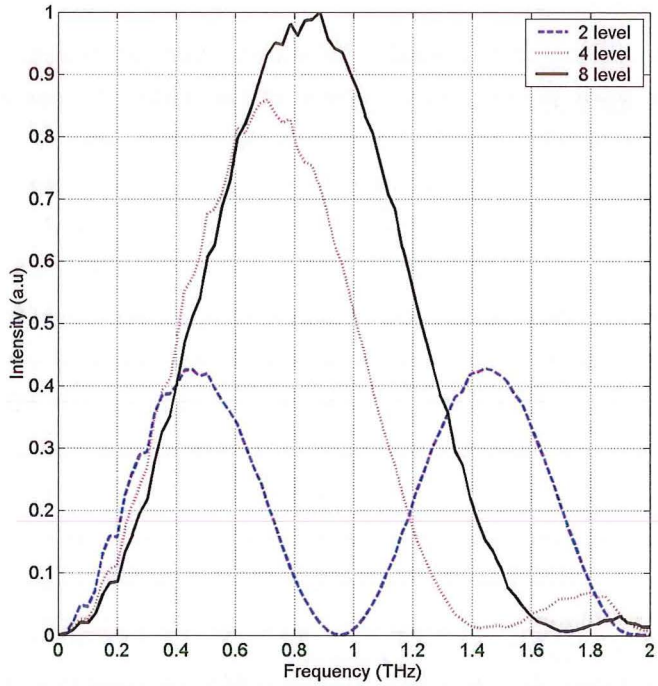

Figure 6.12 Expected performance in the primary focus between 1 - 2 THz for the 2, 4, 8 level lenses fabricated.

Lens	Relative measured peak intensity	Relative simulated peak intensity
2 level lens	0.2	0.01
4 level lens	0.75	0.60
8 level lens	1	1

Table 6.2 Theoretical versus experimental lens diffraction efficiencies.

6.4.3 Design issues

As this process has been designed to be applicable to the formation of a wide range of terahertz lenses it is important to look at certain design issues to give a guideline of the expected performance. Lenses designed for different frequencies or focal lengths result in a diverse range of feature sizes and hence the number of zones that will fit on a set wafer size. This is investigated and some design methods that can be employed to help boost lens efficiency are given.

6.4.3.1 Focal length

In an optics system there will generally be a restriction on the size of the lens. As far as a diffractive optic is concerned the size of the wafer, D, has a direct influence on the number of zones that can fit for a given focal distance, f. As the F number increases, where $F_{\#} = f/D$, for a fixed lens size the number of zones on the wafer goes down. This is because the required angle of diffraction is reduced and to achieve this the zone widths have to be greater. This leads to a drop off in efficiency and ultimately places a restriction on the viable focal distance of a Fresnel lens for a set lens size. To investigate this a range of lenses of equal area were simulated with focal distances between 25 and 225 mm, the results of which are shown in Figures 6.13, 6.14 and 6.15. These focal distances are based around the 125 mm lens that has been designed and constructed since the original lens set. Each lens was created on a 46 mm^2 wafer as per this design. A Gaussian beam was propagated through this so the effect on focal intensity, DOF and FWHM from a changing NA could be investigated.

Figure 6.13 shows how the focal spot intensity is at a maximum around where the lens has a $F_{\#}$ of 1. Where the $F_{\#} < 1$ the intensity goes down as it becomes increasingly difficult to diffract the radiation to such a sharp angle. However it is easier to create high NA diffractive lenses than refractive lenses because of the large curvature that becomes necessary for a short focal length refractive lens. Where the $F_{\#} > 1$, the

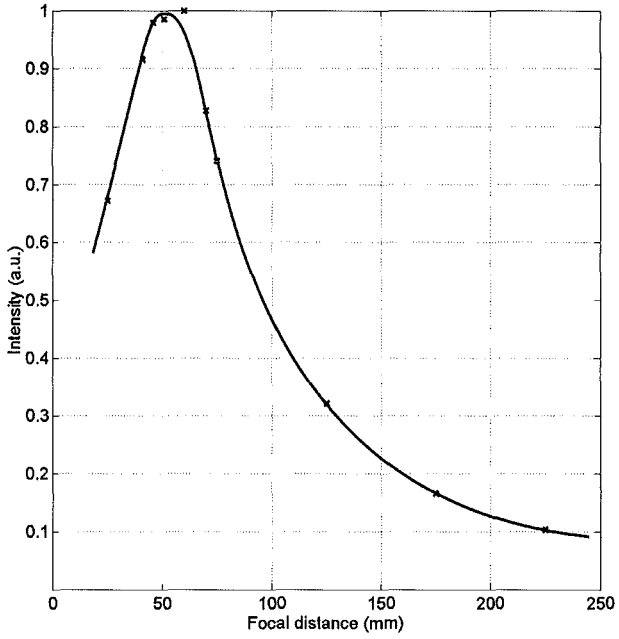

Figure 6.13 Change in the focal point intensity from Fresnel lenses of different focal distance created on a fixed size wafer.

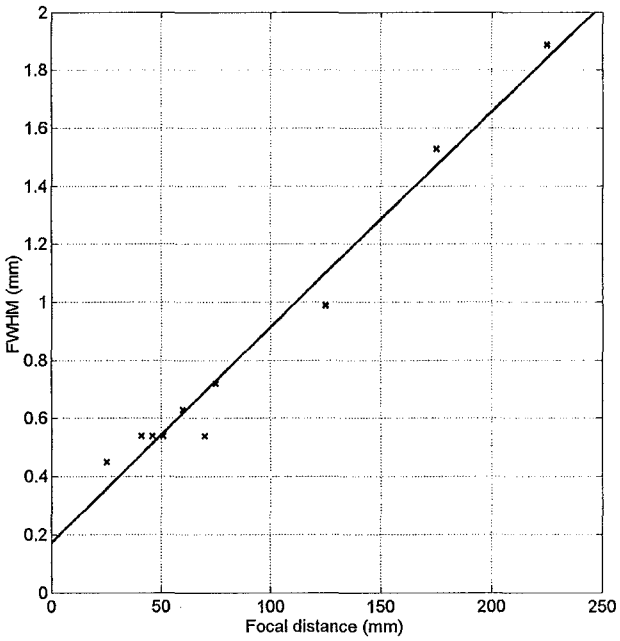

Figure 6.14 Change in the FWHM from Fresnel lenses of different focal distance created on a fixed size wafer.

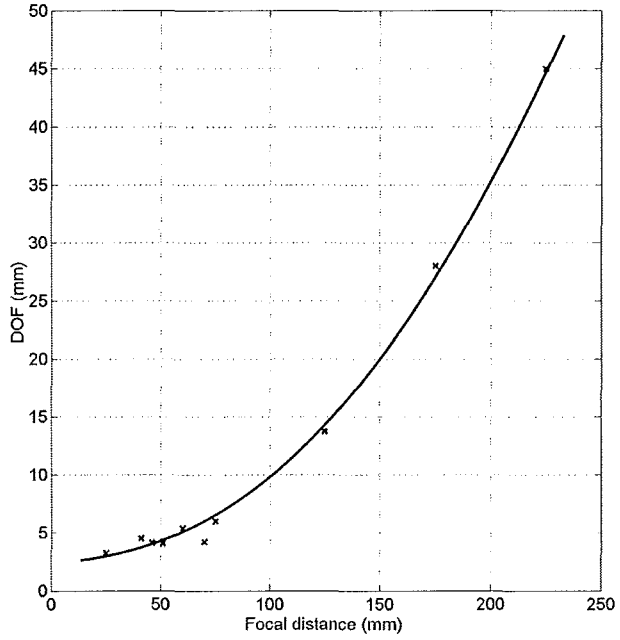

Figure 6.15 Change in the DOF from Fresnel lenses of different focal distance created on a fixed size wafer.

intensity also goes down. As the focal length is increased the number of zones that can fit on the wafer goes down and as a result the focusing power of the lens which relies on the constructive interference of delayed wavefronts is reduced. The decrease in the intensity is coupled with a linear increase in the FWHM and a parabolic increase in the DOF as shown in Figures 6.14 and 6.15. This is due to the large size zone widths and the increasingly shallower diffraction angle. These two components mean the radiation from each zone is dispersed over a large z area.

6.4.3.2 Step dimensions

When designing a Fresnel lens the lateral dimension of each zone is easily determined with simple formulae such that the distance from each zone edge to the focus is a single wavelength different. Following the determination of the full zone widths the dimensions of the steps for each zone need to be calculated.

The simplest method of delineating these steps is to construct a linear blaze such that each step in a given zone is the same width. Practically this is not optimal as a diffractive optic represents a compact version of a refractive lens which has a curved not faceted surface, as shown in Figure 6.16. Hence it is better to create the step widths such that they follow a curved profile. To analyse the benefit of curved profile zones the broadband focal intensity of an 8 level lens with a curved and linear profile are compared in Figure 6.17.

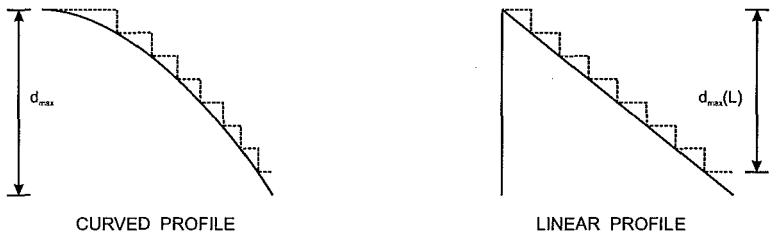

Figure 6.16 Step dimensions determine whether a linear or curved profile is approximated.

A gain in efficiency of nearly 10% can be achieved by using a curved instead of a linear blazed profile. The difference in the step widths between the two designs is most noticable in the largest zones. Because of this, long focal length lenses will be more susceptible to efficiency degradation from a non-optimised zone blaze.

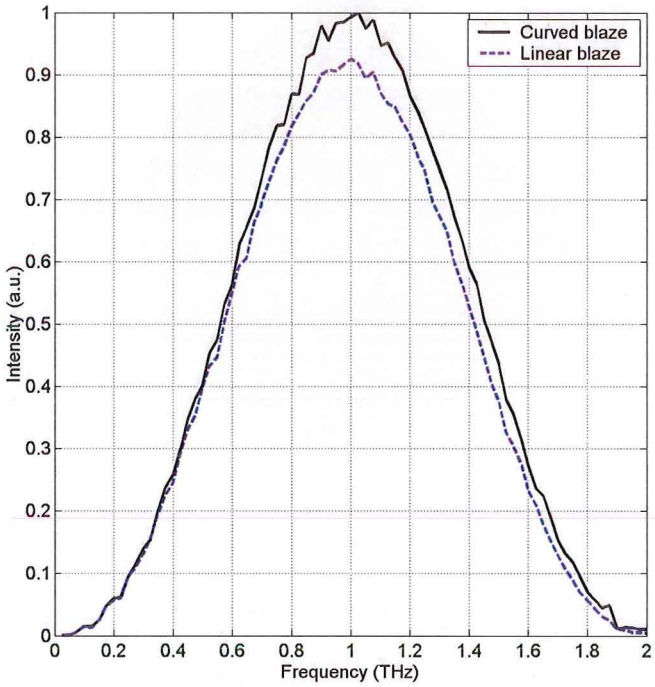

Figure 6.17 Comparison of the broadband focal intensity of an 8 level lens with a curved and linear step profile.

6.4.3.3 Square vs round lens

As the wafers on which the lenses are fabricated are square, it is of no additional expense and only marginally more difficult to fabricate zones across the whole wafer. The lens efficiency can then be boosted without making the wafer larger, expanding the beam to illuminate the whole square and to structure the lens to the corners. Clearly doing this some signal strength is lost and there is a trade off between improved quality and signal strength. These simulations show the benefits of using this for improved focusing. This fabrication enhancement was investigated using a lens with a focal distance of 125 mm. The structures used in the simulation are shown in Figure 6.18 and 6.19 for both a round and square design.

It would be expected that through using a square lens which effectively is a trimmed larger wafer lens that similar benefits would be gained. Using a square design gives an improvement in all aspects of focusing with a 40% increase in the intensity. The difference in the peak intensity down the z axis is shown for each lens in Figure 6.20. The square lens has a reduced DOF and FWHM which is as expected with the smaller dimension of the extra partial zones. A summary of the improvements achieved with this design modification are shown in table 6.3.

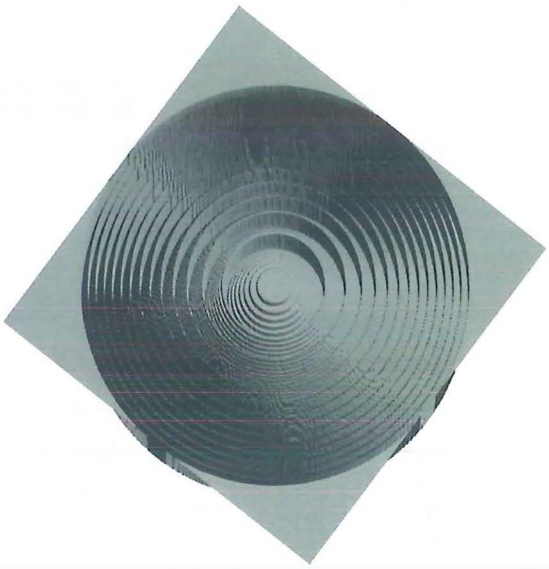

Figure 6.18 Round lens.

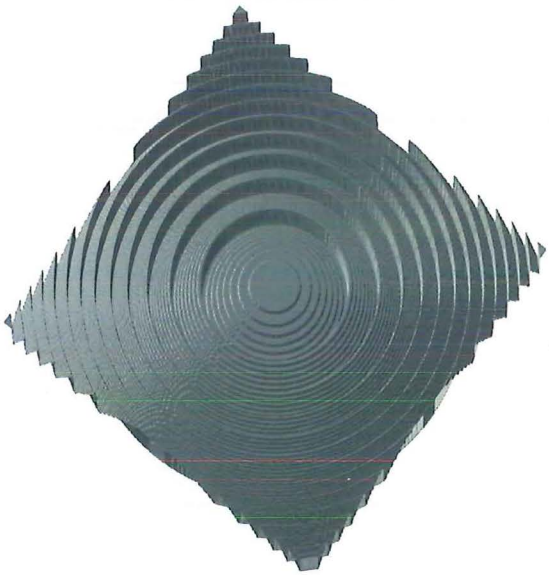

Figure 6.19 Square lens.

Lens	Intensity (a.u.)	DOF (mm)	FWHM (μm)	Smallest feature dimension (μm)
Round lens	0.71	20	584	208
Square lens	1	13.7	494	154

Table 6.3 Comparison of round and square lens design focusing attributes.

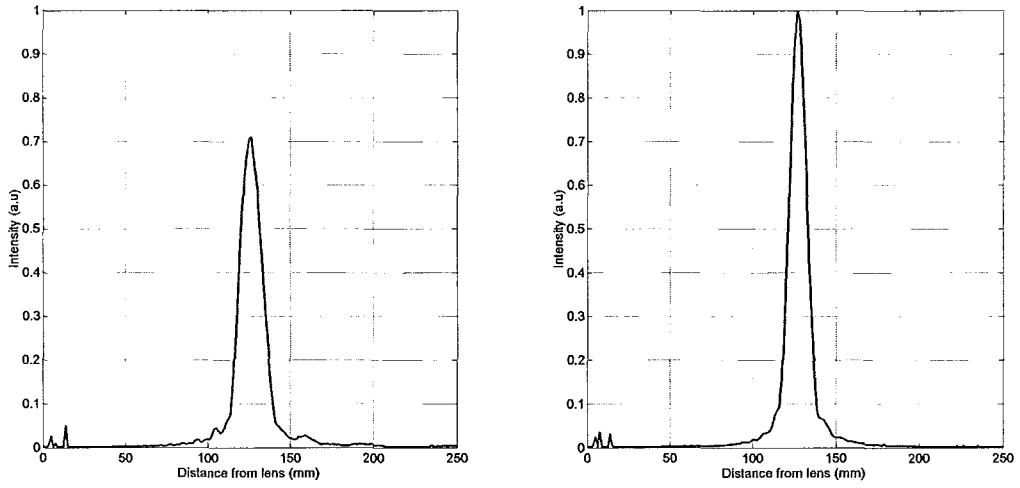

(a) (b)

Figure 6.20 Comparison of the intensity down the z axis for (a) a round lens and (b) a square lens.

6.5 SUMMARY

This chapter has introduced a simulation technique that can determine the broadband focusing ability of a three dimensional lens structure. This was achieved using Fraunhoffer wave propagation using Fourier transforms of phase profiles to determine the intensity of radiation at points beyond the lens. Using this technique the prototype lenses tested were simulated which explains some of the intensity patterns observed. Several design issues were explored and their influence on the focusing ability presented to give an appreciation of how the efficiency of a lens can be maximised. This simulation technique is used in the following chapter to analyse how processing defects can affect lens efficiencies.

Chapter 7

SENSITIVITY ANALYSIS

7.1 INTRODUCTION

In conducting a sensitivity analysis it is important to determine whether the extent to which a particular processing defect may be present will have a marked influence on the efficiency of a lens. Because this process has been designed to work for a broad range of lens designs in the terahertz frequency band, a general set of bounds below which an aberration has become significant enough to drop the efficiency markedly is invaluable. This section explores the major defects that may be present in the multiple level fabrication technique. It is important to be aware of the point at which a defect from multiple level processing may negate the value in performing an additional level of complexity. This chapter aims to determine these bounds with emphasis placed on the fabrication of an eight level lens which yields a high efficiency gain for the level of processing complexity.

There are many components to the fabrication process that can lead to a resulting drop off in efficiency. During the lithographic stages masks can be misaligned causing the formation of additional peaks and trenches. Reactive ion etching (RIE) can introduce a number of problems with issues involving etch depth control, surface roughness, lateral etching and non uniform etching. Clearly in setting an absolute bound for each of these, one is assuming that all other possible errors are not present. Realistically, when processing, the bounds need to be considerably tighter to take into consideration the combined effect of all inaccuracies.

There are ways to mitigate the effects of processing defects. Through modification of the processing parameters to optimize for a certain defect, efficiencies can be optimised. It is also possible to practically eliminate some defects through analysis of the process and subsequently using adaptive mask design to compensate for the error. The process design revolves around trying to gain an optimal result where no particular stage of that process will be perfect. Through analyising the different errors it is possible to determine which can be a cause of most performance degradation and which will be of little or no consequence. This is primarily with respect to the RIE process which

requires a compromise between etch rate, lateral etch control and surface roughness. Poor surface roughness can also have a secondary effect of making the later alignment stages difficult due to the light absorbing nature of a rough silicon surface. Some of the effects investigated are components of the machinery and as such the efficiency drop off would be the same in a lens of any complexity. Where relevant the effect of a defect on different complexity lenses is illustrated.

The simulation methods described in Chapter 6 have been used to perform a series of sensitivity analyses. In these analyses the main determination of relative efficiency is performed with the peak intensity at the design frequency. The effects on the depth of focus, full width half maximum and focal spot position are not as pronounced. The effect of incorrect, and non-uniform etch depths is first investigated combined with a determination of how to maximize the efficiency when non-uniform etching is present. How lateral etching influences the lens profile and efficiency is then shown, illustrating how the order in which the levels are constructed is important. The final etching error investigated is the effect of surface roughness. Misalignment of masks during photolithography is another potential source of error which is discussed in the final section.

7.2 ETCH DEPTH

The functionality of the lenses revolves around manipulating the phase of waves passing through them. Through exploiting the fact that electromagnetic radiation travels at different speeds in different media one can change the exiting phases through structuring the lens surface. In the design of a Fresnel lens it is desirable to create a well defined phase shift profile in the surface. The differing phases and the placement of the etched features create the diffracting structure that in this case focuses radiation to a point. In the case of a Fresnel lens the ideal structure has a perfect blaze with a π phase shift at the zone edges instead of a stepped relief. In this fashion the exiting phase of the radiation at any point in the optic is such that it will interfere constructively at the focus. The path length of the radiation from successive zones to the focus is delayed by an additional wavelength from the zone next closest to the centre.

The process detailed in Chapter 3 describes the binary fabrication process used. This technique approximates the ideal blazed structure using a series of steps. The number of steps used is dependent on the required efficiency and the structuring complexity attainable with the fabrication equipment. It is therefore important to analyse how different complexity optics react to variations in etch depth. Fluctuations in etch rate can lead to incorrect etch depths. Although depths can be monitored and etch rates maintained the corresponding expense of these tasks can also be great. These simulations give insight into the accuracy that may be required for different complexity structures. They also show the optimal etch depth for a given complexity and illustrate

the relative sensitivity to incorrect etch depths of the respective structures.

The initial set of lenses used a full π phase shift or 124 μm as the etch depth for each lens complexity. The simulation results illustrate the relative expected efficiency of different lens complexity for a range of etch depths from 0 to 2 times the π phase shift, and the results are shown in Figure 7.1 for 2-, 4-, and 8-level lenses of 30 mm diameter and 25 mm focal length operating at 1 THz.

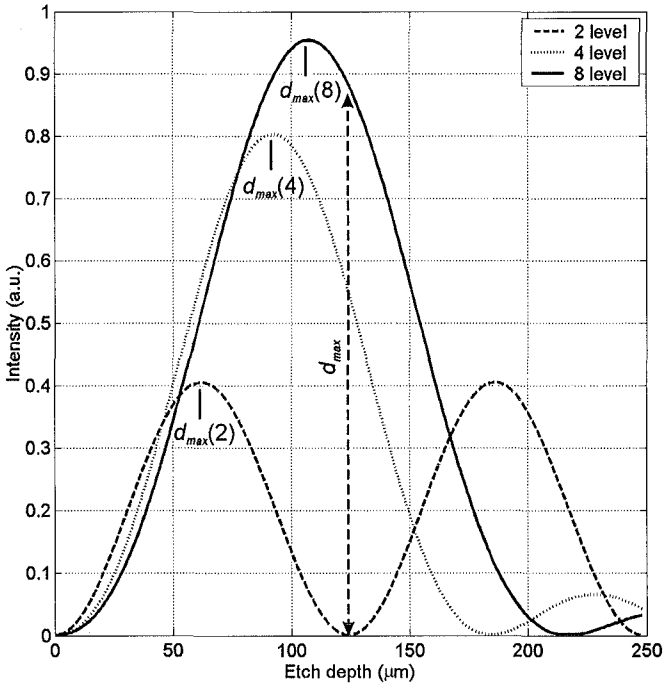

Figure 7.1 Optimal etch depth and the tolerance to etch depth error varies with lens complexity.

These simulations show that lenses of different complexity have different ideal etch depths for maximum intensity. The maximum depth d_{max}, of an ideal or non-stepped blaze would be

$$d_{max} = \frac{\lambda}{(n-1)} \tag{7.1}$$

where n corresponds to the refractive index, which for silicon at 1 THz is 3.42, meaning a 124 μm total depth is required for a perfect blaze. For a binary optic with L levels the optimal etch depth relates to a fraction of this depth according to

$$d_{max}(L) = \frac{L-1}{L}\frac{\lambda}{(n-1)} \tag{7.2}$$

These optimal etch depths are highlighted in table 7.1 alongside the optimal etch depths

extracted from the Fraunhofer simulations. The stepped representation of a blaze is illustrated in Figure 7.2.

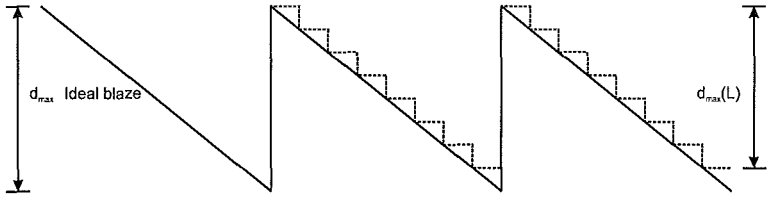

Figure 7.2 Total depth of a stepped approximation is a fraction of an ideal blaze.

Lens type	$\frac{L-1}{L}\frac{\lambda}{(n-1)}$ (μm)	Fraunhoffer approximation (μm)
2 level lens	62	62
4 level lens	93	92.4
8 level lens	108.5	107.3

Table 7.1 Optimal etch depths for binary lenses of different complexity

The expected relative maximum efficiency of the different lenses is extracted from Figure 7.1 in Table 7.2. This table explains the differing intensity values of the experimental structures well. All the etched structures had a total etch depth of 124 μm and comparing this to the simulated data it can be seen that this non ideal depth becomes less critical for the 4 and 8 level structures. The projected drop-off in intensity is shown in Table 7.2. The relatively poor experimental performance of the 2 level lens is explained by this result in that it would hardly be expected to work at all. The fact that the etching is non uniform across the wafer and this depth corresponds to the centre depth only will account for the non-zero performance of the 2-level lens.

Lens type	theoretical maximum efficiency	expected efficiency of structure with 124 μm total depth
2 level lens	41	0
4 level lens	81	55
8 level lens	95	89

Table 7.2 Expected efficiency of a structure etched to 124 μm.

Figure 7.1 also shows how the tolerance to etch depth variation becomes higher for more complex structures. The drop in intensity from the theoretical maximum for each optic from a range of incorrect etch depths is shown in Table 7.3. Here the effect of a ± 5, ± 10 and ± 20 μm etch depth error can be seen and it is clear that the efficiency for the 8-level lens is much less sensitive to etch depth errors than the others. For example

a $\pm 10\mu m$ etch depth error, corresponding to an etch rate error of approximately 10% results in less than 3% drop in efficiency.

Lens type	$\pm 5\mu m$	$\pm 10\mu m$	$\pm 20\mu m$
2 level lens	1.6%	6.2%	23.2%
4 level lens	0.9%	3.5%	13.5%
8 level lens	0.7%	2.7%	10.5%

Table 7.3 Tolerance to incorrect etch depth indicating percentage drop from maximum efficiency.

With the current etch equipment the only practical method of obtaining etch depths is through determining an etch rate and from that etching for the required time. This still enables a structure to be etched to over 100 μm with accuracy to within a micron. More technical methods are available such as laser depth monitoring that could enable etching to the exact required depth, however this is probably an unnecessary expense. Looking at the intensity plots for each different complexity lens it can be seen that when aiming for the correct etch depth, straying either side of that etch depth by even several microns will not have a marked effect on the efficiency of the optic. For the fabrication process outlined in Chapter 3 the etch depth could be controlled to within a micron, and so the expected efficiency reduction is less than 1% for all lenses.

7.3 ETCH UNIFORMITY

The etch rate across a reactive ion etcher electrode is not uniform. This is due to the plasma chemistry where different concentrations of reactive species are available in different areas of the electrode. The plasma density will be higher at points closer to the RF power coil or heating source which in part accounts for the increased etch rate at the periphery of the wafer. This is also due to the loading of the sample at the centre resulting in a relative increase in the ions available at the edges [162]. This effect is often described as macro-loading and will also be influenced by the reaction of species with the electrode. The greater concentration of species leads to an increased etch rate which results in a non-uniform etch rate with an outward slope. Increased diffusion of the reactive species in the plasma can be achieved by operating at lower pressures leading to greater uniformity.

For a diffractive optic lens a non uniform etch rate will lower the efficiency as the diffraction efficiency will become progressively worse as the depth becomes more skewed. Some etch chemistries may be more susceptible than others to this effect as the etch process is a part-chemical, part-physical process. In determining an etch process for a particular purpose the parameters are changed to alter the prominence of a certain etch component. The chemistry used in the lens fabrication was particularly structured

to give a high etch rate while attempting to preserve straight sidewalls, smooth surfaces and resist integrity.

Irrespective of the lens complexity this effect will be detrimental. It is of interest to analyse the effects of non-uniform etching on lenses of different complexities. As less complex lenses are less tolerant to errors in etch depth control, this so called bulls-eye effect should drop the efficiency in these structures more.

The effect of a worsening bullseye etch problem is shown in figures 7.3 and 7.4. For these simulations the centre zone was kept at the optimum etch depth for the respective lenses, Table 7.1, with the centre to edge depth varied from 0 to 35% of this value. As the problem worsens the etch depths at the outer regions become significantly skewed from the ideal value and the energy gets focused into the second order maxima. This is illustrated in Figure 7.3 which shows the effect of an etch depth differential of up to 35% between the outer and inner zone for an 8-level lens. At a 35% differential there is 18% of the radiation focused into the second order maximum, whereas for an ideal structure this is zero.

Figure 7.4 shows the effects on lenses of lesser complexity where the normalised intensity maxima at the focal point are compared. This figure shows how the more complex lenses have a higher tolerance to the bullseye effect. Using this etcher a difference of up to 26% between the centre and the edge has been observed over a 45 mm^2 sample where a loss in efficiency of almost 10% can be expected. All lenses have a similar drop off in intensity once edge to centre disparity becomes large.

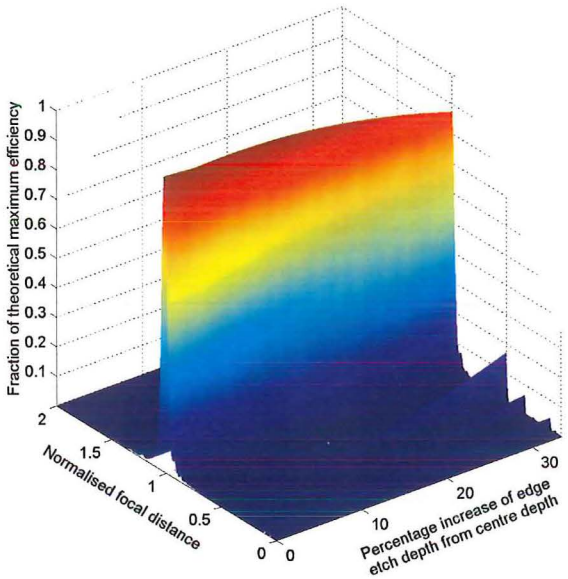

Figure 7.3 The effect on efficiency of non-uniform etching at positions beyond an 8 level lens.

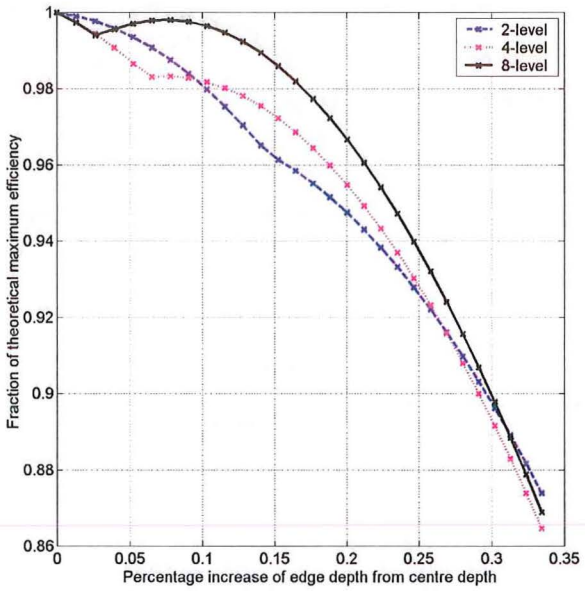

Figure 7.4 Comparison of the bullseye effect at the focal point of a 2-, 4-, and 8- level lens.

Because this effect is something that is inherent in the etch process it is not possible to avoid. However it is possible to optimise the structure taking into consideration this effect. As the etch rate has been observed to vary by 26% from the centre to the outside it is no longer sensible to etch to the optimum target depth of 108 μm at the centre for an 8-level lens. The centre target depth needs to be less than this with the depth of 108 μm being at some mid-point between the center and the outer ring. Through taking the measured etch slope and shifting the etch depth through a range of values the optimum etch target can be determined. Figure 7.5 shows the effects of changing the etch depth at the centre or edge zone on the lens efficiency when there is a bullseye effect with a differential in the etch depths between centre and outside set at 26%. This was the difference measured using the etching process descried in chapter 3. The depths required for a 2-, 4-, and 8-level lens to obtain maximum efficiency in the presence of this effect are shown in Table 7.4. With this stuctural compensation efficiency gains shown in Table 7.5 are attained.

By using these etch depths the efficiency is maximised and the etch depth requirements are lowered. Each lens has a centre target depth of nearly 15% less than that required to etch to the theoretical depth. The efficiency gain from using these depths is 5, 7 and 8% for the 2-, 4-, and 8-level lens respectively. This results in an expected reduction in efficiency of only 2% for an 8-level lens in the presence of 26% etch non-uniformity. The effects on the FWHM and DOF were also studied however no measureable changes were apparent.

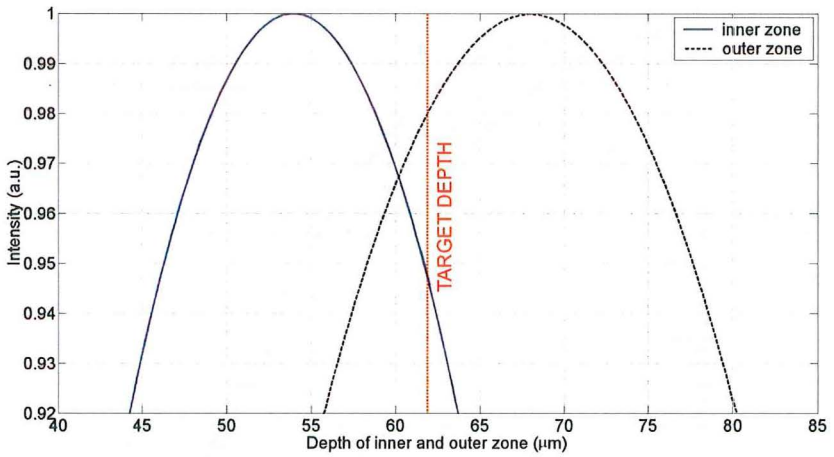

(a)

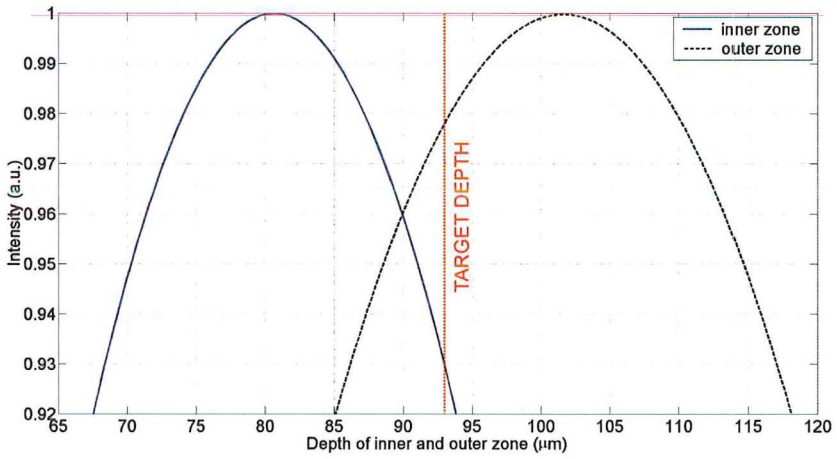

(b)

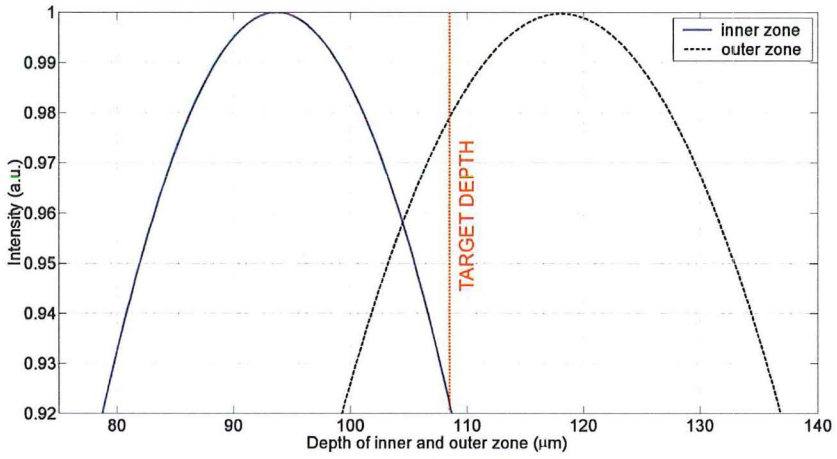

(c)

Figure 7.5 Optimised etch depths of binary lenses when a bullseye effect with a 26% differential between inner and outer zone is present in etching for (a) a 2 level lens (b) a 4 level lens and (c) an 8 level lens.

Lens type	inner zone depth (μm)	outer zone depth (μm)
2 level lens	54.1	68.1
4 level lens	80.7	101.7
8 level lens	93.7	118.1

Table 7.4 Etch depth requirements at inner and outer zone for optimal efficiency in the presence of a 26% inner to outer etch differential.

Lens type	Efficiency gain from modified etch depth	Efficiency loss from ideal structure
2 level lens	5.3%	4%
4 level lens	7%	3%
8 level lens	8%	2%

Table 7.5 Efficiency gain achieved by choosing an etch depth that compensates for the bullseye effect.

7.4 LATERAL ETCHING

The majority of etching processes have a desired preferential etch direction. Etch conditions are created such that etching ensues at the maximum rate in the direction wanted whist minimizing any other etching. This is important for maintaining structural dimensions and for minimizing unwanted sidewall profiles. However there is always some inherent etching in the unwanted directions. In the case of binary optic lens fabrication unwanted lateral etching can cause two different problems.

Firstly, if features are over etched in the lateral dimension, when subsequent lithography stages are performed the mask alignment becomes more difficult. Also the undesired structure sizes can cause problems during photolithography where light may then enter areas that it would not otherwise, causing resulting reflections and exposure that will reduce the resolution achievable. This is effectively an additional problem resulting in a secondary form of efficiency loss.

The main problem from lateral etching however is the fact that the structure is altered. This not only leads to the broadening of feature dimensions but can also lead to the formation of unwanted structure features. This section aims to highlight how two different forms of binary optic fabrication are effected by lateral etching. Observing Figure 7.6 it is possible to see how the order in which a multilevel etch process is conducted significantly changes the effect on the structure from lateral etching.

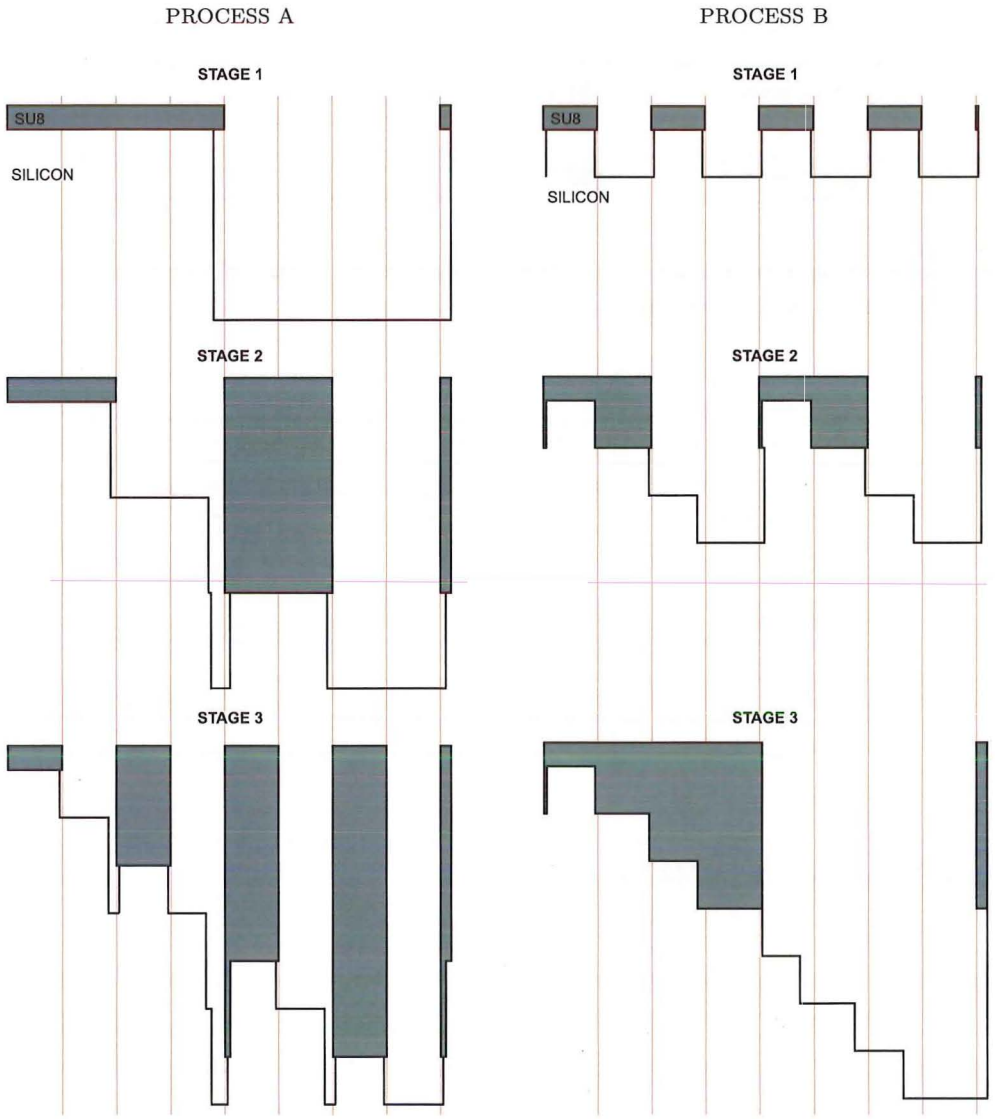

Figure 7.6 Lateral etching effect on structure of different ordered binary processing techniques illustrating deviation from the mask at each stage of the process.

For a given process there will be an etch rate in the lateral dimension as there is in the vertical direction. This means the duration of an etch determines the degree of lateral etching in each stage of etching. The way the resist lies on a laterally etched structure during later stages of the process can correct lateral errors of previous stages. Observing the structural change it can be seen that the process where the small features are etched first leads to a structure that although better preserves the overall profile has a larger lateral change overall. To delineate these two processes consider the process where the large etch is performed first to be Process A and the process where the fine features are etched first as Process B (Figure 7.6). As far as the lithography and etching are concerned there are benefits in each method that could benefit a certain set of fabrication equipment or prove preferential for certain feature sizes. Performing

the longest etch first can be beneficial if the overall depth is high while etching fine features into a deep resist/silicon trench can also be an issue.

These structures were both simulated with differing degrees of lateral etching so the degree to which the efficiency of the respective structures is effected could be observed. This was performed over a range of lateral etching from 0 to 35 μm.

Simulations of lateral etching and the effect on the focal point intensity for both processes are shown in Figure 7.7 for an 8-level lens etched to 108 μm (no bull's eye effect). The most significant observation of the results from this simulation is how high the tolerance to lateral etching is for both processes. Process A loses approximately 10% efficiency for every 0.5 lateral etch rate/vertical etch ratio. Comparatively Process B will only loose about 2.5% for the equivalent lateral etch ratio. The reason for the better performance of process B is due to the self preserving nature of the stepped structure in the presence of lateral etching. This result indicates that significant lateral etching can take place without markedly impairing the efficiency of the structure. This ignores any secondary effects from the unwanted etching such as lithography issues which may exacerbate the problem. The magnitude of such secondary effects would be difficult to quantify.

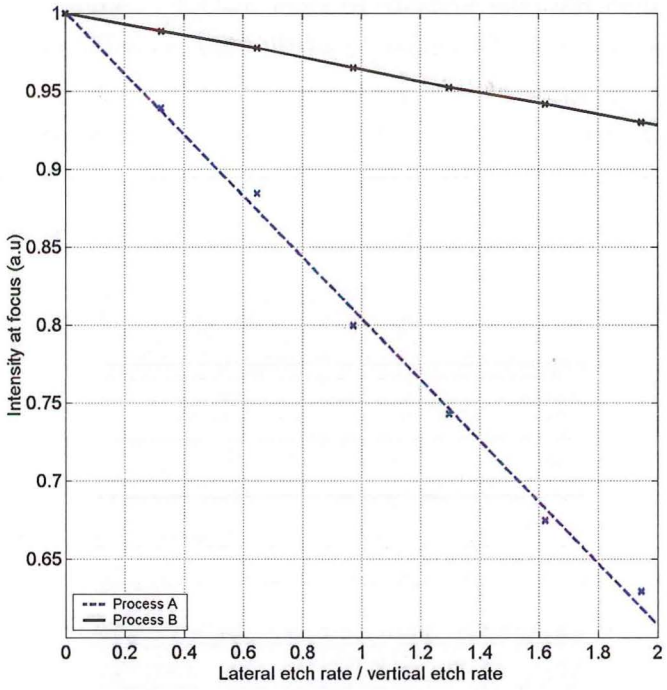

Figure 7.7 Effect of lateral etching on efficiency of Process A and Process B.

Clearly process B is more tolerant to the effects of lateral etching and if this process-

ing defect was significant in a given process then this scheme of multi-level fabrication is preferable. However, most reactive ion etching processes should not have lateral etching of this magnitude, so either scheme should perform suitably. The issue could be circumvented by using a mask which accommodated for the lateral etching. Such a mask would require smaller band features than the ideal design as, seeing that SU8 is a negative resist, this will create larger lateral dimension features.

7.5 SURFACE ROUGHNESS

There are several mechanisms in which surface roughness can occur in reactive ion etching. Firstly the randomness of the etch process can lead to roughness where certain areas etch slightly faster than others. This can then propagate further as the etch continues because uneven surfaces can form areas of increased reactivity through their increased surface area. This is probably the lesser of the contributing factors to roughness. The most prominent problem arises from micromasking. This can arise from two distinct contributing factors. Firstly material can be sputtered from the resist etch mask or from the electrode onto the surface of the etched area. This material can be hard to remove and can even adhere to the surface after it settles to form micro masks. Oxygen introduced to the etch mixture to form $Si_xO_yF_z$ compounds for lateral etch prevention can also result in the oxidation of the silicon on the surface. The current process has been designed to reduce the effect of this as much as possible however it is another cause of surface roughness that needs to be considered. Figure 7.8 shows how surface roughness features can form randomly on the surface. These have been observed to grow up to 20 μm in height forming larger pyramidal structures.

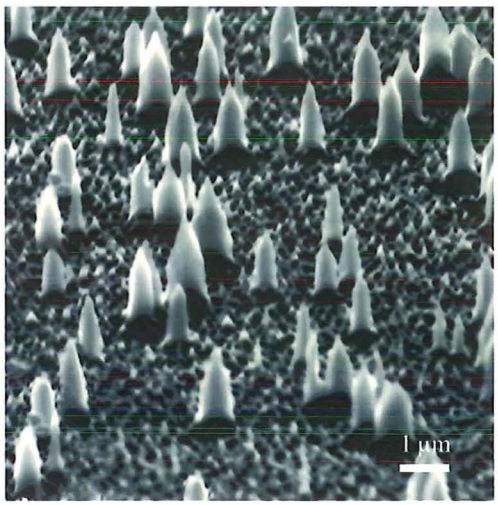

Figure 7.8 Typical formation of surface roughness is from micromasks which can form at any time during the etch in random locations.

When investigating what is a tolerable surface roughness, one must first consider the wavelength of the radiation under consideration. A feature that is less than one tenth of the size of the wavelength should be virtually invisible to the radiation. However discontinuities of this order will still change the depths and hence the outgoing phase of the wavefronts passing through the lens. This may not be as simple as analysing the structure with localized incorrect etch depths. The nature of the silicon pillars are such that they will form an artificial dielectric at the interface between silicon and air. Hence the out going phase error of the wavefront at a given point may be determined from the effective dielectric of silicon and air of a certain ratio.

In this analysis a pixel size of 50 μm was chosen and this pixel size determines the size of the micromasks. This size was selected as it is larger than one tenth of the wavelength under consideration and is therefore a significant visible feature to this radiation. When constructing the structure to be simulated the levels were built up as they would be in the binary fabrication process so the correct degree of roughness would be introduced on each step of the lens. At each stage roughness can be added at a set coverage level with the height set to be a proportion of the height of that stage where the height of each introduced roughness feature has a uniform distribution. An example of the centre zone of a lens simulated with roughness coverage of 12.5% and a max height of 20% of the etch depth is shown in Figure 7.9, where it can be seen that the outer zones are considerably rougher as would be the case in practice.

The prominent effect of micromasking results in a roughness that can arise with several characteristics. The two components of interest are the height of the micromasked pillars and the sparseness of these structures on the surface. A pillar that is formed at the beginning of an etch process will tend to remain even if a piece of material that had caused the original masking is removed. This is because they then form ready oxidation sites where silicon oxide which has a higher selectivity than silicon in

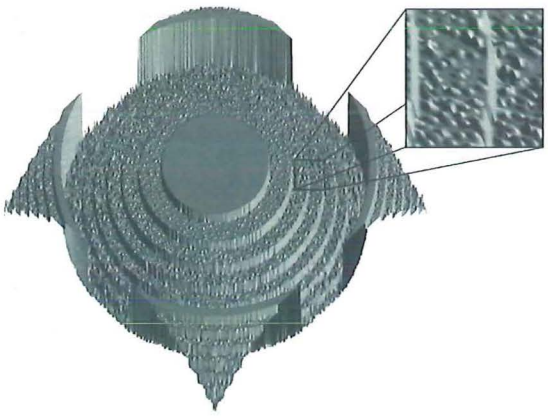

Figure 7.9 Centre zone of an 8 level lens simulated with randomly located roughness of 20% of the etch height with a 12.5% coverage.

this etch process, will continue to act as a mask.

A range of simulations were performed to vary the coverage area of the roughness and the height of the features. Figure 7.10 shows the comparison between lenses with 12.5, 25 and 50% coverage with a total height of features having a uniform distribution between 0 to 30% of the total structure etch depth. The nature of the binary process where areas of the lens are covered by photoresist at different times means that the roughness features with maximum height can only be observed in the bottom most step.

The height of the roughness has a stronger influence on lens efficiency than does the surface coverage. For a lens designed for 1 THz, surface roughness must be greater than 20 μm high before the lens efficiency is reduced by 10%. These trends extracted from the plot have an error of $\pm 1.5\%$. The detrimental effects of surface roughness are minimised by the fact that only a small fraction of the lens is exposed to the full duration of etching. Typical experimental surface roughness pillars are much smaller than this, measuring under half a micron in the process developed in this work, indicating that for lenses of this dimension the surface roughness should have a negligible effect on the efficiency.

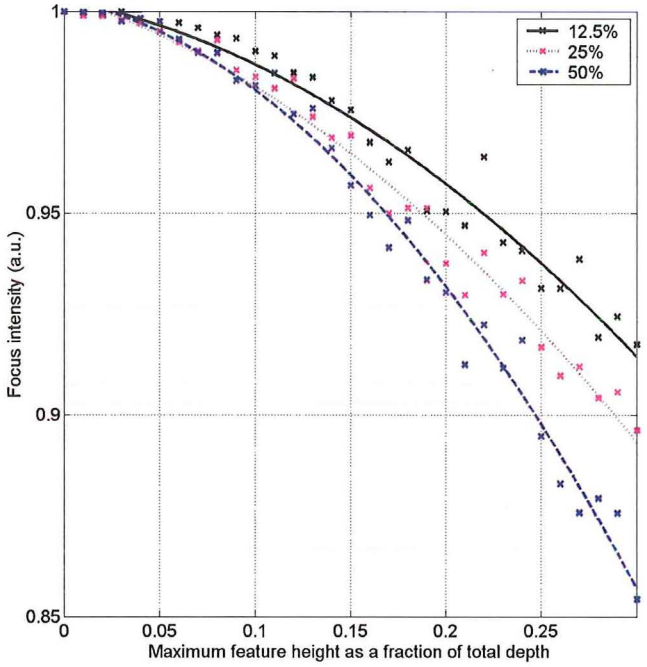

Figure 7.10 Simulated effect of surface roughness with maximum height 0-30% of the total etch depth on the efficiency of an 8 level binary lens with different surface coverage of 12.5%, 25% and 50%.

7.6 MISALIGNMENT

A common problem arising from photolithography is mask misalignment, particularly in multiple level processing. Many lithographic processes can align structures with an exceptional degree of accuracy. This particular process is made more difficult in that the alignment needs to be performed through semi-transparent resist up to 100 μm thick. This can lead to paraxial errors where the mask may appear to be aligned correctly when it is not. Observational errors can also arise from the direction of the light illuminating the structure or surface distortions on the planarised surface. This set of simulations illustrates the shifting of a single layer out of alignment by varying degrees. To gain an appreciation of the severity of this processing defect the second mask was shifted in a diagonal path as shown in Figure 7.11. The degree of this shift was varied between 0 to 0.5 times the width of the smallest feature to observe the effect on the focal point intensity and size. These are plotted in Figure 7.12.

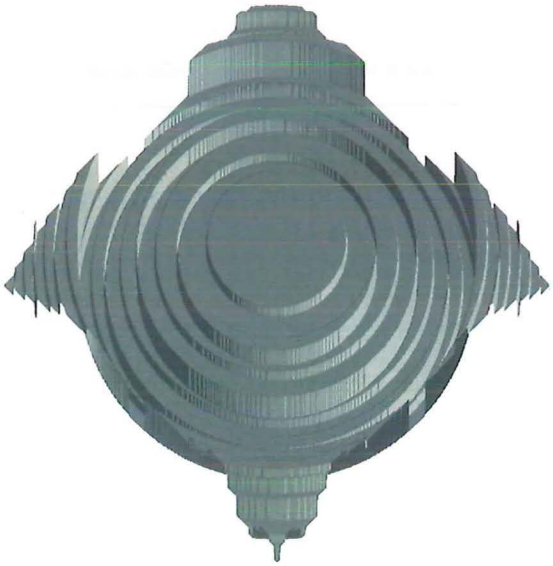

Figure 7.11 Centre zone of an 8 level lens simulated with a diagonally misaligned second stage mask.

The maximum focus intensity was lowered in a linear fashion by 10% for every shift in the mask by 0.25 of the smallest feature size. The FWHM increases with a parabolic relationship getting progressively worse with misalignment, indicating a blurring of the focal spot. However this did not turn out to be very significant, where an increase of only 5% can be seen in Figure 7.12(b) for a misalignment error half that of the smallest feature. From these results it can be summarised that the Fresnel structures are quite tolerant to even quite large misalignment. Because the misalignment error present is fixed and dependent on the lithography alignment system used and not the mask dimensions, this problem becomes more of a concern with lens designs of small focal length or higher frequency where the feature sizes are smaller.

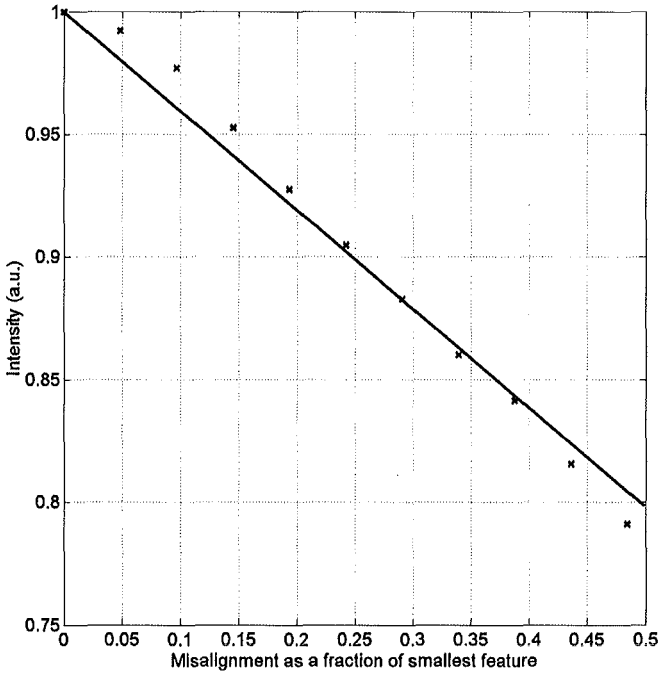

(a)

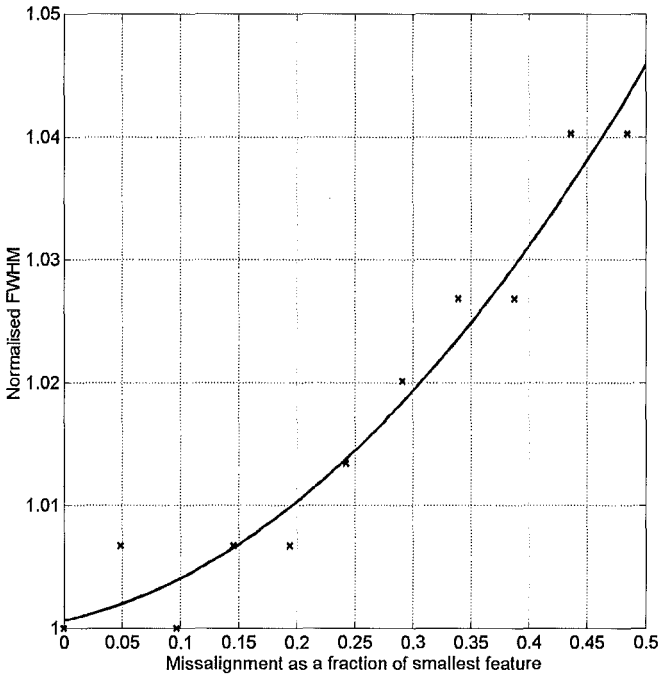

(b)

Figure 7.12 (a) Intensity degradation and (b) FWHM degradation caused by diagonal misalignment of the second stage mask of an 8 level lens.

The micromachining technology used to create the Fresnel structures for this project enabled alignment to within several microns with the smallest feature sizes of 88 μm. This fractional misalignment which was evident would have an insignificant effect (<3%) on the focusing ability of the lenses.

7.7 SUMMARY

The main fabrication issues that can arise during of a multiple level fabrication process for silicon terahertz lenses have been investigated. There is a high tolerance to most defects and the precise microfabrication technologies available should, for the most part, mean that little efficiency is lost using this technique. It is possible that each of these defects could drop the efficiency by up to 20% however and the combined drop in efficiency would be significant. Careful process design and monitoring should enable a lens of any complexity to remain within 10% of its theoretical maximum efficiency. These results illustrate the general bounds to keep within to minimise efficiency loss in a terahertz diffractive optic.

Chapter 8

CONCLUSIONS AND DIRECTIONS FOR FUTURE RESEARCH

8.1 INTRODUCTION

This work has detailed the complete process of designing, fabricating and testing a new technology for creating multiple level diffractive optics for terahertz frequencies. The field of diffractive optics is not new, however, their use in this frequency range between 100 GHz to 10 THz has had little investigation. Because of the wavelengths of the radiation a unique fabrication process had to be designed and refined. This was developed to a point where lenses with eight levels could be created with high yield. Using this process a set of two, four and eight level lenses were constructed for testing so the benefits of this complex multiple level process could be assessed.

There are several different methods of terahertz generation and detection that enable the production of continuous wave or pulsed broadband terahertz radiation. To assess the functionality and focusing ability of the lenses the author collaborated with two institutions to enable access to the two different terahertz sources. Continuous wave testing was conducted at the Johan Wolfgang Gothe Universitat in Frankfurt, Germany and assessment of the lenses in a broadband pulsed terahertz set up was performed at Rensselaer Polytechnic Institute in Troy, New York. Although both of these systems are currently at the forefront of their field they are still under development and the quality of the radiation attained for lens measurements was therefore limited.

Simulations were conducted using Fraunhofer wave propagation to assist in the explanation of the measured results. These simulations were also used to give a detailed analysis on how sensitive the lenses would be to errors in fabrication. This provided valuable information to aid in the design of lenses with maximum efficiency for future terahertz applications.

The major original contributions of this work are therefore:

- Development of a deep multi-level microfabrication applicable to the formation of high diffraction efficiency terahertz optics.

- Integration of diffractive optics into a continuous wave terahertz system.
- Integration of diffractive optics into a pulsed wave terahertz system.
- Simulation of terahertz diffractive optics to determine methodologies for efficiency optimisation.
- Sensitivity analysis of fabrication defects on diffractive optic performance.

This chapter summarises the findings from the fabrication, testing and simulations and highlights future work and applications that can follow from this work, some of which is already research in progress.

8.1.1 Fabrication

The microfabrication process developed to fabricate multiple level diffractive optic Fresnel lenses consists of many steps each of which can influence the others to the detriment of the final product. Because of the interrelated processes and the potential for several aspects to contribute to a certain detrimental effect, determining a high quality repeatable process for terahertz lens fabrication involved unraveling the web of results and resolving the best ways to correct all problems. The final process described is suitable for the production of a broad range of devices in the terahertz frequency band of a large range of focal lengths.

Etch surface roughness was causing many problems, predominantly with alignment during lithography. The size and spiked formation of the roughness formed during etching was light trapping in nature giving it a black non reflective appearance. As optical alignment is critical to the success of a multiple level process, the surface quality needed to be improved. It was identified that the cause of the roughness was a combination of Nichrome sputtering from the etch mask and from oxide micromasking from the etch chemistry. The Nichrome etch mask was initially used due to the requirement of a strong etch mask for etching deep trenches. Development of a multiple spin photoresist deposition process enabled very thick layers of SU-8 to be used for the deep etch steps. To reduce the oxide micromasking of the surface CHF_3 was introduced into the etch chemistry. The result enabled structuring to over 120 μm with sub-micron surface roughness.

Fine feature resolution proved to be difficult when attempting to develop small dimension rings into the already deeply etched trenches. Unwanted resist structures were being resolved into areas which should have been clear. It was determined that the imperfections in the resist planarisation and edge bead were the main cause for these areas getting exposure. Because of the required pre-exposure bake process where the resist reflows it is difficult to fully control or correct for this. The solution required modifying the order in which the stages were completed such that the features became

progressively larger as the processing continued from stage to stage. The elimination of the Nichrome etch mask and the ability to use SU-8 to etch to any of the required etch depths gave the flexibility to make this transition. Multiple spins of SU-8 were required to gain a thick enough etch mask to perform the final and deepest etches.

Resist integrity during the cryogenic etch process could not be maintained when feature sizes became large. For the lenses that were investigated in the course of this work this was not a significant problem. However, it could be if this process was extended to construct lenses with a considerably longer focal length or if the process were to be used to create specific optics for lower terahertz frequencies into the gigahertz frequency band. There is alternative etching equipment that could be applied for the formation of these devices utilizing a room temperature boch process where the differences in thermal expansion between the organic etch mask and the silicon would be minimal. As the lenses are square it was found to be desirable to have rings structured right to the corners. This avoids the larger corner areas of photoresist cracking and then shifting to cover the outer rings, during etching.

8.1.2 Testing

A set of four different lenses were fabricated consisting of a 2-, 4- and 8-level binary lens and an aluminium zone plate. These all had a 30 mm diameter and a design focal length of 25 mm.

A continuous wave terahertz set up was arranged to test the functionality of the diffractive optic structures. Through the use of an antireflection grating etched on one side of a silicon wafer it was possible to obtain transmission of over 80%. The lenses were fabricated on high resistivity wafers which proved to be invaluable as wafers of 1000 Ω.cm absorbed half as much energy as the 10 Ω.cm material.

A four level lens was used to focus energy from a 3 cm collimated beam which was then recollimated with a polyethylene lens. An image of the focal pattern in several different planes could be produced by scanning an aperture between the lenses. From this experiment a FHWM of 570±10 μm was measured compared to the theoretically expected value of a zone plate of 865 μm. The depth of focus was read to be 34 mm which compares to the theoretical value of 33.5 cm. This experiment was repeated using two four level binary lenses where a slightly larger FWHM was measured of 640±10 μm. It is expected that such an arrangement would perform as a narrow band filter in a broadband system.

Two separate pulsed systems were used to get a determination of the operational performance over a broad range of frequencies. A high power scanned system was set up enabling one dimensional scans in front of the lens and a second system with a CCD array detector was used which gave better details where spatial resolution was a factor. With the pulsed set ups it was possible to detect the radiation beyond the

lens without the bias of a second lens as with the continuous wave results. Broadband measurements were taken for a two, four and eight level lens and an aluminium zone plate.

A linear relationship between frequency and focal length was observed although the measured focal distance was slightly longer than the design. This can be attributed to the close proximity of the source not forming a collinear beam. The more complex the lens the tighter and more intense a focus achieved. Also more complex lenses illustrated a considerably narrower band frequency content at a given focal point. The performance gains achieved from processing a high complexity multiple level lens are very apparent and they out perform the simple two level lens and the zone plate in all aspects of focusing.

A comparison was made between the T-ray binary lens and two refractive lenses made from silicon and polyethylene. The binary lens had a more symmetric focus at 1 THz indicating a lower spherical aberration. The refractive lenses displayed a focused spectrum intensity similar to the input spectral content however the binary lens proved to more effectively focus radiation between 0.5 to 1 THz with a marked increase in intensity.

8.1.3 Simulations

Simulations conducted using Fraunhofer wave propagation illustrate the performance characteristics that could be expected from the lenses fabricated and help determine of the effects of processing defects.

Analysing the effect of etch depth on lenses of different complexity illustrated that a complete π phase shift is not desirable for maximum efficiency. Optimally it is better to etch to a total depth of $n - 1/n$ times the depth of a perfect blaze when making a staircase approximation. A curved or parabolic approximation to this blaze will give better efficiency than a linear approximation. There is an inherent bullseye effect in a reactive ion etcher where the middle of the sample which has less access to reactive species in the plasma. Because of this it is necessary to modify the etch depth to account for this.

Analyses were performed on the main error forming components of the fabrication process. These being, mask miss-alignment, lateral etching, surface roughness and the previously mentioned etch depth variation. Because of the size of the structures being fabricated and the quality that the developed microfabrication process provides, it is apparent that aside from the bulls-eye effect the structures should be only mildly affected by the manufacturing defects.

8.2 OUTLOOK FOR TERAHERTZ DIFFRACTIVE OPTICS

The application of this work in future devices is very promising. There are a number of systems that could benefit from the use of diffractive optics in the form of gratings, lenses or elements for beam shaping. Development of a tomography system using the lenses developed is currently underway. For this project a new set of lenses have been developed with longer focal lengths at 125 and 250 mm. The longer focal lengths of these lenses require considerably larger feature sizes which demanded the formulation of a room temperature etch process to avoid SU-8 cracking. This section details some proposals for immediate applications of the technology and details the tomography work recently conducted.

8.2.1 Arbitrary Beam Formation

The fabrication process described in this work can be easily applied to the formation of arbitrary diffractive optic elements. The benefits of creating multiple level structures have been illustrated in the testing results of Chapter 5. The next logical extension of this work is to incorporate the fabrication technology with holographic mask designs to create unique focal patterns. This can include the formation of multiple foci either in a single plane beyond the lens or at different distances away from the lens as in the diagram of Figure 8.1.

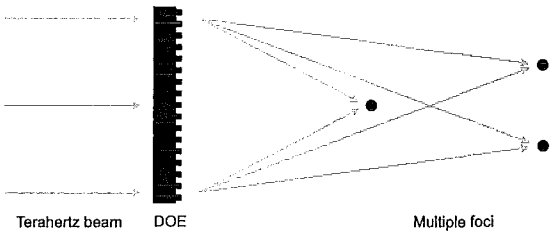

Figure 8.1 Diffractive optics can be used to form points of intensity at multiple points.

A common application of diffractive optics is the formation of lenslet arrays as in Figure 8.2. This is basically a method of creating a grid of multiple foci at a single plane beyond the lens. This is useful in applications where multiple samples need to be assessed enabling measurements to be taken in parallel. Such a system would only demand a small focal length meaning the size of the rings could be reduced. This is important to fit as many lenslets as possible into the array. The number of lenses that can be put in an array is dependent on the number of zones to get the level of efficiency, and the size of the input beam and detector array available. The extent to which the beam can be expanded is dependent on the size of the detector array, the nominal frequency of interest and the power in the terahertz beam to get sufficient signal to noise.

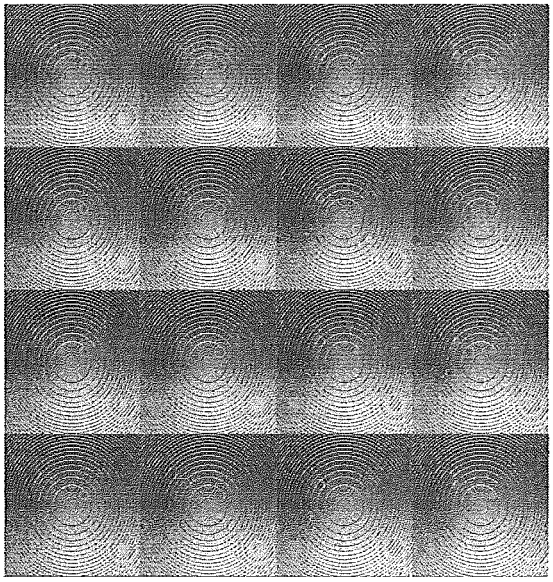

Figure 8.2 Lens arrays enable sample analysis to be performed in parallel greatly improving measurement speed.

Terahertz diffractive optics could also be designed to create focal lines and contours as in the mask and computed intensity pattern of Figure 8.3 [163]. Not only can this be used to customise the focal plane pattern but could be used as a beam correction mechanism. There is potential to use customised diffractive optics to correct abberations in beam patterns which result from antenna emission shapes that are otherwise difficult to correct.

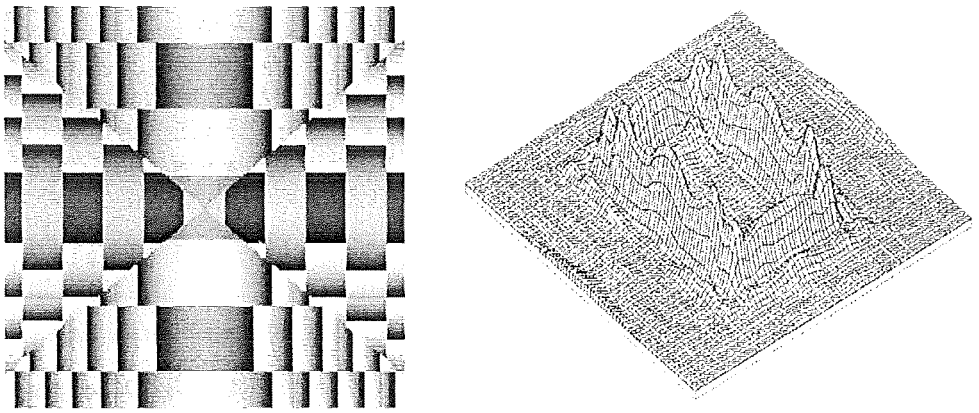

(a) (b)

Figure 8.3 diffractive optic mask design (a) and the calculated focused pattern (b) [162].

8.2.2 Diffractive mirrors

A further extension of creating lenses with unique beam formation is to use this technology to make reflective diffractive optic mirrors. It would be possible to create these as off axis mirrors with careful lens design taking full advantage of the multi level fabrication technique. It is possible that such a design could couple the task of beam focusing with beam distortion correction if a non Gaussian input beam was being obtained from an antenna. As such a device would be working in reflection mode the losses from absorption and back reflection normally seen in transmission through a silicon wafer would not be present. Following fabrication in silicon a metal layer could be evaporated onto the surface of the mirror to increase the reflectivity.

A new mask would need to be created that is basically a skewed version of the current mask. It would look like the current lens when viewed at a 45 degree angle. This means the lens structure will be physically larger requiring larger wafer processing if the same size beam is to be used.

There are several processing issues that would need to be resolved. These would revolve around the fact that the structure will need to be etched much deeper. This is because the phase change is not achieved in the silicon but in air. Because of this the depth needs to be the wavelength on a 45 degree angle requiring an etch depth of nearly double the transmissive lens at 212 μm This may require the use of a high density plasma etcher which is more suited to extremely deep micromachining. Because the photo resist can be spun on to a large range of depths well beyond that used in the fabrication of the lenses in this project there should be little difficulty in using the same photolithography process. It may require the adjustment of some of the process timings to account for the thicker layers.

Considering the low absorbance that was measured in an SU-8 film it is possible that lenses could be made from the photoresist or other similar polymer. This could be achieved by making silicon molds and creating an imprint of these structures by planarising with a polymer. Candidates for the lens material are SU8 which seems to have a reasonably low loss and also Teflon. Again the problem with the construction of such a device is in the increased etch depth that is needed. The lift off procedure that was developed to remove the resist using a sacrificial oxide layer was used in an experiment to see if large areas of resist could be lifted off and it proved successful. The benefits in using these materials lie in the fact that once the mold is made the fabrication of a lens is potentially very cheap. Also the refractive index of the material is much less so for all that the fabrication is harder, the end product should work better with a higher transmission of radiation for focusing. To create a converging lens the steps would have to slope in the opposite direction so, when lifted off, the polymer lens would be of the correct form.

8.2.3 Terahertz tomography

Conventional tomography measurements are made by rotating the sample or rotating detectors around the sample. In many cases this may not be practical eg. when the sample can not be moved. The linear shift in focus with frequency of the terahertz lens enables tomographic images to be taken using a single projection. A binary lens will perform as a conventional lens satisfying the lens law concerning a non infinite object and its image through a lens,

$$\frac{1}{z} + \frac{1}{z'} = \frac{1}{f_v} \tag{8.1}$$

where z is the distance between the object and the lens, z' is the distance from the image to the lens and f_v is the focal length for a given frequency. Hence if the image plane is fixed in front of the lens, as in Figure 8.4, different planes behind the lens will form an image at a frequency determined by their distance from the lens. In a continuing collaboration with Rensselaer Polytechnic Institute this application has been investigated using the eight level lens tested in Chapter 5 [114].

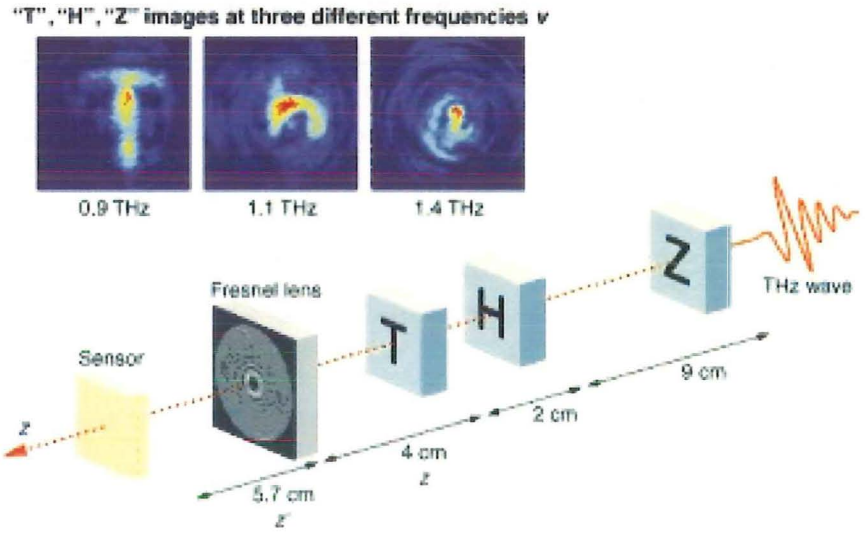

Figure 8.4 A fixed lens and detector exploit the chromatic aberation of a Fresnel lens to take single shot tomographic images of objects.

Current expansion of this concept demands the development of a longer focal length lens to enable the imaging of larger areas and objects. Two lenses under investigation include a 125 mm and a 250 mm focal length lens. Construction of these embraces the same technology described in this work with an altered etching process to enable the etching with large features without SU-8 cracking. The redesigned lenses have been further optimized from the prototype lens set with a higher efficiency rounded step

blaze incorporated into the mask design. The three masks required for each lens design were made and are compared to the 25 mm lens in Table 8.1.

Focal length	25 mm	125 mm	250 mm
Lens diameter	30 mm	45 mm	45 mm
Number of zones	14	6	3
Smallest feature width	88.6 μm	150 μm	300 μm
Largest feature width	3.46 mm	6.03 mm	8.53 mm

Table 8.1 Photolithographic mask statistics.

The new masks were created with zones to the corners so that the full area of each wafer is utilised. This meant that the 125 and 250 mm focal length lens have have an additional 6 and 3 zones extending to the corners. The longer focal lengths demand larger feature sizes that push the limits of the reactive ion etch process. The feature sizes become of a size that, when cryogenically cooled during etching, tend to crack due to the difference in thermal expansion of the SU-8 photoresist and the silicon. For these structures to be fabricated in the Oxford Plasmalab etcher a high temperature process had to be used to eliminate the thermal expansion problem that had resulted in large areas of SU-8 cracking. An oxygen reduced process at 273 K was used as shown in Table 8.2.

SF_6 flow rate	60 sccm
CHF_3 flow rate	20 sccm
O_2 flow rate	5 sccm
Chamber pressure during etching	0.1 Torr
RF power	150 W
Etch temperature	273 K
Etch rate	0.3 μm/min

Table 8.2 High temperature Reactive Ion Etch conditions for deep etching.

The surface roughness was increased slightly compared to the cryogenic process although remained at an acceptable level. A completed 8-level, 125 mm focal length lens is shown in figure 8.5.

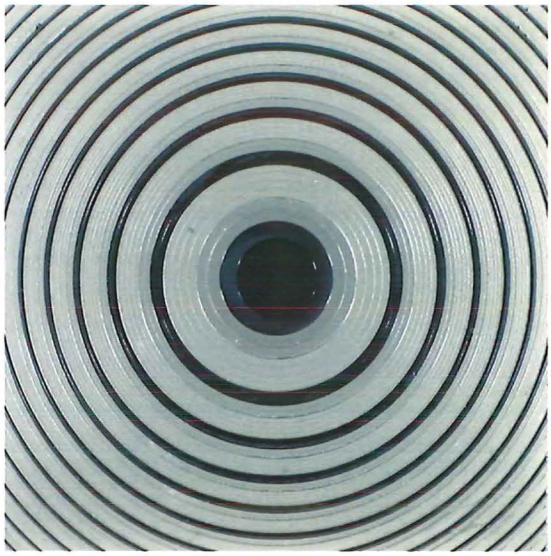

Figure 8.5 Photograph of a 45 mm^2, 8-level, 125 mm focal length lens.

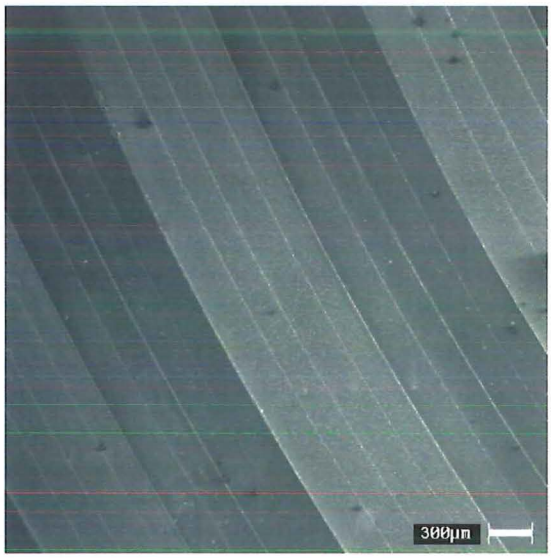

Figure 8.6 SEM image showing outer zones of an 8-level, 125 mm focal length lens.

8.3 SUMMARY

This thesis has successfully demonstrated how diffractive optics can be integrated into terahertz systems and applications. A fabrication process has been described which can be used to make high diffraction efficiency multiple level diffractive optics. The functionality of these were demonstrated with the production and analysis of a set of gratings and Fresnel lenses. Results from this and the design and sensitivity parameters were assessed with scalar Fresnel and Fraunhofer propagation theory. From

this, fabrication tolerances have been determined that provide bounds for maintaining high performance efficiencies. This technology has generated interest from a number of international terahertz research institutions and is the subject of further and ongoing research.

Appendix A

MASK GENERATION CODE

```
// Script to generate circular mask using rectangles
#include <iostream.h>
#include <fstream.h>
#include <math.h>
#include <dos.h>

long round5(double input);

int main( void ) {
   ofstream out("d:/thesis/mask/data.pg");
   out << "$" Fresnel mask pattern " << endl;
   long objects=0;
   const long x_centre = 255500;     const long y_centre = 255500;
   const long x_centre_4 = 255500;     const long y_centre_4 = 145500;
   const long x_centre_8 = 145500;     const long y_centre_8 = 255500;
   int n;
   long a_x_centre[10]={295550,215500,295550,215500,295550,215500,185500,105500,295550,215500};
   long a_y_centre[10]={295550,295550,105500,105500,185500,195040,215500,215500,215500,215500};
   // center points +-40000pg units

   long outer_radius = 49640; // the outer radius of the circle
   long rect_thick[20] = {1160,1195,1240,1285,1340,1405,1485,1580,1705,1870,2105,2475,3200,7645};
   // small dimension of rectangles in um
   long gap_thick[20] = {1160,1195,1240,1285,1340,1405,1485,1580,1705,1870,2105,2475,3200,7645};
   // small dimension of gaps
   long rect_thick_4[40] = {580,580,600,600,620,620,645,645,670,670,705,705,745,745,790,790,855,855,935,935,
     1055,1055,1240,1240,1600,1600,3825,3825};
   long gap_thick_4[40] = {580,580,595,595,620,620,640,640,670,670,700,700,740,740,790,790,850,850,935,935,
     1050,1050,1235,1235,1600,1600,3820,3820};
   long rect_thick_8[80] = {290,290,290,290,300,300,300,300,310,310,310,310,320,320,325,325,335,335,335,335,
     350,350,355,355,370,370,375,375,395,395,395,395,425,425,430,430,470,470,470,470,525,525,530,530,620,
     620,620,620,800,800,800,800,1910,1910,1915,1915};
   long gap_thick_8[80] = {290,290,290,290,295,295,300,300,310,310,310,310,320,320,320,320,335,335,335,335,
     350,350,350,350,370,370,370,370,395,395,395,395,425,425,425,425,465,465,465,465,525,525,525,525,615,
     615,620,620,800,800,800,800,1910,1910,1910,1910};
   const int complexity = 8;
```

```
int num_segs = pow( 2, complexity ); // number of rects for circle
double sector_angle = 2.0 * M_PI / num_segs;
out << endl <<"\" antireflection grating " << endl << endl;
long g_centre_x=94400;
long g_centre_y=100000;
// pg unit length of 12000 length giving total length
// just under 26mm with starting hight of 94325 pg units
for(j = 0; j < 433; ++j) {
for( int i = 0; i < 9; ++i) {
  out << "X" << g_centre_x
  << "Y" << g_centre_y
  << "H" << 11375
  << "W" << 120
  << "A" << 0
  << ";"
  << endl;
  g_centre_y=g_centre_y+11375;
  ++objects;
  }
  g_centre_x=g_centre_x+240;
  g_centre_y=100000;
}

out << "\" 1st mask " << endl << endl;
int band=0;
while( band < 20 ) { // loop through bands
// determine length of rectangles from radius and number of segments
long rect_leng = round5(2.0*sin( sector_angle / 2.0 ) * (outer_radius));
double centre_radius = outer_radius - rect_thick[band]/2.0; // multiply by 5 to change to u inches
// calculate each rectangle
for( int i = 0; i < num_segs; i++ ) {
  long centre_x = round5(cos( i*sector_angle )*centre_radius + x_centre);
  long centre_y = round5(sin( i*sector_angle )*centre_radius + y_centre);
  long angle = i*sector_angle*1800.0/M_PI + 0.5;
  bool swap = false;
  while( angle >= 900 ) {
    angle -= 900;          swap = !swap;       }
  out << "X" << centre_x
  << "Y" << centre_y
  << "H" << (swap ? rect_thick[band] : rect_leng)
  << "W" << (swap ? rect_leng : rect_thick[band])
  << "A" << angle
  << ";"
  << endl;
  ++objects;
}
objects=objects++;
outer_radius=outer_radius-rect_thick[band]-gap_thick[band];
```

```
++band;
}
out << endl << "\" 2nd mask " << endl << endl;
band=0;
outer_radius = 49640; // the outer radius of the circle
while( band < 40 ) { // loop through bands
  // determine length of rectangles from radius and number of segments
  long rect_leng = round5(2.0*sin( sector_angle / 2.0 ) * (outer_radius));
  double centre_radius = outer_radius - rect_thick_4[band]/2.0;
  // calculate each rectangle
  for( int i = 0; i < num_segs; i++ ) {
    long centre_x = round5(cos( i*sector_angle )*centre_radius + x_centre_4);
    long centre_y = round5(sin( i*sector_angle )*centre_radius + y_centre_4);
    long angle = i*sector_angle*1800.0/M_PI + 0.5;
    bool swap = false;
    while( angle >= 900 ) {
      angle -= 900;
      swap = !swap;
    }
    out << "X" << centre_x
    << "Y" << centre_y
    << "H" << (swap ? rect_thick_4[band] : rect_leng)
    << "W" << (swap ? rect_leng : rect_thick_4[band])
    << "A" << angle
    << ";"
    << endl;
    ++objects;
  }
  objects=objects++;
  outer_radius=outer_radius-gap_thick_4[band]-rect_thick_4[band];
  ++band;
}
out << endl << "\" 3rd mask " << endl << endl;
band=0;
outer_radius = 49640; // the outer radius of the circle
while( band < 80 ) { // loop through bands
  // determine length of rectangles from radius and number of segments
  long rect_leng = round5(2.0*sin( sector_angle / 2.0 ) * (outer_radius));
  double centre_radius = outer_radius - rect_thick_8[band]/2.0;
  // calculate each rectangle
  for( int i = 0; i < num_segs; i++ ) {
    long centre_x = round5(cos( i*sector_angle )*centre_radius + x_centre_8);
    long centre_y = round5(sin( i*sector_angle )*centre_radius + y_centre_8);
    long angle = i*sector_angle*1800.0/M_PI + 0.5;
    bool swap = false;
    while( angle >= 900 ) {
      angle -= 900;
```

```
            swap = !swap;
          }
          out << "X" << centre_x
          << "Y" << centre_y
          << "H" << (swap ? rect_thick_8[band] : rect_leng)
          << "W" << (swap ? rect_leng : rect_thick_8[band])
          << "A" << angle
          << ";"
          << endl;
          ++objects;
        }
        objects=objects++;
        outer_radius=outer_radius-gap_thick_8[band]-rect_thick_8[band];
        ++band;
    }
    out << "$" << endl;
    cout << "objects : "<< objects << endl;
    delay(3000);
    out.close();
    return 0;
}

long round5(double input) {
    double temp=input/5+0.5;
    return static_cast<long>(temp)*5; }
```

REFERENCES

[1] J. C. Maxwell. *An Elementary Treatise on Electricity.* Clarendon Press, 2nd edition, 1888.

[2] H. Rubens and E. F. Nichols. ber warmestrahlen von grosser wellenlnge. In *Applied Optics*, volume 11, pages 545–599, 1896.

[3] P. Planken. Terahertz near-field detection: towards a sub-wavelength terahertz microscope. In *Philosophical Transactions of the Royal Society (pre-print)*, 2004.

[4] P. H. Siegel. Terahertz technology. In *IEEE transactions on microwave theory and techniques*, volume 50, pages 910–927, 2002.

[5] Gousev and P. Yu et al. Widely tunable continuous wave THz laser. In *Applied Physics Letters*, volume 75, pages 757–759, 1999.

[6] Teraview Ltd. (http://www.teraview.co.uk).

[7] E. R. Brown, J. R. Soderstrom, C. D. Parker, J. Mahoney, K. M. Molvar, and T. G. McGill. Oscillations up to 712 GHz in InAs/AlSb resonant-tunneling diodes. In *Applied Physics Letters*, volume 58, pages 2291–2293, May 1991.

[8] X.-C. Zhang et al. Terahertz optical rectification from a nonlinear organic crystal. In *Applied Physics Letters*, volume 61, pages 3080–3082, 1992.

[9] Y. Cai, I. Brener, J. Lopata, J. Wynn, L. Pfeiffer, and J. Federici. Design and performance of single electric field terahertz photoconducting antennas. In *Applied Physics Letters*, volume 71, pages 2076–2078, 1997.

[10] R. Heidemann, T. Pfeiffer, and D. Jager. Optoelectronically pulsed slot-line antennas. In *Electronics Letters*, volume 19, pages 316–317, 1983.

[11] D. H. Auston, K. P. Cheung, and P. R. Smith. Picosecond photoconducting hertzian dipoles. In *Applied Physics Letters*, volume 45, pages 284–286, 1984.

[12] Y. Pastol, G. Arjavalingham, and J.-M. Halbout. Characterisation of an optoelectronically pulsed equiangular spiral antenna. In *Electronics Letters*, volume 26, pages 133–134, 1990.

[13] N. Katzenellenbogen and D. Grischkowsky. Efficient generation of 380 fs pulses of thz radiation by ultrafast laser pulse excitation of a biased metal-semiconductor interface. In *Applied Physics Letters*, volume 58, pages 222–224, 1991.

[14] A. Bonvalalet, M. Joffre, J.-L. Martin, and A. Migus. Generaion of ultrabroadband femtosecond pulses in the mid-infrared by optical rectification of 15 fs light pulses at 100 MHz repition rate. In *Applied Physics Letters*, volume 67, pages 2907–2909, 1995.

[15] X.-C. Zhang, Y. Jin, K. Yang, and L. J. Schowalter. Resonant nonlinear susceptibility near the GaAs band gap. In *Applied Physics Letters*, volume 69, pages 2303–2306, 1992.

[16] A. V. Raisanen. Frequency multipliers for millimeter and submillimeter wavelengths. In *Proc. IEEE*, volume 80, pages 1842–1852, November 1992.

[17] B. Rizzi, T. Crowe, and N. R. Erickson. A high power millimeter wave frequency doubler using a planar diode array. In *IEEE Microwave Guided Wave Letters*, volume 3, pages 188–190, June 1993.

[18] A. Maestrini, J. Bruston, D. Pukala, S. Martin, and I. Mehdi. Performance of a 1.2 THz frequency tripler using a GaAs frameless membrane monolithic circuit. In *IEEE International Microwave Symposium Digest*, volume 3, pages 1657–1660, May 2001.

[19] F. Maiwald, S. Martin, J. Bruston, A. Maestrini, T. Crawford, and P. H. Siegel. 2.7 THz tripler using monolithic membrane diodes. In *IEEE International Microwave Symposium Digest*, volume 50, pages 1637–1640, May 2002.

[20] H. Eisele. Two-terminal devices as fundamental solid-state terahertz oscillators. In *Proc. SPIE - Conference on Terahertz Spectroscopy and Applications*, volume 3828, pages 70–80, 1999.

[21] S. Verghese, K. A. McIntosh, S. Calawa, W. F. Dinatale, E. K. Duerr, and K. A. Molvar. Generation and detection of coherent terahertz waves using two photomixers. In *Applied Physics Letters*, volume 73, pages 3824–3826, 1998.

[22] D. H. Austen. Picosecond optoelectronic switching and gating in silicon. In *Applied Physics Letters*, volume 26, pages 101–103, February 1975.

[23] E. R. Brown, K. A. McIntosh, K. B. Nichols, and C. L. Dennis. Photomixing up to 3.8 THz in low-temperature-grown GaAs. In *Applied Physics Letters*, volume 66, pages 285–287, 1995.

[24] S. Matsuura et al. A traveling-wave THz photomixer based on angle-tuned phase matching. In *Applied Physics Letters*, volume 74, pages 2872–2874, May 1999.

[25] S. Verghese, K. A. McIntosh, and E. R. Brown. Highly tunable fiber coupled photomixers with coherent terahertz output power. In *IEEE Transactions on Microwave Theory and Technology*, volume 45, pages 1301–1309, August 1997.

[26] K. Kawase, J. Shikata, K. Imai, and H. Ito. Transform-limited, narrow-linewidth, terahertz-wave parametric generator. In *Applied Physics Letters*, volume 78, pages 2819–2821, 2001.

[27] Committee on Free Electron Lasers. *Free Electron Lasers and Other Advanced Sources of Light: Scientific Research Opportunities.* The National Academies Press, 1994.

[28] S. Fijii, H. Mori, T. Mizuno, T. Ohshima, M. Kawai, H. Saito, and K. Koshiji. Experimental study of compact fel with micro wiggler and electrostatic accelerator. In *22nd International Free Electron Laser Conference*, 2000.

[29] W. Schrenk, N. Finger, S. Gianordoli, L. Hvozdara, G. Strasser, and E. Gornik. Surface-emitting distributed feedback quantum-cascade lasers. In *Applied Physics Letters*, volume 77, pages 1928–1930, October 2000.

[30] C. Waschke, H. G. Roskos, R. Schwedler, K. Leo, H. Kurz, and K. Kohler. Coherent submillimeter-wave emission from bloch oscillations in a semiconductor superlattice. In *Physical Review Letters*, volume 70, pages 3319–3322, 1993.

[31] S. Komiyama. Far-infrared emission from population-inverted hot-carrier system in p-ge. In *Physics Review Letters*, volume 48, pages 271–274, 1982.

[32] C. Chansungsan. Coherent terahertz radiative dynamics of excitons from ultrafast optical excitation of single semiconductor quantum wells. In *Journal of the Optical Society of America B*, volume 13, pages 2792–2800, 1996.

[33] P. C. M. Planken, M. C. Nuss, I. Brener, and K. W. Goosen. Terahertz emission in single quantum wells after coherent optical excitation of light hole and heavy hole exitons. In *Physical Review Letters*, volume 69, pages 3800–3803, 1992.

[34] A. N. Korotkov, D. V. Averin, and K. K. Likharev. Tasers: Possible dc pumped terahertz lasers using interwell transitions in semiconductor hetrostructures. In *Applied Physics Letters*, volume 65, pages 1865–1967, 1994.

[35] J. Ulrich, R. Zobl, W. Schrenk, G. Strasser, K. Unterrainer, and E. Gornik. Terahertz quantum cascade structures: Intra- versus interwell transition. In *Applied Physics Letters*, volume 77, pages 1928–1930, June 2000.

[36] R. Kohler, A. Tredluccl, F. Beltram, H. E. Beere, E. H. Linfield, A. G. Davies, D. A. Ritchie, R. C. Lottl, and F. Rossi. Terahertz semiconductor-heterostructure laser. In *Nature*, volume 417, pages 156–159, 2002.

[37] B. S. Williams, S. Kumar, H. Callebaut, Q. Hu, and J. L. Reno. 3.4 THz quantum cascade laser operating above liquid nitrogen temperature. In *Nature*, volume 39, pages 915–916, 2003.

[38] S. Weinreb and A. R. Kerr. Cryogenic cooling of mixers for millimeter and centimeter wavelengths. In *IEEE J. Solid-State Circuits*, volume 8, pages 58–63, February 1973.

[39] T. G. Phillips and K. B. Jefferts. A low temperature bolometer heterodyne receiver for millimeter wave astronomy. In *Rev. Sci. Instrum.*, volume 44, pages 1009–1014, February 1973.

[40] S. Park and M. Melloch. Analysis of terahertz waveforms measured by photoconductive and electrooptic sampling. In *IEEE Journal of Quantum Electronics*, volume 35, pages 1–10, May 1999.

[41] Y. Cai, I. Brener, J. Lopata, J. Wynn, L. Pfeiffer, J. B. Stark, Q. Wu, X.-C. Zhang, and J. Frederici. Coherent terahertz radiation detection: Direct comparison between free-space electro-optic sampling and antenna detection. In *Applied Physics Letters*, volume 73, pages 475–480, July 1998.

[42] A. Nahata, A. S. Weling, and T. Heinz. A wideband coherent terahertz spectroscopy system using optical rectification and electro-optic sampling. In *Applied Physics Letters*, volume 69, pages 2321–2323, October 1996.

[43] M. Tani, K. Sakai, and H. Mimura. Ultrafast photoconductive detectors based on semi-insulating GaAs and InP. In *Japanese Journal of Applied Physics*, volume 36, pages 1175–1178, 1997.

[44] S. Kono, M. Tani, P. Gu, and K. Sakai. Detection of up to 20 THz with a low-temperature-grown gaas photoconductive antenna gated with 15 fs light pulses. In *Applied Physics Letters*, volume 77, pages 4104–4106, 2000.

[45] J. A. Valdmanis, G. Mourou, and C. W. Gabel. Picosecond electro-optic sampling system. In *Applied Physics Letters*, volume 41, pages 211–212, 1984.

[46] Q. Wu and X.-C. Zhang. Design and characterization of travelling-wave electro-optic terahertz sensors. In *IEEE Journal of Selected Topics in Quantum Electronics*, volume 2, pages 693–700, 1996.

[47] Q. Wu and X.-C. Zhang. Free-space electro-optic sampling of mid-infrared pulses. In *Applied Physics Letters*, volume 71, pages 1285–1286, 1997.

[48] Z. Jiang and X.-C. Zhang. Single-shot spatiotemporal terahertz field imaging. In *Optics Letters*, volume 23, pages 1114–1116, July 1998.

[49] Q. Wu, M. Litz, and X.-C. Zhang. Broadband detection capability of ZnTe electro-optic field detectors. In *Applied Physics Letters*, volume 68, pages 2924–2926, 1996.

[50] Q. Wu and X.-C. Zhang. Terahertz broadband GaP electro-optic sensor. In *Applied Physics Letters*, volume 70, pages 1784–1786, April 1997.

[51] P. Y. Han, M. Tani, F. Pan, and X.-C. Zhang. Use of the organic crystal DAST for terahertz beam applications. In *Optics Letters*, volume 25, pages 675–677, 2000.

[52] P. Y. Han, M. Tani, F. Pan, and X.-C. Zhang. Electro-optic detection of THz radiation in $LiTaO_3$, $LiNbO_3$ and ZnTe. In *Applied Physics Letters*, volume 70, pages 3069–3071, 1997.

[53] D. M. Mittleman, M. Gupta, R. G. Baraniuk, J. V. Rudd, and M. Koch. Recent advances in terahertz imaging. In *Applied Physics B Lasers and Optics*, April 1999.

[54] Z. Jiang and X.-C. Zhang. Electro-optic measurement of THz field pulses with a chirped optical beam. In *Applied Physics Letters*, volume 72, pages 1945–1947, 1998.

[55] Q. Wu, T. D. Hewitt, and X.-C. Zhang. Two-dimensional electro-optic imaging of terahertz beams. In *Applied Physics Letters*, volume 69, pages 1026–1028, June 1996.

[56] Z. Jiang, X. G. Xu, and X.-C. Zhang. Improvement of terahertz imaging with a dynamic subtraction technique. In *Applied Optics*, volume 39, pages 2982–2987, June 2000.

[57] S. Nolen, J. A. Koch, N. Paulter, C. D. Reintsema, and E. N. Grossman. Antenna-coupled niobium bolometers for mm-wave imaging arrays. In *Proc. SPIE*, volume 3795, pages 279–286, 1999.

[58] S.-G. Park, M. R. Melloch, and A. M. Weiner. Comparison of terahertz waveforms measured by electro-optic and photoconductive sampling. In *Applied Physics Letters*, volume 73, pages 3184–3185, November 1998.

[59] F. Natterer and F. Wubbeling. Mathematical methods in image reconstruction. In *Society of Industrial and Applied Mathematics*, 2001.

[60] A. Graps. An introduction to wavelets. In *IEEE Computational Science and Engineering*, volume 2, pages 50–61, 1995.

[61] P. C Ching, H. C. So, and S. Q. Wu. Wavelet denoising and its applications to time delay estimation. In *IEEE Transactions on Signal Processing*, volume 47, pages 2879–2882, 1999.

[62] D. L. Donoho. De-noising by soft thresholding. In *IEEE Transactions on Information Theory*, volume 41, pages 613–627, 1995.

[63] D. M. Mittleman, R. Neelamani, R. G. Baraniuk, and M. C. Nuss. Applications of terahertz imaging. In *Nonlinear optics:Materials, Fundamentals and Applications Topical Meeting*, pages 294–296, 1998.

[64] B. B. Hu and M. C. Nuss. Imaging with terahertz waves. In *Optics Letters*, volume 20, pages 1716–1718, 1995.

[65] S. Hunsche, D. Mittleman, M. Koch, and M. C. Nuss. New dimensions in T-ray imaging. In *IEICE Transactions on Electronics*, volume 81, pages 269–276, 1998.

[66] T. G. Phillips and J. Keene. Submillimeter astronomy. In *Proc. IEEE*, volume 80, pages 1662–1678, November 1992.

[67] J. W. Waters. Submillimeter-wavelength heterodyne spectroscopy and remote sensing of the upper atmosphere. In *Proc. IEEE*, volume 80, pages 1679–1701, November 1992.

[68] G. Melnick et al. The submillimeter wave astronomy satellite: Science objectives and instrument description. In *Astrophys. J. Lett.*, volume 539, pages 1662–1678, August 2000.

[69] G. Gallot and D. Grischowsky. Terahertz time domain spectroscopy (THz TDS) with electro-optic sampling. In *Conference on Lasers and Electro-Optics*, pages 492–493, 1999.

[70] J. T. Kindt and C. A. Schmuttenmaer. Far-infrared dielectric properties of polar liquids probed by femtosecond terahertz pulse spectroscopy. In *Journal of Physical Chemistry*, volume 100, pages 10373–10379, 1996.

[71] M. V. Exter, C. Fattinger, and D. Grischkowsky. Terahertz time-domain spectroscopy of water vapor. In *Optics Letters*, volume 14, pages 1128–1130, 1989.

[72] J. W. Fleming. High resolution submillimeter-wave Fourier-transform spectrometry of gases. In *IEEE Trans. Microwave theory Tech*, volume 22, pages 1023–1025, December 1974.

[73] R. A. Cheville and D. Grischkowsky. Observation of pure rotational absorption spectra in the terahertz band of hot HO in flames. In *Optics Letters*, volume 23, pages 531–533, 1998.

[74] L. Duvillaret, F. Garet, and J. L. Coutaz. A reliable method for extraction of material parameters in terahertz time-domain spectroscopy. In *IEEE Journal of Selected Topics in Quantum Electronics*, volume 2, pages 739–746, October 1996.

[75] T. D. Dorney, R. G. Baraniuk, and D. M. Mittleman. Material parameter estimation with terahertz time-domain spectroscopy. In *Journal of the Optical Society of America A-Optics Image Science and Vision*, volume 18, pages 1562–1571, October 2001.

[76] O. Mitrofanov, I. Brener, M. C. Wanke, R. R. Ruel, J. D. Wynn, A. J. Bruce, and J. Federici. Near-field microscope probe for far infrared time domain measurements. In *Applied Physics Letters*, volume 77, page 591, 2000.

[77] J. F. Federici and O. Mitrofanov. Near field THz microscopy. In *Physics in Medicine and Biology*, volume 47, pages 3727–3734, 2002.

[78] S. Hadjiloucas, L. S. Karatzas, and J. W. Bowen. Measurements of leaf water content using terahertz radiation. In *IEEE Transactions on Microwave Theory and Techniques*, volume 47, pages 142–149, 1999.

[79] M. May. T-rays spell sharper, safer images. In *New Scientist*, volume 154, page 22, 1997.

[80] A. Macovski. *Medical imaging systems.* Prentice-Hall, 1983.

[81] P. Scally. *Medical imaging.* Oxford University Press, 1999.

[82] Bettyann, Holtzmann, and Kevles. *Naked to the bone : medical imaging in the twentieth century.* Rutgers University Press, 1997.

[83] M. Walther, B. Fischer, and M. Schall et al. Infrared vibrational spectra of all-trans, 9-cis and 13-cis retinal measured by THz time domain spectroscopy. In *Chemical Physics Letters*, volume 332, pages 389–395, 2000.

[84] A. Markelz, A. Roitberg, and E. Heilwiel. Pulsed terahertz spectroscopy of DNA, bovine serum albumin and collagen between 0.1 and 2.0 thz. In *Chemical Physics Letters*, volume 320, pages 42–48, 2000.

[85] D. M. Mittleman, R. H. Jacobson, and M. C. Nuss. T-ray imaging. In *IEEE Journal of Selected Topics in Quantum Electronics*, volume 2, pages 679–692, 1996.

[86] J. Handley, A. Fitzgerald, T. Loeffler, K. Siebert, E. Berry, and R. Boyle. Potential medical applications of THz imaging. In *Proceedings of Medical Image Understanding and Analysis*, volume 17, 2001.

[87] T. McKechnie, A. Jahan, I. Tait, A. Cuschieri, W. Sibbett, and M. Padgett. An endoscopic system for the early detection of cancers of the GI tract. In *Rev. Sci. Instrum.*, volume 69, pages 2521–2523, 1998.

[88] D. D. Arnone, C. M. Ciesla, A. Corchia, S. Egusa, M. Pepper, and J. M. Chamberlain. Applications of terahertz (THz) technology to medical imaging. In *Terahertz Spectroscopy and Applications II*, pages 209–219, 1999.

[89] M. Beard, G. M. Turner, and C. A. Schmuttenmaer. Progress towards two-dimensional biomedical imaging with THz spectroscopy. In *Physics in Medicine and Biology*, volume 47, pages 3841–3846, 2002.

[90] C. M. Ciesla, D. D. Arnone, A. Corchia, D. Crawley, C. Long bottom, and E. H. Linfield EH. Biomedical applications of terahertz pulse imaging. In *Commercial and Biomedical Applications of Ultrafast Lasers II*, volume 3934, pages 73–81, 2000.

[91] T. Loeffler, T. Bauer, K. J. Siebert, H. G. Roskos, A. Fitzgerald, and S. Czasch. Terahertz dark-field imaging of biomedical tissue. In *Optics Express*, volume 9, pages 616–621, 2001.

[92] T. Loeffler, K. J. Siebert, S. Czasch, T. Bauer, and H. G. Roskos. Visualization and classification in biomedical terahertz pulsed imaging. In *Physics in Medicine and Biology*, volume 47, pages 3691–3698, 2002.

[93] Hagness SC, Taflove A, and Bridges JE. Two-dimensional FDTD analysis of a pulsed microwave confocal system for breast cancer detection: Fixed-focus and antenna- array sensors. In *IEEE Transactions on Biomedical Engineering*, volume 45, pages 1470–1479, 1998.

[94] P. Lasch and D. Naumann. FT-IR microspectroscopic imaging of human carcinoma thin sections based on pattern recognition techniques. In *Cellular and Molecular Biology*, volume 44, pages 189–202, 1998.

[95] B. E. Cole, R. Woodward, D. Crawley, V. P. Wallace, D. D. Arnone, and M. Pepper. Terahertz imaging and spectroscopy of human skin, in-vivo. In *Proc. SPIE*, volume 4276, pages 1–10, May 2001.

[96] S. Cotton, E. Claridge, and P. Hall. Non invasive skin imaging. In *Information Processing in Medical Imaging*, volume 1230, pages 501–506, 1997.

[97] D. Crawley, C. M. Ciesla, C. Longbottom, D. Arnone, and M. Pepper. Using terahertz pulse imaging (TPI) to detect diseased tissue. In *International terahertz workshop*, September 2000.

[98] J. Handley, A. Fitzgerald, E. Berry, and R. Boyle. Approaches to segmentation in medical terahertz pulsed imaging. In *Proceedings of Medical Image Understanding and Analysis*, volume 3828, pages 157–160, 2002.

[99] N. N. Zinov'ev, C. D. Sudworth, E. Berry, S. M. Strafford, D. J. Wood, F. A. Carmichael, R. E. Miles, and M. A. Smith. Identification of tooth abnormalities using terahertz imaging and spectroscopy. In *Proceedings of SPIE Diagnostic Optical Spectroscopy*, volume 5141, 2003.

[100] P. F. Taday, I. V. Bradley, D. D. Arnone, and M. Pepper. Using terahertz pulse spectroscopy to study the crystalline structure of a drug: A case study of the polymorphs of ranitidine hydrochloride. In *Journal Pharm. Science*, volume 92, pages 831–838, 2003.

[101] P. A. Anquetil, C. J. Brenan, C. Marcolli, and I. W. Hunter. Laser raman spectroscopic analysis of polymorphic forms in microliter fluid volumes. In *Journal Pharm. Science*, volume 1, pages 149–160, 1992.

[102] M. Walther, P. Plochocka, B. Fischer B, H. Helm, and P. Uhd Jepsen. Collective vibrational modes in biological molecules investigated by terahertz time-domain spectroscopy. In *Biopolymers*, volume 67, pages 310–313, 2002.

[103] M. Brucherseifer, M. Nagel, P. H. Bolivar, H. Kurz, A. Bosserhoff, and R. Buttner. Label free probing of the binding state of DNA by time domain terahertz sensing. In *Applied Physics Letters*, volume 77, pages 4049–4051, 2000.

[104] M. C. Kemp. Security applications of terahertz imaging and spectroscopy. In *Proc. of SPIE:Terahertz for Military and Security Applications*, volume 5070, page 131, 2003.

[105] E. N. Grossman, S. Nolen, N. G. Paulter, and C. D. Reintsema. Concealed weapons detection system using uncooled, pulsed, imaging arrays of millimeter-wave bolometers. In *Proc. of SPIE*, volume 4719, pages 364–369, 2001.

[106] S. Wang, B. Ferguson, C. Mannella, D. Gray, D. Abbott, and X.-C. Zhang. Powder detection using thz imaging. In *OSA Trends in Optics and Photonics*, volume 73, page 131, 2002.

[107] T. Heilweil and M. B. Campbell. Non-invasive detection of weapons of mass destruction using THz radiation. In *Proc. of SPIE:Terahertz for Military and Security Applications*, volume 5070, 2003.

[108] D. Woolard, R. Kaul, R. Suenram, A. H. Walker, T. Globus, and A. Samuels. Terahertz electronics for chemical and biological warfare agent detection. In *IEEE MTT-S Int. Microwave Symp. Dig.*, volume 80, pages 925–928, June 1999.

[109] J. Xu, H. Liu, R. Kersting, and X. Zhang. Improved THz TDS for explosive material detection and tracing. In *Proc. of SPIE:Terahertz for Military and Security Applications*, volume 5070, 2003.

[110] R. Osiander, J. A. Miragliotta, Z. Jiang, and J. Xu. Thz imaging and spectroscopy for landmine detection. In *Proc. of SPIE:Terahertz for Military and Security Applications*, volume 5070, 2003.

[111] A. J. Cantor, P. Cheo, M. Foster, and L. Newman. Application of submillimeter wave lasers to high voltage cable inspection. In *IEEE Journal of Quantum Electronics*, volume 17, pages 477–489, April 2002.

[112] D. M. Mittleman, S. Hunsche, L. Boivin, and M. C. Nuss. T-ray tomography. In *Optics Letters*, volume 22, pages 904–906, 1997.

[113] B. Ferguson, S. Wang, and X. C. Zhang. T-ray computed tomography. In *The 14th Annual Meeting of The IEEE Laser and Electro-Optics Society*, November 2001.

[114] S. Wang and X.-C. Zhang. Tomographic imaging with a terahertz binary lens. In *Applied Physics Letters*, volume 82, pages 1821–1823, March 2003.

[115] E. Hecht. *Optics.* Addison Wesley Longman, 3rd edition, 1998.

[116] S. Noach, A. Lewis, Y. Arieli, and N. Eisenberg. Integrated diffractive and refractive elements for spectrum shaping. In *Applied Optics*, volume 35, page 3635, 1996.

[117] J. Turunen and F. Wyrowski. *Diffractive optics for industrial and commercial applications.* Akademie Verlag, 1997.

[118] D. Grischkowsky, S. Keiding, M. van Exter, and Ch. Fattinger. Far-infrared time-domain spectroscopy with terahertz beams of dielectrics and semiconductors. In *Journal of the Optical Society of America B*, pages 2006–2015, May 1990.

[119] M. van Exter and D. Grischkowsky. Carrier dynamics of electrons and holes in moderately doped silicon. In *Physical Review B*, volume 41, pages 12140–12149, 1990.

[120] P. Rai-Choudhury editor. *Microlithography, Micromachining, and Microfabrication.* SPIE IEEE, 1997.

[121] L. R. Harriott. Limits of lithography. In *Proc. Int. Conf. on Multichip Modules*, pages 366–374, 1994.

[122] H. G. Muller, Y. Yanrong, and R. E. Sheets. Large area fine line patterning by scanning projection lithography. In *Proceedings of the IEEE*, volume 89, pages 100–104, 2001.

[123] K. E. Bean. Anisotropic etching of silicon. In *IEEE Trans. Electron Devices*, volume 25, pages 1185–1193, 1978.

[124] H. Siedel, L. Csepregi, A. Heuberger, and H. Boumgartel. Anisotropic etching of crystalline silicon in alkaline solutions, orientation dependence and behavior of passivation layers. In *Journal Electrochemical Society*, volume 137, pages 3612–2626, November 1990.

[125] Y.J. Lii, J. Jorne, K. C. Cadien, and J. E. Schoenholtz Jr. Plasma etching of silicon in SF_6 experimental and reactor modeling studies. In *Journal Electrochem Soc.*, volume 137, pages 3633–3639, 1990.

[126] H. Jansen, M. d. Boer, J. Burger, R. Legtenberg, and M. Elwenspoek. The black silicon method II: The effect of mask material and loading on the reactive ion etching of deep silicon trenches. In *Microelectronic Engineering*, volume 27, pages 475–480, 1995.

[127] Oxford Instruments (http://www.oxford instruments.com/).

[128] E. D. Walsby. *Fabrication of diffractive optic elements for terahertz radiation.* University of Canterbury, 1999.

[129] E. D. Walsby, R. Cheung, R. J. Blaikie, and D. R. S. Cumming. Fabrication of multilevel silicon diffractive lenses for terahertz frequencies. In *Proc SPIE*, volume 79, page 3879, 1999.

[130] MicroChem Inc. (http://www.microchem.com). *1254 Chestnut Street, Newton, MA 02164-1418, USA.*

[131] M. Despont, H. Lorenz, N. Fahrni, J. Brugger, P. Renaud, and P. Vettiger. High-aspect-ratio, ultrathick, negative-tone near-uv photoresist for MEMS applications. In *International Workshop on Micro Electro Mechanical Systems*, pages 518 –522, January 1997.

[132] R. Legtenberg, H. Jansen, M. de Boer, and M. Elwenspoek. Anisotropic reactive ion etching using $SF_6/O_2/CHF_3$ as mixtures. In *Journal Electrochem Soc.*, volume 142, pages 2020–2027, 1995.

[133] SOTEC Microsystem (http://www.somisys.ch/). *11 avenue des Baumettes, 1020 RENENS, Switzerland.*

[134] F. Laerme, A. Schilp, K. Funk, and M. Offenberg. Bosch deep silicon etching: improving uniformity and etch rate for advanced MEMS applications. In *Twelfth IEEE International Conference on Micro Electro Mechanical Systems*, pages 211–216, January 1999.

[135] R. Bowman, J. Griffin, D. Potter, and R. Skinner editors. *Advanced VLSI Fabrication.* Integrated Circuit Corporation, 1995.

[136] S. M. Sze. *Physics of Semiconductor Devices.* John Wiley & Sons, Ltd, 1981.

[137] K. Siebert, F. Siebe, M. Thomson, J. Zare.Baghbidi, R. Leonhardt, and H. Roskos. Advances in continous-wave THz generation. In *SPIE Proceedings Terahertz Spectroscopy and Applications II*, volume 3828, pages 234–243, 1999.

[138] K. Siebert, H. Quast, R. Leonhardt, T. Loffler, M. Thomson, T. Bauer, S. Czasch, and H. G. Roskos. Continuous-wave all-optoelectronic terahertz imaging. In *Applied Physics Letters*, volume 80, pages 3003–3005, April 2002.

[139] Coherent (http://www.cohr.com/).

[140] A. J. Gatesman, J. Waldman, M. Ji, C. Musante, and S. Yngvesson. An antireflection coating for silicon optics at terahertz frequencies. In *IEEE Microwave and Guided Wave Letters*, volume 10, pages 264–266, July 2000.

[141] R. H. Giles, A. J. Gatesman, J. Fitzgerald, S. Fisk, and J. Waldman. Tailoring artificial dielectric materials at terahertz frequencies. In *The Fourth International Symposium on Space Terahertz Technology*, April 1993.

[142] K. Hane Y. Kanamori, M. Sasaki. Broadband antireflection gratings fabricated on silicon substrates. In *Optics Letters*, volume 24, pages 1422–1424, 1999.

[143] Grating Solver Development Company (http://www.gsolver.com). *Gsolver.*

[144] T. Wilhein, B. Kaulich, E. Di Fabrizio, F. Romanato, S. Cabrini, and J. Susini. Differential interference contrast x-ray microscopy with submicron resolution. In *Applied Physics Letters*, volume 78, pages 2082–2084, 2001.

[145] M. L. Meade. *Lock-in amplifiers: principles and applications.* Peter Peregrinus, 1983.

[146] Mathworks (http://www.mathworks.com). *MATLAB.*

[147] G. B. Jin, Y. B. Yang, and M. X. Wu. *Binary Optics.* China Defense Industry Publishing Company, 1st edition, 1998.

[148] M. B. Stern. Binary optics: A VLSI-based microoptics technology. In *Microelectronic Engineering*, volume 32, pages 369–388, 1996.

[149] B. A. Saleh and M. C. Teich. *Fundamentals of Photonics.* Wiley, 1991.

[150] editor V. Illingworth. *The Penguin Dictionary of Physics.* Penguin, 1991.

[151] M. Born and E. Wolf. *Principles of Optics.* Cambridge University Press, 6th edition, 1999.

[152] J. W. Goodman. *Introduction to Fourier Optics.* Mc-Graw-Hill, 1996.

[153] K. Yee. Numerical solutions of initial boundary value problems involving Maxwell's equations in isotropic media. In *IEEE Transactions on Antennas and Propagation*, volume 14, pages 302–307, 1966.

[154] D. W. Prather. Techniques for applying the FDTD method to the electromagnetic analysis of diffractive optic elements. In *OSA Diffractive Optics and Micro-Optics*, pages 5–9, June 2000.

[155] M. S. Mirotznik, D. W. Prather, J. N. Mait, W. A. Beck, S. Shi, and X. Gao. Three-dimensional analysis of subwavelength diffractive optic elements with the finite-difference time-domain method. In *Applied Optics*, volume 39, pages 2871–2880, June 2000.

[156] M. Rodamaker. Finite element analysis extends its domain. In *IEEE Circuits and Devices Magazine*, volume 11, pages 22–27, 1995.

[157] M. G. Moraram and T. K. Gaylord. Diffraction analysis of dielectric surface-relief gratings. In *J. Opt Soc. Am.*, volume 72, pages 1385–1392, 1982.

[158] M. G. Moraram, E. B. Gran, D. A. Pommet, and T. K. Gaylord. Formulation for stable and efficient implementation of the rigorous coupled-wave analysis of binary gratings. In *J. Opt Soc. Am. A*, volume 12, pages 1068–1076, May 1995.

[159] editor G. L. James. *Geometric theory of diffraction for electromagnetic waves.* Short Run Press Ltd., 3rd edition, 1986.

[160] A. G. Kostenbauder. Ray-pulse matrices: a rational treatment for dispersive optical systems. In *IEEE Journal of Quantum Electronics*, volume 26, pages 1148–1157, June 1990.

[161] S. M. Tan. Wave propagation and Fourier optics. In *Course notes Linear systems*, 2003.

[162] K.-S. Chen, A. A. Ayon, X. Zhang, and S. M. Spearing. Effect of process parameters on the surface morphology and mechanical performance of silicon structures after deep reactive ion etching (DRIE). In *Journal of Microelectricalmechanical Systems*, volume 11, pages 211–216, June 2002.

[163] M. Golub and I. Grossinger. Diffractive optic elements for biomedical applications. In *SPIE*, volume 3199, page 220, December 1997.